Monolithic Colliding Pulse Mode-Locking of AlGaAs/GaAs and InGaAs/InGaAsP Quantum Well Lasers

by

Stewart Duncan McDougall.

February 1997.

UNIVERSITY
of
GLASGOW

A thesis submitted for the degree of Doctor of Philosophy to the Faculty of Engineering, Department of Electronics and Electrical Engineering of the University of Glasgow.

ProQuest LLC.
789 East Eisenhower Parkway
P.O. Box 1346
Ann Arbor, MI 48106 – 1346

Acknowledgements:

I would like to sincerely thank all those who by their hard work and kindness made the completion of this thesis possible. In particular I would like to express thanks to my supervisor Dr Charles Ironside for his help, guidance and his ability to encourage and be positive even when situations seamed to me to be entirely hopeless, and to Dr Kevin Smith at BT labs for the financial support through the CASE Studentship.

Of course every member of the Opto-electronics Research Group in the Department of Electronics and Electrical Engineering, both past and present, deserves credit in some way for the success of this work, however I would like to thank the following academics, research assistants, and students for the particularly important contributions that they made to my work through practical support and helpful discussions: Dr. Joaquim Martins-Filho, Jim Gray, Dr. Evgenni Avrutin, Prof. John Marsh, Ivan Evans, Dr. Ooi Boon Siew, Dr. Karen McIlvanney, Prof. Richard De la Rue, Dr. Catrina Bryce, Dr. Thomas Krauss, Bocang Qui, Dr. Brigitte Vögele, Dr. Pasquale Cusumano, Dr. Andrew McKee, Dr. Craig Hamilton, Dr. Olek Kowalski, and Dr. Maolong Ke.

No acknowledgement would be complete without noting the significant contribution from the technical support staff of the Department of Electronics and Electrical Engineering, who continuously endeavour to keep the clean room and dry etching facilities operational and running smoothly. In particular thanks are due to Lois Hobbs, Joan Carson, Margaret Henderson, Ian McNicholl, Jimmy Young, Robert Harkins, Dave Clifton, and Gillian Hopkins. I also gratefully acknowledge the assistance of Dr. John Roberts and Dr. Chris Button from Sheffield University, for growing many of the semiconductor wafers used in this project.

On a personal note, I would like to express appreciation to my family and friends who provided the diversions necessary for the maintenance of my sanity. Special thanks must go to my parents, Rae and Fred McDougall, not only for the last three years, but for all the success I have achieved in my life so far, which has been enabled by their continued love and support. Finally, I would like to thank my partner Jacqueline, who not only applied her excellent editing skills to this thesis, but has also managed to put up with me on a daily basis, which I am sure was often an arduous task.

Abstract:

The fabrication of T-section colliding pulse mode-locked (T-CPM) GaAs/AlGaAs quantum well lasers is described. These devices have MOVPE grown ridge waveguide laser structures, with monolithically integrated side-injection waveguides, orthogonal to the laser waveguide, passing through the saturable absorber from the edge of the laser chip. This orthogonal waveguide is included to enable synchronisation applications which involve the injection of external optical pulse streams into mode-locked diode lasers. Intensity autocorrelations are performed on these devices, the first time for monolithic CPM lasers in this material system, showing a 400 μm long device mode-locked at a repetition rate of 175 GHz producing near transform-limited 1 ps pulses at wavelengths around 0.87 μm.

A new technique for measuring the gain and absorption spectra in semiconductor material is presented, which utilises the multi-section laser fabrication technology developed for the CPM lasers. Using this new technique the TE and TM absorption spectra of the MOVPE grown T-CPM laser saturable absorber is measured *in situ* under the influence of increasing reverse bias, showing large exciton absorption features, which shift and broaden in accordance with the QCSE. With the measurement of the forward bias gain spectra, the sub-linear form of the gain - current density relationship was directly measured for the mode-locked laser wafer.

The crucial role of quantum well doping in the achievement of high repetition rate monolithic mode-locking has been demonstrated by the realisation of short cavity CPM and multiple colliding pulse (MCPM) lasers in MBE grown GaAs/AlGaAs quantum well material only through background doping of the active region to simulate the effects of the residual carbon impurities incorporated in MOVPE grown AlGaAs. By inspection of the absorption spectra, it is shown that a distinct broadening of the exciton absorption peaks occur with the presence of background doping in MBE material. This indicates that the corresponding decease in the exciton lifetime has a beneficial effect on saturable absorber recovery, allowing high repetition mode-locking to take place.

Low damage dry etching and wet etching techniques have been developed to enable the successful fabrication of ridge waveguide CPM lasers in InP/InGaAs/InGaAsP laser material. Spectral measurements show the mode-locked operation of CPM and T-CPM lasers in strained and lattice-matched material at wavelengths around 1.5 μm. Also, spectral results are presented showing harmonic CPM operation at repetition rates of 150 GHz and 300 GHz (two and four pulse CPM action), from a 600 μm MCPM laser (emitting at a wavelength of 1.53 μm). This is the first reported demonstration of an MCPM laser diode in the long wavelength region around 1.55 μm.

Contents:

Acknowledgements. ii
Abstract. iii
Contents. iv
Conference/Journal Publications. vii

Chapter 1- Introduction. 1
1.1 Applications of mode-locked diode lasers. 1
1.2 Thesis Outline. 4
References 6

Chapter 2- Basics of quantum well semiconductor lasers. 7
2.1 Optical properties of semiconductors. 7
2.1.1 Semiconductor band structure. 7
2.1.2 Density of states in bulk semiconductor. 9
2.1.3 Quasi-Fermi levels. 10
2.1.4 Radiative band to band transitions. 12
2.1.5 Non-radiative transitions. 13
2.2 Heterostructure Lasers. 13
2.2.1 Epitaxy and heterostructure materials. 14
2.2.2 Waveguide modes and lateral confinement. 15
2.2.3 Threshold condition and power output. 17
2.3 Quantum wells. 19
2.3.1 Energy levels and density of states. 19
2.3.2 Gain in quantum wells. 21
2.3.3 Threshold conditions and multiple quantum well lasers. 22
2.3.4 Absorption spectra and electric field effects. 24
References 26

Chapter 3- Mode-locked semiconductor lasers. 27
3.1 Gain/Q-switching in semiconductor lasers. 28
3.1.1 Relaxation oscillations and gain switching 28
3.1.2 Frequency chirp and timing jitter. 28
3.1.2 Active and passive Q-switching. 30
3.2 Review of mode-locking in semiconductor lasers. 31
3.2.1 Qualitative introduction to mode-locking. 31
3.2.2 Active mode-locking. 33

3.2.3 Spectral and pulsewidth broadening. 35
3.2.4 Passive mode-locking using saturable absorbers. 36
3.2.5 Passively mode-locked semiconductor lasers. 39
3.2.6 Timing jitter and chirp in mode-locked diode lasers. 41
3.3 Colliding pulse mode-locked (CPM) semiconductor lasers. 42
3.3.1 CPM dye lasers. 42
3.3.2 Implementation of CPM in diode lasers. 42
3.3.3 Theoretical and practical considerations on CPM and SCPM. 44
3.4 Conclusions. 45
References. 46

Chapter 4- MOVPE grown GaAs/AlGaAs T-CPM MQW lasers. **49**
4.1 GaAs/AlGaAs material QT664. 49
4.1.1 Wafer specification. 49
4.1.2 Material Characterisation. 50
4.2 T-CPM laser fabrication. 54
4.2.1 Laser design. 54
4.2.2 Laser fabrication. 56
4.3 T-CPM laser testing. 60
4.3.1 Device cleaving and mounting. 60
4.3.2 CW laser testing. 63
4.4 Conclusions. 68
References. 69

Chapter 5- Characterisation of CPM lasers by autocorrelation techniques. **70**
5.1 Linear cross-correlator. 71
5.1.1 Introduction to the instrument. 71
5.1.2 Correlation function of the output of a multi-mode laser. 72
5.1.3 Output of linear cross-correlator. 74
5.1.4 Linear correlation simulation. 75
5.1.5 Experimental results. 78
5.2 SHG intensity autocorrelator. 80
5.2.1 Advantages of intensity over field correlations. 80
5.2.2 Non-linear mixing in SHG crystals. 82
5.2.3 Intensity autocorrelator instrument. 83
5.2.4 Experimental results. 85
5.3 Conclusions. 90
References. 92

Chapter 6- Absorption spectra measurements. 93
6.1 Two-contact laser absorption spectra measurements. 93
6.1.1 Absorption spectra measurement techniques. 93
6.1.2 Description of the two-contact method. 95
6.2 Experimental results. 97
6.2.1 Saturable absorber reverse bias absorption spectra. 97
6.2.2 Forward bias gain spectra. 101
6.3 Conclusions. 106
References. 108

Chapter 7- GaAs/AlGaAs CPM lasers in MBE grown MQW material. 110
7.1 MCPM lasers. 110
7.2 MCPM lasers in MBE grown material. 113
7.2.1 Fabrication of standard-MBE lasers. 113
7.2.2 Fabrication of backdoped-MBE lasers. 115
7.2.3 Effects of doping on absorption spectra. 118
7.3 Conclusions. 121
References. 123

Chapter 8- Long wavelength CPM lasers. 124
8.1 Long wavelength laser material. 124
8.1.1 Standard (lattice-matched) wafer structure (MR763). 124
8.1.2 Strained layer wafer structure (MR396). 126
8.2 InP/InGaAsP RWG laser fabrication. 127
8.2.1 Wet etching method. 127
8.2.2 Dry etching method. 130
8.2.3 Dry/wet etch RWG laser comparison. 135
8.3 CPM laser results. 136
8.4 MCPM laser results. 140
8.5 Conclusions. 143
References. 144

Chapter 9- Summary and conclusions. 145

Conference/Journal Publications:

J.F.Martins-Filho, S.D.McDougall, E.A.Avrutin, C.N.Ironside, "Multiple colliding pulse mode locked lasers for high repetition rate (up to 375 GHz) shortpulse generation", in *IEE colloquium on Towards Terabit Transmission*, Savoy Place, London 19 May Digest Number 1995/110 pp16/1-16/6.

S.D.McDougall, J.F.Martins-Filho and C.N.Ironside, "T-Junction colliding-pulse mode-locked quantum well laser for all-optical clock recovery", *National Quantum Electronics Conference- QE-12*, P1-4, 1995

S.D.McDougall and C.N.Ironside, "Measurements of reverse and forward bias absorption and gain spectra in semiconductor laser material", *Electronics Letts.* vol.31 pp2179-2181 1995.

S.D.McDougall, J.F.Martins-Filho and C.N.Ironside, "An investigation of monolithic colliding pulse mode locked semiconductor lasers", *Conference on Lasers and Electro-Optics (CLEO) '96,* Anaheim, paper CThK38, 1996.

S.D.McDougall, B.Vögele, C.R.Stanely and C.N.Ironside, "The crucial role of doping for high repetition rate mode-locking multi-quantum well GaAs/AlGaAs lasers," accepted for presentation in *Conference on Lasers and Electro-Optics (CLEO) '97,* Boltimore, paper CWF1, 1997.

Chapter 1-Introduction.

The extremely short optical and electrical pulses that can be generated using semiconductor lasers have many important technological applications[1]. These include: fibre-optic communications systems; microwave generation, switching, and detection; electro-optic sampling; diagnostics of high-speed electrical and optoelectronic components; and a host of novel high speed optoelectronic instrumentation. Before the invention of semiconductor lasers as ultrashort pulse sources, with their small size, low cost, simple operation, and convenient electrical pumping, such applications were considered either simply impossible or economically prohibitive.

This thesis presents an investigation of the properties of a specific type of diode laser pulse source - namely the monolithic colliding-pulse mode-locked (CPM) quantum well semiconductor laser[2]. Such devices are able to produce pulses in the order of picoseconds, at repetition rates of hundreds of gigahertz, and as they are passively mode-locked devices, they require no high speed electronic signals for their operation, only a straightforward DC bias. The term *mode-locking* is used to describe the method of concentrating all the power of an oscillating laser source into short intense optical pulses, by forcing the various emission wavelengths (or modes) present to maintain a fixed phase relationship with each other. CPM lasers differ from conventional mode-locked diode lasers, in that their saturable absorber (the modulating element) is positioned at the centre of the laser cavity and not one of its ends. Collision of pulses in the absorber has the effect of producing shorter pulses with increased stability. Along with ease of operation, the CPM lasers discussed in this work are entirely monolithic, with all the semiconductor elements required for the device integrated in a single semiconductor chip.

In the following section, it is intended to present the reader with a brief overview of the myriad of contemporary and potential future applications that motivate study in the field of mode-locked diode lasers. At the conclusion of this chapter an outline of the contents of the remainder of the thesis is provided.

1.1- Applications of mode-locked diode lasers.

Optical communications systems are perhaps the most important application for short pulse diode lasers[3]. Fibre-optic digital telecommunications networks, in place today, allow data to be transmitted at 2.5 gigabits per second, a speed system designers could only dream of just over a decade ago. Already, trials at the next level of 10 Gbit/s are taking place[4]. With the increasing demand for broad band information

systems world wide, efforts are being made to develop techniques that utilise more fully the almost limitless capacity of the optical fibre, enabling systems to operate at potentially 100's or 1000's of Gbit/s.

GaAs/AlGaAs based semiconductor lasers, which were historically the first to be successfully developed, have a wide spread implementation in short haul fibre-optic communications systems. These devices operate in the wavelength region of 0.65 μm to 0.9 μm, where inexpensive silicon photodetectors are commercially available. Optical fibres offer vast improvements in the distances over which digital signals can be transmitted compared with electrical cables, before dispersion, attenuation and distortion from noise renders a signal unreadable. Current advances, such as dispersion shifted fibre (DSF) and erbium-doped fibre amplifiers (EDFAs), can increase the required signal regeneration spacing for a wavelength centred on the silica fibre low loss window of 1.55 μm[4]. For this reason, it is preferable in long haul optical communications, such as trans-oceanic links, to operate at this low loss wavelength. As the semiconductor material system InP/InGaAs/InGaAsP covers the long wavelength range 1.1 μm to 1.7 μm, diode lasers based on this system are attractive for these applications. However, due to normal fibre attenuation and dispersion effects (as the optical spectrum of the laser light pulses is finite), there is still a need for a periodic regeneration of the optical data signal. Currently the fibre-optic systems are employed merely as links between electronic signal processing stages, which perform the task of regenerating the data signal. As bit rates increase, the inherently slower electronics give rise to so called *electronic bottlenecks* at processing stages, which would effectively limit the speed of future communications networks. High speed all-optical signal processing would be a solution to this problem, removing any intermediate optical-to-electronic conversions, with the signal remaining entirely optical between end users[5]. A vital ingredient, if these new generation lightwave communications systems are to be realised, is the synchronisation of an optical clock signal to the data rate of any incoming signals. This is known as all-optical clock recovery. Recently this has been successfully demonstrated using a number of techniques, including those involving mode-locked fibre lasers[6] and self-pulsating laser diodes (SPLDs)[7]. Although SPLDs are tuneable over a wide frequency range[8], it is unlikely that they will be able to perform all-optical clock recovery at rates of 100's of Gbit/s, whereas the extremely high repetition rates (>THz[9]), and high spectral purity of mode-locked diode lasers make them ideal candidates. All-optical clock recovery using mode-locked diode lasers would also offer advantages of compactness over the fibre laser approaches. Work is currently ongoing to investigate optical synchronisation locking[10,11,12] and all-optical clock recovery in mode-locked semiconductor lasers[13]. Other signal processing such as optical clock distribution[14], and all-optical multiplexing and demultiplexing[12,15] would also be highly suitable for mode-locked diode lasers.

As bit rates increase, the maximum distance before signal regeneration is required becomes shorter. One possible solution to this problem is to invoke *optical soliton* transmission techniques[16]. By careful matching of pulse shape and power to fibre parameters, dispersion in the fibre can be balanced by non-linear self-phase modulation. In this way, solitons can be generated, which maintain their pulse shape for an infinite distance. The spectral purity of the pulses used to generate solitons is extremely important: indeed the pulses are required to be transform-limited (lowest possible pulse width from a given frequency spectrum). Mode-locked semiconductor lasers, and in particular CPM lasers, are important sources of transform-limited pulses[2]. Fibre losses still attenuate solitons, but this can be compensated through in-fibre amplification (EDFAs). However, due to the non-linear nature of solitons, spontaneous emission noise from amplifiers generates timing jitter in a soliton stream. The result is a maximum soliton propagation distance for a given bit rate (Gordon-Haus limit)[17]. Again mode-locked diode lasers could have an application here, as active retiming or *shepherding* (to overcome the Gordon-Haus limit) is possible by interacting the soliton data and an optically recovered clock in a length of non linear medium[18].

Aside from fibre-optics systems, there is another broad band of potential communications applications for mode-locked diode lasers, based on the generation of microwave frequency electromagnetic waves through picosecond photoconductivity in semiconductors. The absorption of picosecond pulses in semiconductors generates an electron-hole pair essentially instantaneously. Hence the leading edge of the generated electrical waveform follows the leading edge of the optical pulse, with the trailing edge decaying with a time governed by electron-hole recombination. In passively mode-locked and Q-switched lasers, absorbers can be monolithically integrated into the laser cavity itself. Thus if antennas are incorporated with the absorber contact, the electrical waveform generated due to the absorption of the ultra short pulses oscillating in the laser cavity at high repetition rates (>GHz) will be emitted as microwave electromagnetic signals[19,20].

An electric field across certain crystals can alter the polarisation of a light signal travelling through it. This is known as the *electro-optic effect*[21]. Thus the intensity of light transmitted through an electro-optic crystal between two crossed polarisers can be altered by varying the electric field applied to the crystal. If laser pulses are fired into an electro-optic crystal through crossed polarisers during the passage of a short electrical pulse, the change in intensity of the light signal received at a photodiode will be proportional to the delay between the optical and electrical pulses. Thus by varying the delay of the incoming laser pulses the electric signal can be effectively sampled. This technique of *electro-optic sampling* can be used as a diagnostic tool to investigate the response of electrical circuits, and is an important potential application for mode-locked diode lasers[22].

There are many other applications for the short pulses produced by diode lasers and these include for example, radar range finding, collision warning sensors, and high speed optoelectronic devices, such as sampling oscilloscopes. Diode lasers in radar applications, with their small size and ease of packaging combined with low cost, are currently in use in wide range of precision industrial manufacturing.

1.2- Thesis outline.

The majority of the work presented in this thesis is concerned with the fabrication, operation and characterisation of CPM lasers in the short wavelength GaAs/AlGaAs material system, although the penultimate chapter describes an extension of this, with the realisation of devices in the long wavelength InP/InGaAs/InGaAsP material system, which are particularly suited to low loss long haul fibre-optic telecommunications applications. Chapters 2 and 3 give a general background to the field of semiconductor mode-locked laser research.

Chapter 2 provides a discussion of the basic theory behind semiconductor optical transitions and semiconductor heterostructure lasers. As quantum wells are used in this project to form the active light emitting regions of the laser material, their special properties are also discussed.

A detailed review of the background theory and the published literature on mode-locking in semiconductor lasers, is presented in Chapter 3, with particular emphasis on CPM lasers. Also included in this chapter is a brief summary of the other pulse generation techniques applicable to diode lasers- gain switching and Q-switching.

Chapter 4 details the processes used to fabricate the GaAs/AlGaAs CPM lasers in this project. The fabrication of novel T-section CPM lasers from a MOVPE grown GaAs/AlGaAs quantum well laser material is described, along with the subsequent frequency domain characterisation.

Linear and non-linear correlation techniques for the time domain characterisation of mode-locked laser pulses are discussed in Chapter 5. Using these techniques, the mode-locking behaviour of MOVPE GaAs/AlGaAs T-CPM lasers is studied.

In Chapter 6, the development of a new method for the measurement of gain and absorption spectra in semiconductor laser structures is described. This method is applied to study the effects of reverse and forward bias on the saturable absorber of the T-CPM lasers, which is important for a complete understanding of the dynamics involved in the mode-locking process.

The important role of active region doping in achieving mode-locking at high repetition rates in GaAs/AlGaAs lasers is discussed in Chapter 7, in the context of MBE grown laser material.

In Chapter 8, the emphasis shifts from the short wavelength of 0.86 μm to the long wavelength region around 1.55 μm. The fabrication processes with their associated problems are discussed for InP/InGaAs/InGaAsP CPM laser. This chapter also presents spectral results that indicate the mode-locking behaviour of the fabricated devices.

Finally in Chapter 9, the results from all the previous chapters are summarised and discussed.

Chapter 1: References.

[1]P.Vasil'ev, Ultrafast *Diode Lasers: Fundamentals and Applications,* Artech House, 1995.

[2]Y.K.Chen & M.C.Wu, "Monolithic colliding-pulse mode-locked quantum-well lasers," *IEEE J.Quantum Electron.*, vol.28, pp.2176-2185, 1992

[3]C.Lin., *Optoelectronic Technology and Lightwave Communications Systems,* New York: Van Nostrand Reinhold, 1989.

[4]R.Heideman, B.Wedding & G.Veith, "10-GB/s Transmission and Beyond," *Proceedings of the IEEE,* vol.81, pp1558-1567, 1993.

[5]S.Shimada, K.Nakagawa, M.Saruwatari & T.Matsumoto, "Very-High-Speed Optical Signal Processing," *Proceedings of the IEEE,* vol.81, pp1633-1646, 1993

[6]J.K.Lucek & K.Smith, "All-optical signal regenerator," *Optics.letts,* vol.18, pp.1226-1228, 1993

[7]P.Barnsley, "All-optical clock extraction using two-contact devices," *IEE Proceedings-J,* vol. 40, pp325-336, 1993.

[8]U.Feiste, M.Möhrle, B.Sartorius, J.Hörer & R.Löffler, "12GHz to 64GHz Continuous Frequency Tuning in Self pulsating 1.55μm Quantum Well DFB Lasers," *14th IEEE International Semiconductor Laser Conference,* Maui, Hawaii, USA, Sept 1994, paperTH2.3, pp.227-228

[9]S.Arahira, Y.Matsui, and Y.Ogawa, "Mode-locking at very high repetition rates more than terahertz in passively mode-locked distributed-bragg-reflector laser diodes," *IEEE.J.Quantum.Electron,* vol.32, pp1211-1224, 1996.

[10]E.A.Avrutin, J.M.Arnold, and J.H.Marsh, "Analysis of dynamics of monolithic passively mode-locked laser diodes under external periodic excitation," *IEE. Proc.Optoelectron.*, vol.143, pp81-88, 1996.

[11]S.Arahira, and Y.Ogawa, "Synchronous mode-locking in passively mode-locked semiconductor laser diodes using optical short pulses repeated at subharmonics of the cavity round-trip frequency," *IEEE Photon.Tech.Lett.*, vol.8, pp191-193, 1996.

[12]X.Wang, H.Yokoyama, and T.Shimizu, "Synchronised harmonic frequency mode-locking with laser diodes through optical pulse train injection," *IEEE Photon.Tech.Lett.*, vol.8, pp617-619, 1996.

[13]R.Ludwig, A.Ehrhardt, W.Pieper, E.Jahn, N.Agrawal, H.-J.Ehrke, L.Kuller, and H.G.Weber, "40Gbit/s demultiplexing experiment with 10GHz all-optical clock recovery using a modelocked semiconductor laser," *Electron.lett.*, vol.32, pp327-329, 1996.

[14]P.J.Delfyett, D.H.Hartman, and S.Zuber Ahmad, "Optical clock distribution using a mode-locked semiconductor laser diode system", *IEEE.J.Lightwave Technol.*, vol.9, pp1646-1649, 1991.

[15]R.S.Tucker, G.Eisenstein, and S.K.Korotky, "Optical time division multiplexing for very high bit-rate transmission," *J.Lightwave.Technol.*, vol.6, pp1737-1749, 1988.

[16]H.A.Haus, "Optical fibre solitons, their properties and uses," *Proceedings of the IEEE,* vol.81, pp970-983, 1993.

[17]J.P.Gordon & H.A.Haus, "Random walk of coherently amplified solitons in optical fibre transmission," *Optic,Lett.*, vol.11, pp665-667, 1986.

[18]T.Widdowson, D.J.Malyon, .D.Ellis, K.Smith & K.J.Blow, "Soliton shepherding: All-optical active soliton control over global distances," *Electron.lett.*, vol.30 pp.990-991, 1994

[19]D.J.Derickson, R.J.Helkey, A.Mar, J.G.Wasserbauer, Y.G.Wey, and J.E.Bowers, "Microwave and millimetre wave signal generation using mode-locked semiconductor lasers with intra-waveguide saturable absorbers," *IEEE International Microwave Theory and Technology Symposium,* Albuquerque, paper V-2 pp753-756, 1992.

[20]Z.Ahmed, H.F.Liu, D.Novak, Y.Ogawa, M.D.Pelusi, and D.Y.Kim, "Locking characteristics of a passively mode-locked monolithic DBR laser stabilized by optical injection," *IEEE Photon.Tech.Lett.*, vol.8, pp37-39, 1996.

[21]A.Yariv, *Quantum Electronics*, Wiley, 1989.

[22]M.Shinagawa, and T.Nagatsuma, "A laser-diode based picosecond electrooptic prober for high speed LSI's," *IEEE Trans.Instrumentation and Measurement,* vol.41, pp375-380, 1992.

Chapter 2-Basics of quantum well semiconductor lasers.

Modern semiconductor diode lasers have active light emitting regions that consist of extremely thin layers, known as quantum wells (QW). These are so thin that quantum confinement of carriers takes place. This becomes vitally important when considering their optical properties and the operation of lasers made from them. The use of quantum wells in diode lasers offers many desirable advantages over conventional bulk semiconductor lasers including improvement in threshold currents, modulation bandwidth, temperature stability and ease of integration with other opto-electronic components.

In this chapter the basics of laser action in semiconductors will be reviewed, along with a discussion of some of the relevant physics, and optical properties of quantum wells and quantum well lasers.

2.1-Optical properties of semiconductors.

2.1.1-Semiconductor band structure.[1]

Semiconductors have regular crystalline lattice formations, and to find a solution for the allowed kinetic energy of electrons in the crystal one must in general solve the Schrödinger wave equation (2.1) for the specific periodically varying potential. This leads to a band model relating allowed energy states given carrier momenta: a dispersion relationship.

$$H(\mathbf{r})\Psi(\mathbf{r})=\left[\mathbf{p}^2/2m+ V(\mathbf{r})\right]\Psi(\mathbf{r})=E\Psi(\mathbf{r}) \qquad (2.1)$$

Here $H(\mathbf{r})$ is the time independent Hamiltonian, the momentum operator $\mathbf{p}=-i\hbar\nabla(\mathbf{r})$, $V(\mathbf{r})$ is some periodic potential and $\Psi(\mathbf{r})$ is the electronic wavefunction.

Bragg diffraction of the electronic waves in the crystalline structure leads to the formation of forbidden energy gaps where no electronic states can exist. A material with its highest occupied energy band only partially filled, with more energetic states readily available, is a conductor. However, if at 0 K all electron states in the highest band are occupied, and separated from empty ones by an energy gap the material has insulating properties. In semiconductors the energy gap, is of the order of 0-2eV, so there is a small probability that the higher energy band is populated thermally. The filled band is the valence band and the unfilled band is the conduction band. Promotion of an electron from the valence band to the conduction band leaves a vacancy which is treated as a positive particle, or *hole*.

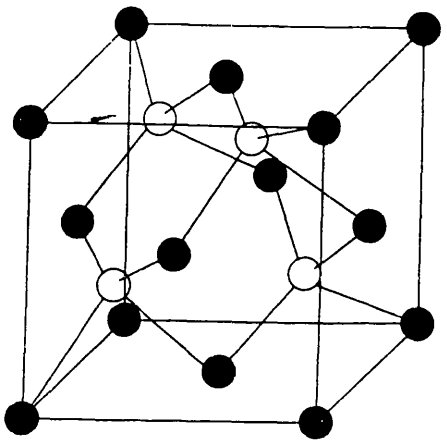

Figure 2.1(a): FCC lattice of III-V semiconductors

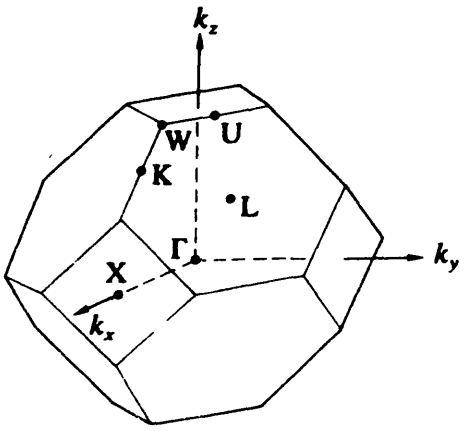

Figure 2.1(b): First Brillouin zone of FCC lattice.

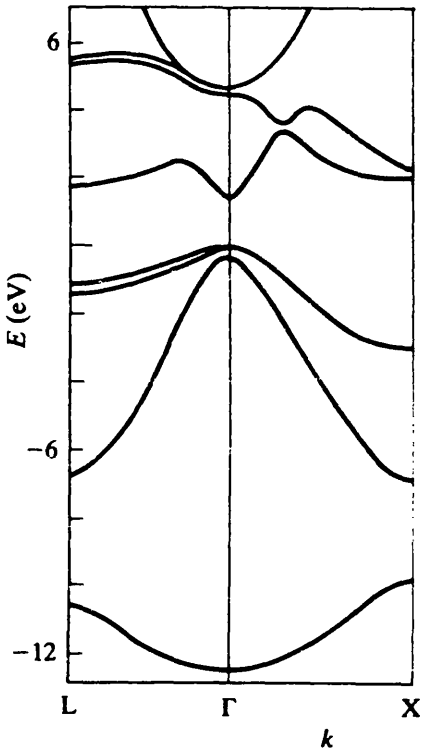

Figure 2.1(c): Band structure of GaAs

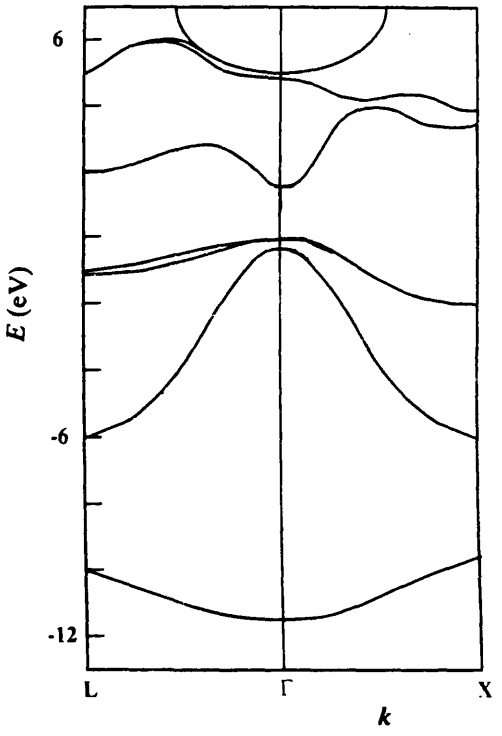

Figure 2.1(d): Band structure of InP

Figure 2.1(a) shows the face-centred cubic (FCC) lattice structure common to the groupIII-groupV semiconductor compounds. The repeatable unit in reciprocal space is the Brillouin zone, which is shown in figure 2.1(b) for a FCC lattice. The energy band structure of two important optical semiconductors, GaAs and InP, both of which have been used in the semiconductor laser structures in this project, are shown for various directions in the first Brillouin zone in Figure 2.1(c),(d). An important feature of these is the coincidence of conduction band minima and valence band maxima at the zone centre $\Gamma(k=0)$. Because of conservation of momentum, *direct gap* semiconductors such as those in figure 2.1 are used in applications involving emission of photons. Photons have negligible momentum, so electronic transitions take place predominately between electrons and holes of equal **k**. This is possible at the direct gap. Indirect band gap semiconductors require the presence of a phonon to conserve momentum, a four particle process, which leads to a lower probability of radiative transition.

The general solution of the Schrödinger wave equation (2.1), for a carrier in a periodic potential is given by a Bloch function:

$$\Psi(\mathbf{r})=u_k(\mathbf{r})\exp(i\mathbf{k}.\mathbf{r}) \qquad (2.2)$$

where $u_k(\mathbf{r})$ is a function that contains the periodicity of the lattice and $\exp(i\mathbf{k}.\mathbf{r})$ is a plane wave with propagation constant **k**. The three dimensional reciprocal space is quantised by the constants $k_x=2\pi s/L_x$, $k_y=2\pi s/L_y$, $k_z=2\pi s/L_z$, where s is an integer and $L_{x,y,z}$ the lengths of the crystal in the x,y,z directions.

Because the effect of the lattice potential is generally weak in a semiconductor, a useful and illustrative approximation for the dispersion relationship is that of free carrier kinetic energy. This is the parabolic band approximation:

$$E(k)=p^2/2m=\hbar^2k^2/2m. \qquad (2.3)$$

So defining the zero energy at the conduction band minimum, and band gap E_g, the following relations are used for carriers in the conduction and valence bands:

$$E_c(k)=\hbar^2k^2/2m_c \quad \text{and} \quad (E_g - E_v(k))=\hbar^2k^2/2m_v \qquad (2.4)$$

where m_c is the effective mass of the electron in the conduction band. Similarly for the valence bands we have $m_v=m_{lh}$ for light hole band and $m_v=m_{hh}$ for heavy holes where $m_{hh}>m_{lh}$.

2.1.2-Density of states in bulk semiconductor.

Using the quantisation defined in the previous section, the volume of each state in k-space is given by $8\pi^3/V$, where $V=L_x.L_y.L_z$. The total number of states up to k is given by N(k)=Volume of sphere radius k/Volume of each state. This gives us $N(k)=k^3V/3\pi^2$, and the increase of N(k) with k is $dN(k)/dk=k^2V/\pi^2$. So the number of states from k to k+dk per unit volume is : $\rho(k).dk=k^2/\pi^2.dk$ (2.5)

This is now converted to energy density by noting $\rho(E).dE=\rho(k).(dk/dE).dE$, and by using equation (2.5) and k from (2.3) the energy density of states per unit volume in a parabolic band is:

$$\rho(E) = \frac{1}{2\pi^2}\left(\frac{2m}{\hbar^2}\right)E^{1/2} \tag{2.6}$$

2.1.3-Quasi Fermi levels.

Electrons and holes in semiconductors obey the Pauli exclusion principle and so ensembles are governed by Fermi-Dirac statistics, which give the probability of occupation of an energy level E (at temperature T) by the Fermi function:

$$f(E) = \frac{1}{e^{(E-E_F)/k_BT}+1} \tag{2.7}$$

where E_F is the Fermi energy (at which probability of occupancy is 50%) and k_B is the Boltzman constant. In thermal equilibrium, a single Fermi level can adequately describe the number of filled hole and electron states. In degenerate semiconductors, where doping is present, the Fermi level is fully in the conduction band for n-type, or in the valence band for p-type. However, with the injection of minority carriers, such as in a forward biased p-n junction, the equilibrium is disturbed. If the injection of electrons and holes is continuous, they can be thought of as being in equilibrium with themselves, and then quasi-Fermi levels E_{Fc}, E_{Fv} can be defined to describe the occupancy of the respective bands.

$$f_c(E_c) = \frac{1}{e^{(E_c - E_{Fc})/k_BT}+1} \quad \text{and} \quad f_v(E_v) = \frac{1}{e^{(E_v - E_{Fv})/k_BT}+1} \tag{2.8}$$

2.1.4-Radiative band to band transitions.[2,3]

There are three main processes involving the interaction of electrons and holes with an electromagnetic field: spontaneous emission, where an electron in the conduction band recombines with a hole in the valence band generating a photon; stimulated absorption, where absorption of a photon promotes a valence electron to the conduction band; and stimulated emission where the presence of a photon stimulates the emission of another photon of equal energy, recombining an electron hole pair. The latter process is equivalent to amplification, and is the basis of laser action.

Consider a direct bandgap semiconductor with degenerate electron/hole populations (Figure 2.2). To obtain an expression for the probability for a photon induced transition of a conduction band electron to the valence band, the interaction of the electron and hole wavefunction with that of an electromagnetic wave, represented by the expression

$\mathbf{E}(\mathbf{r})=\mathbf{E}_0(\mathbf{r})\exp(-i(\omega t-\mathbf{k}_{opt}.\mathbf{r}))$, is considered. From Maxwells equations $\mathbf{E}(\mathbf{r})=-\partial\mathbf{A}(\mathbf{r})/\partial t$ where $\mathbf{A}(\mathbf{r})$ is the vector potential. So $\mathbf{A}(\mathbf{r})=\mathbf{A}_0\exp(-i(\omega t-\mathbf{k}_{opt}.\mathbf{r}))$ with $\mathbf{A}_0=\omega^{-1}\mathbf{E}_0\mathbf{x}$, and $\mathbf{x}$ is a unit vector giving the field polarisation.

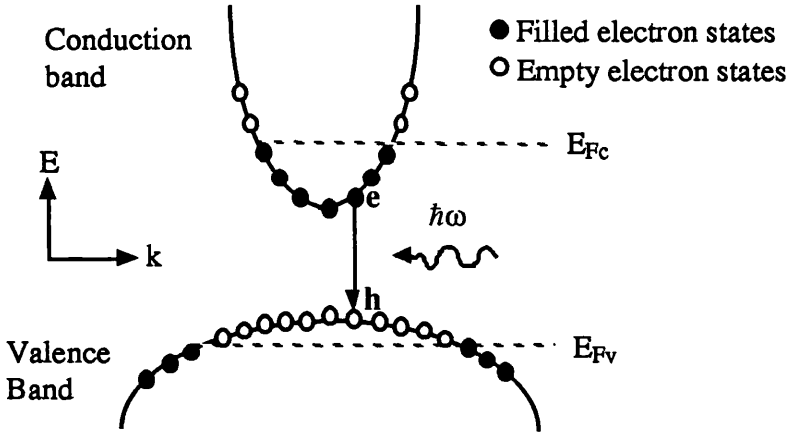

Figure 2.2: Interaction of a photon, energy $\hbar\omega$, with electronic states **e** and **h**, in a degenerate direct gap semiconductor.

From time dependent perturbation theory the vector potential interacts with the carrier momentum via the Hamiltonian:

$$H'(r) = -\frac{e}{m_o}\mathbf{A}.\mathbf{p} \tag{2.9}$$

If the Bloch wavefunctions of the initial and final states of the transition are labelled Ψ_e and Ψ_h corresponding to energies E_e and E_h, Fermi's Golden Rule gives the probability of a transition between these states as:

$$W_{e\to h} = \frac{2\pi}{\hbar}\left|H'_{eh}\right|^2 \delta(E_e - E_h - \hbar\omega) \tag{2.10}$$

$$\text{where } H'_{eh} = \int_V \Psi_h^* H'(r)\Psi_e d^3r \Rightarrow \left|H'_{eh}\right|^2 = \left(\frac{eA_o}{2m_o}\right)^2 |M_T|^2 \tag{2.11}$$

$|M_T|^2$ in (2.11) is known as the transition matrix element and requires detailed knowledge of the hole/electron Bloch functions for evaluation. At an intuitive level it is evident that the integral in (2.11) will contain a summation of terms of the form $\exp(i(\mathbf{k}_h-\mathbf{k}_e-\mathbf{k}_{opt}).\mathbf{r})$, which will be approximately zero unless $\mathbf{k}_h-\mathbf{k}_e=\mathbf{k}_{opt}$ The photon momentum is negligible giving rise to the selection rule stated in section 2.1.1, i.e. $\mathbf{k}_h=\mathbf{k}_e$.

The expression (2.10) above is the transition probability between one pair of initial and final states. The total rate in unit volume is the summation over all the available k-states in the conduction and valence bands, given by:

$$W_{c\to v} = \frac{1}{V}\int W_{e\to h}\, dN_c = \frac{2\pi}{\hbar}\int \left|H'_{eh}\right|^2 \delta(E_{eh} - \hbar\omega)\rho(k)dk$$

$$= \frac{2\pi}{\hbar}\int_0^{\hbar\omega} \left|H'_{eh}\right|^2 \delta(x)\rho(k)\frac{dx}{dE_{eh}/dk} = \frac{2\pi}{\hbar}\left|H'_{eh}\right|^2\left[\frac{\rho(k)}{dE_{eh}/dk}\right]_{\hbar\omega}$$

where the variable $x=E_{eh}-\hbar\omega$ was introduced. Now from equation (2.4) $dE_{eh}/dk=\hbar^2k/m_r$ can be substituted, where m_r is reduced mass $m_cm_v/(m_c+m_v)$. The term in brackets is known as the reduced density of states, and by converting to energy density and multiplying by the Fermi functions to take state occupancy into account, the final result can be expressed by:

$$W_{c\to v} = \frac{2\pi}{\hbar}\left|H'_{eh}\right|^2 \rho_{red}(\hbar\omega - E_g) f_c(1 - f_v) \qquad (2.12)$$

The probability of the reverse transition from valence to conduction is obtained by swapping subscripts on the Fermi functions of equation (2.12).

Knowing the probability of both these transitions the condition for net gain or amplification can be evaluated. Assuming a flux of photons in the x direction of a semiconductor medium, optical gain is defined as the fractional increase in photon flux per unit length:

$$\gamma = \frac{1}{\Phi} d\Phi/dx = \frac{W_{c\to v} - W_{v\to c}}{\Phi} \qquad (2.13)$$

The energy flux of an electromagnetic wave is given by the Poynting vector $S=|\langle ExH\rangle| = {}^1/_2E_o^2n\varepsilon_oc$. So the photon flux is $\Phi=(1/\hbar\omega)^1/_2E_o^2n\varepsilon_oc$. (2.14)

So from equations (2.12)-(2.14), and by putting together all the constants as K, the gain as function of photon energy is written as:

$$\gamma(\hbar\omega) = K(\hbar\omega - E_g)^{1/2}(f_c(\hbar\omega) - f_v(\hbar\omega)) \qquad (2.15)$$

For net gain, (2.15) gives the condition $f_c>f_v$ which by considering (2.8), is equivalent to the inequality $E_g<\hbar\omega<E_{Fc}-E_{Fv}$ (2.16)

So the quasi-Fermi level separation must be larger than the bandgap to achieve a population inversion and net amplification. In an intrinsic or p-doped semiconductor, the conduction band electron concentration is small, hence $f_c-f_v\approx-1$ and the material is highly absorbent. Alternatively with n-doping, $f_c-f_v\approx0$, which only results in transparency at best. The only way to fulfil the criteria for a population inversion is to create a non-equilibrium distribution, which can be achieved in the depletion region of a p-n junction under current injection, giving rise to simultaneous electron and hole populations.

The results given in equations (2.15) and (2.16) correspond to the highly simplified case, in which doping levels have not been taken into account. High concentrations of ionised impurities alter the dispersion relationship at the band minima/maxima due to their locally varying potential interacting with the carrier momenta, leading to a

relaxation in the k-selection rule. Impurities have a *hydrogen like* band structure associated with them, which contribute to the formation of so called band-tail states. The fact that carriers have a finite lifetime in each state and do not simply wait for an interaction with a photon, has also been ignored. Carriers scattering with other carriers or lattice phonons leads to a spread in the possible photon interaction energies which broaden the gain spectrum.

2.1.4-Non-radiative transitions.[4]

Along with band to band transitions involving the emission of photons, carriers can recombine non-radiatively. There are three main processes through which this happens- defect recombination, surface recombination, and Auger recombination

Defects within a crystal structure can give rise to the creation of a local continuum of states that span the bandgap. Carriers within a diffusion length of such a defect can then recombine through these states with no photon requirement.

A high concentration of recombination centres due to defects can appear at facets or exposed surfaces. At these surfaces free bonds can easily absorb impurities from the atmosphere creating the defect sites.

Auger recombination involves four particle states, where the energy released during a band to band transition is not emitted as a photon, but used in promotion of another carrier to a higher energy band, and has a cubic dependence on carrier density. Conservation of energy and momentum leads to a minimum energy requirement for carriers to be involved in the process. This energy is related to the bandgap and effective mass. Hence there is a strong wavelength and temperature dependence on the Auger recombination rate. Auger recombination is dominant in InGaAsP lasers (1.5μm) and is about 100 times faster than for GaAs (0.85μm). Recombination through this process can be assisted by the presence of defect states or phonons which relieve the momentum conservation condition. Quaternary compounds like InGaAsP have a relatively high occurrence of crystal imperfections and defect states due to the complex structure.

2.2-Heterostructure lasers.[4,5]

The first demonstration of laser action in semiconductors took place in 1962, utilising a forward biased GaAs p-n junction, with cleaved facets perpendicular to the junction plane to provide the feedback, forming a Fabry-Perot (FP) cavity. As previously considered, current injection through such a device generates a minority carrier population, providing the optical gain and laser action. However the region over which a sufficient population inversion can be sustained is very thin, due to carrier

diffusion. Hence these devices had extremely high threshold currents for room temperature operation (>50kA/cm^2). Carriers can be confined to an active region if such a region is formed by sandwiching a layer of one type of semiconductor material between two layers of another- a heterostructure. This approach also has the advantage of providing confinement of the optical mode through dielectric waveguiding. These types of structures were made possible through the development of lattice matched crystalline growth of one semiconductor over another, known as epitaxy. With heterostructure lasers, threshold currents had been reduced to 0.5kA/cm^2 by 1975.

2.2.1 Epitaxy and heterostructure materials.

There is a vast range of wavelengths that can be covered by semiconductor laser sources, starting from the near ultraviolet to the far infrared (0.3μm-30μm). This project is concerned with the operation of heterostructure lasers in two material systems: GaAs/AlGaAs which can cover the spectrum from 0.8μm to 0.9μm, and InGaAsP/InGaAs/InP which can operate between 1.1μm and 1.6μm.

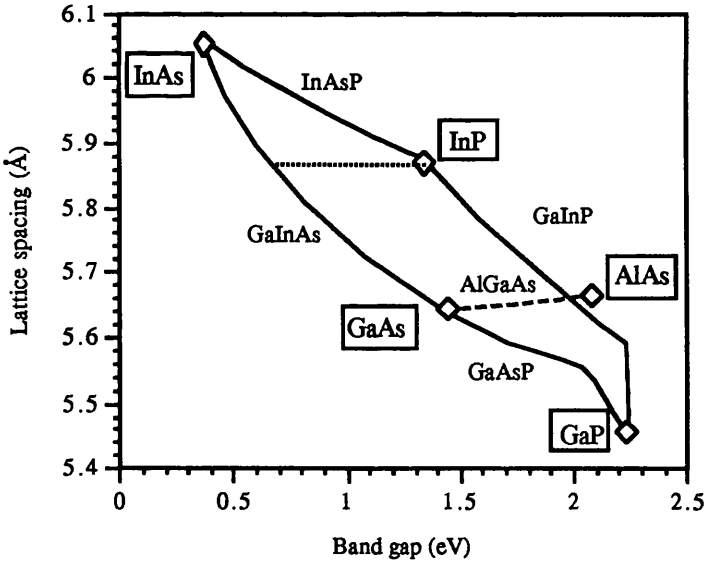

Figure 2.3: Relationship between band gap and lattice spacing for various binary and ternary III-V semiconductors. The dotted line represents the range of energies over which InGaAsP is lattice matched to InP.

As can been seen from figure 2.3, the lattice constants of GaAs and AlGaAs are almost identical, so it is possible to grow heterostructures in this material system with a low concentration of defects at the interfaces. The band gap of $Al_xGa_{1-x}As$ increases with increasing Aluminium concentration. At a heterojunction interface between GaAs and AlGaAs, potential barriers form whose magnitudes have been determined

experimentally as $\Delta E_c=0.67\Delta E_g$ and $\Delta E_v=0.33\Delta E_g$. When GaAs is used as the active region with AlGaAs cladding, carriers injected into the GaAs are confined, causing a high population density and hence a lower required threshold current density to achieve the transparency condition. For maximum usable gain it is essential to confine the generated light to the region of population inversion. This is achieved with heterostructures as the increase in bandgap corresponds to a decrease in refractive index, creating waveguiding properties. InGaAsP also forms a potential energy trap when used as the active layer in a heterostructure with InP cladding, the interface barriers in this case being $\Delta E_c=0.39\Delta E_g$ and $\Delta E_v=0.61\Delta E_g$.

Growth of such structures relies on the development of sophisticated epitaxial techniques. The three most commonly used are liquid phase epitaxy (LPE), vapour phase epitaxy (VPE) and molecular beam epitaxy (MBE). In LPE a substrate is placed in a saturated solution of the epitaxial layer constituents, which then grow on the substrate when cooled. In VPE, the layers are formed by reaction of gaseous elements or compounds at the heated surface of the substrate, composition being controlled by varying the relative flow rates. Here the reactants are in the form of metal chlorides and hydrides. A variant of the technique known as metal organic vapour phase epitaxy (MOVPE) uses metal alkyls as the sources. Reactant velocities are higher in MOVPE than in hydride VPE, allowing quicker changes of composition, leading to smoother heterojunction profiles. In MBE, the epitaxial layer is grown by reacting atomic or molecular beams of the constituent elements with a high temperature substrate in high vacuum. In this project, both MBE and MOVPE have been used to grow mode-locked laser wafers. The characteristics of the growth and implications they might have on the operation of devices are discussed in the relevant chapters.

2.2.2- Waveguide modes and lateral confinement.

Heterostructure lasers provide confinement of the optical mode in the transverse direction, perpendicular to the junction plane. Here the discontinuity of refractive index provides waveguiding through total internal reflection of the optical mode. The field distribution of an electromagnetic wave in such a structure, which can be considered as a general slab waveguide, involves the solution of the three dimensional wave equation for the particular boundary conditions relevant to electric and magnetic fields. This solution consists of a set of discrete guided modes for a wave with its electric field polarised along the heterojunction plane (TE), and with its magnetic field polarised along the junction plane (TM).

For maximum utilisation of the active region gain, it is essential to choose the waveguide dimension to ensure only the fundamental mode is guided. The condition for zero order mode operation is described by the following condition:

$$d < \frac{\lambda}{2}(n_a^2 - n_c^2)^{-1/2} \tag{2.17}$$

where n_a is the active region refractive index, n_c is the cladding refractive index, λ is the wavelength of the mode, and d is the active region thickness. $(n_a^2 - n_c^2)$ is usually large, so this results in a small active region width. With an InGaAsP active layer and InP cladding, for example, it is found that $\lambda(n_a^2 - n_c^2)^{-1/2} \cong 0.95\mu m$, giving a required active layer width for fundamental mode operation of d=0.48μm. It can also be shown that such a dielectric slab waveguide provides more effective TE confinement than TM.

Lasers with no mode confinement along the plane of the junction are known as *broad area lasers* . In such devices the lasing threshold current is entirely defined by the active layer width, and decreases linearly, until around d=0.1μm. At this point a rapid increase occurs due to loss of confinement in thin layers. Typical threshold currents of ~1A limit the potential practical use of broad area lasers. By introducing refractive index variation along the junction plane, it is possible to confine the laser beam to the fundamental lateral mode. This allows continuous wave (CW) operation of diode lasers at room temperature with low currents (10-100mA), thus increasing the lifetime of the device. The production of a zero order mode profile is also essential for applications involving efficient coupling of the laser beam to an optical fibre.

Gain guiding and *index guiding* are used to achieve this effect. In gain guiding laser current injection is limited to a narrow stripe along the cavity length, providing a narrow region of optical gain in the lateral direction. Away from this area, the waveguide is relatively lossy, leading to a channelling of the photons in the zero order mode. At high injection levels these lasers can spontaneously jump to higher order waveguide modes and become unstable.

Index guiding by comparison, uses an actual change in refractive index along the junction plane via lateral changes in material or doping. An example of such a device is a *buried heterostructure laser,* where during fabrication, the structure is etched down through either side of the active layer. Then new material of a lower refractive index is grown around it. This forms a rectangular dielectric waveguide, whose dimensions can be chosen to provide maximum preference to the fundamental mode. A buried heterostructure is an example of a *strong* index guided structure, characterised with threshold currents of 10mA-20mA. As lateral mode confinement does not vary with external pumping, strong index guided lasers have advantages over gain guided ones, although they are relatively difficult to fabricate.

Some index guiding can be induced in gain guided lasers by making the upper cladding layer non-uniform. A *ridge wave guide* (RWG) laser is an example of this type of device. In general their guiding characteristics are complex, and can exhibit varying

degrees of gain or index guiding behaviour, but by careful choice of parameters, such lasers can achieve stable lateral mode operation at reasonable injection levels. Because of the ease of fabrication, this project uses RWG laser structures.

2.2.3- Threshold condition and power output.

The main operating parameter for a semiconductor laser is the current required to achieve lasing action - or *threshold current*. The following section introduces some of the useful concepts that link threshold currents to gain and to the output power of the laser.

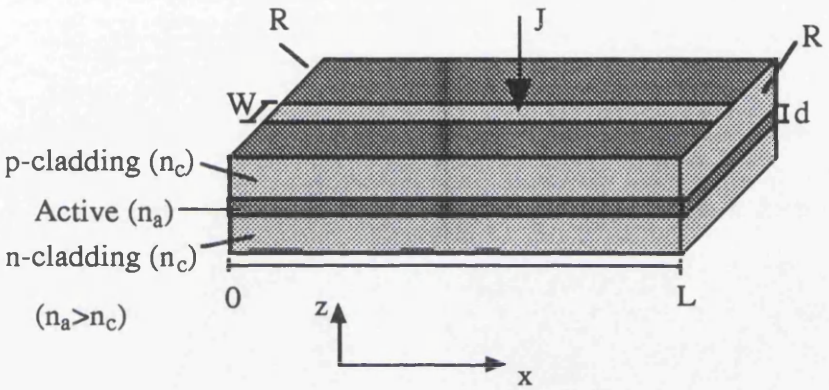

Figure 2.4: Schematic diagram of semiconductor Fabry-Perot laser cavity

Consider the Fabry-Perot semiconductor heterostructure laser cavity in figure 2.4, which is electrically pumped to provide a bulk gain coefficient γ and contains some internal loss mechanisms grouped together as α_{int}. At the laser threshold, the gain from current injection balances the loss from internal sources and from the output coupling at the facets. The cleaved facets form mirrors with Fresnel reflection coefficient R. The total power at x=0 contained in a plane wave oscillating in the cavity is given by P(0). So at some x, the power in the mode is $P(z)=P(0)\exp((\gamma-\alpha_{int})x)$. The condition for net gain over one round trip is then $P(2L)>P(0)$ which gives $R^2\exp(2(\gamma-\alpha_{int})L)>1$. This leads to the laser oscillation threshold gain condition:

$$\gamma = \alpha_{int} + \frac{1}{L}\ln\left(\frac{1}{R}\right) \qquad (2.18)$$

The factor α_{int} represents bulk free carrier absorption in the active region α_a; free electron absorption from the portion of the mode that overlaps with the n-type cladding α_n; free hole absorption from overlap in the p-type cladding α_p; and scattering loss due to non-uniformities in the heterojunction interfaces α_s. The factor Γ_i can now be introduced, representing the fraction of the mode present in a particular layer i. So the *modal gain* at threshold is given by:

$$\Gamma_a \gamma = \Gamma_a \alpha_a + \Gamma_n \alpha_n + \Gamma_p \alpha_p + \alpha_s + \frac{1}{L}\ln\left(\frac{1}{R}\right) \tag{2.19}$$

with: $\Gamma_a = \dfrac{\int_{-d/2}^{d/2} E^2 dz}{\int_{-\infty}^{\infty} E^2 dz}$, $\Gamma_n = \dfrac{\int_{-\infty}^{-d/2} E^2 dz}{\int_{-\infty}^{\infty} E^2 dz}$, $\Gamma_p = \dfrac{\int_{d/2}^{\infty} E^2 dz}{\int_{-\infty}^{\infty} E^2 dz}$, and $\Gamma_{a+}\Gamma_{n+}\Gamma_p=1$.

As long as $\Gamma_a \sim 1$, a decrease in the active region width increases the confinement of the mode, leading to a lowering of the external pumping requirement for threshold gain. Below a critical value of d the amount of the mode contained in the lossy cladding will begin to dominate, resulting in a sharp increase in threshold current.

Deriving the relationship between the injection current and gain is a complex one, involving the inclusion of detailed information of all decay process, band structure, density of states and the full effects of doping. A successful practical approximation is to use a phenomenological approach which relies on the observation, from numerical calculations, that above a certain minimum pumping current level J_o, the peak of the gain spectrum varies almost linearly with injected current density. This can be represented by the following: $\gamma(J)=A(J-J_o)$ (2.20)

J_o is known as the transparency current density and is the injection level required to achieve population inversion. A is the gain factor. Combining equations (2.18) - (2.20) gives the threshold current density as:

$$J_{th} = J_o + \frac{1}{\Gamma A}\left(\alpha_{int} + \frac{1}{L}\ln\left(\frac{1}{R}\right)\right) \tag{2.21}$$

Above the laser threshold, any increase in current injection causes increased stimulated emission, thus shortening the lifetime of inverted carriers, and leading to an effective clamping of the gain at its threshold value. In this case the power emitted through stimulated emission is:

$$P_e = \begin{pmatrix}\text{number of injected carriers}\\ \text{converted to photons}\end{pmatrix} \text{x power per photon} = \frac{(I - I_t)}{e}\eta_i \hbar\omega \tag{2.22}$$

where I_t is the threshold current and η_i is the internal quantum efficiency - the probability of an injected carrier recombining radiatively in the active region. The output power is the fraction of P_e lost through the mirrors, compared to the other loss mechanisms:

$$P_o = \frac{(I - I_t)}{e}\eta_i \hbar\omega\left(\frac{1}{L}\ln\left(\frac{1}{R}\right)\Big/\alpha_{int} + \frac{1}{L}\ln\left(\frac{1}{R}\right)\right) \tag{2.23}$$

Another factor useful when characterising the overall performance of a laser device is the external differential quantum efficiency η_{ex}:

$$\eta_{ex} = d\left(\frac{P_o}{\hbar\omega}\right)\Big/ d\left(\frac{I}{e}\right) = \eta_i\left(\left(\alpha_{int} L \Big/ \ln\left(\frac{1}{R}\right)\right)+1\right)^{-1} \qquad (2.24)$$

2.3-Quantum wells.

If the active region thickness in a double heterostructure laser is reduced so that it is comparable to the electron De-Broglie wavelength then the effects of quantum confinement become evident. Such a structure can be approximated by the quantum mechanical potential well model, where instead of a continuum of available energy states, carriers have their kinetic energy quantised into discrete energy levels. Such lasers are known as quantum well lasers.

The reduction in active region thickness has implications for the threshold current densities, with a reduction in the number of carriers required for transparency roughly scaling in the ratio of the quantum well width to the conventional bulk active region width, a factor of 10 or more. However there are other important considerations arising from carrier confinement that have implications on gain and absorption in quantum well lasers, which will now be reviewed.

2.3.1-Energy levels and density of states.[3]

In a quantum well, width L_z, carriers no longer have three degrees of freedom. They now have two degrees in the plane of the junction and are subject to a potential in the z-direction V(z). This changes the form of the density of states from that of the bulk case given in section (2.1.2), giving rise to a set of sub-bands in the dispersion relationship with energies displaced from the bulk band edge. Consider the conduction band of such a quantum well where the Hamiltonian can be written as :

$$H_c(\mathbf{r}) = V(z) - \frac{\hbar^2}{2m_c}\partial^2/\partial z^2 - \frac{\hbar^2}{2m_c}\partial^2/\partial \mathbf{r}_\perp^2 \qquad (2.25)$$

where $\mathbf{r}_\perp$ is a position vector in the plane of the heterojunction. The Hamiltonian (2.25) is separable giving the eigenvalue equation:

$$H_c(\mathbf{r})\Psi(\mathbf{r}) = (H_z(z)+H_c(\mathbf{r}_\perp)\Psi(\mathbf{r}) = E_c\Psi(\mathbf{r}) \qquad (2.26)$$

With $E_c = E_z + E_{r_\perp}$, and the wavefunction $\Psi(\mathbf{r}) = \Theta(r_\perp)\Phi(z)$:

$$H_z(z)\Phi(z) = \left(V(z) - \frac{\hbar^2}{2m_c}\partial^2/\partial z^2\right)\Phi(z) = E_z\Phi(z) \qquad (2.27)$$

Assuming the barriers at the interface are large enough to be considered infinite, i.e.

$V(z)=0$ $\quad -L_z/2 < z < L_z/2$

$V(z)=\infty$ $\quad z \geq L_z/2$, $z \leq -L_z/2$, then the solution of (2.27) is:

$$\Phi(z)=\begin{Bmatrix}\cos(n\pi/L_z) & n\text{-}odd\\ \sin(n\pi/L_z) & n\text{-}even\end{Bmatrix} \text{ with } E_z=\frac{n^2\hbar^2\pi^2}{2m_c L_z^2} \tag{2.28}$$

The solution for the second part of the Hamiltonian is a 2-dimensional Bloch wavefunction similar to equation (2.3):$\Theta(\mathbf{r})=u_{k\perp}(\mathbf{r}_\perp)\exp(i\mathbf{k}_\perp.\mathbf{r}_\perp)$, which gives $E_{r\perp}=\hbar^2k_\perp^2/2m$. So the dispersion relationships for the conduction and valence bands of a quantum well are:

$$E_c(k_\perp,n)=\frac{\hbar^2k_\perp^2}{2m_c}+\frac{n^2\hbar^2\pi^2}{2m_c L_z^2} \tag{2.29a}$$

$$E_{vl,vh}(k_\perp,n)=\frac{\hbar^2k_\perp^2}{2m_{vl,vh}}+\frac{n^2\hbar^2\pi^2}{2m_{vl,vh} L_z^2} \tag{2.29b}$$

The first few subbands are plotted in figure 2.5(a) along with their associated wavefunctions. Note the lifting of the degeneracy in the heavy/light hole bands at $k_\perp=0$, due to the differing effective mass. A significant consequence of using quantum well active regions in diode lasers is that the bandgap, and hence the lasing wavelength, can be tuned by varying the thickness of the well.

The density of states in this two dimensional case can be worked out in a manner analogous to section 2.1.2. Here there is quantisation of reciprocal space in only two co-ordinates, $k_x=2\pi s/L_x$, $k_y=2\pi s/L_y$, with each state area $4\pi^2/A$, where $A=L_x L_y$. So the number of states up to k is given by the area of a circle radius k divided by the area of each state, $N(k)=k^2A/2\pi$. The number of states per unit area from k to k+dk is $\rho(k).dk=(k/\pi).dk$. Considering the conduction band of a quantum well, $k_\perp$ is expressed as a function of energy from (2.29a), and converting from the density in k-space to the energy density of states per unit area gives:

$$\rho(E)=\sum_{n=1}^{\infty}\frac{m_c}{\pi\hbar^2}H(E-E_{nc}) \tag{2.30}$$

where $E_{nc}=E_z$ from (2.28), and $H(X-X_0)$ is the Heaviside function which is equal to 1 if $X \geq X_0$ and 0 if $X<0$.

Figure 2.5(b) shows the step-like 2-dimensional density of states for a quantum well structure. For comparison, the 3-dimensional density of states is also plotted in the figure 2.5(b) (note the density of states per unit volume is plotted).

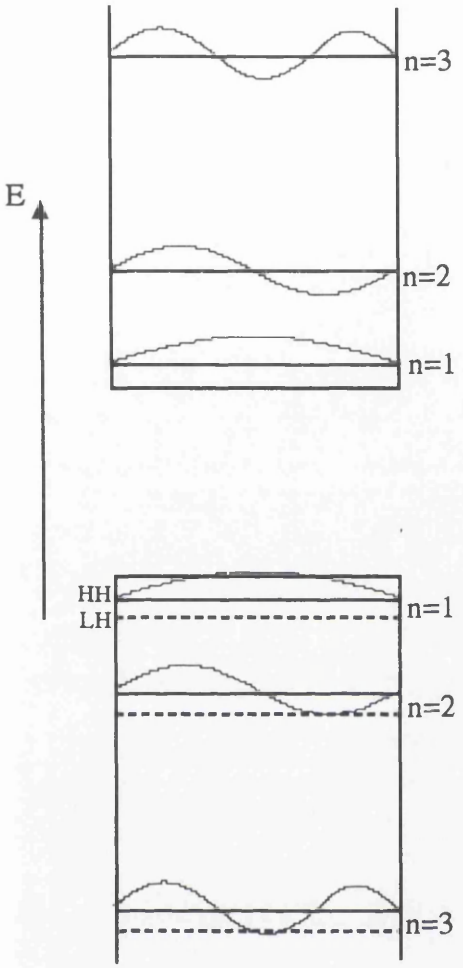

Figure 2.5(a): First 3 subbands and wavefunctions of an infinite quantum well

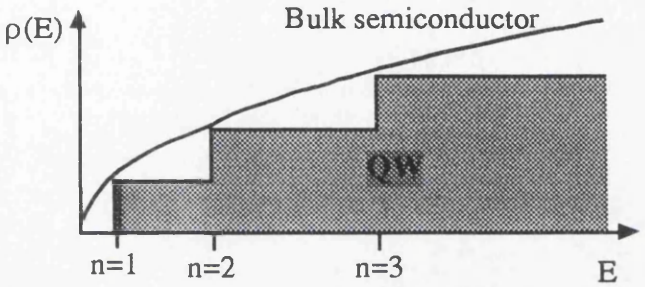

Figure 2.5(b): Volumetric density of states in bulk and QW semiconductor.

2.3.2 Gain in quantum wells[2]

In this section the differences in the form of the gain from a quantum well to that of a bulk active region are discussed.

The derivation of the expression for the probability of a radiative transition in a quantum well is exactly equivalent to that followed in section 2.1.4, given by equation (2.12). However in this case the density of states is replaced by the 2-D density of states function (2.30), which must be divided by L_z to make it volumetric. Expressing the total gain function for a quantum well involves a summation of the individual band gain over all the available subbands. At practical operational current injection levels, it is reasonable to assume that only the n=1 band is occupied. It should be noted that the solution (2.28) provides a set of orthogonal eigenfunctions, which will give a transition matrix element of zero if the initial and final states have differing quantum number n.

Modifying equation (2.15) accordingly it can be seen that the form of the gain in a quantum well is:

$$\gamma_{QW}(\hbar\omega) = \frac{1}{L_z} \sum_{i=lh,hh} K_i (f_c(\hbar\omega) - f_i(\hbar\omega)) \qquad (2.31)$$

The summation in (2.31) is over the n=1 light and heavy hole states, and K_i is the constant in both cases.

The step like density of states gives a much higher band edge population density (N) than in the bulk semiconductor case and hence a higher differential gain ($d\gamma/dN$) at quasi-Fermi level separation close to the band gap, i.e. low current injection above threshold. However band filling leads to gain saturation at high injection levels. The resulting highly sublinear differential gain curve for quantum wells makes them ideal for use as modulators. This feature is utilised in the mode-locked lasers fabricated in this project, which incorporate integrated QW absorber regions (see Chapter 3). Operation in the high differential gain region also leads to low temperature sensitivity and large modulation bandwidths.

An important feature of the quantum well gain is its polarisation dependence. The transition matrix element, as defined in section 2.1.4, is proportional to the matrix element $\langle u_h|\mathbf{x}.\mathbf{p}|u_e\rangle$ where u_e, u_h are the Bloch functions for the electron and hole states, $\mathbf{x}$ is the polarisation vector of the perturbing field and $\mathbf{p}$ is the carrier momentum. By considering the Bloch functions describing the carriers in the various valence bands, the transition matrix elements for the conduction band-heavy hole (C-HH) and conduction band-light hole (C-LH) transitions can be evaluated . For C-HH, $|M_T|^2$ is found to be zero for fields polarised parallel to carrier $\mathbf{k}$, and is at a maximum when perpendicular. In the C-LH case, $|M_T|^2$ has a ratio of 4:1 in favour of the parallel transition.

In a quantum well the carrier momentum is polarised as $\mathbf{k_z}$, a vector perpendicular to the junction plane. So TE interacts with both C-LH and C-HH while TM interacts with C-LH only. In the bulk case, this effect does not appear, as carriers generally have momenta polarised in different directions.

2.3.3 Threshold conditions and multiple quantum well lasers.[6,7]

When determining threshold gain in a quantum well laser it is the modal gain, rather than the absolute material gain, which is important. In a *single quantum well* (SQW) laser structure, Γ can be small which leads to a high current density at threshold. The use of *multiple quantum well* (MQW) structures, where the active region consists of a stack of quantum wells grown on top of each other, can increase the mode-confinement, and thus reduce the required threshold current. In MQW structures the gain saturation

takes place at higher injection levels and the differential gain is greater. Also lower carrier densities reduce the effects of non-radiative recombination such as Auger, which is concentration dependent.

The threshold gain of a multiple quantum well laser with n_w wells, where Γ_w is the confinement factor of each individual well, and the total confinement factor is approximately the product of the two, is given by:

$$\Gamma\gamma = n_w \Gamma_w \gamma = \alpha_{int} + \frac{1}{L}\ln\left(\frac{1}{R}\right) \tag{2.32}$$

Solving (2.32) for n_w, the threshold current density is:

$$J_{th} = n_w J_w = \left(\frac{J_w}{\Gamma_w \gamma}\right)\left(\alpha_{int} + \frac{1}{L}\ln\left(\frac{1}{R}\right)\right) \tag{2.33}$$

where J_w is the current density per well. From numerical simulation and experimental observation of the gain/current density curve a value of (J_w/γ) can be chosen that minimises the value of J_{th}. This point is defined as (J_o/γ_o)[8]. Substituting this in (2.33) and solving for n_w gives us the optimum number of wells for a set cavity length:

$$n_{opt} = \left(\frac{1}{\Gamma_w \gamma_o}\right)\left(\alpha_{int} + \frac{1}{L}\ln\left(\frac{1}{R}\right)\right) \tag{2.34}$$

As can be seen from (2.34) there exists an optimum n_w for any given cavity length that will produce a laser with minimum threshold current. From equation (2.33), the lowest threshold current density can be achieved in a laser with a long cavity, where the mirror loss becomes relatively low. Experimentally, typical QW lasers can have $\alpha_{int}<10cm^{-1}$ and $\Gamma_w\gamma_o>20cm^{-1}$, giving rise to the inequality $\ln(1/R)/L<\alpha_{int}<\Gamma_w\gamma_o$ for long lasers, which results in a single quantum well being the optimum condition. For shorter cavities the minimum threshold current requires the use of MQW structures. The optimum cavity length L_{opt} for a given number of wells can be derived analytically by noting the experimental observation in single quantum well lasers, that in the absence of any n=2 state lasing, the gain has a logarithmic relationship to the current density. This is approximated by[8]:

$$\gamma_w = \gamma_o(\ln(J_w/J_o) + 1) \tag{2.35}$$

Using (2.32) and substituting J_{th} from (2.33) in (2.35) gives:

$$\left(\alpha_{int} + \frac{1}{L}\ln\left(\frac{1}{R}\right)\right) = n_w \Gamma_w \gamma_o (\ln(J_{th}/J_o n_w) + 1)$$

which, when solved for J_{th}, leads to the following expression:

$$J_{th} = (n_w J_o)\exp\left(\frac{\alpha_{int}}{n_w \Gamma_w \gamma_o}\right)\exp\left(\frac{1}{L n_w \Gamma_w \gamma_o}\ln\left(\frac{1}{R}\right)\right)e^{-1} \tag{2.36}$$

It is necessary to minimise the threshold current $I_{th}=WLJ_{th}$, where W is the current injection stripe width. Obviously I_{th} decreases with decreasing L, but the threshold

current density for very short cavities will be dominated by the increase in the mirror loss. The minimum I_{th} in a laser with a fixed number of wells is then found from:

$$\frac{d}{dl}\left(L\exp\left(\frac{1}{Ln_w\Gamma_w\gamma_o}\ln\left(\frac{1}{R}\right)\right)\right) = 0 \Rightarrow L_{opt} = \ln\left(\frac{1}{R}\right)\Big/ n_w\Gamma_w\gamma_o \quad (2.37)$$

Clearly from (2.37) it can be seen that there is an inverse dependence of the optimum cavity length with number of wells. As an increase in the well number lowers the threshold current, it can be stated that with the optimum short cavity conditions, MQW lasers always have lower thresholds than SQW lasers. From (2.37) the lowest threshold achievable would be obtained in a laser of infinitesimal length with an infinite number of wells. However, the physical requirements of laser cleaving limit the minimum cavity length to around 50μm. Also, it has been assumed throughout that the confinement factor scales linearly with n_w, but a large n_w requires wells at the very edge of the active layer where this condition would not hold.

SQW lasers can be grown with graded refractive index (GRIN) active regions, which can result in an improved confinement factor and lower threshold current than considered in the analysis above.

2.3.4 Absorption spectra and electric field effects[9]

Absorption in QW structures is heavily influenced by the increase in the exciton binding energy due to the effects of confinement.

In semiconductors optical absorption creates an electron-hole pair which remains bound due to the Coulombic attraction between them. This can be treated as a hydrogen like particle with the relatively massive positive hole acting as the nucleus with orbiting electron, and a corresponding spectrum of energy states. This particle is known as an exciton and in semiconductors has an effective Bohr radius a_B~100Å. The finite binding energy leads to exciton absorption occurring just below the bandgap. For bulk semiconductor the exciton binding energy is small ~10meV, and because of the presence of lattice phonons at room temperature, excitons are quickly dissociated into free carriers. As a result excitonic effects can only be observed in pure bulk semiconductors at low absolute temperatures.

In quantum wells the exciton is compressed in the z-direction as L_z~a_B. This causes a four-fold increase in the exciton binding energy resulting in the observation of exciton features in room temperature absorption spectra. This exciton resonance is only significant for k=0 so the absorption spectrum of a quantum well semiconductor follows the general form of the 2-D density of states, but with enhanced absorption at the subband edges which can be resolved as heavy hole and light hole exciton peaks.

The exciton absorption spectrum of a quantum well can be radically altered by the application of an electric field in the z-direction, perpendicular to the interface plane. In this case the potential within the well V(z) is no longer constant but sloping. Solution of the eigenvalue equation (2.27) gives rise to electron wavefunctions that are displaced to the low energy side of the well, and hole wavefunctions that are displaced to the high energy side of the well. The eigen energies are also modified, resulting in the decrease of the bandgap with increasing electric field strength. This is known as the *quantum confined stark effect* (QCSE).

Along with the substantial shift in the absorption band edge to lower energy, the exciton absorption peaks are observed to broaden slightly and lower as the applied field strength increases. The broadening can be explained by considering the effect of random fluctuations in the quantum well width across the sample. As the field is applied, the confined carrier wavefunctions are displaced towards the well interfaces, where the relative effects of non-uniformities are stronger and give rise to a broadened exciton spectrum. Other possible mechanisms include the fact that in MQW structures, the field distribution among the wells will be non-uniform due to the effect of the potentials from the residual impurities. Conservation of the total oscillator strength in these cases requires a lower level of peak absorption.

In the derivation of the energy eigen states the potential barriers at the QW interfaces were assumed to be infinite. Obviously in real semiconductors this is not true. As a result, the wavefunctions penetrate the barriers by an amount dependent on the barrier heights and effective mass of the carriers in the different bands. Here, the strict orthogonality between eigenfunctions of differing n no longer applies, giving rise to the appearance of so called *forbidden transitions* as weak features in the absorption spectrum. Forbidden transitions can be enhanced through the QCSE where a reduction in symmetry increases the overlap factor between wavefunctions with different energy quantum numbers.

In bulk semiconductor, the application of an electric field causes the conduction and valence bands to tilt, allowing photon assisted tunnelling to occur, thus creating an absorption tail below the normal bandgap. This is the Franz-Keldysh effect. In quantum wells, the asymmetry produced in the wavefunctions with the application of an electric field perpendicular to the plane of the wells causes a similar broadening of the absorption tail.

Chapter 2: References.

[1]C.Kittel, *Introduction to Solid State Physics*, New York:Wiley 1967.
[2].WCorzine, R.H.Yan, and L.A.Coldren, chapter 1, in *Quantum well lasers*, P.S.Zory (Ed.), Acedemic Press, 1993
[3]A.Yariv, *Quantum Electronics*, Wiley, 1989.
[4]G.P.Argawal, and N.K.Dutta, *Semiconductor Lasers*, New York:Van Nostrand Rienhold, 1993.
[5]G.H.B.Thompson, *Physics of Semiconductor Laser Devices*, Wiley, 1980.
[6]A.Kurobe, H.Furuyama, S.Naritsuka, N.Sugiyama, Y.Kokubun, and Masaru Nakamura, "Effects of well number, cavity length, and facet reflectivity on the reduction of threshold current of GaAs/AlGaAs multiquantum well lasers," *IEEE.J.Quantum Electron.*, vol.24, pp635-640, 1988.
[7]R.W.H.Engelmann, C-L.Shieh, and C.Shu, chapter 3, in *Quantum well lasers*, P.S.Zory (Ed.), Acedemic Press, 1993
[8]P.W.A.McIlroy, A.Kurobe, and Y.Uematsu, "Analysis and application of theoretical gain curves to the design of mult--quantum-well lasers," *IEEE.J.Quantum Electron.*, vol.21, pp1958-1263, 1985.
[9]S.Schmitt-Rink, D.S.Chemla, and D.A.B.Miller, "Linear and non-linear optical properties of semiconductor quantum wells," *Adv.Phys.*, vol.38, pp89-188, 1989.

Chapter 3-Mode-locked Semiconductor lasers.

Methods of producing ultrashort optical pulses from lasers rely on introducing short periods of net loss or gain. There are three generic ways to achieve this- *Q-switching*, *gain switching* and *mode-locking*, all of which can be applied to diode lasers[1].

As it is difficult to directly modulate the gain in most laser systems, Q-switching was the first method used to produce ultrashort pulses from lasers. Initially the laser cavity is held in a low Q (high loss) state whilst the laser is pumped to provide a high level of population inversion. When the gain reaches its peak, the Q is suddenly switched high and the stored energy is released as a short high intensity light pulse. The loss modulation can be applied actively by external influence, or passively by the use of a *saturable absorber*. A saturable absorber acts as like an intensity dependent switch, only allowing the oscillation of high intensity pulses, to which they are transparent.

Pulse formation via gain switching is (conceptually) the simplest method to understand, and is basically the application of short bursts of gain to a laser held below the threshold inversion condition. If the burst is short enough, it can excite the first spike of the relaxation oscillation, and switch off the gain before any following spikes are excited. This is the most straightforward method to implement with semiconductor lasers, where the variation in gain can readily be introduced by modulation of the injection current.

The output of a CW laser contains many individual lasing wavelengths or modes. In general these modes have no fixed phase relationship, so they interfere randomly to produce a chaotically varying output. However, if every mode is forced to maintain a constant phase relationship, their interference will produce a train of ultrashort pulses, with a repetition rate given by the photon round trip time in the laser cavity (inversely proportional to the laser length). This is known as mode-locking and, if it can be accomplished, it can generate the shortest possible pulsewidths from lasers. In order to achieve mode-locking in any laser, there must be some method of actively or passively modulating the optical loss at the rate of the round trip time in the cavity. This will induce a continuously oscillating light signal to form a steady stream of pulses at this rate, which correspondingly phase locks the modes.

Along with a brief summary of gain switching and Q-switching in semiconductor lasers, this chapter will present a review of the pertinent literature relating to mode-locking in semiconductor lasers including an introduction to the basic concepts, concentrating specifically on colliding-pulse mode-locked semiconductor lasers which are studied in this project.

3.1- Gain/Q-switching in semiconductor lasers.

3.1.1- Relaxation oscillations and gain switching.

When a semiconductor laser is switched from below to above the inversion condition by an increase in the applied current, the system output goes through a transient stage before a steady state is reached. This transient response lasts in the order of 10ns, and takes the form of a time-varying power distribution among longitudinal and lateral modes, and oscillations in the total output power. The latter effect is known as the *relaxation oscillation*[2] , and arises through the interplay between the oscillating field and the material inversion, which has a natural frequency in the gigahertz range.

The origin of relaxation oscillations in semiconductor lasers can be explained by considering a laser biased well below threshold. There is a negligible initial photon density in the cavity, so on application of an electrical pulse, the photon density will increase slowly through spontaneous emission. In the absence of much stimulated emission, the carrier density will quickly increase to inversion, thus producing an intense pulse corresponding to the first spike of the relaxation oscillation. As long as the electrical pulse does not terminate, the ensuing depletion of carrier density reduces the stimulated emission rate, and the process continues through several cycles, with the oscillations dampening until the carrier density reaches its equilibrium value.

By repetitively applying current pulses of around 100ps to semiconductor laser structures, it is very easy to achieve gain switching action and produce a steady stream of pulses at gigahertz rates. The typical pulsewidths produced are around 20ps[1,3]. However, application of too wide or too intense a current pulse gives rise to multiple optical pulse formation.

It is instructive to note that it is the speed at which the carrier density is depleted by the build up of the pulse, that determines how quickly the stimulated emission rate falls. Hence it is the initial inversion condition that defines the width of a gain switched pulse. This is dependent on the initial bias condition, the amplitude of the input pulse, and the differential gain of the semiconductor media. The use of QW active regions, with the corresponding improvement in differential gain, has led to gain switched diode lasers attaining pulses less than 2ps in duration[4].

3.1.2- Frequency chirp and timing jitter.

Although gain-switched diode lasers are extremely easily realised and perform very reliably, they are two important factors limiting their use in optical communications: excessive frequency chip and timing jitter.

In semiconductor media the quantity that relates the electric field to the induced polarisation is the complex susceptibility χ, which varies with carrier density $(N)^2$. The real part is related to the refractive index, and the imaginary part to the gain. Through the Kramers-Kronig relations, any change in the real part of χ results in a change in the imaginary part. In gain switched lasers the carrier density, and hence the gain, experiences large fluctuations, which are coupled to a change in the refractive index. This variation in the refractive index modulates the phase of each laser mode, broadening the spectrum. This is known as *self-phase modulation* (SPM). The coupling of changes in gain to refractive index is usually described by the linewidth enhancement factor[5] :

$$\alpha = \frac{\mathrm{Re}(\chi)}{\mathrm{Im}(\chi)} = -2k\frac{dn/dN}{d\gamma/dN} \tag{3.1}$$

on which many of the noise, modulation, and spectral properties of semiconductor lasers are dependent. There is a minimum product of the pulse duration in time ,$\Delta\tau$, with the supporting frequency bandwidth ,$\Delta\nu$, that is possible with an optical pulse, and is found from the fourier-transform limit : $\Delta\tau.\Delta\nu=K$ (3.2)

where K is a constant specific to a given pulse shape. Due to the frequency chirp induced by SPM gain switched pulses have blue shifted leading edges, and red shifted trailing edges. This gives a value of the time-bandwidth product which is usually far from its transform limited value, and has been found to follow the formula[5]:

$\Delta\tau.\Delta\nu=K(1+\alpha^2)^{1/2}$ (3.3)

This drawback in gain switched lasers can be used to their advantage by using pulse compression techniques that rely on chirp. Group velocity dispersion (GVD), for example in a fibre optic, leads to faster propagation for the trailing edge of the pulse over the leading edge, thus it can be used to compress chirped pulses to a few picoseconds[6] . Soliton compression has also proved successful, transforming ps gain switched pulses to the order of a 100 fs[7] .

Timing jitter is a random fluctuation in the repetition period of the output pulsestream of a laser. In gain switched lasers, timing jitter arises from the reliance on random spontaneous emission of photons at the start of each pulse. A large 10-15ps jitter has been measured from gain switched diode lasers[8] . Such high values can have serious implications for communications systems, where signal to noise resolution can be degraded, and maximum operational bandwidths can be placed on optical time division multiplexed (OTDM) systems.

3.1.3- Active and passive Q-switching.

While gain switching can readily be accomplished using single contact semiconductor lasers, for Q-switching, multi-section lasers with either the p- or n-contact split into two isolated sections are usually required. Here, one section provides the gain and one is used to modulate the loss.

In an actively Q-switched diode laser, the gain section is continuously pumped and an RF electric field, at the required repetition rate, is applied to the modulator section. To maximise the effectiveness of the loss modulation, the bandgap of the gain section must be made smaller than that of the modulator. In conventional bulk active region diode lasers, this is achieved by heavy Zn diffusion to create band tail states, thus lowering the gain section bandgap. The variable loss is realised by shifting the absorption edge of the modulator section via the Franz-Keldysh effect[9] . Carrier induced bandgap shrinkage in the gain region, and the increased absorption in the modulator due to the QCSE in MQW lasers, make them particularly attractive for implementation in active Q-switching[10] .

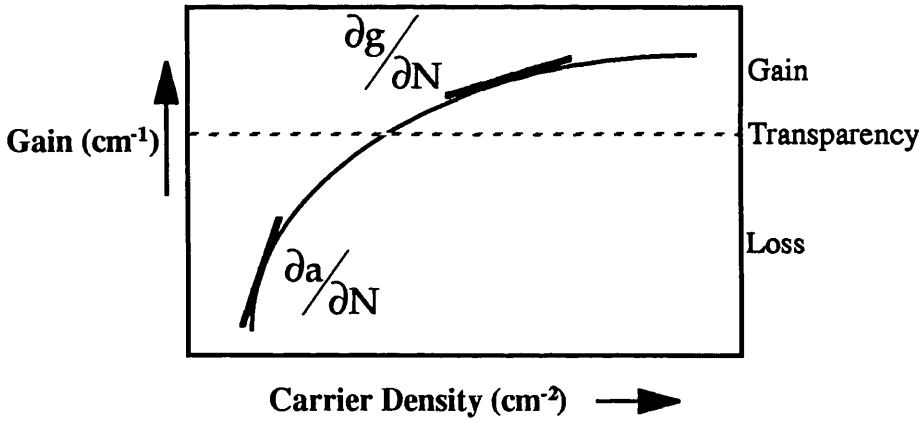

Figure 3.1: Gain/carrier density relationship in a semiconductor showing the decrease in differential gain with increasing carrier density.

Single contact laser diodes have been observed to produce sustained pulsation behaviour without the influence of an actively modulated gain or loss[2]. These self-pulsations have been explained in terms of passive Q-switching via saturable absorption[11]. To understand how saturable absorption can provide self-pulsating action in semiconductor lasers, consider a diode laser with a large number of defect recombination centres localised in a specific region. For example, such a situation can arise from surface recombination at a cleaved facet. High non-radiative recombination velocities in these areas will lower the carrier density to below transparency, so they will act as absorbers. Figure 3.1 shows a schematic representation of the sublinear

gain/carrier density relationship for a semiconductor[2]. Comparing the differential gains in the absorption and gain regions the following condition holds:

$$\partial a/\partial N > \partial g/\partial N \tag{3.4}$$

where a and g are the gains in the absorption and gain sections respectively. In this situation the high absorption will prevent stimulated emission while the laser is continuously pumped. Consequently, a high carrier density ensues in the gain section. Eventually spontaneous emission will start to saturate the absorber, allowing stimulated emission to increase in the laser cavity. Now a large photon density is generated which starts to saturate the gain, but from expression (3.4) it is evident that the absorption saturates faster, resulting in the emission of a pulse of large peak intensity. The passage of the pulse causes gain saturation, with the corresponding drop in carrier density allowing the absorption to recover, and the cycle to begin over again.

Proton bombardment can produce a saturable absorber , but a more controllable and reproducible method is to use a two-contact laser, one section of which is strongly forward biased, the other weakly, providing the gain and absorption regions[12] . Two-section self-pulsating laser diodes (SPLDs) have an advantage over gain switching or active Q-switching in that gigahertz pulsations can be produced using no external modulation, with the repetition rates controlled by the ratio of the relative pumping strengths. A maximum repetition rate of 80GHz has been achieved in SPLDs with continuous tuning from 12-64GHz[13] . Many useful communications functions have been demonstrated using SPLDs, including optical multiplexing/demultiplexing[14] and clock recovery from RZ and NRZ data[15] .

In Q-switching the initial population inversion is higher than in gain switching, which can result in both shorter pulse and larger peak pulse powers. Timing jitter and chirp are substantial in Q switched diode lasers for similar reasons to gain switching. Saturable absorbers can also be integrated in gain switched lasers. These delay the production of the optical pulse by a sufficient time to allow the initial photon density to build to a higher level. In this way shorter gain switched pulses can be produced.

3.2- Review of mode-locking in semiconductor lasers.

3.2.1- Qualitative introduction to mode-locking.

With strong forward bias, the peak of the gain spectrum of a semiconductor laser will increase above the inversion condition. Only those frequencies in the gain bandwidth, $\Delta\nu$, that correspond to allowed Fabry-Perot cavity modes, will oscillate in the cavity to produce the stimulated amplification and laser output. The condition for

the oscillation of a wavelength λ_q in a Fabry-Perot resonator is that the optical pathlength must be equal to an integral multiple of half wavelengths:

$$q\frac{\lambda_q}{2} = nL \tag{3.5}$$

where q is an integer, n is the refractive index, and L is the laser cavity length. Now if the corresponding frequency of each mode is $\nu_q=c/\lambda_q$, then the frequency mode spacing $\delta\nu=\nu_{q+1}-\nu_q$ is given by:

$$\nu_q = \frac{qc}{2nL} \quad \Rightarrow \quad \delta\nu = \left(\frac{(q+1)c}{2nL} - \frac{qc}{2nL}\right) = \frac{c}{2nL} \tag{3.6}$$

Note that the round trip time for a photon in the cavity is given by $T=2nL/c=1/\delta\nu$. The mode spacing in wavelength is related to $\delta\nu$ in the following way:

$$\frac{\partial\nu}{\partial\lambda} = -\frac{c}{\lambda^2} \quad \Rightarrow \quad \delta\nu = -\frac{c\delta\lambda}{\lambda^2} \tag{3.7}$$

So the output field of such a laser consists of N oscillating modes, where $N\approx\Delta\nu/\delta\nu$, which interfere to give the total output in time[1,16]:

$$E(t) = \sum_{n=-(N-1)/2}^{(N-1)/2} E_n \exp\left[i((\omega_o + n\delta\omega)t + \phi_n(t))\right] \tag{3.8}$$

where n is an integer, $\phi_n(t)$ is the phase of mode n, E_n is the amplitude of the nth mode, and ω_o is the frequency of the central mode of the gain spectrum ($\omega=2\pi\nu$). For the output to be periodic at the cavity round trip time requires $E(t+T)=E(t)$.

$$\begin{aligned} E(t+T) &= \sum_n E_n \exp\left[i((\omega_o + n\delta\omega)t + \phi_n(t+T))\right]\exp\left[i\frac{(\omega_o + n\delta\omega)}{\delta\nu}\right] \\ &= \sum_n E_n \exp\left[i((\omega_o + n\delta\omega)t + \phi_n(t+T))\right]\exp[2\pi i(m+n)] \\ &= E(t) \end{aligned}$$

The above is true if and only if the phase and amplitude of each mode remain constant in time. In a standard multi-longitudinal mode laser, variations in mode phase and intensity leads to a chaotic output. If the phases are forced to maintain a constant relationship of the form $E_n\exp(i\phi_n)=E_o\exp(i(\phi_o+n\delta\phi))$, where ϕ_o and $\delta\phi=\phi_{m+1}-\phi_m$ are constants, then the output of the laser is periodic in T. Using the summation identity:

$$\sum_{n=-(N-1)/2}^{(N-1)/2} \exp[inx] = \frac{\sin(Nx/2)}{\sin(x/2)} \tag{3.9}$$

results in the following expression for the laser output under fixed phase and amplitude conditions (mode-locked):

$$E(t) = E_o \frac{\sin\left(N(\delta\omega t + \delta\phi)/2\right)}{\sin\left((\delta\omega t + \delta\phi)/2\right)} \exp(i\omega_o t + \phi_o) \tag{3.10}$$

Expression (3.10) describes the output of a mode-locked laser as a carrier wave, frequency ω_0, with a pulse envelope repeating at period $T=2\pi/\delta\omega$. Figure 3.2 shows a plot of the intensity profile of such a pulse envelope. The width of the pulse is found from the first zero of the function (3.10):

$$\frac{N\delta\omega\Delta\tau}{2} = \pi \quad \Rightarrow \quad \Delta\tau \approx \frac{1}{N\delta\nu} = \frac{1}{\Delta\nu} \tag{3.11}$$

So for a mode-locked laser, the output pulsewidth is proportional to the inverse of the gain bandwidth. In semiconductor media the broad gain spectra of up to 100nm makes it theoretically possible to produce pulses with durations below 100fs. In a mode-locked laser pulsestream, the ratio of the peak power to the average output power is given by the Mark/Space ratio, which is the ratio of pulse repetition time to the pulse width:

$$M.S.R = \frac{P_{peak}}{P_{ave}} = \frac{T}{\Delta\tau} \approx \frac{\Delta\nu}{\delta\nu} \approx N \text{ the number of oscillating modes.} \tag{3.12}$$

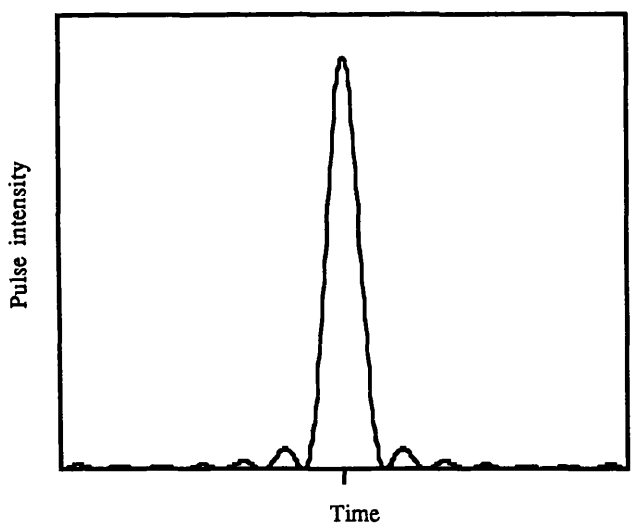

Figure 3.2: Plot of the pulse intensity profile of a mode-locked laser electric field from equation (3.10), with 10 modes.

3.2.2- Active mode-locking.

Mode-locking can be produced in semiconductor lasers by actively modulating the gain at the frequency of the intermode spacing $\delta\nu$[1]. In this way the carrier density in the cavity can be lifted above threshold for a short period in each round trip. The width of the gain waveform above threshold is short, so the laser will not oscillate in a single mode. Similarly, multi-longitudinal modes with arbitrary phases will not oscillate. The only possible condition for a laser to continuously oscillate is for the modes to be phase

locked, with the ensuing pulses only seeing the gain, and not experiencing any loss from the modulation. Any drift in phase during the operation of a mode-locked pulse will lead to the pulse broadening into the loss region. The loss mechanism continuously chops off these tails, effectively restoring the phases to the ideal state. In mode-locked diode lasers peak powers are generally lower than in gain or Q-switching, so frequency chirp from carrier density variations is less significant, leading to mode-locked diode lasers producing near transform-limited pulses without the requirement of external pulse compression techniques[3,22].

Typical diode lasers have cavity lengths of a few hundred microns, so the round trip frequency is very large (>100GHz). Direct electrical modulation at these high frequencies is difficult, so in order to actively mode-lock a semiconductor laser some form of elongated cavity is usually essential. An external cavity actively mode-locked diode laser, shown in figure 3.3, can be realised by anti-reflection coating one of the diode facets, and using an external mirror at a controllable distance to form the cavity. Extended cavity lasers have produced pulses with widths as low as 0.6ps[17] .

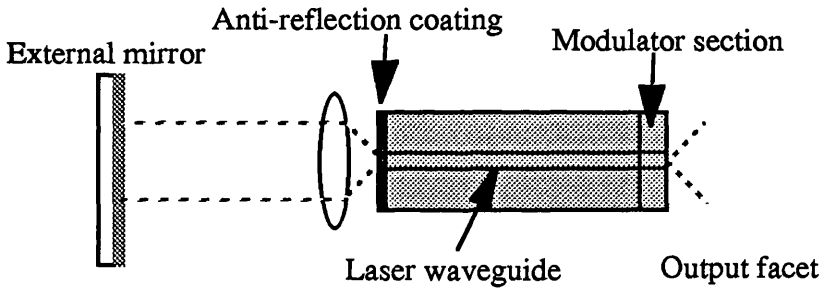

Figure 3.3: Top view of an external cavity mode-locked diode laser.

A major complication in the use of external cavity mode-locked lasers is multiple pulse formation resulting from non-perfect anti-reflection coatings on the inner diode facet. Reflection coefficients as low as 10^{-4} are still large enough to create a composite Fabry-Perot cavity[18] , in which bursts of mode-locked pulses, separated by the external cavity round trip time, are generated at the diode cavity repetition rate Multiple pulse formation has two derogatory effects: the total available power is distributed among many pulses instead of concentrated in one, and the total temporal width of the output pulse is that of the group and not the ultrashort individual pulses.

There are several methods practised to remove the composite Fabry-Perot cavity[1]. The output frequency spectrum of an external cavity laser, with insufficient anti-reflection coating, consists of groups of modes at the diode cavity intermode spacing, separated by the external cavity spacing. By placing a bandwidth limiting element in the resonator, such as a Fabry-Perot etalon, or replacing the external mirror with a

diffraction grating, a single group of modes can be selected. Reflection can be totally eliminated from the internal facet by the use of a diode with a curved waveguide structure. Split contact lasers in external cavity actively mode-locked lasers, producing a saturable absorber at one of the diode facets, will also suppress multiple pulse formation, providing the absorption recovery is longer than the diode round trip time.

In QW lasers , the modulation frequencies can be reduced to practical levels without the requirement of an external cavity. For longer cavity diode lasers, 5mm for 10GHz operation, high threshold currents cause heating effects which seriously impair operational lifetimes, the problem being particularly acute in multi-section lasers which must be operated junction side up, i.e. the heat is generated farthest away from the heat sink. The solution is to render a large part of the diode length non-absorbing. Such lasers are known as extended cavity lasers, and can be fabricated using quantum well intermixing techniques[19]. Here the QW region is disordered, converting it to bulk semiconductor, thus increasing the bandgap. Now photons emitted from the active gain region of the diode are unaffected by the extended cavity, which can remain unpumped.

Actively mode-locked lasers can be operated at harmonics of the round trip frequency and also exhibit a tuning bandwidth, over which the frequency of the driving electrical signal can be varied from the resonance condition[20]. Positive detuning results in the peak gain appearing ahead of the optical pulse, which will then tend to broaden. Conversely, negative detuning causes the formation of an intensity tail on the pulse.

3.2.3- Spectral and pulsewidth broadening.

Along with a finite gain bandwidth, it is necessary to include other factors when contemplating the minimum attainable pulsewidth from mode-locked semiconductor lasers.

With the generation of large optical pulses, whose intensities are approaching that required for gain saturation, the corresponding carrier density variations (coupled to changes in refractive index through the linewidth enhancement factor) cause self phase modulation to occur. This chirp broadens the pulse spectrum, but not the pulsewidth. It is observed, however, that mode-locked laser pulsewidths increase with rising pulse energy. This can be explained by the increase in the effect of GVD as the spectrum broadens.

Dispersion is not sufficient to account for the discrepancy between the experimentally measured values and the theoretical pulsewidth limited only by bandwidth and dispersion. *Dynamic detuning*, which arises from gain saturation, describes the physical mechanism that sets a fundamental lower limit for the pulsewidth of mode-locked semiconductor lasers[21]. Modulation of the loss or gain in the cavity of a diode laser cavity at the cavity round trip time, results in the formation of short

windows of peak gain repeated at this rate. The formation of mode-locked pulses occurs at the peak of this gain waveform. But as a pulse increases in intensity, the leading edge starts to saturate the gain, so the trailing edge experiences a lower level of gain. This results in the peak of the pulse moving away from the peak of the gain waveform. Detuning continues until the slope of the gain waveform balances the slope caused by the gain saturation. This equilibrium is the only position at which the pulse is stable, and is a few picoseconds earlier than the peak of the gain spectrum in the absence of optical output. As there is a stringent requirement on the amount of gain saturation, this in turn fixes the temporal intensity profile of the pulse. In active mode-locking, an increase in the injection current or modulation frequency provides a higher slope on the gain waveform requiring a higher level of gain saturation to fulfil the stability criteria, permitting the creation of shorter pulses.

3.2.4- Passive mode-locking using saturable absorbers.

It is possible to generate mode-locked pulses from a semiconductor laser without any external RF driving signal, using the pulse itself to provide the gain modulation employing saturable absorption. The following argument describes the development of such a pulse.

Consider a laser cavity with two isolated sections providing both saturable amplification and saturable absorption. If the unsaturated gain is greater than the unsaturated loss, as the laser is switched above threshold, spontaneous emission will begin to be amplified. Random noise fluctuations in the photon density at some point will produce an amplified noise spike with an intensity high enough to produce some saturation of the absorption. As this pulse sees the highest net gain in the cavity it will be preferentially amplified. The growth in intensity of this pulse lowers the level of gain encountered by photons in the trailing edge of the pulse, until eventually only the single pulse is present circulating in the cavity. Net pulse shortening during one pass of the absorber is achieved, providing the loss saturates easier than the gain. In this case the leading edge of the pulse is attenuated, bleaching the absorption and allowing amplification for the central portion of the pulse. To ensure net pulse shortening, the trailing edge must also see a high loss. This situation occurs as long as the saturated absorption recovers faster than the saturated gain. Ultimately a steady state is reached where pulse shortening from the saturable absorber is balanced by the various broadening mechanisms detailed in the last section (SPM, GVD, dynamic detuning).

It is useful to introduce the concept of *saturation energy* to quantify the assertion made above that the absorption saturates easier than the gain. If A is the optical mode cross sectional area, and $\partial g/\partial N$ and $\partial a/\partial N$ are the differential gains in the gain and absorber sections respectively, then their corresponding saturation energies are[22] :

$$E_G = \frac{\hbar\omega A}{\partial g/\partial N} \quad , \quad E_A = \frac{\hbar\omega A}{\partial a/\partial N} \tag{3.13}$$

Expressions (3.13) are a measure of the required energy needed to saturate a segment of the particular section. Easier absorption saturation forces the condition: $E_G > E_A$. (3.14) From the discussion in section 3.1.3 on the sublinear differential gain characteristic (equation (3.4), figure 3.1), it is apparent that the condition (3.14) can be fulfilled in inhomogeneously pumped semiconductor laser media.

Haus developed a time domain analysis of passive mode-locking with *fast*[23] and *slow*[24] absorbers, providing closed form solutions and parameter ranges for stable pulse formation[25]. Here a fast saturable absorber is one where the absorption recovery time τ_a, is short compared to the mode-locked pulse width, $\Delta\tau$. Saturable absorbers in semiconductors can be considered as slow, where $\tau_a > \Delta\tau$. By considering the conditions for a pulse envelope v(t) mapping on to itself, after one round trip in a cavity with lumped gain, loss, and dispersive media, Haus derived the *mode-locking master equation*[24] :

$$\left(g_T(t) - \frac{\delta}{\Delta\omega}\frac{d}{dt} + \frac{1}{\Delta\omega^2}\frac{d^2}{dt^2} \right) v(t) = 0 \tag{3.15}$$

where the net gain is defined as $g_T(t) = g(t) - 1 - a(t)$, (3.16)

g(t) is the time varying gain and a(t) is the time varying absorption. Note that the second derivative in (3.15) is a dispersion operator that causes broadening of the pulse, which is restored by the gain modulation over the round trip. The values of unsaturated loss and gain in the respective regions are a_o and g_o. With the passage of a pulse in the absorber section the change in carrier density is given by the following rate equation:

$$\frac{\partial N}{\partial t} = -\frac{N - N_e}{\tau_a} - \frac{|v(t)|^2}{E_a} N \tag{3.17}$$

where N_e is the equilibrium carrier density, and τ_a is the absorber recovery time. In the slow absorber case, τ_a is assumed to be longer than the duration of the pulse so the first term in (3.17) can be neglected, giving:

$$\frac{\partial N}{\partial t} = -\frac{|v(t)|^2}{E_a} N \quad \overset{\text{integration}}{\Rightarrow} \quad N = N_i \exp(-E_P(t)/E_A) \tag{3.18}$$

where N_i is the population inversion before the arrival of the pulse, and the cumulative pulse energy $E_p(t) = \int_0^t |v(t)|^2 \, dt$. The time dependent absorption is proportional to (3.18) giving $a(t) = a_i \exp(-E_P(t)/E_A)$ (3.19)

where a_i is the absorption on the arrival of the pulse. Analogously the time dependent gain is given by $g(t) = g_i \exp(-E_P(t)/E_G)$. (3.20)

In these cases, after the passage of a pulse the absorption/gain relaxes to the value a_i/g_i with time constants τ_a/τ_g.

Considering the net gain function (3.16) using the functions (3.19) and (3.20), results in a set of conditions being required for stable pulse generation. To avoid any perturbations preceding the pulse, a negative net gain is necessary when the pulse enters the absorber: $g_i<1+a_i$. (3.21)

For positive net gain during the passage of the central portion of the pulse, the absorber must saturate faster than the gain, i.e. $E_A>E_G$ equivalent to expression (3.14). Negative net gain is required to stop stimulated emission trailing the pulse:

$g(t)<1+a(t) \Rightarrow \tau_a<\tau_g$, (3.22)

i.e. the absorber must recover faster than the gain. For the mode-locking to be self-starting the initial net gain at turn on must be positive i.e. $g_o>1+a_o$ - the level of unsaturated gain must exceed unsaturated loss. Now if the gain relaxed fully to its unsaturated value between pulses, then from (3.21) $g_o<1+a_i$, and since $a_i \leq a_o$, mode-locking will not start. Hence the gain recovery time must be at least slightly greater than the cavity round trip time. A further constraint on the gain and loss parameters arises from the requirement for net loss before the arrival of the pulse being converted to net gain with rising pulse energy. By expanding (3.19) and (3.20) to the first order, since $E_A<<E_G$, and substituting in the master equation of mode-locking (3.15) leads to the following condition:

$g_i<sa_i$ where s is New's stability parameter[26] : $s=E_G/E_A$ (3.23)

The plot in figure 3.4 shows the gain and absorber dynamics during the generation of a mode-locked pulse stream using a slow saturable absorber.

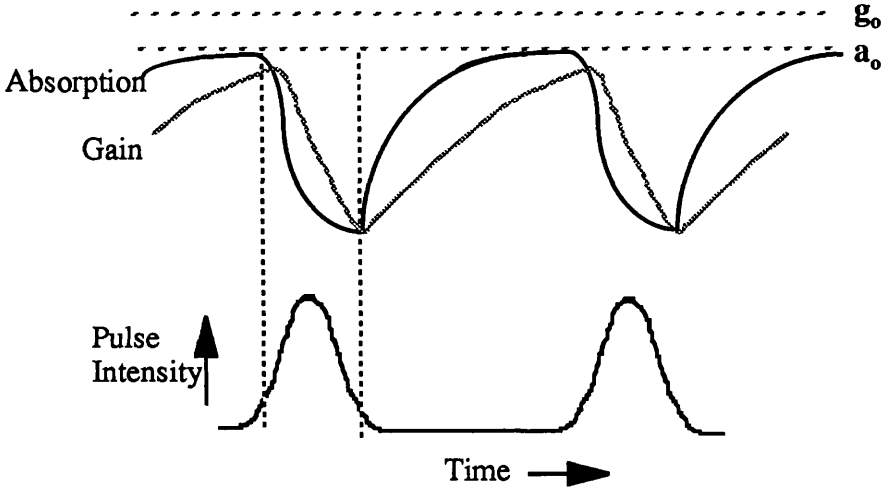

Figure 3.4: Dynamics of gain and absorption during the evolution of a mode-locked pulse via saturable absorption.

The self-consistent solution to the master equation (3.15) results in a set of pulsewidth, pulse energy and detuning characteristics for passively mode-locked pulses.

Haus' model has been expanded to include the effects of chirp from SPM and group velocity dispersion[27] .

3.2.4- Passively mode-locked semiconductor lasers.

Passive mode-locking was first demonstrated in diode lasers with uncontrollable saturable absorbers, formed by fast recombination in damaged sections due to ageing[28]. Although pulses as short as 0.6ps were produced[29], such devices were very unreliable. In a similar way to passive Q-switched lasers, these damage centres can be formed by proton or nitrogen bombardment of the laser facet to lower the carrier recombination time and form an inhomogeneously pumped laser[30,31]. These external cavity mode-locked lasers produced transform limited 0.65 ps pulses at a 1 GHz repetition rate.

Two section lasers, with one section reverse biased to form the saturable absorber, are a more reliable method of realising passively mode-locked diode lasers[32]. Here, during the passage of the pulse, the band to band transition in the reverse biased section is saturated. The condition stated in the previous section that the absorption is obliged to recover significantly faster than the gain, requires the use of a reverse bias on the absorber. Recovery via spontaneous emission is a very slow process, typically in the order of 1 ns. The reverse sweeps out generated carriers after the pulse has left the absorber, substantially decreasing the recovery time.

Monolithic multi-section lasers (with no external cavity) have been used to increase the repetition rate of mode-locked lasers. Successful passive mode-locking of diode lasers at very high frequencies (>50 GHz) requires the consideration of two important factors: the ratio of differential gains in the absorber and gain sections, and absorption recovery time. The highly sublinear nature of the MQW active region makes this material ideal for fast absorber saturation, but conceptually the requirement of ultrafast absorption recovery is not as easily fulfilled. Pump-probe experiments were performed on reverse biased GaAs/AlGaAs bulk and MQW material to ascertain the time taken for bleached absorption to recover to its maximum value[33]. The value, found to be 15 ps, would limit mode-locking frequencies to below 100 GHz, too low to allow the mode-locking of conventionally sized lasers monolithically. However monolithic mode-locking of MQW lasers at 200 GHz was reported by Portnoi *et al*[34] and 108 GHz with 2.4 ps pulsewidths by Sanders *et al* [35].

A possible mechanism to enable ultrafast mode-locking is the non-linear absorption characteristics associated with the excitonic absorption line in MQW structures. In an external cavity configuration, Silverberg *et al* produced passively mode-locked 1.6 ps pulses using a GaAs/AlGaAs MQW structure at the external mirror, operated near the excitonic resonance[36] . The slow 30 ns recovery time of the absorber[37] , as compared to the gain recovery of 2 ns, was overcome by tight focusing of the beam on the MQW

absorber allowing recovery via carrier diffusion out of the excited region. In a similar experiment[38], the absorption recovery was reduced to 150 ps by proton bombardment of the absorber. It has been found that before the dissociation into free carriers, excitonic absorption saturates at an optical intensity around ten times lower than the corresponding band to band transition[39]. The ultrafast exciton decomposition time of approximately 300 fs[40] can be included as a fast component of the absorber recovery time, and is considered to make an important contribution to mode-locking with MQW structures[41].

It is possible to generate passive mode-locked pulse streams at harmonics of the cavity round frequency. With a two-section extended cavity GaAs/AlGaAs quantum well mode-locked diode laser, Sanders *et al* [42] observed 10 ps pulses at the first through to the sixth harmonic of the cavity repetition rate of 1.17 GHz by adjusting the gain section current input. Multi-stable mode-locking was also observed in an InGaAsP extended cavity mode-locked laser[43]. With monolithic cavity devices, ultrahigh repetition rates have been generated using harmonic mode-locking techniques. In monolithic colliding-pulse mode-locked (CPM) semiconductor lasers (discussed in section 3.3) repetition rates of up to 375 GHz have been observed[44,45]. Also, with the monolithic integration of an intracavity distributed bragg reflector (DBR) forming one of the output mirrors, harmonic mode-locking at 1.54 THz has been achieved by Aahira *et al*[46,47] . These devices had a fundamental repetition rate of 38.8 GHz, but by varying the current in the gain section, they were mode-locked at harmonics of the DBR frequency mode spacing 400 GHz. As well as the ultrafast contribution from excitonic saturation effects, other mechanisms are thought to play an important part in absorption recovery at these high repetition rates. By considering carrier-carrier scattering, carrier-photon scattering and bandgap re-normalisation, a fast absorber relaxation component of 150 fs can be introduced[48]. Carrier heating effects, with time constants of the order of tens of fs[49] , are thought to be primarily responsible for the achievement of mode-locking above THz. Time domain studies of passive mode-locking show that ultrahigh repetition rate mode-locking is often accompanied by a self-pulsation envelope[50,51,52].

With the addition of another section in a semiconductor laser cavity, hybrid mode-locking is possible. Here pulse shaping from the saturable absorber is assisted by an RF gain modulation. This has been achieved in both external[53] and monolithic[22] geometries. Passively mode-locked lasers can also be tuned in wavelength[54] and repetition rate[55] by varying the currents applied to the various sections of a monolithic diode laser with integrated DBR. Liu *et al*[55] realised a tuning bandwidth of more than 1 GHz with transform limited pulse output.

3.2.5- Timing jitter and chirp in mode-locked diode lasers.

In mode-locked diode lasers, spontaneous emission causes noise in gain, refractive index, and photon density. Refractive index noise can cause timing jitter directly as random variations are made to the optical cavity length, and correspondingly the round trip time. Gain and photon density noise introduces random fluctuations in the gain and absorption saturation dynamics, which again can produce variation in the timing of each mode-locked pulse. Although not as severe as in gain switching or Q-switching, jitter in a mode-locked laser degrades the timing resolution essential for many applications. In many cases pulsewidths are effectively defined by the root mean square (rms) value of the timing jitter[56]. Because of the influence of the driving electrical signal, active and hybrid-mode-locked lasers generally have lower values of timing jitter than passively mode-locked lasers. Also the length of the monolithic cavity has a tangible effect, with external cavity devices or diodes with integrated passive regions returning lower rms jitter than those all-actively pumped[22].

Experimentally, blue chirp (frequency increase with time) in passively mode-locked semiconductor lasers, and red chirp (frequency decrease with time) in actively mode-locked lasers, is commonly observed. This difference has been predicted by consideration of the α-parameter in the gain and absorption sections in a time domain model[57], which includes the influence of carrier heating dynamics. However a more simplistic explanation for this phenomena is as follows.

If the linewidth enhancement factor α was zero, mode-locked pulses would be blue chirped due to material dispersion. However, with a realistic non-zero α-parameter which is constant along the cavity, the pulse shortening mechanism in active mode-locking (negative gradient in the gain waveform) gives a positive refractive index gradient, and therefore a predominantly red chirp. In the passive mode-locking case, the contribution from α-parameters in the absorber and gain sections are generally not equal in magnitude or sign. The decrease in carrier density from gain saturation causes an instantaneous frequency drop, and the increase in carrier density during absorption saturation leads to a instantaneous rise in the frequency. Thus it is a balance between both these mechanisms that decides the overall nature of the chirp. The low α-parameter in the absorber coupled with large differential gain generally results in net blue chirp.

Salvatore *et al* [58] demonstrated a passively mode-locked laser, at high repetition rates, with controllable chirp. By using a cross-correlation technique to measure the chirp they were able to produce chirp free (transform-limited) and down chirped pulses (frequency drop across the pulse). Their frequency domain analysis, which is suited to the low number of modes present in high repetition rate lasers, successfully predicted these results[59] .

3.3- Colliding pulse mode-locked (CPM) semiconductor lasers.

3.3.1- CPM dye lasers.

In conventional passive mode-locking a single pulse is generated in a laser cavity, which is shortened in the saturable absorber through the combination of fast absorber saturation and slow gain recovery. If a cavity is set up to allow two pulses to oscillate simultaneously, and they can be timed to arrive at the saturable absorber at exactly the same time, then this causes an increase in the effectiveness of the pulse shortening through the interaction of the counter-propagating pulses. This type of laser geometry was first shown to work in mode-locked dye ring lasers[60], producing extremely short pulses, < 0.1 ps. Such lasers are known as colliding pulse mode-locked (CPM) lasers.

The increased level of pulse shortening from collisions in the absorber arises because of the enhancement in the stability factor s (ratio of differential gain in absorber and gain regions), as twice as much energy saturates the absorption medium than the gain medium. This is an incoherent geometrical effect. In dye lasers there is a further coherent effect, in which interference between the two pulses causes the formation of an optical standing wave in the absorber[61,62]. The high intensity of the optical field near the peaks of the standing wave create a large inverted population in the absorber dye At the low intensity nulls, the generation of energetic molecules is much lower. In this way a grating is bleached into the absorber, coupling together the counter-propagating pulses. Here, the length of the absorber that requires saturation is effectively halved, further improving stability and pulse shortening effects.

3.3.2- Implementation of CPM in diode lasers.

Unlike the ring cavity dye lasers, standard semiconductor lasers have a linear Fabry-Perot type cavity. In the previous discussion on monolithic passively mode-locked diode lasers (section 3.2.4), the multi-contact laser structures had the saturable absorber section placed at one of the cleaved facets. An alternative geometry is to place the saturable absorber section in the centre of the laser cavity (see figure 3.5), which should give rise to colliding pulse effects[22].

The first demonstration of CPM action in laser diode was by Vasilev *et al*[63] in 1986. Here 0.8 ps pulses were generated at a repetition rate of 710 MHz from an external cavity GaAs/AlGaAs double heterostructure laser. The first implementation of a monolithic CPM laser was by Wu *et al*[64], with a hybrid mode-locking scheme producing near transform limited 1.4 ps pulses at 32 GHz. The laser used had a graded index separate confinement heterostructure (GRIN-SCH), with InGaAs/InGaAsP MQW active region. RF modulation was applied at twice the cavity round trip frequency to

regions either side of the centrally positioned saturable absorber, to generate two mode-locked pulses in the cavity. They showed that these devices could be wavelength tuned by over 8.8 nm whilst maintaining constant pulsewidths[65], and their repetition frequency bandwidth was up to 5% of the cold cavity value[44]. Passive CPM operation was demonstrated by Chen *et al* [66,44] in similar laser structures, achieving pulses as low as 0.64 ps in duration at repetition rates from 40 to 350 GHz. InGaAsP-based quantum well CPM lasers have been used in communications experiments[67], and with hybrid CPM lasers, RF synchronisation to external electrical clock signals has been characterised[68].

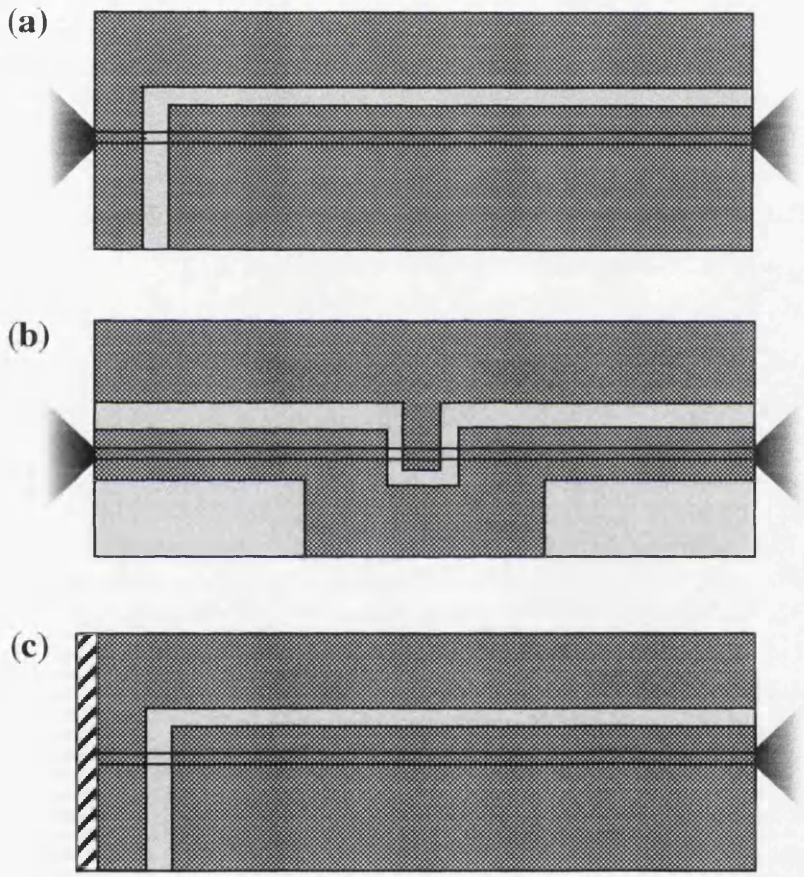

Figure 3.5: Configurations for monolithic mode-locking in diode lasers.
(a) Standard configuration, with the absorber at one of the facets.
(b) CPM configuartion, with the absorber in the centre of cavity.
(c) SCPM configuration, with 100% reflection coating at absorber facet.

Using GaAs/AlGaAs MQW material, Martins-Filho *et al*[69] at the University of Glasgow showed CPM operation of a ridge waveguide structure with repetition rates in the range 73-129 GHz. Recently the multiple colliding-pulse mode-locked laser (MCPM)[45,70] has also been developed, which is able to produce pulses at higher harmonics of the standard mode-locking repetition rate. In this scheme three intracavity saturable absorbers are placed at 1/4,1/2, and 3/4 of the cavity length. Reverse biasing

of all three absorbers produces four pulses travelling simultaneously in the cavity. In this way pulsewidths of ~1 ps with repetition rates up to 375 GHz have been achieved. By varying the biasing conditions on the three absorbers 1,2,3, or 4 colliding pulse mode-locking can be generated. Asymmetric-CPM where one absorber is placed at a sub-multiple of the cavity length, has produced harmonic mode-locking in InGaAsP laser diodes[71] .

Other geometries are possible to implement CPM in semiconductor lasers. The most common is the self-colliding pulse mode-locked (SCPM) laser[56], where the absorber is placed at a diode facet which has been ~100% reflection coated (figure 3.5(c)). In this case, the pulse collides with itself in the facet absorber to produce the pulse shortening effects. Obviously there are some colliding pulse effects from standard passively mode-locked lasers with non-coated facets. It is also possible to fabricate ring laser cavities in semiconductor material. The symmetry conditions lead to mode-locked semiconductor ring lasers being inherently CPM[72] .

3.3.3-Theoretical and practical considerations on CPM and SCPM

The incoherent CPM effect in semiconductor lasers is important for pulse shortening as the required pulse energy for absorption saturation is reduced. The corresponding reduction in the saturation of the gain region leads to less chirp through SPM and dispersion. The coherent coupling of the forward and reverse pulses causes an optical standing wave to form. Depending on the phase of the generated standing wave, either the even or odd longitudinal cavity modes are suppressed, doubling the frequency mode spacing[52]. The expression for the cavity mode-spacing from equation (3.6) now becomes:

$$\delta\nu = \frac{c}{nL} \tag{3.22}$$

which corresponds to a doubling of the repetition rate of a CPM laser compared to that of a conventional single pulse mode-locked laser of the same cavity length. Therefore either by time or frequency domain measurements, CPM effects are evident.

While the coherent CPM effects are clearly important for the mode-coupling and spectral output, the theoretically induced carrier density grating is potentially less significant in semiconductor lasers than in dye lasers. This is due to the presence of carrier diffusion, which tends to smooth out any carrier density variations[22,52]. In a physical model of CPM in a MQW laser, Chen *et al*[73] showed that induced carrier gratings can effectively shorten pulses. However, compelling experimental evidence exists that indicates the main pulse shortening mechanism is due to incoherent CPM[56]. The study showed that by decreasing the reflectivity of the absorber mirror in the SCPM laser from R=0.8 to R=0.55, to reduce the standing wave ratio, the effect on the

pulsewidth was minimal. Also, with measurements on CPM laser diodes in external cavities, substantial increases in the output pulsewidths when the absorbers were offset with respect to the central position were observed. The offsets were large enough to allow absorption recovery between the arrival of the two pulses, decreasing the effectiveness of pulse shortening from incoherent CPM. These results imply that incoherent CPM is more significant than coherent CPM in diode lasers.

In accordance with qualitative expectations, an experimental[74] and theoretical[75] study of wavelength chirp in CPM laser diodes has shown nearly chirp free transform-limited pulses from short monolithic cavity devices, but significant chirp for long monolithic cavity devices.

While it seems that CPM and SCPM, from a theoretical stance, are both able to successfully produce ultrashort pulses at high repetition rates[22.52,76], there are also some practical considerations that must be accounted for. Precision laser facet cleaving, which in many cases is difficult to achieve, is essential for the coherent CPM action. From this standpoint SCPM lasers are easier to fabricate. However it could also be important to avoid the high optical intensities present at the absorber facet in a SCPM laser which may cause damage. CPM laser configurations also offer higher repetition rates over SCPM lasers with identical cavity lengths.

3.4- Conclusions.

In this chapter it has been shown how semiconductor lasers can be used as sources of short optical pulses at multi-gigahertz repetition rates. In particular the suitability of quantum well structures for passive mode-locking of laser diodes was discussed.

The pronounced gain saturation with increasing injected current, due to the step-like density of states in quantum well structures, results in a highly sublinear gain-carrier density relationship. This allows a very effective saturable absorber to be formed in quantum well material simply by applying reverse bias. In addition, the absorption edge can be controlled easily via the QCSE, and high repetition rate mode-locking can be enabled from the contribution from ultrafast exciton dynamics. When saturable absorbers are integrated monolithically in diode laser cavities by employing a split electrical contact to allow inhomogeneous current injection, lasers can be passively mode-locked at hundreds of gigahertz. An important geometry for monolithic passive mode-locking with diode lasers, is to place the absorber section in the centre of the laser cavity to allow colliding pulse mode-locking to take place. With this geometry two mode-locked pulses arise simultaneously in the cavity and collide in the absorber. With twice the intensity to saturating the absorption as opposed to the gain, the pulse broadening effects associated with gain saturation are reduced, and hence CPM lasers have been shown to produce near transform-limited pulses at up to 375 GHz.

Chapter 3: References

[1] P.Vasil'ev,*Ultrafast Diode Lasers: Fundementals and Applications*, Artech House, 1995.

[2] G.P.Argawal, and N.K.Dutta, *Semiconductor Lasers*, New York:Van Nostrand Rienhold, 1993.

[3] K.Y.Lau, "Short-pulse and high-frequency signal generation in semiconductor lasers," *J.Lightwave.Tech.* ,vol.7,pp400-419, 1989.

[4] T.Sogawa, Y.Arakawa, "Picosecond lasing dynamics of gain-switched quantum well lasers and its dependence on quantum well structures," *IEEE.J.Quantum.Electron.*, vol.27, pp1648-1654, 1991.

[5] M.Osinski, and J.Buus, "Linewidth broadening factor in semiconductor lasers-an overview," *IEEE.J.Quantum.Electron.*, vol.27, pp1648-1654, 1991.

[6] H.F.Liu, Y.Ogawa, and S.Oshiba, "Generation of an extremely short single mode pulse (2 ps) by fibre compression of a gain-switched pulse from a 1.3 μm distributed-feedback laser diode," Appl.phys.lett., vol.59, pp1284-1286, 1991.

[7] K.A.Ahmed, K.C.Chan, and H.F.lui, "Femtosecond pulse generation from semiconductor lasers using soliton-effect compression technique, *IEEE.J.Sel.Topics.Quantum.Electron*, vol.1, pp529-600, 1995.

[8] A.G.Weber, W.Ronghan, E.H.Bottcher, M.Schell, and D.Bimberg, "Measurement and simulation of the turn-on delay time jitter in gain-switched semiconductor lasers," *IEEE.J.Quantum.Electron.*, vol.28, pp441-446, 1992.

[9] D.Z.Tsang, J.N.Walpole, Z.L.Liau, S.H.Groves, and V.Diadiuk, "Q-switching of low threshold buried heterostructure diode lasers at 10 GHz,"*Appl.Phys.Lett.*, vol.45, pp204,-206, 1984.

[10] Y.Arakawa, A.Larsson, J.Paslaski, and A.Yariv, "Active Q-switching ina GaAs/GaAlAs multiquantum well laser with an intracavity loss modulator," *Appl.Phys.Lett.*, vol.45, p204, 1984.

[11] R.W.Dixon, and W.B.Joyce, "A possible model for sustained oscillations (pulsations) in AlGaAs DH lasers," *IEEE.J.Quantum.Electron.*, vol.15, pp470-475, 1979.

[12] Farrell, P.Phelan & J. Hegarty, "Self-pulsation operating regime for absorber of twin section laser diode," *Electron. letts*, vol. 27, pp.1403-1404, 1991.

[13] U.Feiste, M.Möhrle, B.Sartorius, J.Hörer & R.Löffler, "12GHz to 64GHz continuous frequency tuning in selfpulsating 1.55μm quantum well DFB lasers," *14th IEEE International Semiconductor Laser Conference*, Maui, Hawaii, USA, paperTH2.3, pp227-228, Sept 1994.

[14] G. Farrell, P.Phelan & J. Hegarty, "All-optical synchronisation and frequency division of mode-locked pulses," *IEEE.Photon.tech.letts*, vol.4,pp.930-932, 1992.

[15] P.Barnsley, "All-optical clock extraction using two-contact devices," *IEE Proceedings -J*, vol. 140, pp325-336, 1993.

[16] A.Yariv, *Quantum Electronics*, Wiley, 1989.

[17] J.E.Bowers, P.A.Morton, A.Mar, and S.W.Corzine, "Actively mode-locked semiconductor lasers," *IEEE.J.Quantum.Electron.*, vol.25, pp1426-1439, 1989.

[18] H.A.Haus, "Theory of mode-locking of a laser diode in an external cavity," *J.Appl.Phys.*, vol.51, pp4042-4049, 1980.

[19] J.H.Marsh, "Quantum well intermixing," *Semicod.Sci.Technol.*, vol.8, pp1136-1155, 1993

[20] A.J.Lowery, N.Onodera, and R.S.Tucker, "Stability and spectral behaviour of grating-controlled actively mode-locked lasers," *IEEE.J.Quantum.Electron.*, vol.27, pp2621-2633, 1991.

[21] P.A.Morton, R.J.Helkey, and J.E.Bowers, "Dynamic detuning in actively mode-locked semiconductor lasers," *IEEE.J.Quantum.Electron.*, vol.25, pp2621-2633, 1989.

[22] D.J.Deickson, R.J.Helkey, A.Mar, J.R.Karin, J.G.Wasserbauer, and J.E.Bowers ," Short pulse generation using multisegment mode-locked semiconductor lasers," *IEEE J.Quantum.Electron.*, vol.28, pp.2186-2201, 1992.

[23] H.A.Haus,"Theory of mode-locking with a fast saturable absorber," *J.Appl.Phys*, vol.46, pp3049-3058, 1975.

[24] H.A.Haus,"Theory of mode-locking with a slow saturable absorber," *IEEE J.Quantum.Electron*, vol.11, pp.736-746, 1975

[25] H.A.Haus,"Parameter ranges for CW passive mode-locking," *IEEE J.Quantum.Electron*, vol.12, pp169-176, 1976.

[26] G.H.C.New, "Pulse generation in mode-locked quasi-continuous lasers," *IEEE J.Quantum.Electron*, vol.10, pp115-124, 1974.

[27] O.E.Martinez, R.L.Fork & J.P.Gordon, "Theory of passively mode-locked lasers including self-phase modulation and group velocity dispersion," *Optics Lett.*, vol.9, pp.156-158, 1984.

[28] E.P.Ippen, D.J.Eilenberger, and R.W.Dixon, "Picosecond pulse generation by passive mode-locking of diode lasers," *Appl.phys.lett.*, vol.37, pp267-269, 1980.

[29] H.Yokoyama, H.Ito, and H.Inaba, "Generation of subpicosecond coherent optical pulses by passive mode-locking of an AlGaAs diode laser," *Appl.phys.lett.*, vol.40, pp105-107, 1982.
[30] J.P.Van Der Ziel, W.T.Tsang, R.A.Logan, R.M.Mikulyak, and W.M.Augustyniak, "Subpicosecond pulses from passively mode-locked GaAs burried optical guide semiconductor lasers," *Appl.phys.lett.*, vol.39, pp525-527, 1981.
[31] E.L.Portnoi and A.V.Chelnokov, "Characteristics of heterostructure lasers with a saturable absorber fabricated by deep ion implantation," *Sov.Tech.Phys.Lett.*,vol.15, pp432-433, 1989.
[32] C.Harder, J.S.Smith, K.L.Lau, and A.Yariv, "Passive mode-locking of buried heterostructure lasers with non-uniform current injection," *Appl.phys.lett.* vol.42, pp772-774, 1983.
[33] J.R.Karin, D.J.Derickson, R.J.Helkey, J.E.Bowers, and R.L.Thornton, "Field-enhanced GaAs/AlGaAs waveguide saturable absorbers," *Ultrafast Phen. VIII conf.*, France, 1992.
[34] E.L.Portnoi and A.V.Chelnokov, "Passive mode-locking in a short cavity diode laser," *IEEE 12th International Semiconductor Laser Conference*, Switzerland, pp140-1255, 1991.
[35] S.Sanders, L.Eng, J Paslaski, and A Yariv, "108 GHz passive mode-locking of a multiple quantum well semiconductor laser with an intracavity saturable absorber," *Appl.phys.lett.* vol.56, pp310-311, 1990.
[36] Y.Silverberg, P.W.Smith, D.J.Eilenberger, D.A.B.Miller, A.C.Gossard, and W.Wiegmann, "Passive mode locking of a semiconductor diode laser," *Optic.lett.* vol.9, pp507-509, 1984.
[37] D.S.Chemla, D.A.B.Miller, P.W.Smith, A.C.Gossard, and W.Wiegmann, "Room temperature excitonic nonlinear absorption and refraction in GaAs-AlGaAs multiple quantum well structures," *IEEE.J.Quantum.Electron*, vol.20, pp265-275, 1984.
[38] P.W.Smith, Y.Silverberg, and D.A.B.Miller, "Mode locking of semiconductor diode lasers using saturable excitonic nonlinearities," *J.Opt.Soc.Am.B*, vol.2, pp1228-1236, 1985.
[39] D.S.Chemla, and D.A.B.Miller, "Room temperature excitonic nonlinear-optical effects in semiconductor quantum well structures," *J.Opt.Soc.Am.B*, vol.2, pp1155-1173, 1985.
[40] W.H.Knox, R.L.Fork, M.C.Downer, D.A.B.Miller, D.S.Chemla, C.V.Shank, A.C.Gossard, and W.Wiegmann, "Femtosecond dynamics of resonantly excited excitons in room temperature GaAs quantum wells," *Phys.Rev.Letters*, vol.54, p1306, 1985.
[41] H.A.Haus, and Y.Silverberg, "Theory of mode locking a laser diode with a multiple-quantum-well structure," *J.Opt.Soc.Am.B*, vol.2, pp1237-1243, 1985.
[42] S.Sanders, A.Yariv, J.Paslaski, J.E.Ungar, and H.A.Zarem, "Passive mode locking of a two-section multiple quantum well laser at harmonics of the cavity round-trip frequency," *Appl.phys.lett.* vol.58, pp681-683, 1991.
[43] M.Kuznetsov, D.Z.Tsang, J.N.Walpole, Z.L.Liau, and I.P.Ippen, "Multi-stable mode-locking of InGaAsP semiconductor lasers," *Appl.phys.lett.* vol.51, pp895-897, 1987.
[44] Y.K.Chen, and M.C.Wu, "Monolithic colliding-pulse mode-locked quantum-well lasers," *IEEE.J. Quantum.Electron*, vol.28, pp2176-2185, 1992.
[45] J.F.Martins-Filho, E.A.Avrutin, C.N.Ironside, and J.S.Roberts, "Monolithic multiple colliding pulse mode-locked quantum-well lasers: experiment and theory," *IEEE.J.Sel.Topics.Quantum.Electron*, vol.1, pp539-551, 1995.
[46] S.Arahira, S.Oshiba, Y.Matsui, T.Kunii, and Y.Ogawa, "Terahertz-rate optical pulse generation from passively mode-locked semiconductor laser diode," *Optic.lett.* vol.19, pp834-836, 1994.
[47] S.Arahira, Y.Matsui, and Y.Ogawa, "Mode-locking at very high repetition rates more than terahertz in passively mode-locked distributed-bragg-reflector laser diodes," *IEEE.J.Quantum.Electron*, vol.32, pp1211-1224, 1996.
[48] J.R.Karin, R.J.Helkey, D.J.Derickson, R.Nagarajan, D.S.Allin, J.E.Bowers, and R.L.Thornton, "Ultrafast dynamics in field-enhanced saturable absorbers," *Appl.phys.lett.* vol.64, pp676-678, 1994.
[49] A.V.Uskov, J.R.Karin, R.Nagarajan, and J.E.Bowers, " Dynamics of carrier heating and sweepout in waveguide saturable absorbers," *IEEE J.Sel.Topics. Quantum.Electron*, vol.1, pp552-561, 1995.
[50] K.Y.Lau, and J.Paslaski, "Condition for short pulse generation in ultrahigh frequency mode-locking of semiconductor lasers," *IEEE Tran.Photon.Tech.Lett.*, vol.3, pp974-976, 1991.
[51] W.Yang, and A.Gopinath, "Study of passive mode-locking of semiconductor lasers using time-domain modeling," *Appl.phys.lett.* vol.63, pp2717-2719, 1993.
[52] D.L.Jones, L.M.Zhang, J.E.Carroll, and D.D.Marcenac, "Dynamics of passively mode-locked semiconductor lasers," *IEEE.J.Quantum.Electron*, vol.31, pp1051-1058, 1995.
[53] A.Mar, D.Derickson, R.Helkey, J.Bowers, R.-T.Huang, and D.Wolf, "Actively mode-locked external-cavity semiconductor lasers with transform-limited single pulse-output," *Optic.Lett*, vol.17, pp868-870, 1992.
[54] H.F.Liu, S.Arahira, T.Kunii, and Y.Ogawa, "Generation of wavelength-tunable transform-limited pulses from a monolithic passively mode-locked distributed bragg reflector semiconductor laser," *IEEE.Photon.Tech.Lett*, vol7, pp1139-1141, 1995.

[55] H.F.Liu, S.Arahira, T.Kunii, and Y.Ogawa, "Tuning characteristics of monolithic passively mode-locked distributed bragg reflector semiconductor lasers," *IEEE.J.Quantum.Electron*, vol.32, pp1965-1975, 1996.
[56] R.Helkey, and J.Bowers, in *Semiconductor Lasers: Past, Present and Future*, G.Agrwal Ed., American Institute of Physics Press, 1993.
[57] M.Schell, M.Tsuchiya, and T.Kamiya, "Chirp and stability of mode-locked semiconductor lasers," *IEEE.J.Quantum.Electron*, vol.32, pp1180-1190, 1996.
[58] R.A.Salvatore, and A.Yariv, "Demonstration of down-chirped and chirp-free pulses from high repetition-rate passively mode-loced lasers," *IEEE.Photon.Tech.Lett*, vol.7, pp1151-1153, 1995.
[59] R.A.Salvatore, S.Sanders, T.Schrans, and A.Yariv, "Supermodes of high-repetition-rate passively mode-locked semiconductor lasers," *IEEE.J.Quantum. Electron*, vol.32, pp941-952, 1996.
[60] R.L.Fork, B.I.Greene, and C.V.Shank, "Generation of optical pulses shorter than 0.1 ps by colliding pulse mode locking," *Appl.phys.lett.*, vol.38, pp671-6729, 1981.
[61] W.Dietel, "Transient absorber gratings shorten the pulses of a passively mode-locked CW dye laser," *Opt.Commun.*, vol43, pp69-71, 1982.
[62] M.S.Stix, and E.P.Ippen, "Pulse shaping in passively mode-locked ring dye lasers," *IEEE.J. Quantum.Electron*, vol.19, pp1520-525, 1983.
[63] P.P.Vasil'ev, V.N.Morozov, Y.M.Popov, and A.B.Sergeev, "Subpicosecond Pulse Generation by a tandem-type AlGaAs DH laser with colliding pusle mode-locking," *IEEE.J.Quantum.Electron*, vol.22, pp1149-1151, 1986.
[64] M.C.Wu, Y.K.Chen, T.Tanbun-Ek, R.A.Logan, M.A.Chin, and G.Raybon, "Transform-limited 1.4 ps optical pulses from a monolithic colliding-pulse mode-locked quantum well laser," *Appl.phys.lett.*, vol.57, pp759-761, 1990.
[65] M.C.Wu, Y.K.Chen, T.Tanbun-Ek, R.A.Logan, and M.A.Chin, "Tunable monolithic colliding pulse mode-locked quantum-well lasers," *IEEE.Photon. Tech.Lett.*, vol.3, pp874-876, 1991.
[66] Y.K.Chen, M.C.Wu, T.Tanbun-Ek, R.A.Logan, and M.A.Chin, "Subpicosecond monolithic colliding pulse mode-locked multiple quantum well lasers," *Appl.phys.lett.*, vol.58, pp1253-1255, 1991.
[67] Z.Wang, J.M.Nielsen, S.D.Brorson, B.Christensen, T.Frank, N.G.Jensen, A.M.Larsen, J.Nørrergaard, and E.Bødtker, "15.8 Gbit/s system transmission experiment using a 5.2 mm long monolithic colliding-pulse-modelocked quantum well laser diode," *Electron.Lett.*, vol.31, pp272-274, 1995.
[68] T.Frank, S.D.Brorson, A.Møller-Larsen, J.M.Nielsen, and J.Mørk, "Synchronization phase diagrams of monolithic colliding pulse-mode-locked lasers," *IEEE.Photon.Tech.Lett*, vol.8, pp40-42, 1996.
[69] J.F.Martins-Filho, C.N.Ironside, and J.S.Roberts, "Quantum well AlGaAs/GaAs monolithic colliding pulse modelocked laser, " *Electron.Lett..*, vol.29, pp1135-1136, 1993.
[70] J.F.Martins-Filho, and C.N Ironside, "Multiple colliding pulse mode-locked operation of a semiconductor laser," *Appl.phys.lett.*, vol.65, pp1894-1896, 1994.
[71] T.Shimuzu, X.Wang, and H.Yokoyama, "Asymmetric colliding-pulse mode-locking in InGaAsP semiconductor lasers," *Optical Review*, vol.2, pp401-403, 1995.
[72] J.P.Hohimer, and G.AVawter, "Passive mode locking of monolithic semiconductor ring lasers at 86 GHz," *Appl.phys.lett.*, vol.63, pp1598-1600, 1993.
[73] W.Chen, J.Zhu, and S.Liu, "A physical model for mode-locking process of colliding pulse mode-locked multiquantum-well semiconductor laser," *IEEE.J.Quantum.Electron*, vol.31, pp1663-1667, 1996.
[74] S.D.Brorson, Z.Wang, T.Frank, S.Bischoff, A.Møller-Larsen, J.M.Nielsen, J.Mørk, and M.P.Sørensen "Characteristaion of wavelength chirping in modelocked monolithic CPM lasers," *IEEE.Photon.Tech.Lett*, vol.7, pp1148-1150, 1995.
[75] S.Bischoff, M.P.Sørensen, J.Mørk, S.D.Brorson, T.Frank, J.M.Nielsen, and A.Møller-Larsen, "Pulse shaping mecahnism in colliding-pulse mode-locked laser diodes", *Appl.phys.lett.*, vol.67, pp3877-3879, 1995.
[76] R.G.M.P.Koumans, and R.van Roijen, "Theory for passive mode-locking in semiconductor laser structures including the effects of self-phase modulation, dispersion, and pulse collisions," *IEEE.J. Quantum.Electron*, vol.32, pp478-492, 1996.

Chapter 4- MOVPE grown GaAs/AlGaAs T-CPM MQW lasers.

In Chapter 3, details were given on how monolithic CPM lasers could be realised, by introducing a multi-contact laser design to semiconductor heterostructures. This chapter describes how, by application of these ideas, CPM lasers were fabricated in MOVPE grown GaAs/AlGaAs MQW material. In these lasers, the refractive index guiding was provided by dry etched ridge waveguides, which were produced from the clean room and dry etching facilities in the Department of Electronics and Electrical Engineering in the University of Glasgow. The design of the devices fabricated here was based on the CPM laser developed by Martins-Filho *et al*[1] in this department.

An important potential application of mode-locked semiconductor lasers is in all-optical lightwave communications systems, where synchronisation to external optical signals is often required, so with this in mind changes to the standard CPM configuration were made which would allow the saturable absorber to be made optically accessible. The final devices are referred to as T-section colliding pulse mode locked lasers (or T-CPM lasers) since the design includes a perpendicular waveguide crossing the laser waveguide through the saturable absorber region.

The initial section of this chapter will describe the wafer used for the fabrication and its characterisation of its optical properties through broad area lasers. After this, the ridge waveguide (RWG) T-CPM laser fabrication is described, and the chapter concludes with a report on the operational testing of these devices using spectral measurements.

4.1- GaAs/AlGaAs Material QT664.

4.1.1- Wafer specification.

Following the discussion at the end of chapter 3, it is evident that MQW structures are ideal for the application of monolithic mode-locking in semiconductors for the following reasons among others: high differential gain; useful saturation characteristics from highly sublinear gain/carrier density relationship; ultrafast non-linear absorption recovery through exciton effects; and low levels of self-phase modulation through the reduction of the linewidth enhancement factor. The GaAs/AlGaAs laser wafer used in this project consisted of a four GaAs QW active region, nominally emitting at a wavelength of 860 nm. The wafer was grown using MOVPE by Dr John Roberts at the central EPSRC III-V facility at Sheffield University.

The specification of the wafer QT664 (shown schematically in figure 4.1) is as follows from the p-side down: a 0.2 μm highly doped ($2x10^{19}$ cm^{-3} zinc) GaAs contact layer; a 1 μm p-type carbon doped ($2.2x10^{17}$ cm^{-3}) $Al_{0.43}Ga_{0.57}As$ upper cladding layer; an unintentionally doped 0.25 μm waveguide core with a multi-quantum well active region: a 1.7 μm n-doped $Al_{0.43}Ga_{0.57}As$ lower cladding layer ($1.4x10^{17}$ cm^{-3}); and finally, a 400 μm n+GaAs substrate. The active region contained four 10nm GaAs quantum wells with three lattice matched 10 nm $Al_{0.20}Ga_{0.80}As$ barriers and cladding of 0.1 μm $Al_{0.20}Ga_{0.80}As$ layers.

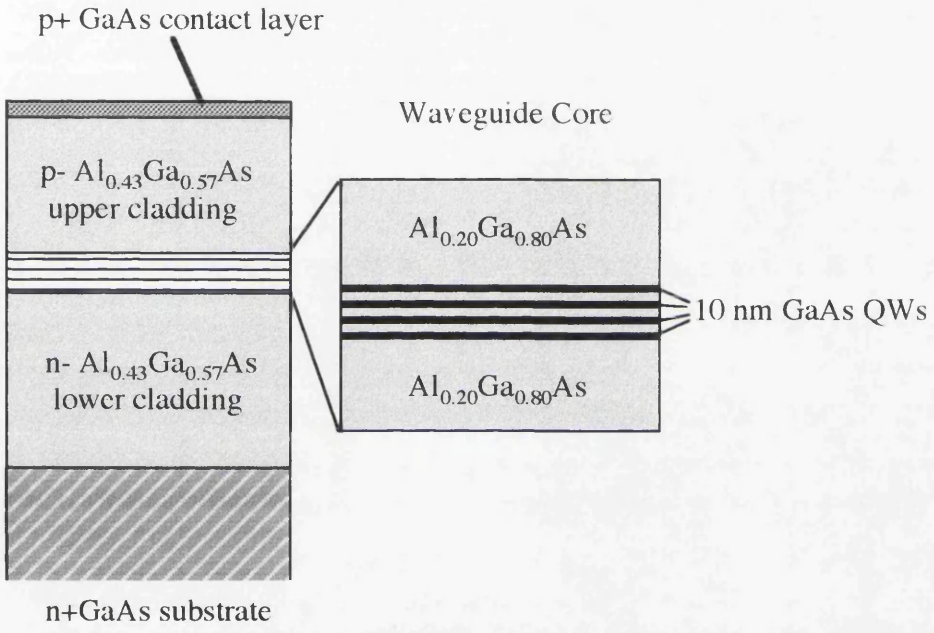

Figure 4.1: QT664, MOVPE grown 4 QW wafer schematic diagram.

4.1.2- Material characterisation.

Broad area lasers are useful in providing measurements of the optical quality of a semiconductor laser material, i.e. threshold current density, internal losses, internal quantum efficiency, etc. This is due to the fact that the wide current injection window of these structures allows effects of current spreading to be neglected. In narrow stripe devices, the region over which the current spreads after injection is wide compared to the region of induced gain, which leads to errors in estimation of the material characteristics deduced from their operation[2].

The broad area lasers fabricated to test QT664 were 75 μm wide oxide-stripe lasers. A schematic diagram of such a device is shown in figure 4.2. Wide oxide-stripe lasers are extremely simple to make as they only require a single photolithographic step. Firstly, silica is deposited onto the p-side of the sample substrate, and a 75 μm wide darkfield photolithography mask is used to define the current injection windows, which

are then etched in buffered HF (4 RO water : 1 HF). After the substrate is thinned to around 200 nm and the p/n contacts are evaporated the devices are ready to be cleaved and tested.

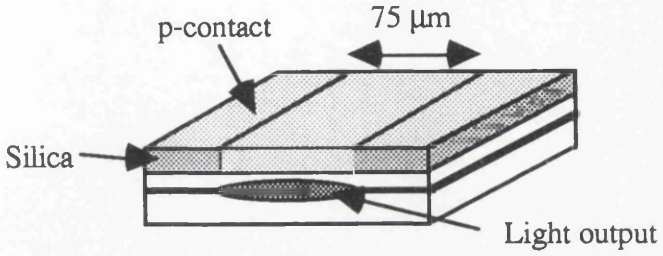

Figure 4.2: 75 μm oxide stripe laser.

The full fabrication process used for the wide oxide-stripe laser fabrication in QT664 was as follows:

1:-Clean sample using optoclear/acetone/methanol/RO water in ultrasonic bath.
2:-Deposit 200 nm of silica by PECVD.
3:-Spin on S1400-31 photoresist at 4000 rpm for 30 seconds. Bake for 30 minutes at 90°C.
4:-Align and expose darkfield 75 μm wide current injection mask
5:-Develop in 50/50 developer/RO water for 1 minute 15 seconds.
6:-Bake resist at 120°C for 1 hour.
7:-Etch silica in buffered HF for 30 seconds, and remove resist
8:-Prepare for p-contact: deoxidise in 1HCL/4ROwater
9:- Evaporate p-contact: 15 nm NiCr , 250 nm Au
10:-Thin substrate to 200 μm using 9 μm alumina.
11:-Evaporate n-contact: 14 nm Au, 14 nm Ge, 14 nm Au, 10 nm Ni, 200 nm Au.

Cleaved mirrors provide the optical feedback in diode laser cavities. The semiconductor wafer cleaves smoothly along crystal planes, so to ensure that the mirrors are perpendicular to the waveguide, the current injection mask must be carefully aligned along one of these planes. The flats present as standard on semiconductor wafers are parallel to crystal planes. Plasma enhanced chemical vapour deposition (PECVD) was used to deposit the 200 nm of silica, however other methods such as RF sputtering or e-beam evaporation could be used with equal success. The nickel/chromium alloy nichrome (NiCr), along with gold (Au), is used as the p-contact metalisation. Although theoretically a Schottky barrier, diffusion of the NiCr into the GaAs contact layer decreases the depletion region at the interface significantly allowing

conduction through tunnelling to take place: so in practice the form of the contact is generally Ohmic. If contacts display rectifying properties or have a high resistance, they can be annealed after evaporation to induce diffusion of the metal into the semiconductor. The substrate is thinned to 200 μm to reduce the series resistance when the diode is forward biased, and this will in turn reduce the heating effects caused by power dissipation in the material.

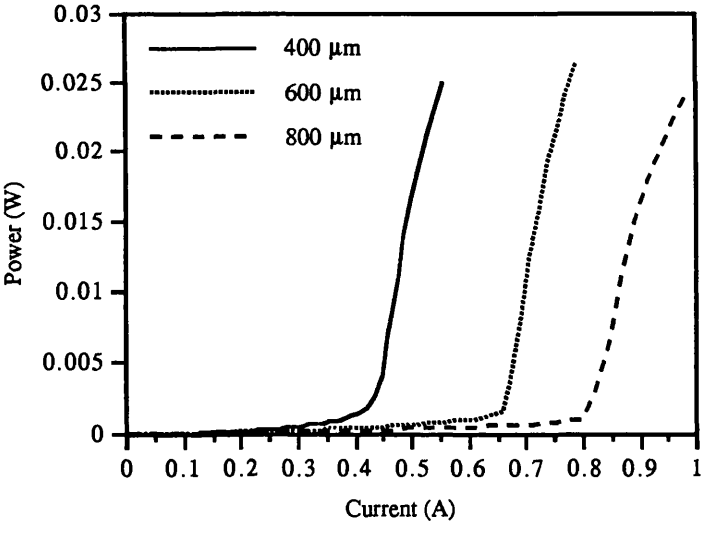

Figure 4.3: lxi curves for 75 μm wide oxide strip lasers in QT664.

After fabrication, individual devices are produced from the sample by scribing and cleaving. This is performed by aligning a diamond tipped scribe, under a microscope, perpendicular to the waveguide direction. The wafer is then scribed at its edge, forming a line of weakness parallel to the crystal planes. With the application of pressure to both sides of the scribe mask, the sample will be cleaved all along its length. Under the scribed portion, the semiconductor facet is severely damaged and cannot be used. However along the cleaved portion the surface is mirror smooth having around a 30% reflectance. Using this technique, oxide-stripe lasers were cleaved at 400 μm, 600 μm and 800 μm long cavity lengths.

An important measurement in characterising the operation of diode lasers is the light power against injection current curve (lxi). Operation of a diode laser with a continuous wave current supply (CW) causes a large amount of heat to be dissipated in the laser chip. This can severely diminish the performance of the laser, as temperature dependent non-radiative recombination is enhanced, but it can also destroy the diode by diffusion of impurities (or aluminium in the case of AlGaAs devices) into the active region. To avoid this, adequate heat sinking and cooling is required. As this is a laborious and time consuming task, it is impractical to test the large number of devices required for a proper characterisation of the material. It is practical, however, to

circumvent this situation by supplying the driving current to the laser as a series of short pulses. By using a Boxcar integrator to record the average photocurrent detected by a photo-diode, a laser lxi curve can be effectively measured without the requirement of proper heat sinking. Using such a set up, the lxi curves were recorded for ten devices at each of the cleaved cavity lengths. The lasers were mounted in a simple clip, which provides both p, and n contacts. In the system used, the current and output power were automatically recorded by a Macintosh computer system running a LabView interface program.

Figure 4.3 shows the recorded lxi curves for three typical devices. Note the increase in threshold current and decease in slope efficiency as the cavity length is increased. In equation (2.24), the external quantum efficiency is defined. By measuring the slope efficiency (W/A) of each device, the external quantum efficiency η_{ex} can be calculated by multiplying by $e/\hbar\omega$. The graph in figure 4.4(a) shows the average inverse external quantum efficiency for each cavity length plotted against the cavity length. By inspection of equation (2.24), it is evident that the y axis intercept provides a measure of the internal quantum efficiency η_{int}, and the gradient provides the internal losses α_{int}. Also, by plotting the threshold current density J_{th}, evaluated by dividing the threshold current by the injection window area, against the inverse laser length (figure 4.4(b)), the threshold current at infinite length can be evaluated from the y-axis intersection.

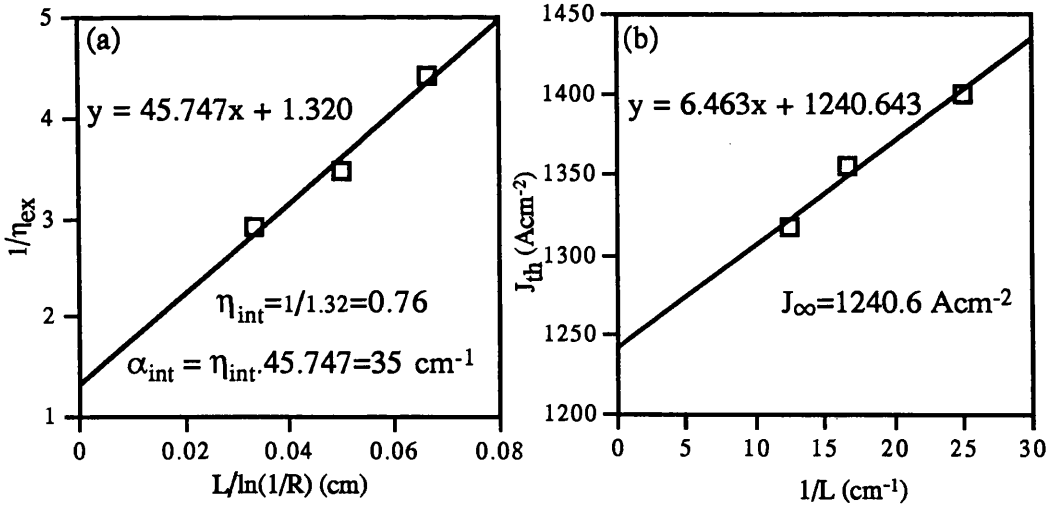

Figure 4.4: Characterisation of wafer QT664, (a) external quantum efficiency against laser length (parameters calculated from equation (2.24)), and (b) threshold curent density against inverse laser length.

From figure 4.4(a), the least squares linear fit allows the evaluation of the internal quantum efficiency at 76% and internal losses at 35 cm^{-1}. Although the quantum efficiency is quite high, so is the internal loss, leading to the high value obtained for the threshold current density at infinity of 1240.6 Acm^{-2} (from figure 4.4(b)). For a typical

400 μm long cavity laser, the threshold current density was measured at 1367 Acm^{-2}. In the best quality laser material, external quantum efficiencies can reach above 90% with losses recorded below 10 cm^{-1}, so the material used in this experiment is relatively poor[3]. For example Martins-Filho *et al*[1] reported α_{int}=5.5 cm^{-1} with η_{int}=69%, for 75μm wide-oxide stripe lasers fabricated in a similar 4 QW GaAs/AlGaAs MOVPE wafer. For a 400 μm long laser they reported typical J_{th} of 583 Acm^{-2}. The high threshold current densities from QT664 would result in the CW operation being difficult to achieve in diode lasers with longer cavity lengths (i.e. 1mm and above). However this was not a great problem with the devices in this project, where the CPM lasers were designed to operate at 100 GHz repetition frequencies and above, so the cavity lengths were only in the order of 100s of μm.

4.2- T-CPM laser fabrication.

4.2.1 Laser design.

As discussed in section 2.2.1, the GaAs/AlGaAs structure of QT664 provides optical confinement in the direction parallel to the QW layers, through total internal reflection with the waveguide core consisting of $Al_{0.20}Ga_{0.80}As$, which has a higher refractive index (lower bandgap) than the waveguide cladding layers of $Al_{0.43}Ga_{0.57}As$ surrounding the core. To restrict the optical field to the fundamental mode, it is also necessary to induce waveguiding in the lateral direction (section 2.2.2), perpendicular to the wells. For the T-CPM lasers fabricated in this project, this is achieved by a combination of gain guiding and weak index guiding. The index guiding is introduced via a ridge waveguide, 3 μm wide and 0.7 μm deep, etched into the p-cladding layer parallel to a crystal plane (ensuring cleaved facets are perpendicular to waveguide); the gain guiding was introduced by allowing only a narrow window (5 μm) for current injection along this ridge.

Figure 4.5 shows a schematic diagram of the T-CPM lasers that were produced. Along with the etched ridge forming the laser waveguide, there is another waveguide monolithically integrated perpendicular to it, starting from the edge of the laser chip and passing through its centre. The split p-side contact allows the definition of a long section that is forward biased to inject current and provide the laser with optical gain. It also allows the definition of a short electrically isolated section in the centre of the cavity that can be reverse biased to form a saturable absorber in CPM geometry.

In the introductory discussion in Chapter 1, all-optical communications signal processing, such as clock recovery and multiplexing, was suggested as a prime motivation for the study of mode-locked semiconductor lasers. To synchronise digital laser oscillators, such as mode-locked lasers or self-pulsating lasers, to an external

optical signal, requires the injection of the signal directly in to the laser waveguide. There are two main approaches to this: one is to inject the external signal directly into the facet and along the laser waveguide, an approach which has been shown to be successful in the synchronisation of self-pulsating lasers to optical data streams[4]; the other is to inject the signal into the saturable absorber perpendicular to the laser waveguide, an approach which theoretical studies have shown would allow synchronisation over a larger range of repetition frequencies for CPM laser diodes[5]. A simple method of coupling the light into the absorber is via the integration of a perpendicular side injection waveguide passing through the absorber[6]. In the T-CPM implementation, the injected signal is amplified at the input to the side injection waveguide (see figure 4.5), so that the majority of the absorption of the signal will take place in the reverse biased saturable absorber. Current injection windows were opened up all along the laser waveguide, but only under the amplifier contact on the side-injection waveguide. Therefore, after the saturable absorber the waveguide is unpumped and has high loss and this will prevent the waveguide from lasing. The facet of the side-injection waveguide at the gain section can be used to monitor the coupling after the external light signal is directed into the waveguide.

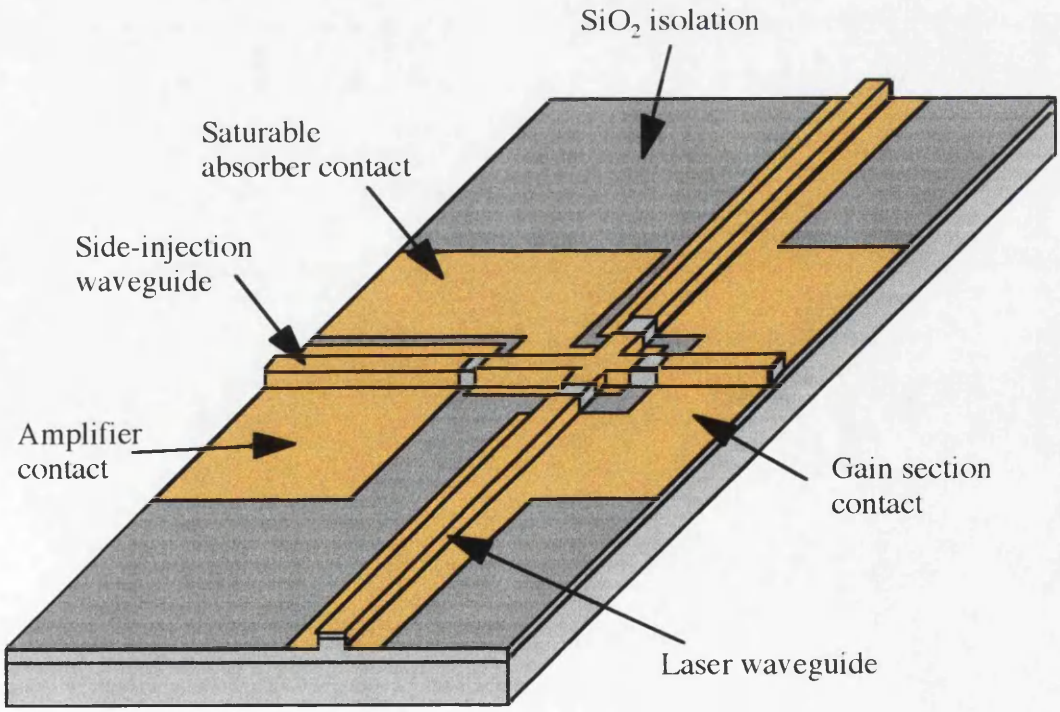

Figure 4.5: Schematic diagram of T-section CPM laser.

4.2.2 Laser fabrication.

Fabrication of the T-CPM lasers involved a higher degree of complexity than that of oxide-stripe lasers because of the addition of one important new step- namely the ridge waveguide (RWG) etching. Wet chemical etching of GaAs and AlGaAs is a simple method of transferring patterns, but due to the nature of wet etching, e.g. crystal orientation dependence or isotropic etching (same rate in all directions), it is often difficult to reproduce straight ridge sidewalls. However, as long as a low damage process can be found, dry reactive ion etching (RIE) can provide highly anisotropic features, perfect for the production of RWG lasers. RIE involves the high energy impact of ions from a plasma breaking down the sample surface, then removing surface constituents by forming volatile compounds. Dry etching using $SiCl_4$ plasmas is a low damage and highly anisotropic method of etching waveguides in Ga containing compounds[7,8].

In this project $SiCl_4$ etching was used to form the crossed waveguides for the T-CPM lasers in the GaAs/AlGaAs material system. Dry etching required the use of a hard unreactive mask for proper pattern transference. Silica, photoresist, or metal can be used for this purpose. In this project a thin 15 nm NiCr mask, defined by photolithography, metal evaporation, and lift-off, was used for the dry etch. Silica masks could be used with equal success, although the need for a further dry etch step to define the mask makes it less attractive. It was found that resist masks produced ragged etch profiles, that were not as uniform as those provided by metal or silica. The machine used for etching GaAs/AlGaAs with $SiCl_4$ in the dry etching facility of the University of Glasgow is the RIE80. This machine has been adapted to allow *in situ* monitoring of the etch depth, by the addition of an interferometer system[9]. In this system, a laser is shone on the sample during the etch., and as the semiconductor laser structures contain many thin layers of different refractive indices, the reflected signal from the laser goes through several peaks and troughs as the etch progresses. By modelling the reflectance properties of any particular heterostructure material using a specially written program, and comparing it to the recorded reflectance during the etch, precise control of the etch depth can be obtained.

Another difference between the T-CPM and the oxide stripe lasers is the definition of a split contact on the p-side. Again this can be performed in two ways: evaporation of the metal contact over the whole of the p-side, then selectively etching sections away to form the pattern; or alternatively, using a resist mask to lift-off evaporated metal to define the pattern. The latter process is easier to implement in practice, and was used in this project. The design of the p-contact mask is shown in figure 4.6. The most important dimensions are the total length of each device, 800 μm, the saturable absorber length, 10 μm, and the gap between the absorber and the gain section on the waveguide,

which is also 10 μm. The small squares outside the main body of the mask are alignment marks to assist the cleaving of devices at various cavity lengths. The resist used to provide the lift-off mask was Shipley S1400-31, which results in a 1.8 μm thickness when spun on at 4000 rpm for 30 seconds. To aid in the lift-off process, the resist was undercut by soaking in chlorobenzene prior to mask exposure and development. Without this undercut, it would have been extremely difficult to lift off the metal from around the saturable absorber region, due to the small scale of the dimensions.

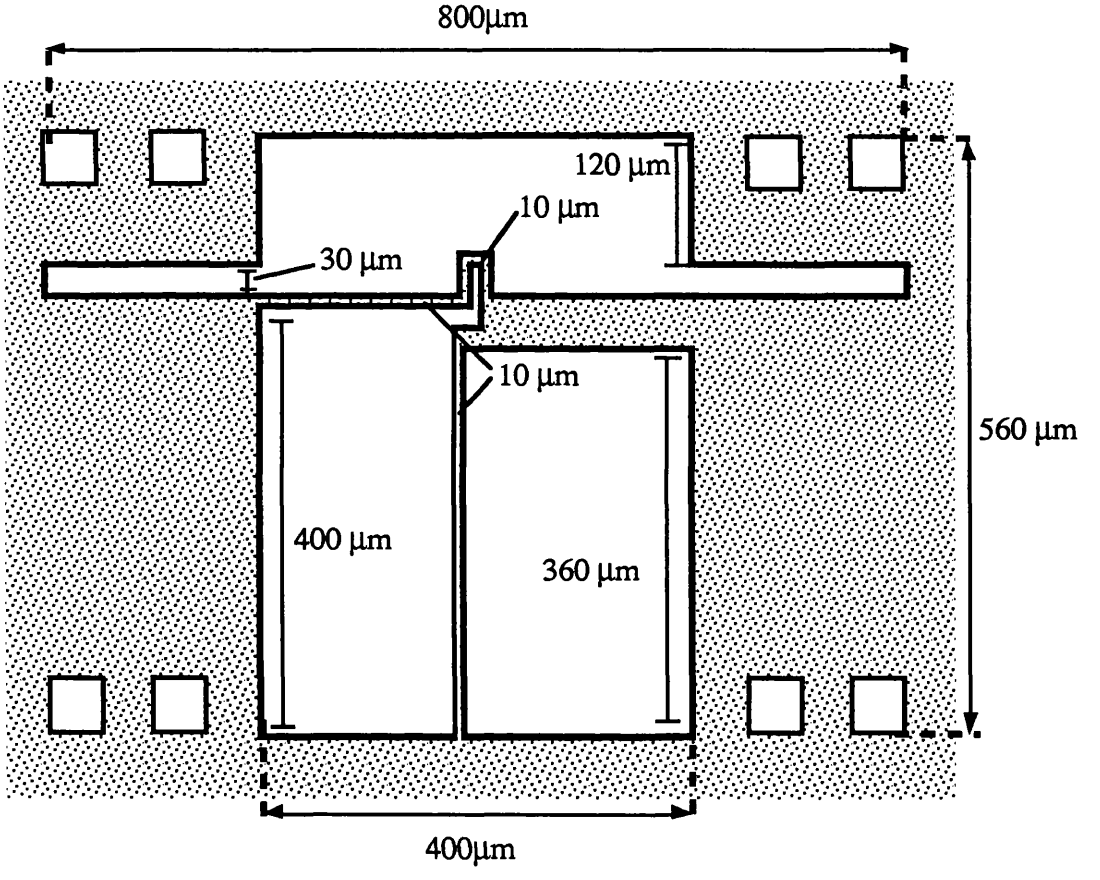

Figure 4.6: Dimensions of lift-off mask used to define the p-contact for the T-CPM laser.

The complete fabrication process for T-CPM lasers in QT664 is given below (also shown diagramatically in figure 4.7):

1:-Clean sample using optoclear/acetone/methanol/RO water in ultrasonic bath.

2:-Spin on resist primer at 4000 rpm for 30 seconds.

3:-Spin on S1400-17 photoresist at 4000 rpm for 30 seconds. Bake for 30 minutes at 90°C.

4:-Align and expose 3 μm darkfield waveguide mask (aligned parallel to crystal plane).

5:-Develop in 50/50 developer/RO water for 1 minute.
6:-Evaporate 15 nm NiCr
7:-Lift-off in acetone
8:-$SiCl_4$ dry etch in RIE80 using interferometer system to judge etch depth of 0.7 μm.
9:-Remove NiCr mask in 4 HCL:1 ROwater 3 minutes (approx 50% over etch).
10:-Deposit 200nm PECVD silica.
11:-Spin on S1400-17 photoresist at 4000rpm for 30 seconds Bake for 30 minutes at 90°C.
12:-Align and expose 5 μm darkfield contact window mask.
13:-Develop in 50/50 developer/RO water for 1 minute.
14:-Remove 200nm in buffered HF for 14 seconds.
15:-Remove resist mask in acetone.
16:-Spin on S1400-31 photoresist at 4000rpm for 30 seconds. Bake for 15 minutes at 90°C, soak in chlorobenzene for 15 minutes , then bake again for 15 minutes at 90°C
17:-Align and expose to p-contact lift-off mask.
18:-Develop in 50/50 developer/RO water for 1 minute.
19:-Prepare for p-contact: deoxidise in 1HCL/4ROwater.
20:-Evaporate p-contact: 20 nm NiCr and 250 nm Au while rocking sample at 45°.
21:-Thin substrate to 200 μm using 9 μm alumina.
22:-Evaporate n-contact: 14 nm Au, 14 nm Ge, 14 nm Au, 10 nm Ni, 200 nm Au.
23:-Selective $SiCl_4$ dry etch in RIE80. Etch GaAs contact layer only to isolate the various sections on the p-side.

As mentioned in section 4.2.1 above, the side-injection waveguide is only pumped before the saturable absorber region. So in contrast with the current injection window of the laser waveguide, which is continuous, a window was etched only along part of the side-injection waveguides length. Figure 4.8(a) shows a photograph of the cross-waveguide structure after the dry etch and subsequent mask removal (stage 9). After the silica deposition and contact window etching (step 15) the same sample is shown in figure 4.8(b), with the laser waveguide in the vertical direction.

The sample was rocked at a 45° angle during the evaporation of the p-contact (step 20) to ensure that the sidewalls of the ridge were adequately covered. Otherwise the layer of metal connecting the large contact pads to the p+ GaAs contact layer on top of the ridge, would have been extremely thin and could easily have formed an open circuit during operation with a CW current supply. The NiCr alloy was used in the p-contact recipe because the chromium content (10%) gave the gold contact a better adhesion to the silica than if pure nickel was used. This became extremely important when wires were bonded to the contact pads in order to provide external connections to bias voltage and current supplies. If there was an inadequate adhesion to the silica, the contact was

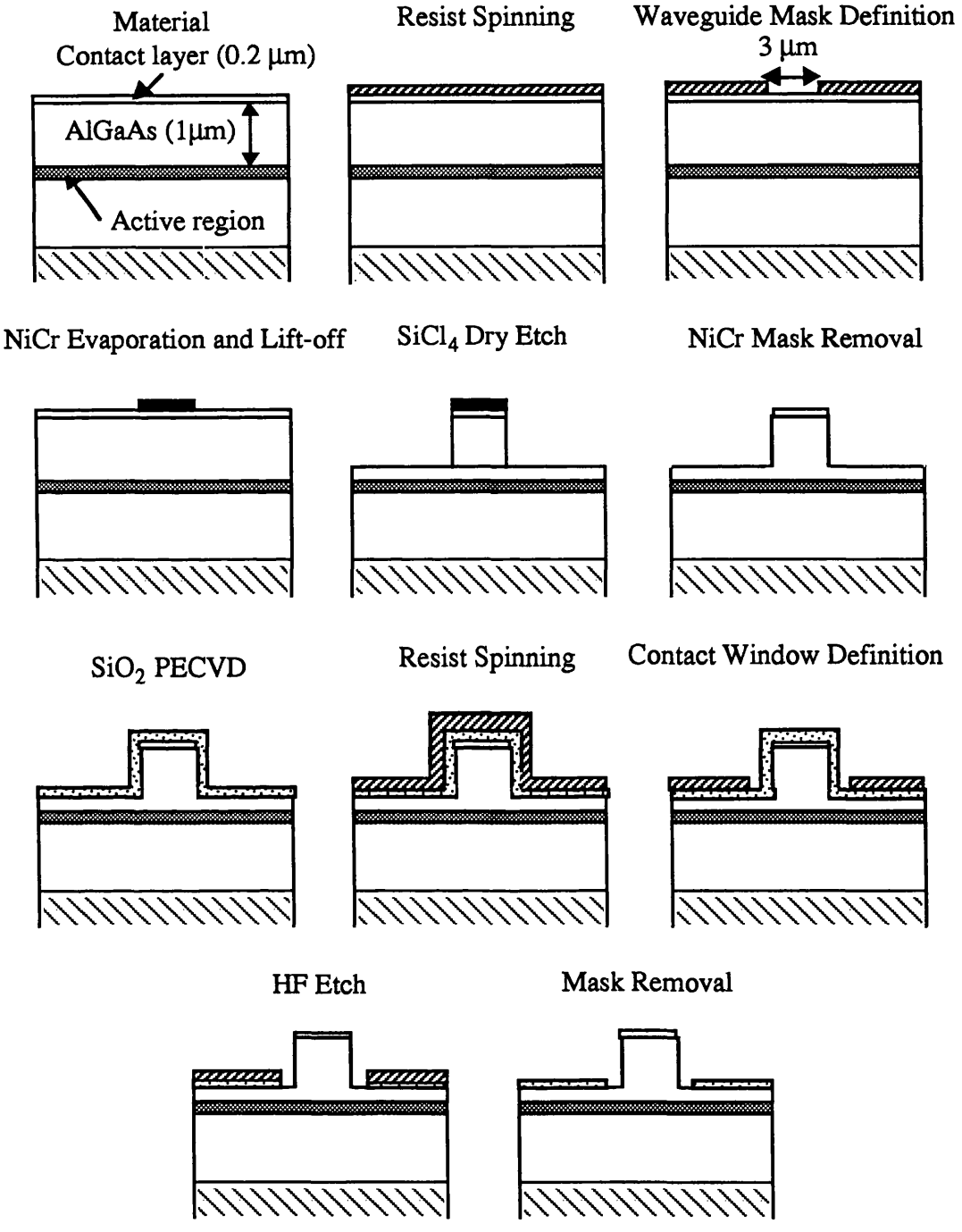

Figure 4.7: Process diagrams for RWG laser fabrication in GaAs/AlGaAs structures.

easily ripped off during the bonding process The technique used to wire bond the devices is described in the next section.

The final stage in the fabrication process, step 23, was a selective etch to remove the p+ GaAs contact layer on top of the ridge from between the sections. This increases electrical resistance between the sections, which is extremely important for the successful operation of mode-locked diode lasers as any carriers leaking from the gain section into the absorber have a substantial effect on saturation characteristic, and also reduce the effect of the reverse bias. The selective etch used was a low power $SiCl_4$ etch, specifically developed to etch GaAs but to stop on AlGaAs[7]. Figure 4.9 shows the electrical characteristics of a completed T-CPM laser. These were tested using a Hewlett Packard 4145 semiconductor parameter analyser which included a probe station to automatically provide a range of bias levels, then record and plot the results. The forward bias diode characteristic was taken (figure4.9(a)) by probing the gain section contact and the ground. The turn on voltage of 1.3V was typical of GaAs diodes indicating a non rectifying contact, and the slope resistance was a low 26.8 Ω. The effect of the final isolation etch is shown in figure 4.9(b), which displays the voltage-current relationship (VxI) when the sample is probed between the absorber and the gain section contact pads. The straight lines through the origin indicate that the contact is Ohmic in nature, and the resistance was seen to increase from 986 Ω to 1.85 kΩ when the isolation etch was performed. The corresponding resistance between the gain section and the amplifier section was 4.1 kΩ.

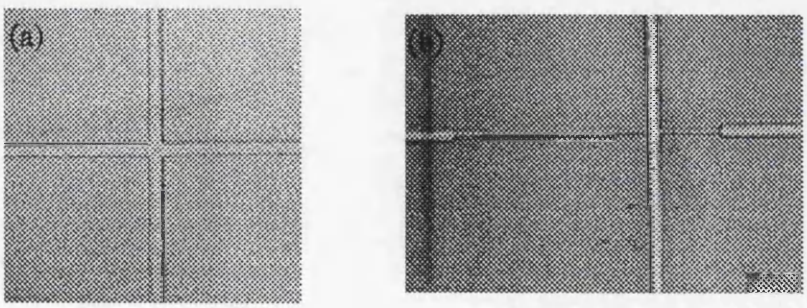

Figure 4.8: Photographs of crossed waveguide structure (a), and contact window etching (b).

4.3 T-CPM laser testing.

4.3.1- Device cleaving and mounting.

After fabrication of the T-CPM lasers, they were cleaved into 400 μm and 600 μm cavity lengths. For mode-locked semiconductor lasers, where the repetition rate is

fundamentally determined by the cavity length, accurate cleaving is of the utmost importance. In CPM lasers, accuracy in cleaving becomes increasingly essential as there is a stringent requirement for the saturable absorber to be precisely in the centre of the laser cavity. The standard method of cleaving lasers is to measure the required cavity length with a micrometer. With the T-CPM laser, the symmetry condition requires two scribe marks for each device to be made at exactly the same distance from the centre of the saturable absorber. Measuring these distances via a micrometer introduces inaccuracy through reading errors and backlash in the micrometer motion. To aid in the cleaving process, marks were added to the p-contact photolithography mask. Figure 4.10 shows a photograph of a fabricated T-CPM laser, just before the cleaving stage. The cleaving marks can be seen as the gold squares outside the main three section laser body, placed symmetrically around the central saturable absorber. Cleaving was then carried out by a simple alignment of the scribe to the edges of these cleaving marks. If used appropriately, the maximum estimated error in cavity length is around 3-5 μm with this cleaving technique. Although many laser waveguides are fabricated simultaneously on the same chip, the required accuracy prevents them from being cleaved from the same scribe mark. Instead of this, rows of devices on each waveguide are cleaved out first, and then the individual devices are cleaved at the required size from each bar. Note also that care was taken here to cleave rather than scribe out the rows, since the side-injection waveguide must also have an optically smooth surface, to allow efficient input coupling of the external light signal.

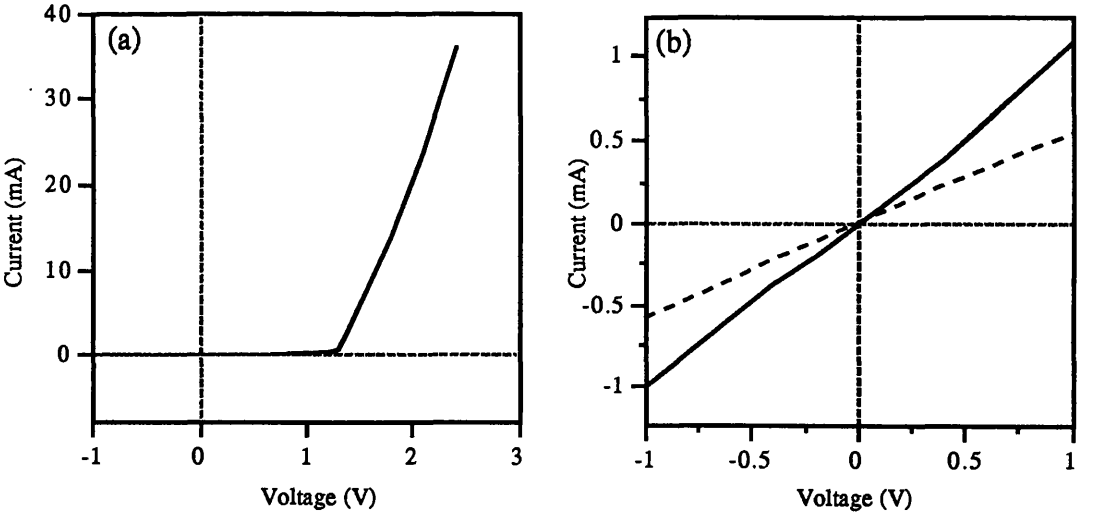

Figure 4.9: (a) Forward bias diode characteristaic of T-CPM laser from QT664, and (b) VxI between absorber and gain sections before (solid line), and after (dashed line) the final isolation etch.

To obtain an initial impression of how well the lasers were operating, without having to heat sink the devices, it was useful to test them with a non-CW current source. Using

the pulsed-current test rig described in section 4.1.2, the T-CPM lasers were tested, with the clip supplying the forward bias to the gain section, and the absorber and amplifier left unbiased. Typical lxi curves taken using this technique are displayed in figure 4.11(a). The threshold currents of the 400 μm devices were around 70 mA, and the 600 μm devices around 100 mA. These values are high compared to other results reported by researchers[1] using similar laser structures, although this was expected due to the high internal loss measured via the oxide-stripe lasers. The power spectrum of a 400 μm T-CPM is shown in figure 4.11(b), where the normal cavity longitudinal wavelength separation was approximately 0.24 nm, as expected from the theoretical expressions (3.6) and (3.7). The wavelength spectra in this project were measured with an Advantest Q8381 optical spectrum analyser. The laser light was coupled into the analyser via a multi-mode optical fibre.

Although pulsed current measurements are useful to characterise the performance of laser devices, any practical application requires that they are operated continuously. The heat produced in diode lasers during CW operation must be removed as efficiently as possible to avoid damage to the device. To achieve this the lasers were indium-soldered onto gold plated copper blocks. The soldering was accomplished by heating small balls of indium on the copper blocks, with the ball positioned on the intended final position of the laser diode chip. Flux was added during the heating to stop the indium surface from oxidising which would prevent a good adhesion to the semiconductor and create a layer of poor heat conduction. Once the indium was melted the cleaved laser chips are placed on top of it, and the block is removed from the heat. The devices were then cleaned free of the solder flux by immersion in trichlorethane. The T-CPM lasers were mounted p-side up on the copper blocks, as the split p-side contact must remain accessible to several external connections for mode-locked operation.

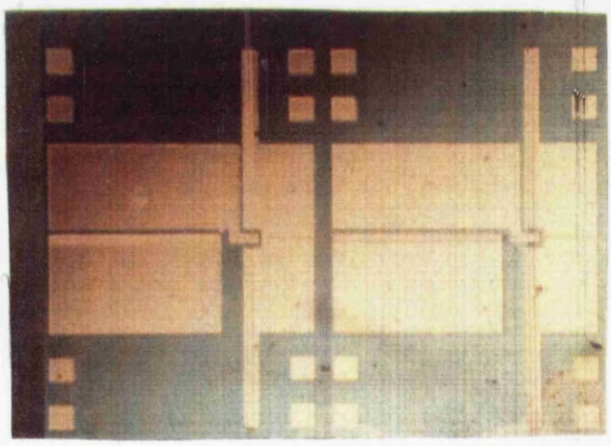

Figure 4.10: Fabricated T-CPM laser in QT664 before the cleaving stage.

It was possible after mounting the devices to apply the various currents and bias voltages via probes. As the contact pads on the T-CPM lasers were very small, it was difficult to carry out the probe alignment every time a device is operated. In an experimental situation, it is infinitely preferable to bond wires from an external circuit board to the contact pads on the diode surface. A 25 μm thick gold wire was bonded to the amplifier, gain section, and absorber contact pads of 400 μm and 600 μm T-CPM lasers. The bonding was carried out using a Kulicke & Soffa 4123 wedge bonder. If the contacts are not adhered sufficiently to the underlying silica, the pads were often ripped off with the harsh action of the ultrasonic bonder. For this reason, great care was taken to ensure that the silica surface was clean before the evaporation of the NiCr/Au p-contact, and to accomplish this, the surface was treated with 1HCL: 4R0 water etch (step 19 of section 4.2.2). Also, the metals had to be thoroughly degassed before evaporation. As previously mentioned NiCr rather than just Ni was used in the p-contact recipe to increase the adhesion to the silica. It is also noted that if the NiCr/Au contacts were annealed the NiCr diffusion into the silica, reduced the adhesion of the gold making it almost impossible to make an ultrasonic wire bond. Therefore, the contacts of the T-CPM lasers were not annealed. However, from figure 4.9(b), it can be seen that the contacts were already Ohmic in nature.

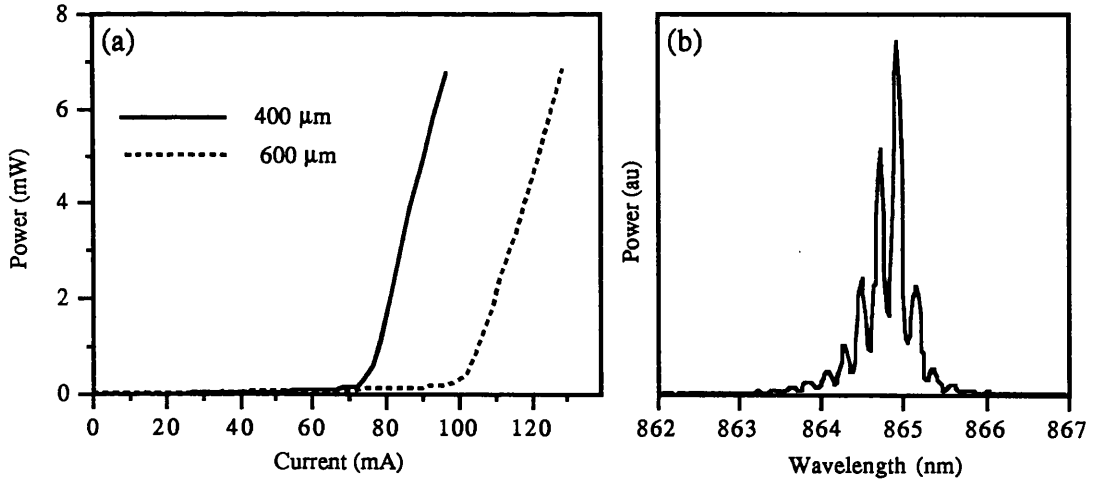

Figure 4.11: (a) Light output power versus current input (lxi) for QT664 400 μm and 600 μm T-CPM lasers (absorber/amplifier floating) tested using a pulsed current supply. (b) Power spectrum for 400 μm device operating at 75 mA.

4.3.2- CW laser testing.

After mounting and bonding, the devices were tested with a CW current supply. During the testing, the mounted T-CPM lasers were operated in a Peltier cooled heat

sink, with a built-in probe station to apply the necessary bias. Figure 4.12 shows the experimental set-up used in the characterisation of the T-CPM lasers, along with a diagram of the bonding scheme for the laser chip. The CW current supply used was an ILX Lightwave LDC-3752 laser diode controller, which also had a thermo-electric cooler module to control the temperature of the mount through the Peltier. In the experiment, the laser beam was collimated with a x20 microscope objective lens, and coupled either into an Anritsu ML9001A optical power meter, or via x10 objective lens into a fibre for the Advantest spectrum analyser.

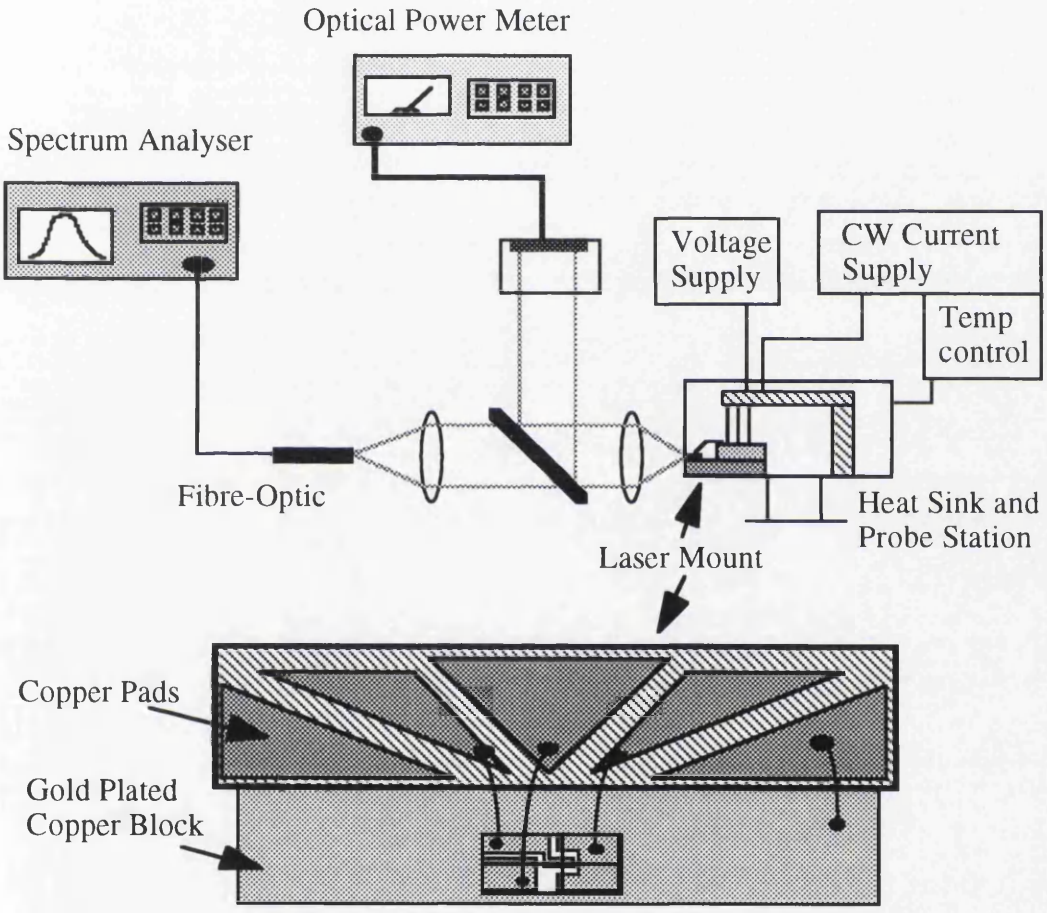

Figure 4.12: Experimental set-up for the CW characterisation of T-CPM lasers, including a top view of the bonding arrangement for the mounted device.

To operate the T-CPM devices as mode-locked lasers, forward bias was applied to the gain section, and reverse bias voltage was applied to the absorber section (for a detailed explanation of how a reverse biased MQW waveguide acts as saturable absorber, see Chapter 3). In figure 4.13, the output power from the facet of a 400 μm T-CPM laser is displayed as a function of the CW current supplied to the gain section, for several values of absorber reverse bias. From a reverse bias voltage of -3.6V to -5V,

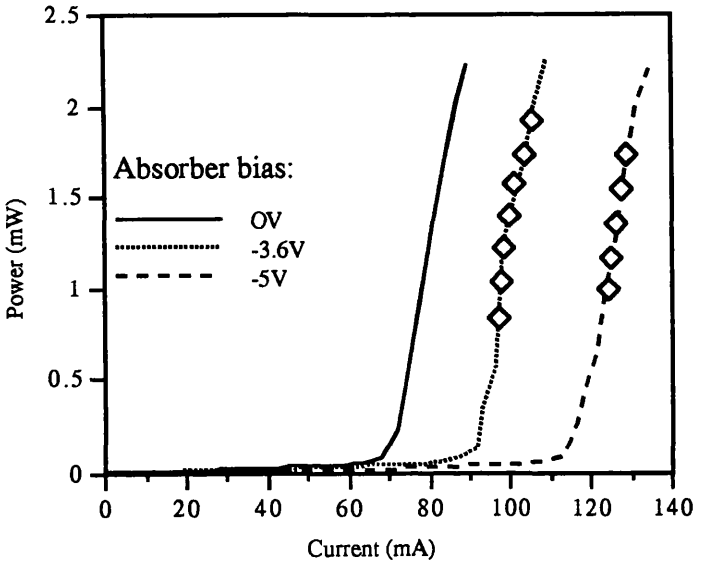

Figure 4.13: CW lxi curves for a 400 μm T-CPM laser from QT664, showing bias range where CPM action was observed (diamonds).

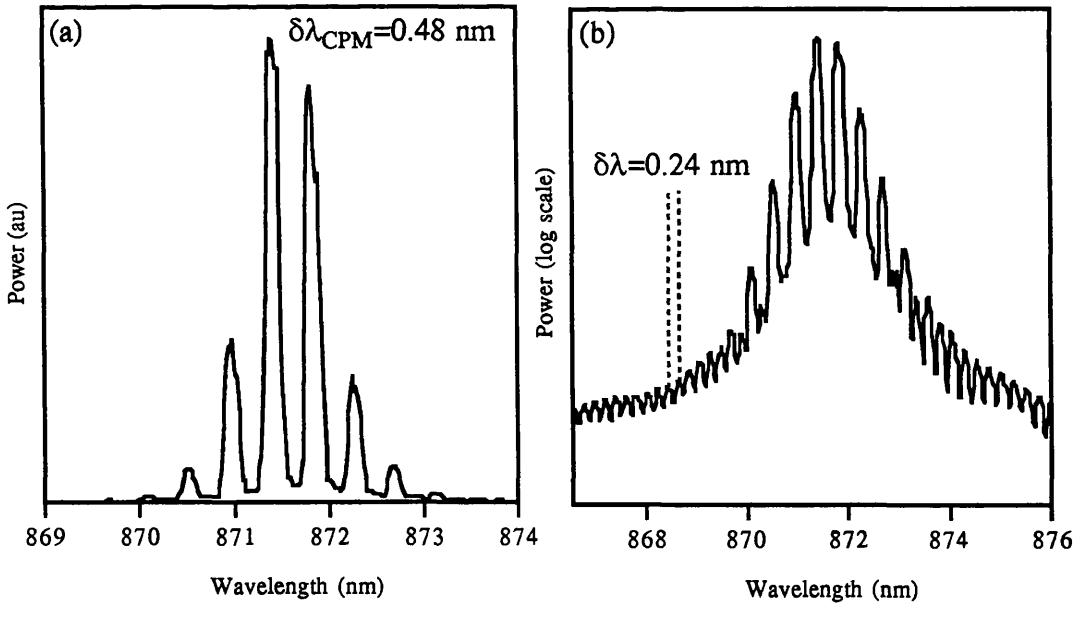

Figure 4.14: Mode-locked power spectrum of a 400 μm T-CPM laser on a linear scale (a), and a logarithmic scale (b).

the longitudinal cavity mode wavelength doubled. This arises from the coherent interaction of two optical pulses colliding in the saturable absorber, forming an optical standing wave which suppresses either the even or odd cavity modes, depending on the phase of the standing wave (Section 3.3.3). This is the characteristic action of a CPM laser[10,11]. Figure 4.14(a) shows the power spectrum of the 400 μm long device, operated at 93 mA with an absorber bias of -3.6V. The spectrum is highly symmetric and consists of eight prominent cavity modes at double the normal wavelength spacing at approximately 0.48 nm. In figure 4.14(b) the same spectrum is shown on a logarithmic scale, and as can be seen, at wavelengths far removed from the centre of the gain spectrum the cavity mode spacing is the normal 0.24 nm for a 400 μm GaAs/AlGaAs laser. This type of CPM spectrum could be obtained only for reverse bias levels in the range -3.6V to -5V. Outwith this range, and at higher and lower currents than those indicated on figure 4.13, a non-doubled multi-longitudinal mode spectrum similar to figure 4.11(b) was observed. From equation (3.7) in Section 3.2, the mode-locked repetition frequency of these 400 μm T-CPM lasers is 190 GHz.

Similarly, CW lxi curves and symmetric CPM spectra were obtained for a 600 μm long T-CPM laser, as displayed in figures 4.15, and 4.16. With this device CPM-like doubled spectral mode spacing was recorded in the range -4V to -5.5V, for the current ranges indicated in figure 4.15. In this case (figure 4.16), the mode spectrum changes from 0.16 nm to 0.32 nm with the onset of CPM action, and showed this doubling over a wide spectral range covering eight modes. This wavelength spacing of 0.32 nm corresponds to a mode-locked pulse repetition frequency of 127 GHz.

Application of reverse bias to the MQW absorber section has two important effects that allow it to act as a saturable absorber and mode-lock the laser diode. One is to control the magnitude of the absorption by shifting the absorption band edge onto the lasing wavelength via the QCSE; the other is to sweep out the carriers generated by the passage of pulses in the absorber, allowing the absorption to recover quickly after its passage. This reverse bias current can cause a degradation in the electrical characteristics of the absorber section, which can lead to it not providing gain when forward biased. To avoid this damage, the current from the absorber was limited by a resistor (50 Ω) during the CW testing of the T-CPM devices.

Although indicating that the 400 μm and 600 μm T-CPM lasers from QT664 were mode-locked, the evidence provided by the doubled spectral modes was not sufficient by itself to obtain any information about the actual mode-locked pulse output from the devices, such as their temporal width or the presence of significant chirp. Although all previous work on short cavity CPM lasers has shown that in general the pulses produced are Fourier transform-limited[1,11,12], this must be confirmed in these experiments. In the following chapter, the pulse trains produced by these devices are investigated using time-domain autocorrelation techniques.

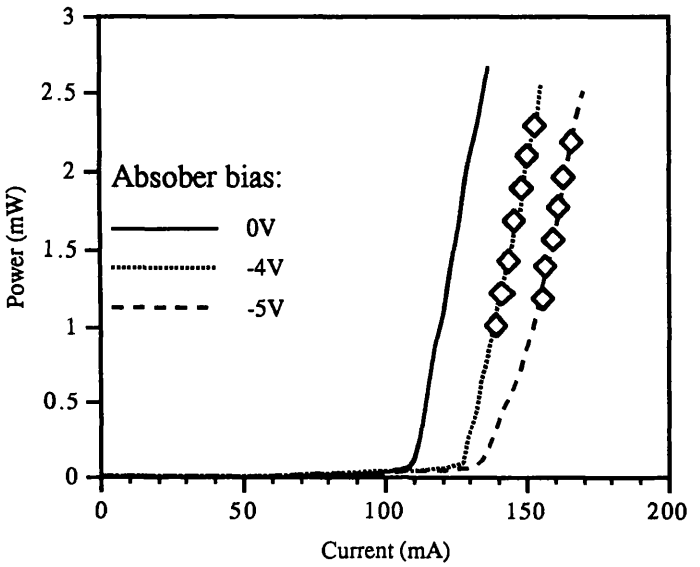

Figure 4.15: CW lxi curves for a 600 μm T-CPM laser from QT664, showing bias range where CPM action was observed (diamonds).

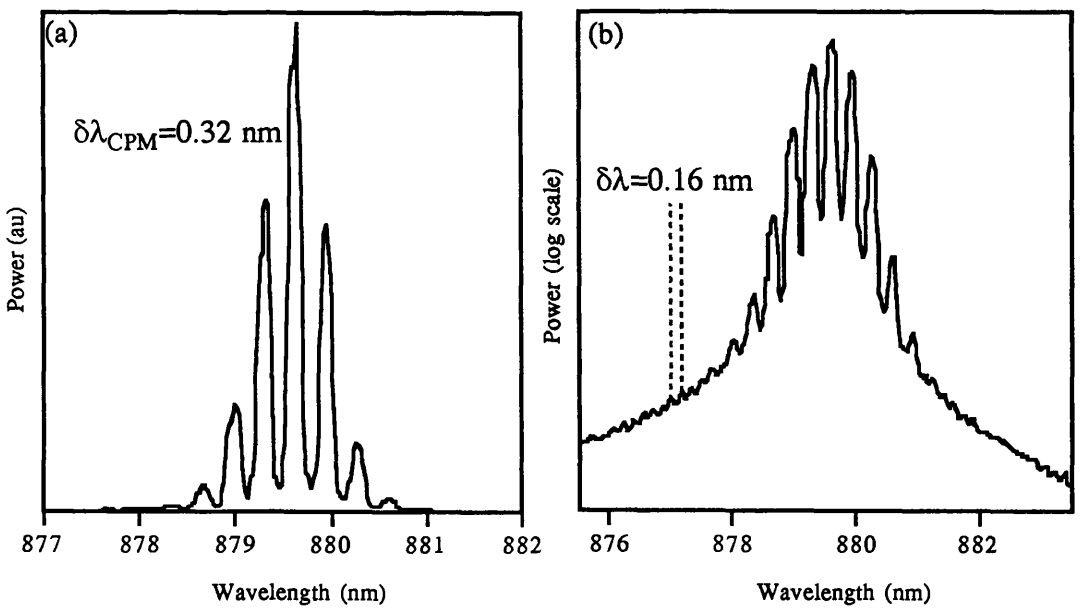

Figure 4.16: Mode-locked power spectrum of a 600 μm T-CPM laser on a linear scale (a), and a logarithmic scale (b).

Along with the CPM operation, the effect of external light applied through the side-injection waveguide has also been briefly investigated. Light from a Ti:Sapphire laser, tuned to 860 nm, was coupled into the side injection waveguide of a 600 μm T-CPM, using a lens ended fibre arrangement. Coupling of the beam into the waveguide was monitored by observing the output from the waveguide at the gain section side. The Ti:Sapphire laser was operated CW, with a constant intensity output power of 20 mW. With the T-CPM operated at 110 mA, the absorber floating, and the amplifier section pumped at 100 mA, a bias change of 1V could be observed across the saturable absorber on injection of the external light. With the amplifier left unpumped, the bias only changed by a few mV on injection of the Ti:Sapphire light. This result indicates that the saturable absorber can be affected by an external light source, although no switching behaviour was observed. Further experiments to characterise any bistable switching behaviour, or synchronisation were beyond the scope of this project, which was primarily concerned with the fabrication of CPM lasers and the characterisation of their mode-locked output.

4.4- Conclusions.

This chapter has described the fabrication and operation of T-CPM lasers in MOVPE grown 4 QW GaAs/AlGaAs material. Also, a method for the characterisation of semiconductor laser material has been detailed. Important points to be brought out of the fabrication process are: special cleaving requirements due to symmetry of CPM lasers; isolation etching to provide high resistance between the sections of the split p-contact; careful preparation for p-contact to enable successful ultrasonic wire bonding; and adequate heat sinking to extend lifetime during CW current operation.

Low damage $SiCl_4$ dry etching was successfully employed to produce the crossed ridge waveguide structure that provides the index guiding for the laser oscillator, while rendering the saturable absorber accessible to external light signals. Using etched RWG structures for mode-locked semiconductor lasers offers considerable improvements in cost and simplicity over the buried heterostructure lasers employed by most authors reporting CPM operation of diode lasers[11], which involve post processing epitaxial regrowth.

From the evidence provided from measurement of their optical spectra, while operating with a CW current supply, lasers of both 400 μm and 600 μm cavity lengths fabricated from MOVPE grown 4 QW GaAs/AlGaAs material (QT664) have been shown to act as CPM lasers with mode-locked repetition rates of 190 GHz and 126 GHz respectively.

Chapter 4: References.

[1]J.F.Martins-Filho, *Monolithic Colliding Pulse Mode-locked Quantum-well Lasers*, Ph.D. Thesis, University of Glasgow, 1995.

[2]G.P.Argawal, and N.K.Dutta, *Semiconductor Lasers*, New York:Van Nostrand Rienhold, 1993.

[3]G.H.B. Thompson, *Physics of Semiconductor Laser Devices*, Wiley 1980.

[4]P.Barnsley, "All-optical clock extraction using two-contact devices," *IEE Proceedings-J*, vol. 40, pp325-336, 1993.

[5]E.A.Avrutin, J.M.Arnold, and J.H.Marsh, "Analysis of dynamics of monolithic passively mode-locked laser diodes under external periodic excitation," *IEE. Proc.optoelectron.*, vol.143, pp81-88, 1996.

[6]H.Tsuada etal., "Wide range wavelength conversion experiments using a side-injection light controlled bistable laser diode," *Appl.Phys.Letts.*, vol.63, pp3116-3118, 1993.

[7]S.K.Murad, S.P.Beaumont, and C.D.W.Wilkinson, "Selective and non-selective RIE of GaAs/AlGaAs in a $SiCL_4$ plasma," *Microelectronic.Eng.*, vol.23, pp357-360, 1994.

[8]B.S.Ooi, A.C.Bryce, C.D.W.Wilkinson, and J.H.Marsh, "Study of reactive ion etching-induced damage in GaAs/AlGaAs structures using a quantum well intermixing probe," *Appl.Phys.Letts.*, vol.64, pp598-600, 1993.

[9]T.R.Hayers, P.A.Heimann, V.M.Donnelly, and K.E.Strege, "Maskless laser interferometric monitoring of InP/InGaAsP heterostructure reactive ion etching," *Appl.Phys.Letts.*, vol.57, pp2817, 1990.

[10]D.L.Jones, L.M.Zhang, J.E.Carroll, and D.D.Marcenac, "Dynamics of passively mode-locked semiconductor lasers," *IEEE.J.Quantum.Electron*, vol.31, pp1051-1058, 1995.

[11]Y.K.Chen, and M.C.Wu, "Monolithic colliding-pulse mode-locked quantum-well lasers," *IEEE.J. Quantum.Electron*, vol.28, pp2176-2185, 1992.

[12]S.D.Brorson, Z.Wang, T.Frank, S.Bischoff, A.Møller-Larsen, J.M.Nielsen, J.Mørk, and M.P.Sørensen "Characteristaion of wavelength chirping in modelocked monolithic CPM lasers," *IEEE.Photon.Tech.Lett*, vol.7, pp1148-1150, 1995.

Chapter 5- Characterisation of CPM Lasers by Autocorrelation Techniques.

There are two main methods of directly characterising the output of mode-locked lasers in the time domain: fast photodiodes, and streak cameras. For a full characterisation, such techniques must be able to obtain a value for the repetition rate and the temporal width of the mode-locked laser pulses. With monolithic mode-locked semiconductor lasers, repetition rates are generally 100 GHz and above, with pulse widths of the order of 1 ps.

With the present commercially available photodiode technology, such high speeds cannot as yet be reached[1]. Even if ultrafast detectors, currently being researched, are eventually commercially exploited the cost of obtaining the equipment, including ultrafast oscilloscopes, would be extremely prohibitive.

Streak cameras have a resolution limited to around 2 ps, which, again would lead to incomplete temporal characterisation of mode-locked laser pulses from monolithic diode lasers. The general low level of power in mode-locked semiconductor laser pulses leads to further complications when using streak cameras. Synchroscan operation (rather than single shot) is required, where the detected signal is integrated over a large number of periods to obtain a large enough signal to noise discrimination. To achieve this, the camera must be triggered by a sub-multiple of the mode-locked laser repetition rate. While useful in determining the general pulsation behaviour[2], the use of streak cameras is generally limited for use with high repetition rates and low pulsewidths.

The alternative is to use indirect interferometric autocorrelation techniques[3,4]. In interferometers light beams are split, and path differences are introduced between them so that on analysis of the recombined beams information about the original signal can be deduced. By using interferometers, time scales on the order of femtoseconds are converted into pathlength differences of micrometers, easily obtainable using piezoelectric motors. The interference signals produced can also be processed with low speed electronics.

This chapter describes the application of linear and non-linear correlation techniques to study the mode-locked pulses of the MOVPE grown GaAs/AlGaAs T-CPM lasers, as fabricated in Chapter 4, providing a complete time and frequency domain description of their operational characteristics. The linear correlation method is described first, which although not as useful as the non-linear measurements, avoids the requirement for the high average powers desirable for non-linear work. The non-linear correlation measurements were performed using second harmonic generation (SHG) on the output

of the CPM lasers. Simple numerical computer simulations are presented along with the experimental results for both methods in order to assist in their analysis.

5.1- Linear cross-correlator.

5.1.1-Introduction to the instrument.

The basic principle behind this measurement is the performance of a cross-correlation of the mode-locked laser pulses using a Michelson-type interferometer. The pulsewidth is inferred, as is the pulse separation from the interferograms produced[5]. Figure 5.1 shows the linear cross-correlator set up, with the light signal from the CPM laser being split and sent down to two mirrors, where they are reflected back to recombine at a photodiode. One of the mirrors is controlled by a piezo-electric motor, introducing a variable path difference between the two interfering beams. The interference pattern produced in a Michelson interferometer consists of a series of concentric rings. In order to detect changes in the interference pattern as the path difference changes in one of the arms, a narrow aperture is placed in front of a photodiode. The aperture is made narrow enough to allow the intensity change of a single interference fringe to be detected.

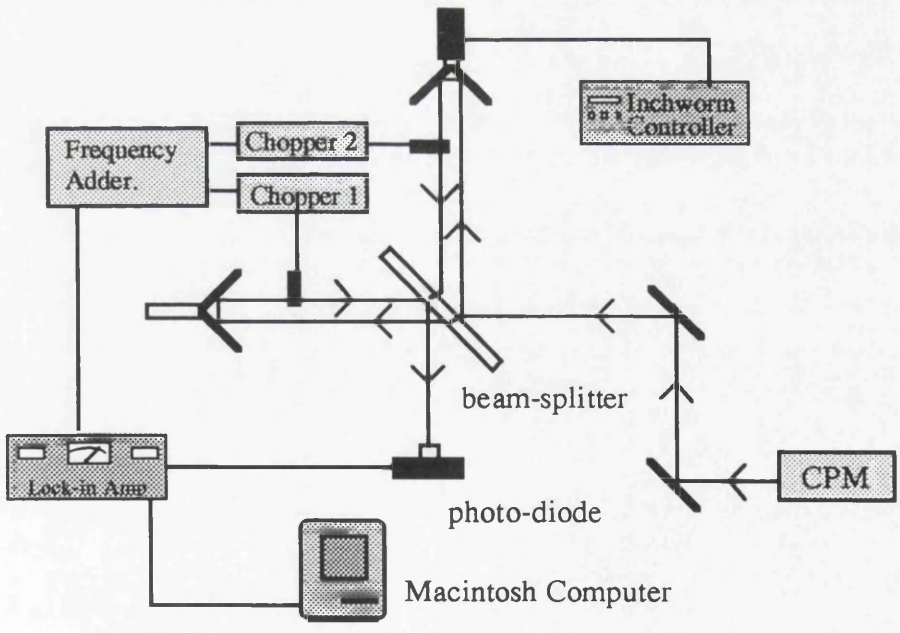

Figure 5.1: Linear cross-correlator instrument layout.

The signal produced by the photodiode in such an interferometer can be expressed mathematically as : $|E(t) + E(t+\tau)|^2$, where E(t) is the electric field at t, and τ is some time delay introduced between the two arms. So the output will contain a term

$E(t).E(t+\tau)$. The first order correlation function of two time varying signals $f_1(t)$ and $f_2(t)$ can be defined as: $G(\tau)=\int f_1(t).f_2(t+\tau)dt$. Hence the output signal of the interferometer is proportional to the first order, or linear, correlation function of the electric field. The discussion in following sections introduces these concepts more formally, and gives an analytical description of the interferometer output.

Using a T-CPM laser as the light source, the output around zero path difference will be the *autocorrelation* of the CPM pulses. At time delays separated by the cavity round trip time, the output represents the *cross-correlation* of consecutive pulses. In order to provide information on the mode-locked nature of the laser output, it is necessary to observe the cross-correlation terms, so the interferometer used in these experiments is known as a linear cross-correlator. By using two optical choppers, one placed in each of the interferometer arms and set at a different frequency from the other, and a lock-in amplifier tuned to their sum frequency, the background contribution from pulses arriving individually at the photo-diode is removed. In this way the lock-in amplifier not only improves signal recovery by reducing noise levels, but it also discards all the information apart from the component due to the interference of the pulses.

Corner cube reflectors are used as the mirrors in the two interferometer arms to remove any back reflections into the laser. Both the mirrors and ~50:50 beamsplitter are mounted on an optical rail system. Variable path difference is achieved via a Burleigh 7000 piezo-electric inchworm motor and controller system. The inchworm has a built in interferometric translation encoder with a maximum resolution of 0.5μm (3 fs delay) which can be read directly from the controller as a digital readout in μm. The maximum scanning range of the inchworm is 7.443 mm, which corresponds to a total time delay of around 50 ps, but for delays over this, the inchworm is mounted on a 3 cm micrometer translation stage. The Scitec optical choppers are set to 230 Hz and 540 Hz respectively, and their electrical reference signals are taken, mixed and filtered at the sum frequency 770 Hz, and used to synchronise the EG&G 5210 lock-in amplifier to the optical signal. The T-CPM laser sources in this experiment have a wavelength around 860 nm, so a low speed broad area silicon photodiode is used as the detector. A Macintosh computer using a specifically written N.I. LabView GPIB interface program reads and automatically plots the magnitude of the output of the lock-in.

5.1.2-Correlation function of the output of a multi-mode laser.

The analysis below follows the work on interferometer effects on diode laser noise by Pettermann *et al*[6]. The variation in time of the complex electric field of a multi-longitudinal mode laser can be represented by a sum of all the oscillating modes. Recalling equation (3.8) in section 3.2.1. the total field can be written as:

$$E(t) = \sum_{n=-(N-1)/2}^{(N-1)/2} E_n \exp\left[i\left((\omega_o + n\delta\omega)t + \phi_n(t)\right)\right] \tag{5.1}$$

where E_n is the time invariant mode amplitude, ω_o is the central frequency, $\delta\omega$ is the frequency spacing of the modes, $\phi_n(t)$ is the phase of mode n, and N is the total number of modes present in the gain bandwidth. Note that the time varying phase of mode n, $\phi_n(t)$, introduces phase noise that gives rise to a spread in the instantaneous frequency of the mode:

$$\omega_n(t) = \omega_n + \frac{d\phi(t)}{dt} \tag{5.2}$$

The normalised complex first order correlation function of an electric field E(t), is defined as[7]:

$$G(\tau) = \frac{\int_{-\infty}^{\infty} E(t)E^*(t+\tau)dt}{\int_{-\infty}^{\infty} E(t)E^*(t)dt} = \frac{\langle E(t)E^*(t+\tau)\rangle}{\langle E(t)E^*(t)\rangle} \tag{5.3}$$

where τ is some time variable. Correlation functions are in general a measure of the similarity of two signals when they are shifted by time delay τ with respect to one another. The correlation of a signal with itself is the autocorrelation, and with another separate signal is cross-correlation. A large value of $G(\tau)$ indicates a good match between two signals for some specific τ. Consider the correlation function for a single laser mode n (assuming mode amplitude does not depend on time):

$$G(\tau) = \frac{\int_{-\infty}^{\infty} E_n \exp[i(\omega_n t + \phi_n(t))]E_n^* \exp[-i(\omega_n(t+\tau) + \phi_n(t+\tau))]\,dt}{\int_{-\infty}^{\infty} E_n \exp[i(\omega_n t + \phi_n(t))]E_n^* \exp[-i(\omega_n t + \phi_n(t))]dt}$$

$$= \exp(i\omega_n\tau)\langle \exp[i\Delta\phi_n(t,\tau)]\rangle \tag{5.4}$$

where the phase change variable $\Delta\phi_n(t,\tau) = \phi_n(t) - \phi_n(t+\tau)$ has been introduced. Expanding equation (5.4) to the multi-mode case gives the correlation function:

$$G(\tau) = \sum_{n=-(N-1)/2}^{(N-1)/2} \exp\left[i(\omega_o + n\delta\omega)\tau\right]\langle \exp[i\Delta\phi_n(t,\tau)]\rangle \tag{5.5}$$

As the phase noise essentially arises from random carrier fluctuations it is reasonable to assume that each mode experiences approximately the same, i.e. $\Delta\phi_n(t,\tau) \sim \Delta\phi(t,\tau)$ for all n. If a Gaussian probability distribution for the phase noise of the form[8]:

$$f\left(\Delta\phi(t,\tau)\right)=\frac{1}{\sqrt{2\pi\left\langle\Delta\phi^2(t,\tau)\right\rangle}}\exp\left[\frac{-\Delta\phi^2(t,\tau)}{\left\langle 2\Delta\phi^2(t,\tau)\right\rangle}\right] \tag{5.6}$$

is assumed, then the time averaged phase noise term in equation (5.5) can be evaluated as:

$$\begin{aligned}\left\langle\exp\left[i\Delta\phi(t,\tau)\right]\right\rangle &= \int_{-\infty}^{\infty} f\left(\Delta\phi(t,\tau)\right)\exp\left[i\Delta\phi(t,\tau)\right]d\left(\Delta\phi(t,\tau)\right)\\ &= \exp\left[-1/2\left\langle\Delta\phi^2(t,\tau)\right\rangle\right]\end{aligned} \tag{5.7}$$

Substitution of the result from the expression (5.7) in (5.5) gives the final equation for the correlation function of a multi-longitudinal mode laser:

$$G(\tau)=\exp\left[-1/2\left\langle\Delta\phi^2(t,\tau)\right\rangle\right]\sum_{n=-(N-1)/2}^{(N-1)/2}\exp\left[i\left(\omega_o+n\delta\omega\right)\tau\right] \tag{5.8}$$

5.1.3-Output of the linear cross-correlator.

For the cross-correlator shown in figure 5.1, the total recombined electric field at the photo-diode can be written as:

$$E_T(t)=E(t)\cos(\omega_1 t)+E(t+\tau)\cos(\omega_2 t) \tag{5.9}$$

where ω_1 and ω_2 represent the modulation on the fields from the optical choppers in each arm of the interferometer, and τ is the introduced time delay between the arms. The photo-diode is an example of a 'square law' detector, so the generated photocurrent is given by:

$$\begin{aligned}i(t) &\propto \left(E_T(t)E_T^*(t)\right)\\ &\propto |E(t)|^2\cos^2(\omega_1 t)+|E(t+\tau)|^2\cos^2(\omega_2 t)\\ &+2\left(E(t)E^*(t+\tau)\right)\cos(\omega_1 t)\cos(\omega_2 t)\\ &\propto \left(E(t)E^*(t+\tau)\right)[\cos((\omega_1+\omega_2)t)+\cos((\omega_1-\omega_2)t)]+H.O.\end{aligned} \tag{5.10}$$

where H.O. represents second order terms in ω_1, or ω_2. The result in equation (5.10) relied on the fact that the electric fields are real, so the fields and their conjugate are equivalent, i.e. $E(t)=E^*(t)$. The lock-in amplifier is tuned to the frequency $\omega=\omega_1+\omega_2$ so the detected photocurrent is:

$$i_\omega(t)\propto\left(E(t)E^*(t+\tau)\right) \tag{5.11}$$

An interference experiment of this type can only provide a measurement of the statistical average of the photocurrent of equation (5.11), and this is given by:

$$\left\langle i_\omega(t)\right\rangle\propto\left\langle E(t)E^*(t+\tau)\right\rangle \tag{5.12}$$

hence the magnitude of the photocurrent reading is proportional to the magnitude of the linear correlation of the optical field from the laser given by equation (5.8):

$$\left|\left\langle i_{\omega}(t)\right\rangle\right| \propto \left|G(\tau)\right| \tag{5.13}$$

5.1.4-Linear correlation simulation.

A mode-locked laser gives out a pulse train with a repetition rate equal to the photon cavity round trip time (crt). However an incoherent multi-mode laser (non-mode-locked) will also have a general pulsation behaviour at this rate. This arises from the modes beating together as they chaotically drift in and out of phase with one another. The pulses produced from an incoherent multi-mode laser vary significantly in amplitude, phase, and width, and contain many sub peaks[9]. Thus, it should be expected that due to the averaging effects in a linear correlation of the output of such a device, a correlation signal should be observed, not only at zero delay, but also at delays equal to multiples of the round trip time in the laser. Due to the increase in the drift of the mode phases as time passes, it is also reasonable to expect that magnitude of the correlation peaks should decrease with increasing delay.

The above intuitive statements can be checked against the theoretical expression (5.8) for the linear correlation of a general multi-mode laser. For time delays not equal to the round trip time (crt=1/$\delta\nu$ from section 3.2.1), i.e. $\delta\omega\tau \neq 2\pi m$, the real part of the sum in expression (5.8) contains terms with different sign. So for a large number of modes $G(t)\approx 0$. But if $\delta\omega\tau = 2\pi m$, then all the modes have the same phase through the interferometer which corresponds to a peak in the correlation signal. This condition can be expressed formally as:

$$\left|G(\tau)\right| = \begin{cases} \exp\left[-1/2\left\langle \Delta\phi^2(t,\tau)\right\rangle\right] & \delta\omega\tau = 2\pi m \\ 0 & \delta\omega\tau \neq 2\pi m \end{cases} \tag{5.14}$$

The average phase change of each mode $\Delta\phi(t,\tau)$ is assumed to increase with delay, so the output for a linear correlator consists of a series of peaks, or *coherence spikes*, at delays corresponding to the inverse modal frequency separation, with amplitudes exponentially decreasing with increasing delay. Obviously the more modes present in the laser the narrower the coherence spikes will be. The average time over which a laser mode is self-coherent is the *coherence time* t_c. In general, t_c is defined as the time over which a correlated signal falls to 1/e of its value at zero delay[10]. Thus a linear correlator can be used to study the coherence properties of semiconductor lasers[11,12].

Obviously, the presence of coherence spikes alone in a linear correlation of the output of a laser is not enough to indicate the presence of mode-locking. For an incoherent multi-mode diode laser, the coherence time and cavity round trip time are very close, resulting in a rapid fall off in the magnitude of the coherence spikes in a

linear correlation of their output[11,12]. However, in an ideal mode-locked diode laser the coupling of the modes prevents the phases from drifting, resulting in an infinite coherence time. Even for the practical non-ideal mode-locking case where some broadening of the pulse is present through GVD and SPM, the extension of the coherence time to well beyond that of the cavity round trip leads to a high level of inter-pulse coherence. Thus observation of the cross-correlation of laser output pulses can distinguish between mode-locked and incoherent multi-mode operation in diode lasers.

The Wiener-Khintchine theorem states that the autocorrelation and the power spectral density of a function are related by the Fourier transform[8]. Since the power spectral density contains no phase information, a linear correlation cannot in principle provide measurements of actual pulsewidths. In this case the width of the measured coherence spikes represent the transform limited pulsewidth, the shortest possible pulsewidth attainable with the given spectrum.

To corroborate the assertions made above that the linear cross-correlator can be employed to determine the presence of mode-locked laser output, simple numerical computer simulations were performed. The programming was executed in THINK Pascal using numerical algorithms for FFT (fast Fourier transforms). Equation (5.1) was used to generate the time domain electric field for the output of a 400 μm GaAs/AlGaAs semiconductor laser operating at a central wavelength of 870 nm. The number of modes used during the simulations was N=13. Incoherent multi-mode operation was simulated with each mode having an initial random phase, and a random time varying instantaneous frequency, deviated from the nominal mode frequency by up to 5% of $\delta\omega$. The amplitudes of each mode were derived from a Gaussian distribution centred at 870nm with small random amplitude variations superimposed (figure 5.2(b)). The electric field in the mode-locked case was modelled with a Gaussian mode amplitude distribution (figure 5.2 (a)), phases identically zero, and instantaneous frequencies varying from the nominal values by an equal amount across the spectrum.

The correlations were performed using a Fourier transform technique. The correlation theorem states that the correlation of two functions in the time domain corresponds to a multiplication in the frequency domain of one of the functions with the complex conjugate of the other. The computation method was to generate the electric field of pulses with equation (5.1), convert them to frequency domain with the FFT, multiply them together, then perform the inverse Fourier transform to obtain the correlation. In an actual linear correlation, the experiment measures the average of very large number pulses. With the constraints of computation time, one hundred pulses, all with different phase characteristics with a Gaussian distribution, were auto-correlated, cross-correlated and then averaged, with the magnitudes extracted as the result.

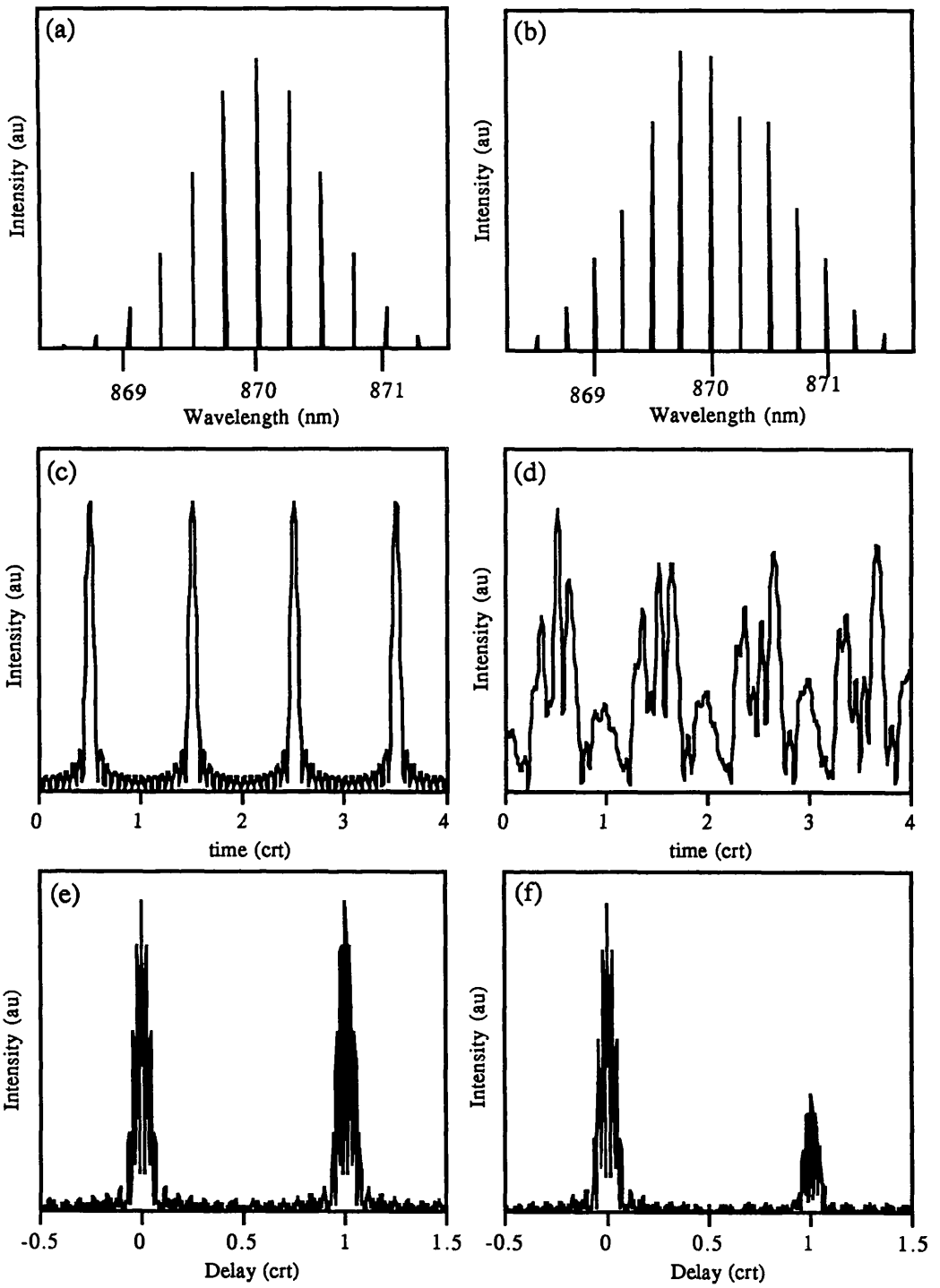

Figure 5.2: Results of the linear correlation simulation on the output of a 400μm GaAs/AlGaAs laser. In the mode-locked case the graphs show the simulated spectrum (a), the calculated intensity profile (c), and the calculated correlation (e). The spectrum (b), intensity profile (d), and correlation (f), correspond to the incoherent multi-mode case.

Figure 5.2(c) and (d) show the simulated evolution of the intensity profiles with time for the mode-locked and incoherent multi-mode cases respectively. Note that the time scales are plotted in term of the cavity round trip time, ~11 ps. Although the

pulsewidths are clearly very different in the two cases, their corresponding correlations in figures 5.2(e) and (f) both show equally wide coherence spikes. While the amplitude of the autocorrelation and first cross-correlation are exactly the same in the mode-locked trace, the loss of coherence in the laser output field of the non-mode-locked laser is evident by the large decrease in the magnitude of the cross-correlation.

The results of this simulation indicate that it is possible to use the output of a linear cross-correlator as an indication of the presence of mode-locking in a diode laser, although it is unable to provide accurate pulsewidth information.

5.1.5- Experimental results.

The output of a 400 μm T-CPM GaAs/AlGaAs laser from MOVPE grown QT664 material was tested using the linear cross-correlator instrument. The initial stage of the measurement is to ensure that the zero path difference position is accurately set up in the interferometer. A practical way of achieving this is to first perform a rough alignment of the interferometer by approximately measuring the lengths in each arm, and then attempt to observe interference fringes from the laser while it is biased below the threshold current. Below threshold, the output light is extremely incoherent, so interference fringes are only observed for a small range of values around the zero path difference position. If the device is lasing several coherence spikes should be observed, at each crt, which can confuse the situation. The inchworm encoder can be reset to zero at the position that gives a peak in the interference fringes from the below threshold device. To ensure that this position is truly the zero path difference, another device of differing cavity length can be tested, and fringes should be observed in the same place.

To perform the linear correlation on the 400μm T-CPM laser output when it is non-mode-locked, the device was fully forward biased i.e. both gain and absorber sections are connected to the current supply. For this experiment the side-injection waveguide amplifier contact is left unbiased. Figures 5.3 (a), and 5.3(b), show a typical power spectrum and linear correlation obtained from a fully forward biased 400 μm T-CPM laser. The longitudinal cavity mode wavelength separation taken from the spectrum is 0.24 nm, as expected for a 400 μm GaAs/AlGaAs laser. From equation (3.7) the corresponding cavity round trip time, assuming that GaAs has a refractive index of 4, is 10.7 ps. In the linear correlation coherence spikes appear at this period. From the correlation trace the coherence time is measured as 33 ps, equivalent to only three cavity round trip periods. This is typical behaviour for an incoherent multi-mode laser from both the theoretical simulation (section 5.13), and previous experimental results[11,12,25].

The absorber section of the same device was then reverse biased. The gain section current and the absorber bias were adjusted until the longitudinal mode-spacing in the

power spectrum doubled, shown in figure 5.3(c), indicating CPM operation. Correspondingly, the spacing between the peaks in the measured linear correlation halved, as shown in figure 5.3(d). Over the entire 40 ps scan, the CPM correlation peaks show an essentially constant level of intensity. The high level of inter-pulse coherence illustrated by the cross-correlations provides the time domain corroboration, which along with the power spectrum, demonstrates that the device is mode-locked. The correlation peaks are 5.77 ps apart, giving the CPM repetition rate of 173 GHz for this 400 μm device.

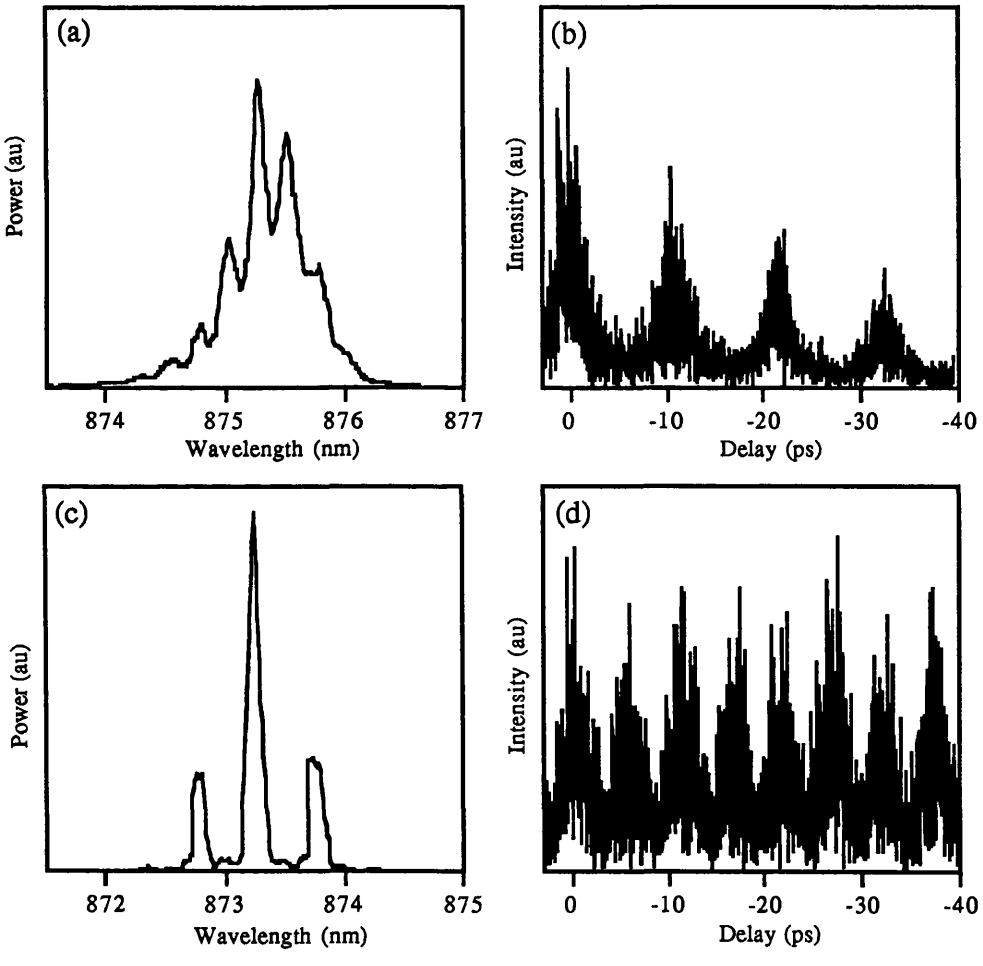

Figure 5.3: Power spectrum (a), and linear correlation (b) of 400μm GaAs/AlGaAs T-CPM laser with the 10μm absorber forward biased. The same device is operated in reverse bias, with the doubled spectrum (c), and linear correlation (d) indicating the CPM action.

Figure 5.4(a) shows the power spectrum of a 600 μm long T-CPM laser, operated in CPM mode. This spectrum shows the doubling of the standard wavelength separation of 0.16 nm to 0.32 nm. Again mode-locking is indicated in the linear correlation trace, figure 5.4 (b), by the high inter-pulse coherence. The separation of the correlation peaks is 8.25 ps indicating mode-locked pulses repeating at 121 GHz.

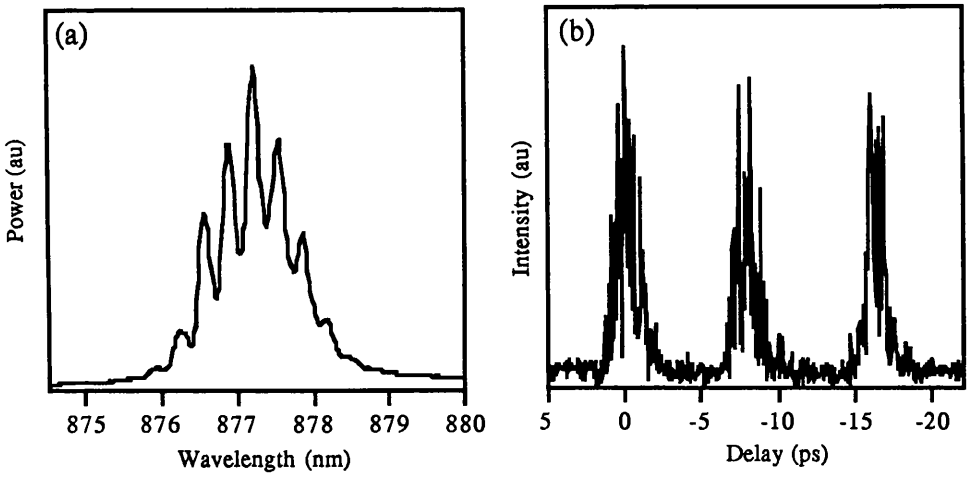

Figure 5.4: CPM spectrum (a) of a 600 μm long T-CPM GaAs/AlGaAs laser, with 10μm saturable absorber section, showing the doubled logitudinal mode separation of 0.32nm. The correlation in (b) shows the high inter-pulse coherence associated with mode-locking.

While these measurements provide evidence of CPM operation and pulse repetition rates of the 400 μm and 600 μm T-CPM lasers, interpretation of pulsewidth information from the correlations is less definite. As a general rule of thumb, assuming transform limited pulses, the full widths of correlation peaks at half the maximum value (FWHM) are on the order of double that of the pulses producing them. Accurate evaluation of this relationship requires the knowledge of the original pulse intensity profiles. Using this approximation to give an idea of the pulsewidths produced from the T-CPM lasers tested here, results in pulses with a FWHM of ~1.5 ps for the 400 μm laser in figure 5.3(d), and ~1.1 ps for the 600μm T-CPM laser in figure 5.4(b). This is consistent with the fact that the spectral width of this particular 600μm device (figure 5.4 (a)) was greater than that of for the 400 μm device (figure 5.3(c)).

5.2- SHG intensity autocorrelator.

5.2.1-Advantages of intensity over field correlations.

In the linear cross-correlation experiment described in Section 5.1, the output of the Michelson interferometer, as increasing time delay was introduced, was proportional to the correlation function of the electric field of the mode-locked laser pulses. In this experiment an ambiguity exists as to whether a tested laser is actually mode-locked since this manifests itself only as a change in the coherence time measured by the interferometer. In addition the only pulsewidth information that can be derived is that of the transform-limited value, which can easily be estimated from a measurement of

the power spectrum of the laser output as they are linked via the Fourier transform. In other words, even if mode-locking is assumed, a linear correlation of the pulse electric field will not differentiate between chirped and transform-limited pulses. However, if a correlation can be performed on the intensity of the laser output, the measurement will provide information on the actual intensity profile of the optical pulses. As the intensity profiles of the short mode-locked pulses are vastly different to those of the periodic noise intensity profile of the incoherent multi-mode laser (figures 5.2(c),(d)), an intensity autocorrelation can distinguish between both these operational regimes. Also, as chirped mode-locked pulses have temporally broadened intensity profiles, their true pulsewidths can be inferred. Equation (5.15) is a definition of the second order or intensity correlation function, where $I(t)=|E|^2$:

$$G^2(\tau) = \frac{\int_{-\infty}^{\infty} I(t)I(t+\tau)dt}{\int_{-\infty}^{\infty} I(t)I(t)dt} = \frac{\langle I(t)I(t+\tau)\rangle}{\langle I(t)I(t)\rangle} \qquad (5.15)$$

The standard method of producing an intensity autocorrelation is second harmonic generation (SHG) on the output of a Michelson interferometer. Under the correct circumstances SHG crystals can double the frequency of an incident optical beam, and as the process is non-linear the level of SHG is proportional to the square of the field, or the intensity, of the optical input[8]. Other methods can be used to perform non-linear correlations such as those based on two photon fluorescence, and optical Kerr shutters[4]. A potential difficulty in the implementation of non-linear correlations with diode lasers is the relatively low level of power available compared with most other mode-locked laser systems, such as dye lasers.

Although the intensity autocorrelation provides useful information about the pulsewidth it does not fully establish it. The width of an autocorrelation does not correspond to a unique pulsewidth, but instead requires knowledge of the original pulse shape for its evaluation. An intensity autocorrelation is an example of a second order correlation function, which by its nature is symmetrical, no matter the state of the original correlated function (a linear correlation is also symmetrical). With the measurement of higher order correlation functions it is possible to establish the presence of any asymmetry in a pulse. It also possible by the use of a combination of non-linear autocorrelations, cross-correlations of pulses with altered copies of themselves, and linear correlations, to extract information of pulse chirp, which when measured in conjunction with the power spectral density, can allow the complete temporal profile of an ultrashort pulse to be determined[13,14,15].

5.2.2- Non-linear mixing in SHG crystals.

The following is a brief account of second harmonic generation in non-linear crystals used for autocorrelation. For a more thorough introduction to SHG see for example the non-linear optics chapter in Yariv[8].

The polarisation induced in a crystal with a finite non-linear susceptibility from an incident optical field E, is given by $P=\varepsilon_o(\chi E+2dE^2+...)$, where χ is the linear susceptibility and d is the relevant second order non-linear coefficient for the given orientation of the incident beam with respect to the optical axis of the crystal. The output of a Michelson interferometer consists of the sum of the form $E_T=[E(t) + E(t+\tau)]$. If an optical pulse is represented as a carrier wave $\cos(\omega_1 t)$ with a time varying amplitude, then two optical pulses from the output of an interferometer will interact with the non-linear crystal through the E_T^2 term to induce a polarisation at the second harmonic: $\omega_2=2\omega_1$. For efficient conversion of this energy into a photon at ω_2, the total energy and momentum must be conserved:

$$\hbar\omega_2 = 2\hbar\omega_1 \quad \text{and} \quad \hbar k_2 = 2\hbar k_1 \tag{5.16}$$

Thus the phase velocity $v_p=c/n=\omega/k$ must be conserved in second harmonic generation. So this *phase matching* condition requires the refractive indices of the fundamental and second harmonic frequency to be equal:

$$n^{2\omega_1} = n^{\omega_1} \tag{5.17}$$

In naturally birefringent crystals, two indices of refraction exist for any given wavelength. The *ordinary* index of refraction n_o applies for a ray polarised perpendicular to plane formed by the crystal's optical axis and direction of propagation of the ray. The *extraordinary* index $n_e(\theta)$ corresponds to rays polarised orthogonally to the ordinary ray (with magnitude dependent on the angle of deviation from the optical axis θ) By careful choice of the angle of incidence and polarisation with respect to the optical axis of a birefringent crystal, the condition (5.17) can be met for the fundamental and second harmonic, where one is the ordinary ray and the other is the extraordinary.

A comprehensive analysis of SHG requires consideration of the tensor nature of the non-linear second order susceptibility. The coefficients contained in the tensor are relevant to the various components of the incident optical fields. The relative magnitudes of these components for specific crystals determine the input polarisation states for the most efficient non-linear mixing. In *type I* mixing, both input beams are polarised as ordinary waves with the output second harmonic as the extraordinary. Alternately *type II* mixing has one ordinary and one extraordinary beam for input, again with the output being an extraordinary wave. In type I mixing, SHG can be produced by either input alone, so there is a background SHG signal generated during an autocorrelation even if there is no interaction between pulses. But as type II mixing

requires the presence of both polarisations, autocorrelations based on it are referred to as *zero-background.*

With high power mode-locked lasers, significant amounts of SHG can be produced from standard non-linear material, such as KDP, making intensity autocorrelations easy to obtain. In mode-locked diode lasers, with peak powers of only a few tens of mW, it can be difficult to recover SHG from amongst the background noise. Lithium Iodate ($LiIO_3$) is a useful non-linear material for SHG with diode lasers, as it has a high non-linear coefficient (x10 of KDP) for type I phase matching across most of the semiconductor laser spectrum (0.35μm-5.5μm)[16].

5.2.3- Intensity Autocorrelator instrument.

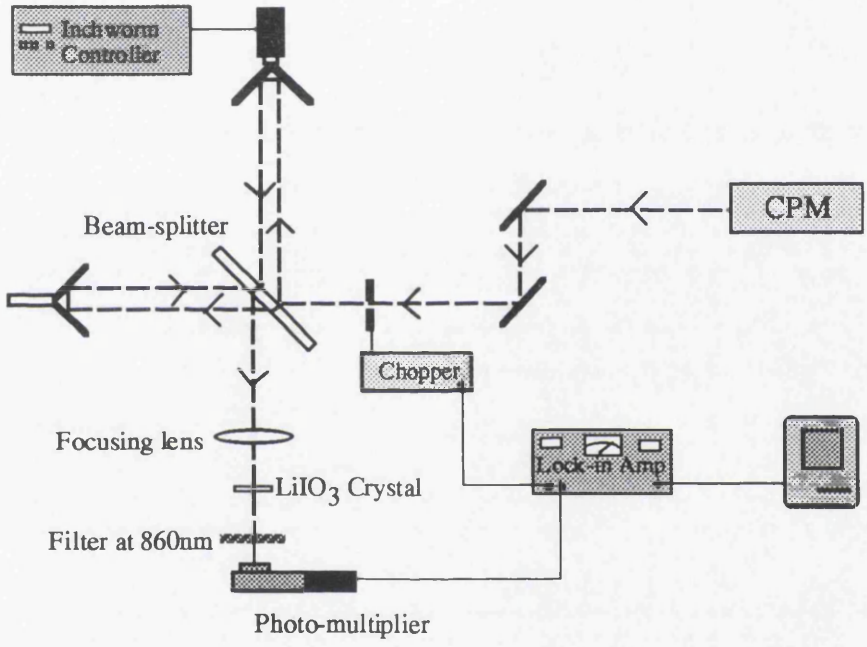

Figure 5.5: Intensity autocorrelator instrument layout.

The linear cross-correlator described in Section 5.1.1 was adapted to perform the intensity autocorrelations on the output of the T-CPM lasers. Figure 5.5 shows the experimental layout of the new instrument, which is similar to the one employed by Kurobori *et al*[17] for autocorrelations on mode-locked dye lasers. A 1.5 mm long $LiIO_3$ crystal was used for the SHG, and it was polished for type I phase matching at 860 nm with beams incident normal to the polished surface. The crystal itself was mounted on a rotatable stage for the fine incidence angle tuning required to obtain proper phase matching at the lasing wavelength of the T-CPM lasers. The beams from each of the interferometer arms were brought into the crystal in a collinear geometry (overlapping beams). It is also possible to do a non-collinear type I autocorrelation where the beams

are brought in spatially separated, focused into the crystal, and diverge after it. A non-collinear type I autocorrelation is also an example of a zero-background measurement. Although used by other diode CPM laser groups[26,28], there is little practical benefit introduced by having zero-background in the autocorrelation, and as more efficient use of the crystal can be obtained if the beams pass overlapped through the crystal, a collinear geometry was used here.

While a silicon photo-diode was sufficient for use as the detector in the linear correlation, the tiny level of SHG produced from a diode laser requires the use of a more sensitive photo-multiplier tube. The photo-multiplier used had a response centred on the second harmonic (~430 nm). To ensure only the second harmonic signal entered the detector, a Schott glass low pass filter was used to remove the light at the fundamental 860 nm wavelength. Again a lock-in amplifier was used to detect the output, but here the beam was only chopped once, at 500 Hz, at the output of the laser.

In the autocorrelator instrument shown in figure 5.5, the second harmonic signal, reaching the photo-multiplier is given by the square of the sum of the fields from the two interferometer arms, i.e. $|E(t) + E(t+\tau)|^2$. The output of the lock-in is then the statistical average of the 'square law' current (c.f Section 5.1.2):

$$\langle i(t)\rangle \propto \int \left[|E(t)+E(t+\tau)|^2 \right]^2 dt \tag{5.18}$$

Expanding the brackets in (5.18) results in the following integral:

$$\langle i(t)\rangle \propto \int \begin{Bmatrix} E^2(t)+E^2(t+\tau)+6E^2(t)E^2(t+\tau) \\ +4E^3(t)E(t+\tau)+4E(t)E^3(t+\tau) \end{Bmatrix} dt \tag{5.19}$$

If the laser pulse is described by a time varying complex amplitude A(t) (amplitude and phase) at a carrier frequency ω, i.e. $E(t)=A(t)\cos(\omega t)$, then averaging over τ yields the following result[18]:

$$\langle i(t)\rangle \propto 1 + 2\frac{\int I(t)I(t+\tau)dt}{\int |I(t)|^2 dt} + 2F(\tau) \tag{5.20}$$

where $I(t)=|A(t)|^2$, and $F(\tau)$ is given by:

$$F(\tau) = \frac{2[I(t)+I(t+\tau)]A(t)A(t+\tau)\cos(\omega\tau)+I(t)I(t+\tau)\cos(2\omega\tau)}{\int |I(t)|^2 dt}$$

The expression for $F(\tau)$ contains terms that rapidly vary with τ. Resolution of these fast variations requires a high degree of accuracy in each path length change, which must be at most around 1/10 of the smallest wavelength present. Autocorrelations where these requirements are adhered to are known as *fringe resolved*, and contain some phase information through the term A(t). In this experiment, these fast variations are unresolved and are generally averaged out to zero[19] giving the final result of the autocorrelator from (5.20) as:

$$\langle i(t)\rangle \propto 1 + 2G^2(\tau) \tag{5.21}$$

i.e. it is proportional to the intensity autocorrelation function (5.15) as required.

Analysis of expression (5.21) shows that the intensity correlation can distinguish clean, well defined mode-locked pulses and periodically modulated noise. In both cases at $\tau=0$, $G^2(\tau)=1$ by definition. For well defined mode-locked pulses, the modulation depth is 100%, so as τ increases $G^2(\tau) \rightarrow 0$. This gives an intensity autocorrelation peak to background ratio of 3:1 in the mode-locked case. For the modulated noise of an incoherent multi-mode laser, the average modulation depth is statistically half of the peak value, so in this case the contrast ratio is 3:2.

Curtis *et al*[20] give a general review of the implementation of intensity autocorrelation systems for diode laser pulse measurements.

5.2.4- Experimental results.

A Ti:Sapphire laser was used to investigate the level of optical power required to produce SHG from the $LiIO_3$ crystal. The laser was tuned to 860nm and operated at an average output power of 100 mW. At this power level, the SHG signal from the photo-multiplier tube, could easily be obtained. With neutral density filters bringing the power down to below 0.5 mW, the SHG was only resolvable amid the detector noise by employing a high degree of averaging from the measuring oscilloscope. As the GaAs/AlGaAs T-CPM lasers only have a sustainable CW average output power of a few mW, and at least half of that is lost through the beamsplitter in the interferometer, the intensity autocorrelations are performed close to the delectability limit.

An intensity autocorrelation was performed on a QT664 MOVPE grown 400 μm GaAs/AlGaAs T-CPM laser. A comparison between the measured autocorrelation on a mode-locked and fully forward biased device is presented in figure 5.6. When operated in CPM mode the average output power of the T-CPM device was 2 mW for this experiment. At this power, the detected SHG signal was only on the order of ten times the noise produced from the photo-multiplier dark current. As a result, these autocorrelations were performed in complete darkness, with a time constant of 100 ms on the lock-in amplifier. In the CPM spectrum, shown on a log scale in figure 5.6(a), there are nine modes doubled across the spectrum. Figure 5.6(b) displays the autocorrelation produced by the laser with this spectrum. Note that the peak to background ratio is very close to the ideal 3:1 value, implying mode-locked operation. For comparison, the corresponding spectrum and autocorrelation of the laser operated in full forward bias is presented in figures 5.6(c), and (d), respectively. The distinct reduction in the contrast ratio in this case indicates the non-mode-locked, periodic noise nature of the laser output.

Deviations from the expected contrast ratios of 3:1 for mode-locking , and 3:2 for non-mode-locking could be explained by an imperfect overlapping of the beams in the

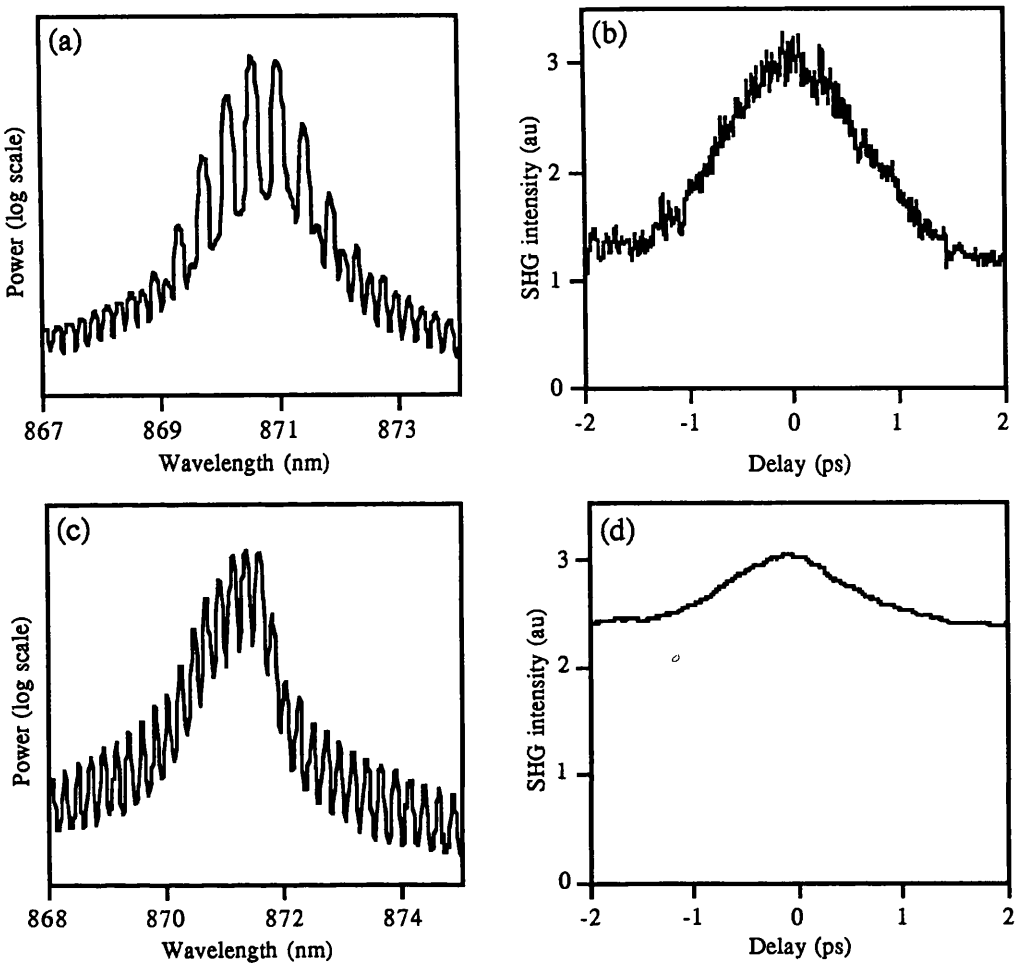

Figure 5.6: Comparison of intensity autocorrelations for CPM and forward bias operation of 400μm T-CPM laser. (a) shows the CPM spectrum, and the corresponding ~3:1 ratio in the autocorrelation (b) indicates mode-locking action. The spectrum (c) is for the fully forward biased laser, with a reduced contrast ratio in the autocorrelation (d).

interferometer. Another explanation, however, can be postulated by considering the fact that monolithic cavity mode-locked diode lasers can have a very low mark-space ratio. Consequently, the modulation depth is not always 100 %, even for fully transform-limited pulses. This is illustrated in figure 5.7 (a), with the theoretical mode-locked pulse intensity envelope, calculated for a 400 μm AlGaAs CPM laser with a power spectrum identical to that experimentally measured in figure 5.6 (a). By amending the numerical simulation developed for linear correlations in section 5.1.3, to model the correlation function of a multi-mode laser intensity output, the autocorrelations of a 400 μm laser in CPM, and incoherent multi-mode operation were simulated. The simulated laser spectra were similar to those experimentally measured (figures 5.6 (b) and (c)). The results of the simulation, in figure 5.7 (b), show almost

identical autocorrelation widths and contrast ratios when compared to traces in figure5.6.

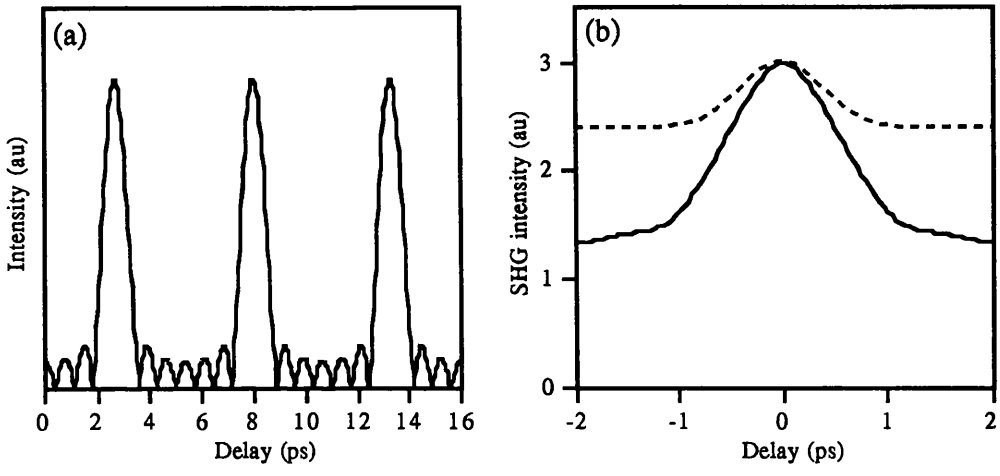

Figure 5.7: (a) Simulated pulse intensity profile for 400μm GaAs/AlGaAs CPM laser, showing non-100% modulation depth. (b) Simulated autocorrelation of 400μm AlGaAs/GaAs CPM laser in mode-locked (solid- line), and incoherent multi-mode (dashed line) conditions.

To further demonstrate the effects of the non-100% modulation depth on the autocorrelation contrast ratio, the intensity output and autocorrelation of various cavity length GaAs/AlGaAs CPM lasers have been simulated, and displayed in figure 5.8. In this simulation, the experimental spectral width of figure 5.6 (a) was used to generate the pulses. By studying figure 5.8, the contrast ratio of the autocorrelation can be seen to get closer to the ideal with the increasing cavity length, and hence modulation depth of the CPM pulses, but even at cavity lengths of 10 mm, the background level is still slightly above 1.

On a longer scan of the fully forward biased 400 μm laser, shown in figure 5.9, correlation spikes at the normal crt are observed, along with a corresponding slowly decreasing amplitude. Correlation spikes such as these are routinely detected in autocorrelations of non-mode-locked semiconductor lasers. In intensity autocorrelations of self-pulsing lasers[21] and gain switched lasers[22], the main pulse autocorrelation contains superimposed coherence spikes repeated at the cavity round trip time. Also, the intensity autocorrelation on the output of a commercial Sharp diode laser by Lopes *et al*[23], over a delay range of over 400 ps, produced similar correlation peaks, with amplitudes reflecting the effects of the relaxation oscillation.

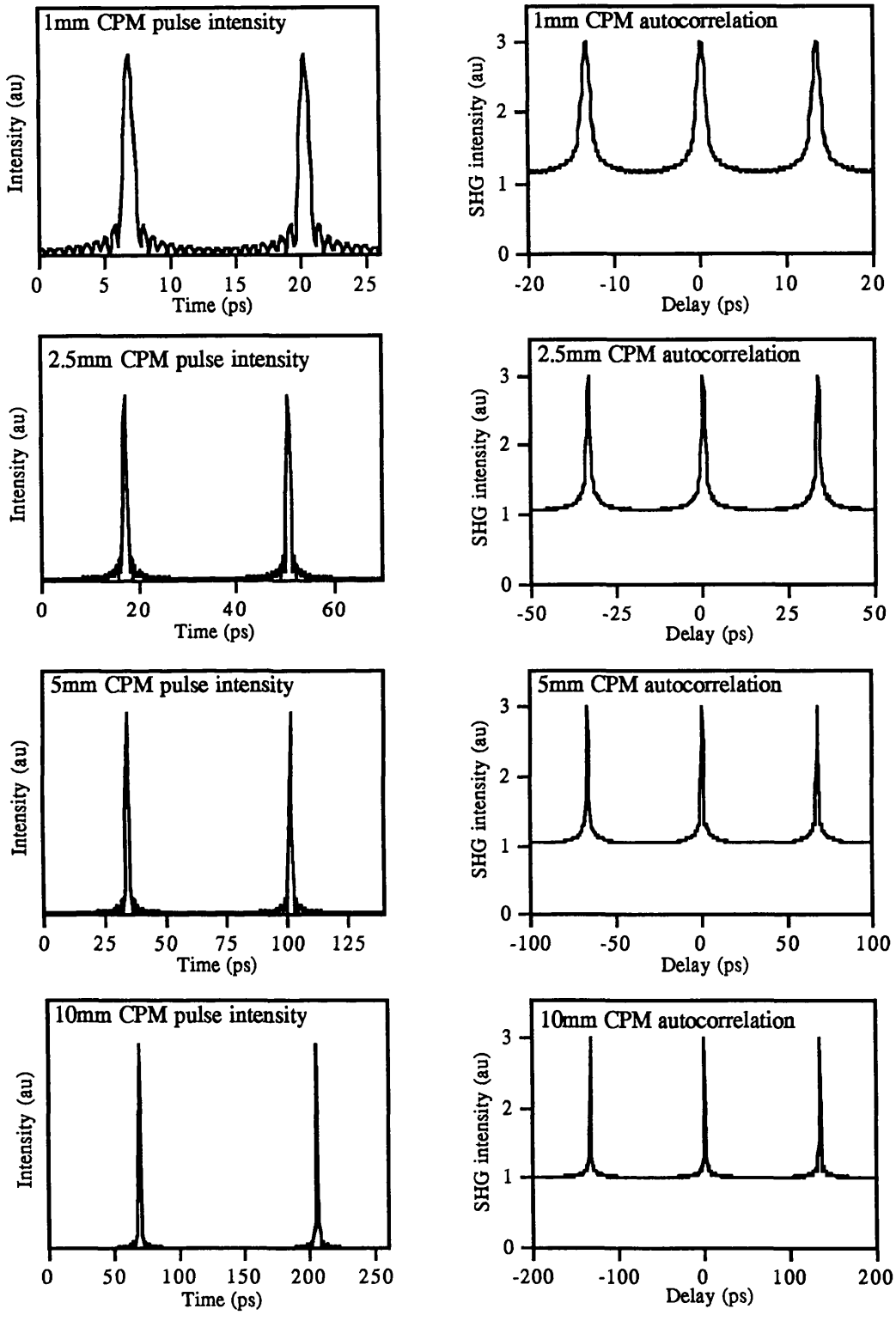

Figure 5.8: Simulation showing evolution of the pulse modulation depth, and convergence of the autocorrelation contrast ratio to 3:1, with increasing GaAs/AlGaAs CPM laser length.

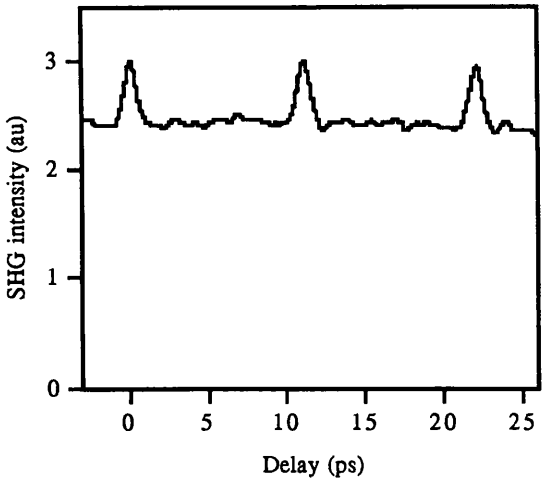

Figure 5.9: Intensity correlation of fully forward biased 400μm T-CPM laser showing peaks repeating at the standard cavity round trip time.

In Figure 5.10, the spectrum, and longer autocorrelation scan of the 400 μm T-CPM laser operated in CPM mode are plotted. The correlation peaks are now repeated at a period of 5.7 ps, which is half the normal cavity round trip time shown in figure 5.9. This corresponds to a CPM pulse frequency of 175 GHz. The autocorrelation must be deconvolved to provide the actual pulsewidth, as autocorrelation peaks are non-unique and depend on the type of pulse shape for their evaluation, i.e. Lorentzian, Gaussian, hyperbolic sech, etc, all have different pulsewidth to autocorrelation width ratios[19]. An inspection of figure 5.10(a) reveals that the CPM spectrum fits extremely well to a Gaussian type envelope function. The transform-limited pulse intensity profile corresponding to a Gaussian spectrum also has a Gaussian form. The simulated autocorrelation using the bestfit Gaussian spectral width is overlaid on the experimental autocorrelation in figure 5.10(b), and they can clearly be seen to closely match. Simulations with both Lorentzian and hyperbolic sech pulse shapes did not show such a good fit with the experimental data. Consequently the mode-locked pulses output from these GaAs/AlGaAs T-CPM lasers are assumed to have Gaussian-like pulse intensity envelopes. In this case the FWHM of the pulse, Δt, can be evaluated from the autocorrelation FWHM, $\Delta\tau$, by using the expression : $\Delta t = 0.7071\ \Delta\tau$[19]. Using the value for $\Delta\tau$ from figure 5.10(b), the pulsewidth of these pulses is calculated at 1.05 ps. The minimum time-bandwidth product for a Gaussian pulse in the Fourier transform-limit is $\Delta t.\Delta\nu=0.441$[19]. From figure 5.10, the time-bandwidth product is 0.436 indicating that the pulses are essentially chirp free (transform limited).

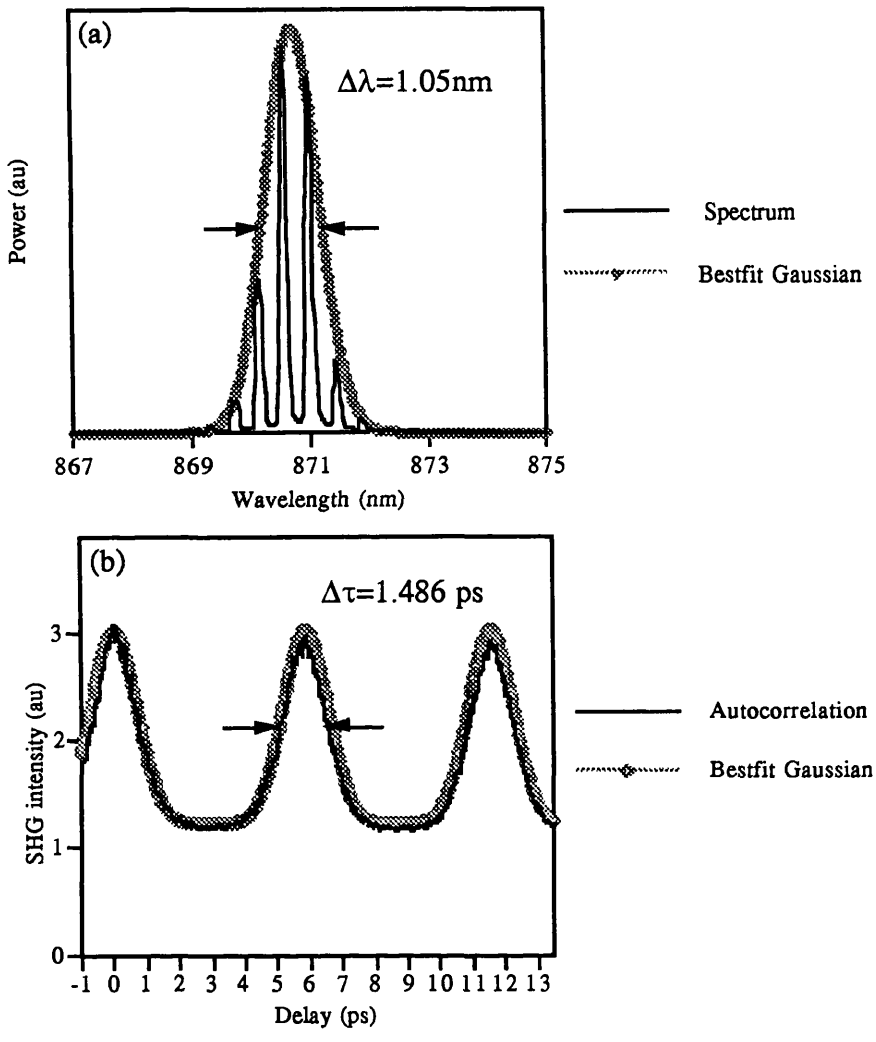

Figure 5.10: CPM spectrum (a) and intensity autocorrelation (b), of 400μm T-CPM laser, overlaid with best-fit Gaussian spectral envelope, and calculated autocorrelation.

5.3- Conclusions.

The temporal characteristics of T-CPM lasers, fabricated from MOVPE grown GaAs/AlGaAs MQW wafer QT 664, have been studied using both a linear, and non-linear correlation technique. Along with the power spectra, these measurements have confirmed the CPM operation of the devices, in particular demonstratied that a 400 μm T-CPM laser produced near transform-limited 1 ps mode-locked pulses at a repetition rate of 175 GHz.

The linear cross-correlation technique was very easy to implement with the modest powers available from mode-locked diode lasers. By modelling the output of a multi-mode diode laser as a summation of the cavity modes present in a given gain bandwidth, and imposing certain phase characteristics to represent mode-locking and incoherent multi-mode behaviour, a simulation of the linear correlation of the output

was performed using simple numerical algorithms for Fourier transforms. From this simulation two broad correlation regimes can be delineated: short coherence time for multi-mode incoherent output, and extended coherence time for mode-locked output. This was validated experimentally by observation of the high inter-pulse coherence from a 400 μm T-CPM laser operating with a CPM type doubled spectrum, and the rapid decrease in amplitude of the correlation signal in a few round trip periods for the non-mode-locked laser when it was operated fully forward biased. Martins Filho *et al*[24,25] have also produced similar results for the output of GaAs/AlGaAs MCPM lasers. The application of this technique has a limited usefulness as it is unable to return accurate pulsewidth information. Also, the lack of a difference in contrast ratio of the interference fringes produced from a mode-locked and incoherent multi-mode laser leads to potential ambiguities in their interpretation, which do not permit the conclusion of mode-locking to be drawn beyond dispute.

Whilst the SHG autocorrelations were complicated, and arduous to implement experimentally with diode lasers, the added pulsewidth information and distinguishing contrast ratios are required for the confirmation of mode-locked operation. The amended numerical model provided interesting data for the consideration of the contrast ratios that can be expected from intensity autocorrelations of short diode lasers with low mark-space ratios. Experimentally, the intensity autocorrelations of the output of the non-mode-locked and CPM output, fitted precisely to that expected from theoretical considerations, proving both the accurate use of the instrument and the mode-locked nature of the T-CPM laser output.

Other published work on intensity autocorrelations of the output of monolithic CPM lasers, has exclusively been confined to InGaAsP/InP based devices operating at wavelengths around 1.55 μm. The transform-limited pulses produced from the 400 μm GaAs/AlGaAs T-CPM in this work is consistent to the results presented by Chen *et al*[26] and Brorson *et al*[27] which show that short cavity InGaAsP/InP CPM lasers produce essentially transform limited pulses. Using a method for retrieving actual pulse shapes from correlation measurements Salvatore *et al*[28] show that standard geometry short cavity mode-locked diode lasers produce pulses with some significant chirp present. For CPM lasers such chirp only becomes apparent in longer laser cavities[27].

Chapter 5: References

[1]J.E.Bowers, and Y.G.Wey, Chapter 17, *Handbook of Optics*, M.Bass, E.Van Stryland, D.Williams, and W.Wolfe, (Eds.), Optical Society of America, 1994.

[2]F.Camacho, D.A.Barrow, E.A.Avrutin, A.C.Bryce, and J.H.Marsh, "Two-contact semiconductor mode-locked lasers," *Int.J.Optoelectron.*, vol.10, pp433-437, 1995.

[3]S.LShapiro (Ed.), *Ultrashort light Pulses-Picosecond Techniques and Applications*, Topics in Applied Physics, vol 18, Springer-Verlag 1977.

[4]D.J.Bradley, and G.H.C.New, "Ultrashort pulse measurements," *Proc.IEEE.*, vol.62, pp313-670, 1974.

[5]K.N Choi & H.F. Taylor, "Novel cross-correlation technique for characterization of subpicosecond pulses from mode-locked semiconductor lasers," *Appl.Phys.Lett*, vol.62, pp.1875-1877, 1993

[6]K.Petermann, and E.Weidel, "Semiconductor laser noise in an interferometer system," *IEEE.J.Quantum.Electron.*, vol.17, pp1251-1256, 1981.

[7]F.G.Stremler, *Introduction to Communication Systems*, Addison Wesley, 1990.

[8]A.Yariv, *Quantum Electronics*, Wiley, 1989.

[9]A.E.Stegman, *Lasers*, Oxford University Press, 1986.

[10]L.Mandel, and E.Wolf, "The measures of bandwidth and coherence time in optics," *Proc.Mod.Phys.*, vol.80, pp894-897, 1962.

[11]A.R.Reisinger, C.D.David,JR., K.I.Lawley, and A.Yariv, "Coherence of room-temperature CW GaAs/AlGaAs injection laser," *IEEE.J.Quantum.Electron.*, vol.15, pp1382-1387, 1979

[12]Y.Ning, K.T.V.Grattan, B.T.Meggitt, and A.W.Palmer, "Characteristics of laser diodes for interferometric use," *Appl.Optics.*, vol.28, pp3657-3661, 1989.

[13]K.Nagauma, K.Mogi, and,H.Yamada, "General Method for ultrashort light pulse chirp measurement," *IEEE.J.Quantum.Electron.*, vol.25, pp1225-1233, 1989.

[14]J.C.Diels, J.J.Fontaine, and W.Rudolph, "Ultrafast diagnostics," *Revue Phy.Appl.*, vol.22, pp1605-1611, 1987.

[15]J.L.A.Chilla, and O.E.Martinez, "Analysis of a method of phase measurement of ultrashort pulses in the frequency domain," *IEEE.J.Quantum.Electron.*, vol.27, pp1228-1235, 1991.

[16]G.Nath, and S.Haussuhl, "Large non-linear optical coefficient and phase matched second harmonic generation in $LiIO_3$," *Appl.Phys.Lett.*, vol.14, pp154-155, 1969.

[17]T.Kurobori, Y.Cho, and Y.Matsuo, "An intensity/phase autocorrelator for the use of ultrashort optical pulse measurements," *Optics.Commun.*, vol.40, pp156-160, 1981.

[18]T.Mindl, P.Hefferle, S.Schneider, and F.Dorr, "Characterisation of a train of subpicosecond laser pulses by fringe resolved autocorrelation measurements," *Appl.Phys.B*, vol.31, pp201-207, 1983.

[19]K.L.Sala, G.A.Kenney-Wallace, and G.E.Hall, "CW autocorrelation measurements of picosecond laser pulses," *IEEE.J.Quantum.Electron.*, vol.16, pp990-996, 1980.

[20]J.P.Curtis, and J.E.Carroll, "Autocorrelation systems for the measurement of picosecond pulses from injection lasers," *Int.J.Electron.*, vol.60, pp87-111, 1986.

[21]D.Gloge, and T.P.Lee, "Signal structure of continuously self pulsing GaAs lasers, " *IEEE.J.Quantum. Electron.*, vol.7, pp43-45, 1971.

[22]H.Ito, H.Yokoyama, S.Maruta, and H.Inaba, "Generation of picosecond optical pulses with highly RF modulated AlGaAs DH laser," *IEEE.J.Quantum..Electron.*, vol.17, pp663-670, 1981.

[23]W.A.Lopes, M.O.Morales, M.A.Rieffel, J.AGiacoletti, J.T.Thorpe, and L.A.Westling, "Intensity autocorrelation measurements of an AlGaAs diode laser," *Optics.lett.*, vol.18, pp820-822, 1993.

[24]J.F.Martins Filho, E.A.Avrutin, C.N.Ironside, and J.S.Roberts, "Monolithic multiple colliding pulse mode-locked quantum-well lasers: Experiment and Theory," *IEEE.J.Sel.Topic.Quantum.Electron.*, vol.1, pp539-551, 1995.

[25]J.F.Martins Filho, *Monolithic Colliding Pulse Mode-locked Quantum-well Lasers*, Ph.D. Thesis, University of Glasgow, 1995.

[26]Y.K.Chen, and M.C.Wu, "Monolithic colliding-pulse mode-locked quantum-well lasers," *IEEE.J.Quantum.Electron*, vol.28, pp2176-2185, 1992.

[27]S.D.Brorson, Z.Wang, T.Frank, S.Bischoff, A.Møller-Larsen, J.M.Nielsen, J.Mørk, and M.P.Sørensen, "Characteristaion of wavelength chirping in modelocked monolithic CPM lasers," *IEEE.Photon.Tech.Lett*, vol.7, pp1148-1150, 1995

[28]R.A.Salvatore, and A.Yariv, "Demonstration of down-chirped and chirp-free pulses from high repetition-rate passively mode-loced lasers," *IEEE.Photon. Tech.Lett*, vol.7, pp1151-1153, 1995.

Chapter 6- Absorption spectra measurements.

Measurements of gain and absorption spectra of semiconductor laser material can give valuable insights into the operation and performance optimisation of QW lasers[1]. This is especially important for the monolithic CPM lasers fabricated in this project. The ultrafast mode-locking of these lasers, as demonstrated in Chapter 5, requires the presence of a fast component to the saturation recovery time of the absorber section, enabling sufficient recovery within the pulse repetition period (every 6 ps). The existence of excitonic absorption features in MQW structures, and the ultrafast dynamics associated with them, may contribute significantly to pulse shaping at these high frequencies[2]. Observation of how the absorption spectrum of a saturable absorber varies under reverse bias can provide essential information required for a more complete understanding of the dynamics involved in ultrafast mode-locking.

This chapter describes the employment of a new, simple technique for directly obtaining the absorption and gain spectra of semiconductor laser material under forward and reverse bias conditions. The technique utilises the multi-section semiconductor laser technology developed for the fabrication of the CPM lasers (Chapter 4). The use of this new method allows the direct measurement of the absorption spectrum of the saturable absorber used in the actual CPM laser structures. After a discussion of the measurement technique itself, the experimentally obtained absorption spectra are presented and analysed.

6.1- Two-contact laser absorption spectra measurements.

6.1.1- Absorption spectra measurement techniques.

The standard methods used to obtain measurements of the absorption spectra of semiconductor structures use a wavelength tuneable external light source as a probe. In transmission experiments, probe light is incident normal to the semiconductor surface, the intensity of light coupled in is estimated, and the amount of light transmitted through the structure is recorded over a range of wavelengths, and used to calculate the absorption spectrum[3,4]. The simple analytical model used to interpret the transmission results into spectra does not consider the interference effects due to the Fabry-Perot oscillations in the structure. To eliminate these one of the surfaces must be anti-reflection coated or roughened to reduce the reflections. The accuracy of this method obviously depends on how accurately the optical power incident on the sample is estimated. If the semiconductor sample has a p-i-n type diode structure, such as

semiconductor laser material, then it is possible to extract the absorption coefficient by measurement of the photocurrent generated in the device by the injected probe light[5]. If the internal quantum efficiency is known accurately enough then the current can be related directly to the absorption coefficient. Carrier leakage or a built-in electric field will reduce the accuracy of the technique as the detected photocurrents will be lower than those generated.

Although conceptually simple the above methods involve the use of complicated external equipment. Hakki and Paoli[6] showed that the absorption spectra could be obtained directly from analysis of the semiconductor laser emission spectra at pumping levels close to, but below, the threshold current. Here, the gain spectrum is determined by recording the depth of the modulation in the Fabry-Perot fringes close to the peak in the gain bandwidth, as the lasing threshold approaches. The modal gain for mode q in the spectrum is calculated directly from the formula:

$$\Gamma\gamma_q - \alpha_{int} = \frac{1}{L}\left[\ln\left(\frac{1}{R}\right) + \ln\left(\frac{\sqrt{r(\lambda)}-1}{\sqrt{r(\lambda)}+1}\right)\right] \qquad (6.1)$$

where $r(\lambda)$ is the maximum to minimum intensity ratio between peak q and its neighbouring valleys, with the other symbols defined as in section 2.2.3. A number of researchers have successfully employed this technique[7,8], but it has the disadvantage of its applicability being restricted to the centre of the gain bandwidth. Henry *et al*[9] reported a method for deriving absorption spectra over a wider spectral range by measurement of the spontaneous emission spectrum of laser diodes and linking it to the absorption spectrum through consideration of the fundamental relationships between the various emission and absorption processes. Using these relations, an expression is derived for the gain coefficient $g(h\nu,\Delta E_F)$, which is proportional to the spontaneous emission spectrum $L(h\nu,\Delta E_F)$, where ΔE_F is the quasi-Fermi level separation:

$$g(h\nu,\Delta E_F) = K\frac{L(h\nu,\Delta E_F)}{(h\nu)^2}\left[1-\exp\left(\frac{h\nu-\Delta E_F}{kT}\right)\right] \qquad (6.2)$$

Here K is a proportionality constant. K and ΔE_F can be found by measuring the differential quantum efficiency, the lasing wavelength, and the spontaneous emission spectrum at different injection currents. This gives rise to gain spectra with a range equal to that of the spontaneous emission itself. This technique has been applied in both long and short wavelength semiconductor laser structures[10,11,12]. A discrepancy between theoretically derived absorption spectra broadened by intraband scattering, and the calculated absorption spectra using this method, has been resolved by formulating the gain function with separate consideration of the linewidth broadening of hole and electron states[13].

The above methods of deriving the gain and absorption spectra from semiconductor laser structures are relatively involved experiments and include detailed information

about device structures and material parameters, and rely heavily on theoretical assumptions. The new method detailed here is much simpler in practice and analysis, and is in essence a transmission measurement without the experimental complexity, as the light source is integrated with the probed sample. It is also versatile in that it can be used to measure absorption spectra under both reverse and forward bias conditions.

6.1.2- Description of the two-contact laser method.

The initial, and most complex stage in the technique is the fabrication of the two-section RWG laser device from the desired material. Chapter 4 has a detailed account of the fabrication procedure for GaAs/AlGaAs devices, and similarly Chapter 8 describes their fabrication for InGaAsP/InP based semiconductor material. Figure 6.1 shows the layout of such a device. In this experiment the longer section **a** is forward biased in order to provide the probe light source. The integrated shorter section **b** can then be either forward, or reverse biased with a range of values, and its effect on the light from section **a** can be recorded and analysed to provide a measurement of the absorption spectrum for the material. To facilitate the absorption measurements, feedback from the output facet (section **b**) must be eliminated, either by coating or roughening.

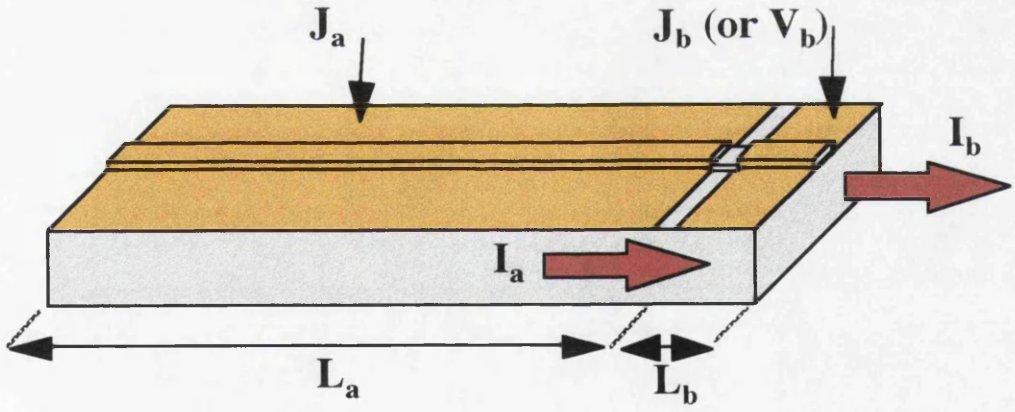

Figure 6.1: Layout of two-section laser used in spectral measurements .

The details of the procedure for measuring the gain are as follows, with the various parameters defined in figure 6.1. Here, $J_{a,b}$ are the current densities applied to the sections **a** and **b** which have lengths L_a and L_b respectively. I_a is the optical intensity at the end of section **a**, and I_b is the optical intensity at the end of section **b**, which also forms the output of the device.

The first action is to obtain a measurement of the reference spectrum, i.e. the output from section **a**, I_a, which is the average emission from all points in section **a**. After this

is achieved, the absorption spectra under any bias condition can be easily calculated by comparison with the corresponding emission spectra, I_b, using a simple analytical formula. To achieve this, the current densities are set at $J_a=J_b=J_1$ and the output spectrum $I_b(J_1)$ is measured over a range of wavelengths. This spectrum contains amplified emission from section **a**, and some spontaneous emission from section b, $I_{b,sp}(J_1)$. The complete expression for the output intensity spectrum is given by

$$I_b(J_1) = I_a \exp[-\alpha(J_1)L_b] + I_{b,sp}(J_1) \tag{6.3}$$

where $\alpha(J_1)$ is the absorption coefficient at current density J_1. By setting $J_a=0$, but keeping J_b at J_1, $I_{b,sp}(J_1)$ alone is measured. Subtracting these two spectra gives the reference intensity spectrum I_{ref}:

$$I_{ref} = I_b(J_1) - I_{b,sp}(J_1) \tag{6.4}$$

It is clear from expressions (6.3) and (6.4) that I_{ref} still differs from I_a by the factor $\exp[-\alpha(J_1)L_b]$. The current density J_1 is chosen to bias section **b** approximately at the transparency condition, so it is assumed that any absorption or gain present is small, i.e. $\alpha \approx 0 \Rightarrow I_{ref} \approx I_a$. If this approximation does not hold (and it may not for all wavelengths) then any absorption spectra measurements using I_{ref} are only relative to level of absorption present at I_{ref}. Therefore any absorption spectra calculated using this method will only provide relative, not absolute values of the absorption coefficient, even though the difference is likely to be small.

To measure the absorption coefficient at some current density J, relative to the reference level I_{ref}, J_a is set back to J_1 and section **b** is pumped with $J_b=J$. The resultant output spectrum is then measured.

$$I_b(J) = I_{ref} \exp[-\alpha(J)L_b] + I_{b,sp}(J) \tag{6.5}$$

where $I_{b,sp}(J)$ is found by setting $J_a=0$, $J_b=J$, and measuring the output spectrum. By solving for α in equation (6.5) the expression for the absorption coefficient is given by:

$$\alpha(J) = -\frac{1}{L_b} \ln\left[\frac{I_b(J) - I_{b,sp}(J)}{I_{ref}}\right] \tag{6.6}$$

So by using formula (6.6) the absorption coefficient for each wavelength relative to the reference level gain can be calculated.

Using this technique the absorption spectra of the semiconductor laser material can also be measured when a reverse bias voltage level is varied. When a reverse polarity electric field, E, is applied to section **b**, there is no spontaneous emission component to the output spectrum from section **b**, so in this case the absorption spectrum can be calculated from the formula:

$$\alpha(E) = -\frac{1}{L_b} \ln\left[\frac{I_b(E)}{I_{ref}}\right] \tag{6.7}$$

As it is only the bias conditions of the two-sections that are altered during the course of the experiment, it can be assumed that any optical coupling to the spectrum

analyser remains constant throughout the measurement, ensuring that all spectra recorded in a single experiment are directly comparable.

6.2- Experimental Results.

6.2.1- Saturable absorber reverse bias absorption spectra.

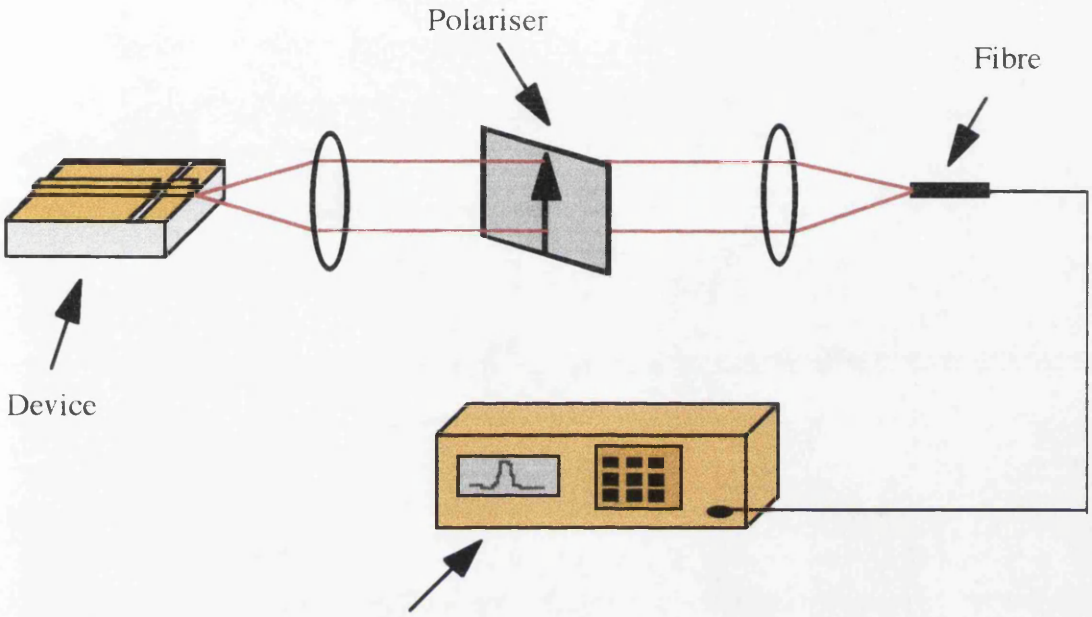

Figure 6.2: Experimental set up for absorption measurements.

In order to obtain absorption spectra measurements of the saturable absorbers of the MOVPE grown (QT 664) GaAs/AlGaAs T-CPM lasers tested in chapter 5, the devices were cleaved along the edge of the saturable absorbers. Thus the geometry is similar to that shown schematically in figure 6.1. T-CPM lasers, 800 μm long, with 10 μm saturable absorbers (section **b**) were used, so that after cleaving the entire device was 400 μm long, with the gain section (section **a**) 380μm, and a gap of 10 μm between the sections. To eliminate the optical feedback from the absorber facet the laser was simply scribed right through the waveguide and not nicked and cleaved as would normally be the case for a laser. The devices were mounted on a heat sink and bonded in the normal manner.

The experimental set up is shown in figure 6.2. The optical output of the device is collimated by a x20 microscope objective lens, sent through a polariser, which allows the TE and TM spectra to be measured separately, and then focused in to a fibre-optic which is coupled directly into a spectrum analyser. All spectral measurements were carried out using an Advantest Spectrum Analyser and the data was collected and then

processed by a Macintosh computer running a LabView interface program. The absorption spectra were calculated from the recorded emission spectra using a Think Pascal program.

From section 4.3.1, the threshold current of a 400 μm T-CPM laser was measured as 70 mA. The current corresponding to the same current density for the absorber section is 1.6 mA. This current density was used as the J_1 for the reference spectra measurements. Figure 6.3(a) shows a comparison of the TE emission spectra from the device with the gain section biased at J_1, and the absorber biased at J=0 and J=J_1. Figure 6.3(b) shows the same situation for the TM polarised output. The high degree of asymmetry of the absorbed emission spectra from the gain section indicates the presence of a sharp absorption peak at the band edge. When J_1 is injected into the absorber section, the symmetry recovers, implying that the device is biased close to transparency. The graphs in figures 6.3(a), and 6.3(b) are plotted on the same intensity scale, normalised to the peak of the TE emission spectra.

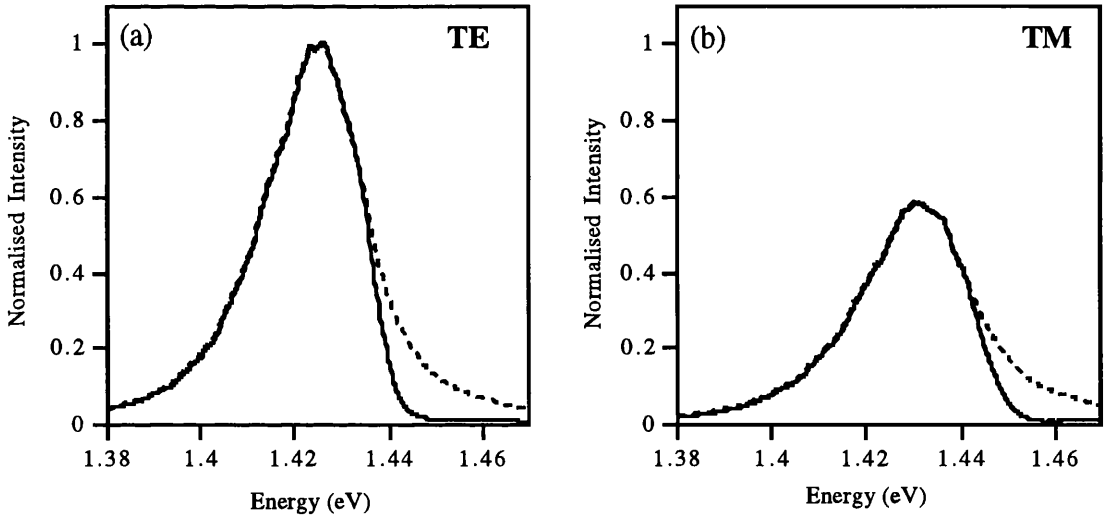

Figure 6.3: (a) TE emission spectra, and (b) TM emission spectra from absorber section of QT 664 device: with no current applied to the absorber (solid line), and with 1.6 mA (J_1) applied to the absorber (dashed line).

The emission spectra were recorded for a reverse bias range of 0 V to -4 V for both the TE and TM cases. As the technique uses spontaneous emission from the same material as the probed sample, there is sufficient light to observe absorption features from the n=1 transition only. Figures 6.4(a) and (b) show the calculated absorption spectra for both the TE and TM respectively (the electric field values were estimated from the applied voltage with the assumption that the field is distributed evenly across the quantum wells). These spectra clearly show the presence of exciton absorption peaks at the band edge. On application of increasing reverse bias, the absorption edge shifts to lower energy, and the exciton peak broadens slightly in accordance with that

expected from the QCSE[14] (see section 2.3.4). The Franz-Keldysh effect is also in evidence with a substantial broadening of the absorption tail below the band gap with the increasing applied field[14]. In the TE spectra of figure 6.4(a), both the n=1 heavy-hole (C1-HH1) and light-hole (C1-LH1) exciton transitions are present, and in the TM case of figure 6.3(b), only a single peak is present corresponding to light-hole exciton absorption (see section 2.3.2). The two peaks in the TE spectra are not clearly resolvable, with the light-hole peak appearing as a slight shoulder on the broad dominant heavy-hole peak. The two spectra are self-consistent, in that the shoulder on the TE peak appears at the same energy as the TM peak from the light-hole only. The experimentally measured energy separation of the two peaks in 10nm GaAs quantum wells is around 0.006eV[5]. This too is consistent with the positions of the peaks from figure 6.4.

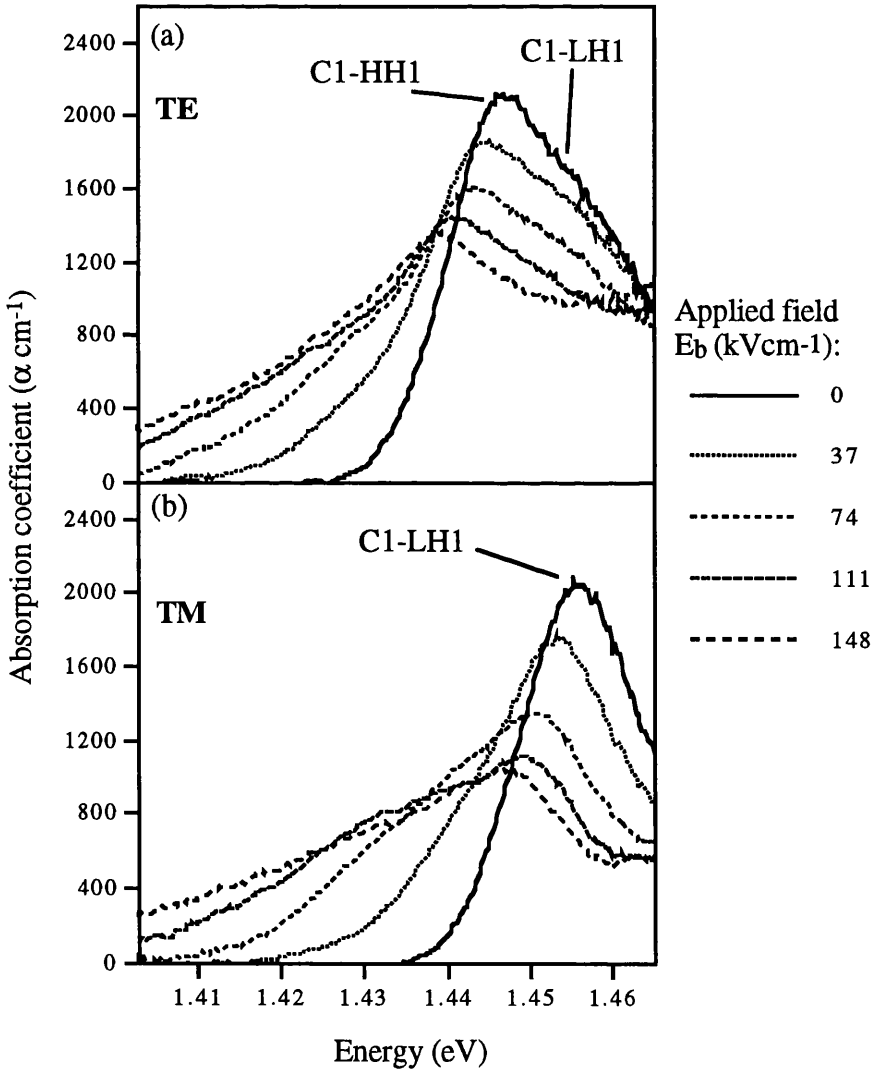

Figure 6.4: (a) TE and (b) TM reverse bias absorption spectra of QT664 showing broadening and shifting of light and heavy hole exciton absorption peaks.

A possible explanation for the lack of resolution of the two exciton peaks in the TE spectra, is the presence of variations in the distribution of the electric field along the four quantum wells. This could be caused either by slight variations in the thickness of wells through and along the sample or by the presence of a large concentration of randomly distributed impurity atoms, with their associated local potential causing a broadening in the absorption peaks[14]. The wafer QT664 used for the fabrication of the CPM lasers and for these absorption measurements, was grown by MOVPE. GaAs/AlGaAs growth by MOVPE causes the incorporation of a high level of carbon into the structure as the precursor molecule used to supply the aluminium is trimethylaluminium (TMAl). The strong bond between aluminium and carbon in TMAl can lead to the presence of carbon at the level of 10^{16} - 10^{18} cm^{-3} in AlGaAs layers [15], and these can diffuse easily into the GaAs quantum wells during growth. MBE grown GaAs/AlGaAs QW laser structures are significantly purer[16], resulting in a sharp resolution of light- and heavy-hole transitions in absorption spectra[17]. However, it has been shown that inadvertent incorporation of the p-dopant beryllium (Be) in quantum wells through diffusion, can act to smooth out exciton absorption features[18]. Further evidence that background impurities are responsible for the broadening of the absorption peaks in the MOVPE material is given in Chapter 7 of this thesis, where the absorption spectra of standard MBE material, and MBE material with deliberately introduced active layer doping, were measured (see figure 7.7). In the former the band edge showed two distinct absorption peaks , while the absorption peaks of the doped MBE material were unresolved, and had a similar form to the spectra measured from the MOVPE material QT664.

To compare the spectra in figure 6.4 quantitatively with other published work, it is necessary to realise that the measured absorption coefficients must be modified by the overlap factor Γ, as this technique measures the net modal gain. In general, rigorous evaluation of equation (2.19) is required to obtain a value for Γ, but for a first order approximation for GaAs/AlGaAs QW lasers the following expression can be used[19]:

$$\Gamma = 0.3 n_w (L_z/L_o) \qquad (6.8)$$

where n_w is the number of wells, L_z is the QW width in nm, and L_o is a constant equal to 100 nm. In QT664 there are four 10 nm QWs giving an approximate value of Γ=0.12. Results from transmission experiments by Gerber *et al*[16] on a 54 x 10 nm GaAs QW sample, and by Lengyel *et al*[20] using 10.5 nm QWs, give values for the peak of the C1-HH1 exciton absorption as ~20000 cm^{-1}. Multiplied by the value of Γ reduces this level to 2400 cm^{-1}, which is comparable, but very slightly larger than the values measured here. The discrepancy may be due to a small level of gain present during the measurement of I_{ref}. Whitehead *et al* measured a value of 25000 cm^{-1} for the absorption coefficient at the peak[5] using a photocurrent technique with 9.8nm GaAs QWs, which when converted by the overlap factor gives α=3000 cm^{-1}. This larger

value may be attributed to an under estimation of the generated photocurrent due to carrier leakage.

It is also interesting to compare the magnitude of the shift in the energy of the exciton peaks due to the QCSE as the applied field is increased, with other theoretical and experimental results. Figure 6.5 shows the shift of the dominant TE peak, and the TM peak with applied field for QT664 (values taken from figure 6.4). As can be seen the shifts were broadly linear in nature, with the TE C1-HH1 peak decreasing in energy by 7 meV (with respect to its position at zero external bias) on the application of a field of 148 $kVcm^{-1}$ (-4V). At this same applied field, the TM C1-LH1 peak was shifted by around 8.25 meV. The shift of electron and hole state energies with increasing field is broadly parabolic in nature, with the contribution from the Coulombic attraction in the exciton not significantly perturbing this relationship[14]. The linear shift observed in the experimental results presented here differs from those observed by other researchers, who observe a general dependence of the magnitude of the shift to the square of the electric field[14]. The reason for this discrepancy is as yet unknown, but it could arise again from the random impurity distribution in the MOVPE MQW active region leading to the uneven distribution of the electric field. Another potential explanation for the linear nature of the shift verses bias is the fact that the p-i-n structure of the laser wafer leads to the presence of a built-in electric field across the active region. This is calculated at 18 $kVcm^{-1}$ for QT664, assuming that the field is constant over the waveguide core. This field could be sufficient to displace the starting point of the energy shift - electric field relation onto the linear portion of the parabolic curve.

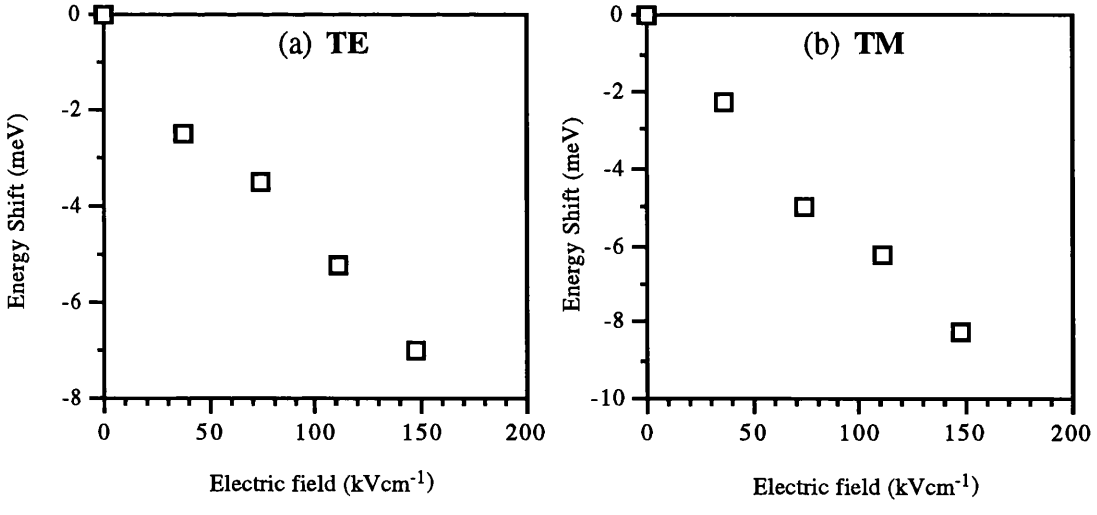

Figure 6.5: (a) Energy shift against applied electric field for the C1-HH1 TE exciton absorption peak (from figure 6.4(a)). (b) Corresponding shift for C1-LH1 peak in the TM spectra (from figure 6.4(b)). Shifts are relative to peak position at zero applied field.

6.2.2- Forward bias gain spectra.

The absorption spectra were then measured, for the same device and set-up as in section 6.2.1, but now the absorption section was forward biased. In this way the semiconductor sample can be studied under gain conditions. The TE and TM absorption spectra for pumping levels from 0 to $2.5J_1$ are shown in figure 6.6(a),(b). Both sets of spectra show that the exciton absorption peaks disappear as the forward bias is increased, and eventually gain (negative absorption coefficient) is apparent at forward bias current densities above the transparency current. The TE spectra show higher gain than the TM spectra at a given current injection, and the TM spectra peak at higher energy compared to the TE spectra. These observations are in accordance with theory as the TE spectra are dominated by the heavy-hole transitions which have a higher density of states associated with them. The TM transitions which are exclusively light-hole are shifted to a higher energy compared to TE.

Gain spectra from QW lasers can be analysed by application of the equation (2.31) derived in Chapter 2. Equation (2.31) is the function representing QW gain in the absence of any intraband scattering processes, such as carrier-carrier and carrier-phonon scattering. To include these effects Asada[21] convolutes the gain function with a Lorentzian linewidth broadening function of the form:

$$G(\hbar\omega) = \int \gamma(\hbar\omega) L(E_{eh})\, dE_{eh} \tag{6.9}$$

where $L(E_{eh})$ is the linewidth broadening function:

$$L(E_{eh}) = \frac{1}{\pi} \frac{\hbar/\tau_{in}}{(E_{eh} - \hbar\omega)^2 + (\hbar/\tau_{in})^2} \tag{6.10}$$

in which τ_{in} is the intraband relaxation time, and has been found, by fitting to experimental gain curves, to be ~ 50 fs at room temperature[22]. This Lorentzian broadening tends to cancel out any sharp features associated with light and heavy holes, giving a smooth continuous spectrum over the range of each of the transition energy levels[1,23,24] Modelling of material gain functions using this type of equation for GaAs/AlGaAs MQW laser structures by Avrutin *et al*[7] and Corzine *et al*[24], results in absorption spectra for TE and TM of the same form and order, as those shown in figure 6.6.

Because of the expected large level of current spreading present in the RWG laser structures that were used in this experiment, it is difficult to make a quantitative comparison of the gain-current density relationship measured with theory. This is evident by the approximately four times larger value of threshold current density in the RWG T-CPM lasers fabricated from QT664, as compared to wide oxide-stripe lasers (see Chapter 4). In order to allow comparison, a rough estimate of the effect of the

current spreading is made here. The threshold current density of a 400 μm long oxide stripe laser in QT664 was found in section 4.1.2 to be 1367 Acm^{-2}, and the corresponding value for a 400 μm RWG laser was 5263 Acm^{-2}. Assuming that the excess current in the RWG lasers was lost through current spreading, the value of the current densities that produced the optical gain were approximated by dividing the values in figure 6.6 by 3.85 (i.e. the ratio of the threshold current densities in the broad area and RWG lasers).

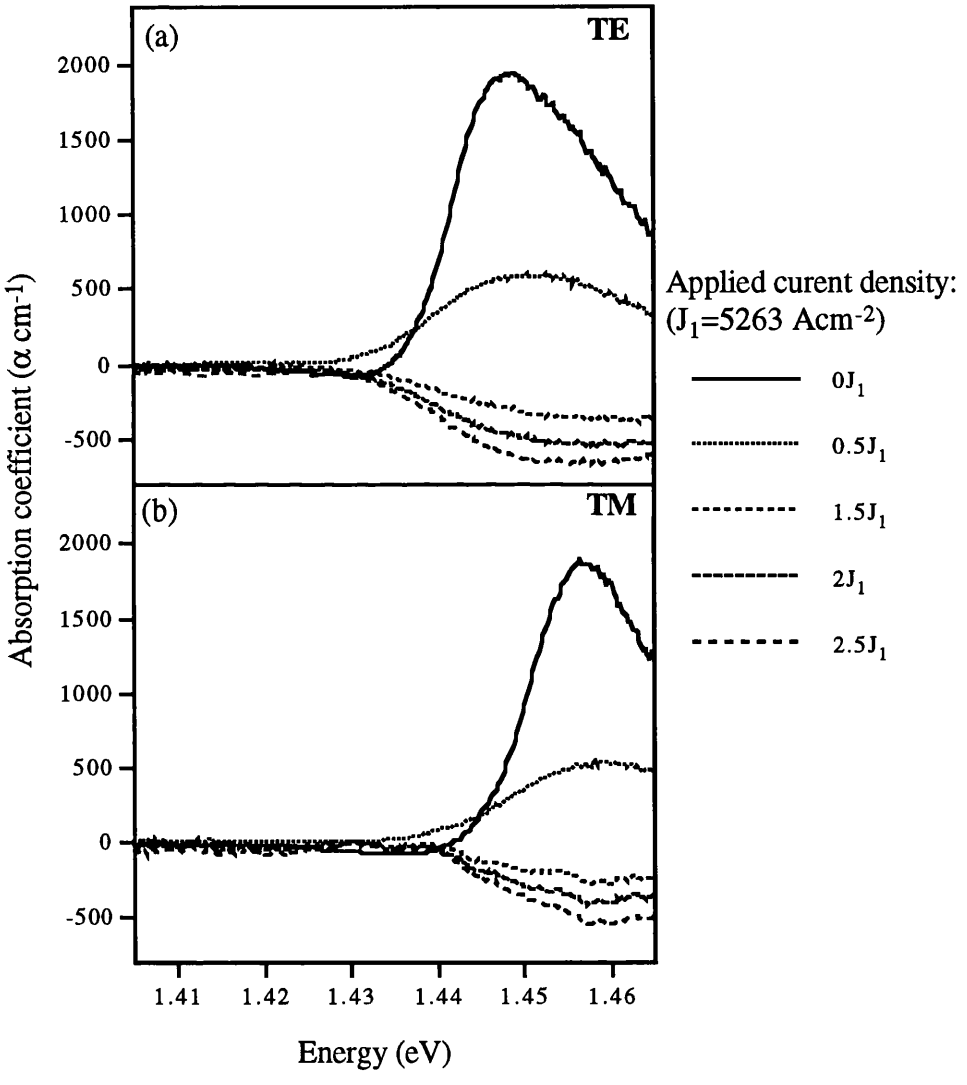

Figure 6.6: TE and TM forward bias absorption spectra for QT 664 showing transition from absorption to gain under increasing injected current density.

Using these approximate values of current density, the peak TE gain, taken from figure 6.6(a), is plotted in figure 6.7 as a function of the injected current density, where experimental points are represented by the boxes and the solid line is a least squares logarithmic fit to the data. A decrease in the gradient of the slope of gain-current

density curve as pumping switches the material from loss to gain is clearly shown in the plot. This effect arises from the step-like density of states of the quantum well which leads to significant gain saturation as the injected current increases. In addition, the data shows a good fit to a logarithmic function, which is expected from theoretical studies (section 2.3.3)[25,26]. The highly sub-linear nature of the gain-current density curve in figure 6.7, and by extension the gain-carrier density curve, is extremely important for the successful realisation of monolithic mode-locking in the T-CPM lasers. The larger gradient of the curve in the negative gain region shows that there exists a higher differential gain in the reverse biased absorber section than in the forward biased gain section of the GaAs/AlGaAs T-CPM lasers. This results in the absorber having a lower saturation energy than the gain section (see equation (3.13)), and hence it saturates faster than the gain, allowing the leading edge of a pulse to be absorbed, but the central portion to be amplified.

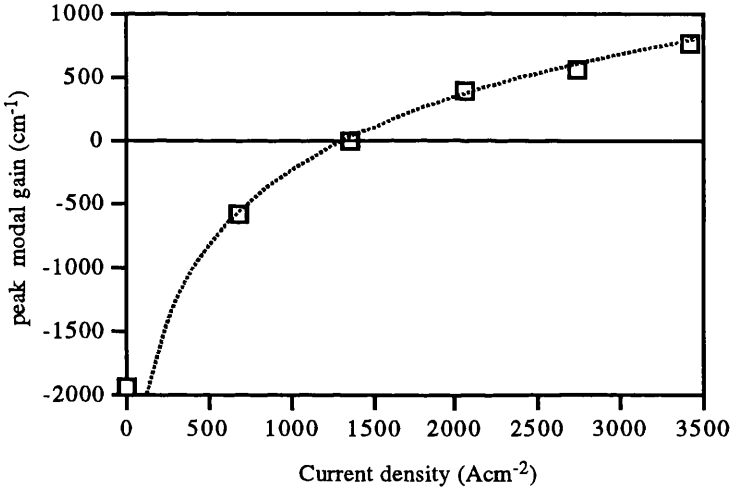

Figure 6.7: Peak TE gain versus injected current density (boxes), with natural logarithm curve fit (dashed line).

To quantitatively compare the gain-current density relationship of figure 6.7 with theory, the phenomenologically introduced logarithmic gain-current density relationship from equation (2.35) is recalled[26]:

$$\gamma_w=\gamma_o(\ln(J_w/J_o)+1) \qquad (6.11)$$

In this equation γ_w represents the gain from a single quantum well, in the absence of any n=2 state lasing, from the injected current density J_w. The values γ_o and J_o represent the so called *saturation parameters*: the point on the gain-current density curve of a single quantum well laser that intersects with the tangent drawn from the origin. The *transparency current density* J_{tr} can be evaluated from equation (6.11) by setting the gain equal to zero:

$$J_{tr} = J_o / e \qquad (6.12)$$

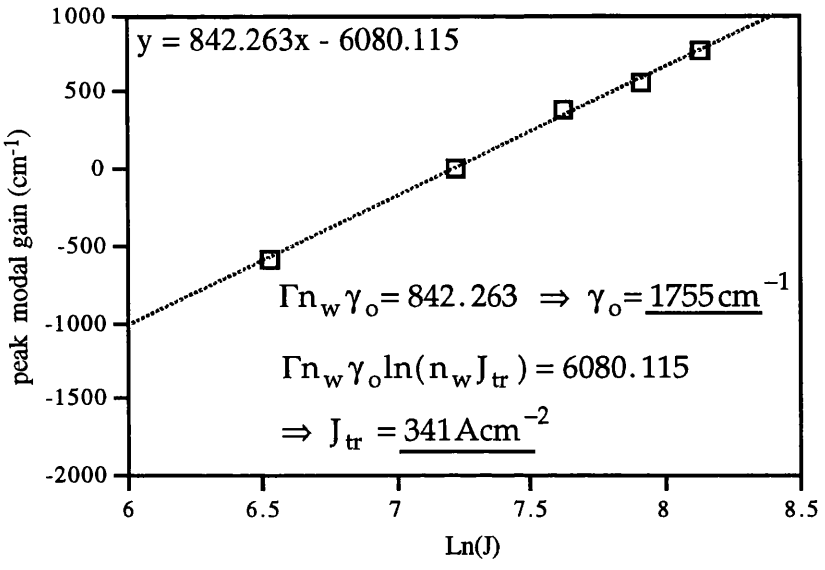

Fgure 6.8: TE peak modal gain for QT664 against the natural logarithim of the injected current density (corrected for current spreading). The dotted line represents a linear least squares fit.

As equation (6.11) gives the material gain for a single quantum well laser, it requires modification before it can be applied to the experimental results shown in figure 6.7. In this experiment it is the modal gain, G, from four quantum wells that is measured, so expression (6.11) is multiplied by the overlap factor Γ and the quantum well number n_w to give (using 6.12):

$$G = \Gamma n_w \gamma_w = \Gamma n_w \gamma_o \ln\left(\frac{J}{n_w J_{tr}}\right) \tag{6.13}$$

In the above expression it is assumed that the current is distributed evenly among all four quantum wells, so the current density per well (J_w) has also been replaced by the total current density injected into the wells (J) divided by the number of wells (n_w). By expanding the logarithm, equation (6.13) can be rewritten as:

$$G = \Gamma n_w \gamma_o \ln(J) - \Gamma n_w \gamma_o \ln(n_w J_{tr}) \tag{6.14}$$

Figure 6.8 shows a plot of the modal gain against the natural logarithm of the injected current density (values from figure 6.7). Using a least square linear fit (dotted line in figure 6.8), estimates of the values of γ_o and J_{tr} were obtained from the gradient and the y-axis intercept (according to equation (6.14), with Γ=0.12, and n_w=4). The value for the single well transparency current density is J_{tr}= 341 Acm^{-2}. When multiplied by four to give the current density for the four quantum wells contained in QT664, this value of J_{tr} is close to the threshold current density of 1367 Acm^{-2} measured for a 400 μm long oxide stripe laser. McIlroy *et al*[26] calculated the theoretical value of the gain saturation parameter γ_o for a quantum well laser with a 10

nm well width as 840 cm^{-1}. Although in the same order of magnitude, the value obtained here of 1755 cm^{-1} is approximately twice the theoretically derived value. Carrier leakage effects, non-radiative recombination, quantum well doping, and non-uniform current distribution, all of which are not included in the model from McIlroy *et al*[26], could all be important mechanisms in creating this discrepancy.

6.3- Conclusions.

This chapter presents a simple new technique for the measurement of relative absorption and gain spectra of semiconductor laser material for both forward and reverse bias. It is relatively simple, both in its experimental complexity and in the low level of theoretical background required to extract absorption coefficients from spontaneous emission data. Although the technique has the above advantages there are still some unresolved problems which will require further investigation.

By using this technique, the absorption spectrum of a passively mode-locked semiconductor laser saturable absorber section has been measured *in situ* for the first time. The presence of strong exciton features in the spectrum indicate that the associated ultrafast absorption relaxation processes could be an important mechanism for the attainment of passive mode-locking with the MOVPE grown GaAs/AlGaAs QW lasers studied in this project. The action of a reverse bias on the exciton absorption edge has been observed in this experiment and shows a broad qualitative agreement with the properties of the QCSE, and Franz-Keldysh effect, with the absorption peaks for TE and TM shifting and broadening to lower energies with increasing reverse bias. The values obtained for the absorption coefficient in these measurements are consistent with those obtained by other researchers using different experimental methods. An interesting observation from this experiment has highlighted a possible problem with this technique in that the shift in the exciton peak has a linear rather than quadratic dependence on the increasing electric field strength. However this inconsistency could be explained by consideration of the built-in electric field over the quantum wells, due to the p-i-n structure of the laser material, which results in the presence of a band edge shift before the application of any external field.

Theoretical models of gain in QW semiconductor material predict spectra with broadly similar features to those measured with the MOVPE GaAs/AlGaAs multi-quantum well wafer using the two-contact laser technique. The sub-linear form of the differential gain characteristic of multi-quantum well active regions, also vital for the realisation of monolithic mode-locking in diode lasers, has been experimentally verified here with the MOVPE CPM laser material. The gain-current curve shows an excellent fit to logarithmic function used as an approximation for the complex theoretically evaluated relationship, although the value of the gain saturation parameter extracted

deviates significantly from the theoretical value. The use of a ridge waveguide structure for the gain spectra measurements, and its associated high level of current spreading results in problems with the estimation of the current densities that are actually injected into the well. For this reason analysis of gain spectra recorded using this technique is fundamentally limited to a qualitative nature. The use of broad area laser structures, with negligible current spreading, could overcome this problem, although adequate isolation between the sections would then become an important consideration.

The one outstanding problem concerning this technique is the accurate measurement of the reference spectrum. As all subsequent gain and absorption measurements are compared with the reference to evaluate the magnitude of the gain coefficient, it is extremely important to measure it correctly. If some level of gain is present in section **b** when the reference is taken, errors of up to several hundred cm^{-1} in the absorption coefficient could potentially be introduced, although if the value of the current applied is chosen close to the transparency density this should be minimised. One possible approach to resolve this problem involves a three section laser structure. Here, the addition of a section on the opposite facet to section **b**, with the same length, could enable the reference spectra from the same length of semiconductor as is used during the absorption spectra measurements to be measured, and thus remove the present ambiguity. Another approach could be to calibrate the measurement using another of the techniques mentioned in the introductory section of this chapter, although this would remove some of the advantages of employing the two-section technique at all.

In addition to the work required to produce a more accurate reference spectrum, further improvements could be made to the system to allow exploration of the absorption spectra at energies corresponding to the higher order QW level transitions. This could be achieved by the use of sophisticated data recovery techniques, such as a more sensitive monochromator, along with phase sensitive lock-in detection.

Chapter 6: References

[1]Y.Arakawa, and A.Yariv, "Theory of gain, modulation response, and spectral linewidth in AlGaAs quantum well lasers," *IEEE.J.Quantum Electron.*, vol.21, pp16661674, 1985.

[2]H.A.Haus, and Y.Silverberg, "Theory of mode locking a laser diode with a multiple-quantum-well structure," *J.Opt.Soc.Am.B*, vol.2, pp1237-1243, 1985.

[3]H.C.Casey, D.D.Sell, and K.W.Wecht, "Concentration dependence of the absorption coefficient for n- and p-type GaAs between 1.3 and 1.6 eV," *J.Appl.Phys.*, vol.46, pp250-257, 1975.

[4]J.Filipowicz, C.Ghezzi, and LTarricone, "Temperature dependence of optical absorption induced by exciton resonances in GaAs/GaAlAs multi-quantum-well structures," *Solid-State Commun.*, vol.74, pp533-538, 1990.

[5] M.Whitehead, G.Parry, K.Woodbridge, P.J.Dobson, and G.Duggan, "Experimental confirmation of a sum rule for room-temperature electroabsorption in GaAs-AlGaAs multiple quantum well structures," *Appl.Phys.Lett.*, vol.52, pp345-347, 1988.

[6]B.W.Hakki, and T.L.Paoli, "Gain spectra in GaAs double-heterostructure injection lasers," *J.Appl.Phys.*, vol.46, pp1299-1306, 1975.

[7]E.A Avrutin, I.E.Chebunina, I.E.Eliachevtch, S.A.Gurevich, M.E.Portnoi, and G.E.Shtengel, "TE and TM optical gains in AlGaAs/GaAs single quantum well lasers," *Semicond.Sci.Technol.*, vol.8, pp80-87, 1993.

[8]T.Hayakawa, T.Suyama, K.Takahashi, M.Kondo, S.Yamaoto, and T.Hijikata, "Polarization-dependent gain-current relationship in (111)-oriented GaAs/AlGaAs quantum-well lasers," *J.Appl.Phys.*, vol..64, pp1297-302, 1988.

[9]C.H.Henry, R.A.Logan, and F.R.Merrit, "Measurement of gain and absorption spectra in AlGaAs buried heterostructure lasers," *J.Appl.Phys.*, vol..51, pp3042-3050, 1980.

[10]R.O.Miles, M.A.Dupertuis, F.K.Reinhart, and P.M.Brosson, "Gain measurements in InGaAs/InGaAsP multiquantum-well broad-area lasers," *IEE Proc.-j*, vol.139, pp33-38, 1992.

[11]P.Blood, A.I.Kucharska, J.P.Jacobs, and K.Griffiths, "Measurements and calculation of spontaneous recombination current and optical gain in GaAs-AlGaAs quantum-well structures," *J.Appl.Phys.*, vol.70, pp1144-1156, 1991.

[12]G.E.Kohnke, and G.W.Wicks, "Second quantized state lasing and gain spectra measurements in n-type modulation doped GaAs-AlGaAs quantum-well lasers," *IEEE.J.Quantum Electron.*, vol.31, pp1941-1946, 1995.

[13]P.Rees, and P.Blood, "Derivation of gain spectra of laser diodes from spontaneous emission measurements," *IEEE.J.Quantum Electron.*, vol.31, pp1047-1050, 1995.

[14]S.Schmitt-Rink, D.S.Chemla, and D.A.B.Miller, "Linear and non-linear optical properties of semiconductor quantum wells," *Adv.Phys.*, vol.38, pp89-188, 1989.

[15]T.F.Kuech, D.J.Wolford, E.Veuhoff, V.Deline, P.M.Mooney, R.Potemski, and J.Bradley, "Properties of high purity $Al_xGa_{1-x}As$ grown by the metal-oraganic vapour-phase-epitaxy technique using methyl precursors," *J.Appl.Phys.*, vol.62, pp632-643, 1987.

[16]T.Achtnick, G.Burri, and M.Ilegems, *J.Vac.Sci.Tecnol.*, vol.7 p2537, 1989.

[17]D.SGerber, and G.N.Maracas, "A simple method for extraction of multiple quantum well absorption coefficient from reflectance and transmittance measurements," *IEEE.J.Quantum Electron.*, vol.29, pp2589-2595, 1995.

[18]G.E.Kohnke, M.W.Koch, C.E.C.Wood, and G.W.Wicks, "Beryllium diffusion in GaAs/AlGaAs single quantum well seperate confinement heterostructure laser active regions," *Appl.Phys.Lett.*, vol.66, pp2786-2788, 1992.

[19] A.Sigimura, "Threshold current for AlGaAs quantum well lasers,"*IEEE.J.Quantum Electron.*, vol.20, pp336-343, 1984.

[20]G.Lengyel, K.W.Jelley, and R.W.H.Engelmann, " A semi-empirical model for electro absorbtion in GaAs-AlGaAs multiple quantum well modulator structures," *IEEE.J.Quantum Electron.*, vol.26, pp296-304, 1990.

[21]M.Asada, chapter 2 in *Quantum well lasers*, P.S.Zory (Ed.), Acedemic Press, 1993

[22]D.J.Erskine, A.J.Taylor, and C.L.Tang, "Femtosecond studies of intraband relaxation in GaAs, AlGaAs, and GaAs/AlGaAs multiple quantum well structures," *Appl.Phys.lett.*, vol.45, no1, pp54-56, 1984.

[23]T.Makino, "Analytical formulas for the optical gain of quantum wells," *IEEE.J.Quantum Electron.*, vol.32, pp493-501, 1996.

[24]S.WCorzine, R.H.Yan, and L.A.Coldren, chapter 1; and R.W.H.Engelmann, C-L.Shieh, and C.Shu, chapter 3; in *Quantum well lasers*, P.S.Zory (Ed.), Acedemic Press, 1993

[25]T.A.Detemple, and C.M.Herzinger, "On the semiconductor laser logarithmic gain-current density relation, "*IEEE.J.Quantum Electron.*, vol.29, pp1246-1252, 1993.
[26]P.W.A.McIlroy, A.Kurobe, and Y.Uematsu, "Analysis and application of theoretical gain curves to the design of mult--quantum-well lasers," *IEEE.J.Quantum Electron.*, vol.21, pp1958-1263, 1985.

Chapter 7- GaAs/AlGaAs CPM lasers in MBE grown MQW material

The previous three chapters have documented the fabrication, operation, and characterisation of the mode-locked laser pulses, and monolithically integrated saturable absorber of short cavity monolithic CPM lasers from MOVPE MQW laser wafers. The Ph.D. thesis of J.F.Martins-Filho[1] used similar MOVPE GaAs/AlGaAs material to fabricate both monolithic cavity CPM and MCPM (multiple colliding pulse mode-locked) diode lasers. As yet there has been no report of successful demonstration of the operation of very high repetition rate GaAs/AlGaAs lasers fabricated from MBE grown material.

This chapter describes the realisation of CPM and MCPM operation in MBE grown RWG laser structures. A crucial difference between laser material grown by MOVPE and MBE is the increased concentration of the impurity carbon in the active region of the former. This arises from the particular form of the compounds used to provide the various constituent atoms. The role that this doping has to play in the achievement of monolithic mode-locking is investigated in this chapter. As will be shown CPM and MCPM action was only accomplished through background doping of the MBE grown active regions to simulate the doping present in MOVPE grown mode-locked laser wafers. In this chapter the term *standard-MBE* is adopted to describe a laser wafer that has no intentional doping present in the active region. Laser structures grown by MBE with intentionally incorporated background doping in the active region are referred to as *Backdoped-MBE*.

In the initial section of this chapter, a brief experimental and theoretical review of the MCPM laser is provided, in order to enable comparisons with the current work. Following this is a description of the experimental results from the fabrication of mode-locked lasers in MBE material, and a discussion of their implications.

7.1- MCPM lasers.[1,4]

There are several different methods employed to produce mode-locked pulses from diode lasers at higher harmonics of the cavity round trip time in the laser oscillator[2,3], and these are discussed in section 3.2.4 of Chapter 3. One important technique is that of multiple CPM, where several saturable absorbers are monolithically integrated at integer sub-multiples of the laser cavity length. The resulting production of several mode-locked pulses at repetition frequencies that permit pulse-collisions in the various

saturable absorbers, extends the standard CPM geometry to higher harmonic mode-locking, while still maintaining the advantages conferred by the colliding pulse effects.

Figure 7.1 shows a schematic diagram of a RWG MCPM laser. The device has three individually addressable waveguide absorber sections and one gain section contact. The centre of each absorber is positioned at a quarter, a half, and three quarters of the cavity length respectively. During CW operation of such a laser, if the two end absorbers are forward biased, but the central absorber is reverse biased, the device has a standard CPM laser geometry, and consequently the device mode-locks with two pulses circulating simultaneously in the cavity. However by changing the bias conditions, several different modes of operation can be contrived. When all three absorbers are reverse biased, four pulse mode-locking is produced. As collisions will take place between pulses in each of the absorbers, the presence of four concurrent pulses in the cavity makes the most efficient use of absorber saturation. Generation of further harmonics of this rate, i.e. 8 pulses, does not occur possibly because this would cause increased instabilities through pulse collisions in gain regions. Single pulse mode-locking can be achieved by applying reverse bias to one of the end absorbers only, and three pulse mode-locking by reverse biasing both end absorbers.

In summary, by using the MCPM geometry, the mode-locked repetition rate of a single device can be tuned through the first, second, third, and fourth harmonic of the fundamental cavity round trip frequency, and is calculated from the following expression:

$$f = \frac{mc}{2nL} \tag{7.1}$$

where m is the integer 1,2,3,or 4 depending on the mode of operation.

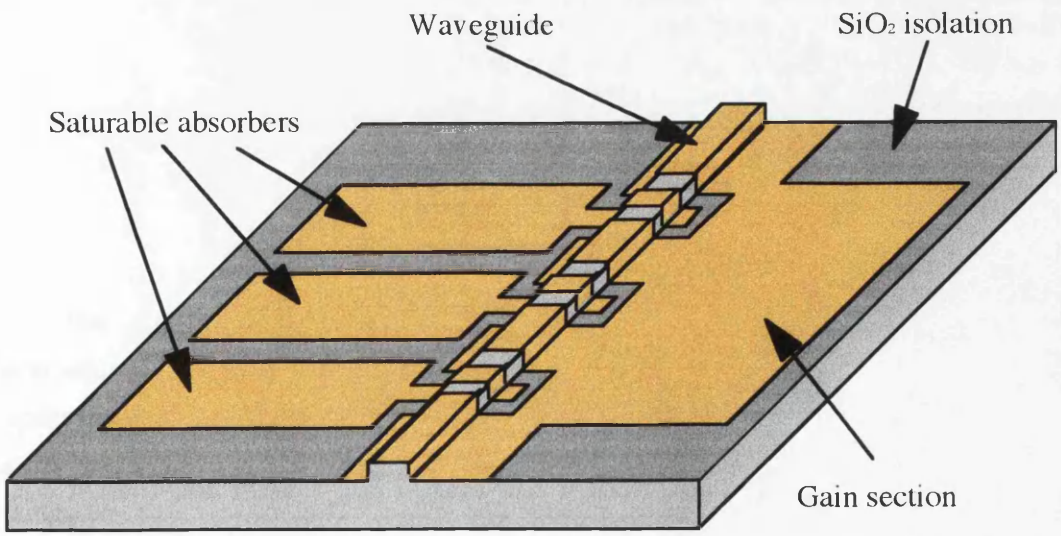

Figure 7.1 Schematic diagram of MCPM laser.

Using spectral measurements, and the linear cross-correlation technique for time domain characterisation, Martins-Filho *et al*[4] achieved mode-locking at 60 GHz, 120 GHz, 180 GHz, and 240 GHz from a 600 μm 4 QW GaAs/AlGaAs MCPM grown by MOVPE. Four pulse operation at 375 GHz, from a 400 μm MCPM laser was also reported, as yet the highest frequency attained for diode lasers employing a colliding pulse scheme.

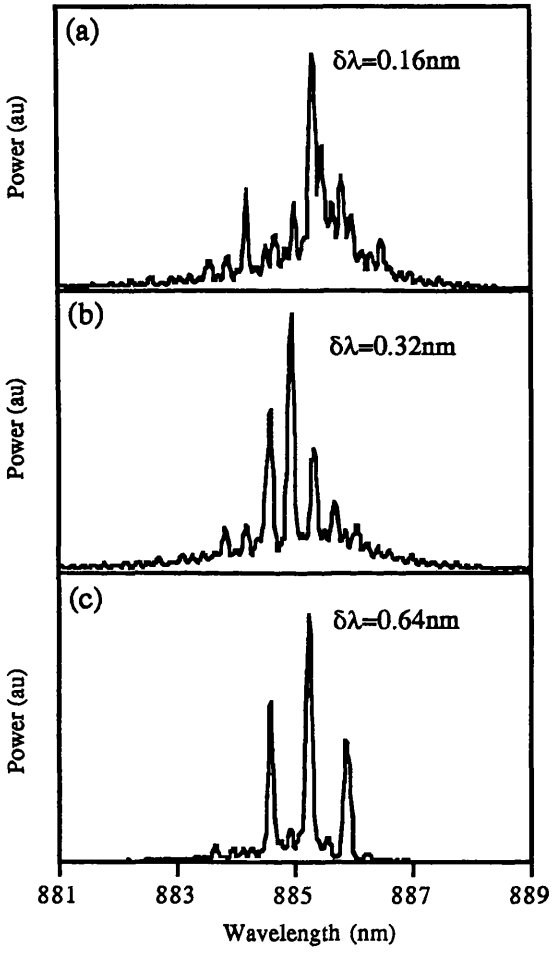

Figure 7.2: 400 μm MCPM laser in MOVPE grown QT664 showing (a) forward bias, (b) CPM, and (c) 4-pulse MCPM operation

In the theoretical model for MCPM, E.A.Avrutin[4] showed that by introducing parameters corresponding to the geometrical layout of absorption and gain sections in expressions for the coupling between the various cavity modes (overlap factors), that cavity modes between every second, third, or fourth mode could be suppressed during lasing, depending on the relevant biasing scheme. The corresponding simulated pulse intensity profiles showed that clean short-pulse mode-locked output was generated in the two-pulse and four-pulse MCPM. One-pulse operation produced heavily broadened pulses, and in the three-pulse scheme there existed large variations in the amplitude and

width of each consecutive pulse in the output train. For stable mode-locking at the repetition rates observed experimentally, the model required the presence of a fast component to the saturable absorber recovery time, and predicted that this time must be at most 0.5 ps.

Using the fabrication method detailed in Chapter 4, MCPM lasers were fabricated in the QT664 MOVPE material, the only differences being the use of a MCPM patterned p-contact mask, with three 15 μm long absorber sections, for the p-contact evaporation and lift-off stage, and no orthogonal waveguide was required. These devices were mounted and bonded, and the spectra were taken under CW operational conditions. The recorded spectra corresponding to fully-forward bias operation, 2-pulse mode-locking and 4-pulse mode-locking of a 400 μm long laser, are displayed in figures 7.2 (a)-(c) respectively. Note the doubling of the inter-mode wavelength spacing and quadrupling of the mode-spacing, indicating the harmonic CPM action.

7.2- MCPM lasers in MBE grown material.

7.2.1- Fabrication of standard-MBE lasers.

Using a wafer with a structure nominally identical to that of the MOVPE QT664, mode-locked laser wafer, but grown at the University of Glasgow MBE facility, T-CPM, and MCPM lasers were fabricated. The structure was processed using the techniques described in Chapter 4. The layer specifications are shown below:

Material: B 456

P-contact layer	-	0.2μm Be-GaAs ($1x10^{19}$ cm^{-3})
P-buffer	-	1.1μm Be-40% AlGaAs ($2x10^{17}$ cm^{-3})
	-	0.1μm 20% AlGaAs
MQW region		
	-	0.1μm 20% AlGaAs
N-buffer	-	1.8μm Si-40% AlGaAs ($1.1x10^{17}$ cm^{-3})
N-contact layer	-	0.5μm Si-GaAs ($5x10^{18}$ cm^{-3})

SUBSTRATE

MQW: {10nm GaAs }
{10nm 20% AlGaAs } x3
10nm GaAs

The optical properties of the material were tested by the fabrication of 75 μm wide oxide-stripe lasers. The threshold current density of a 400μm long device was measured at 573 Acm^{-2}, the internal efficiency at 72%, and internal losses at 18 cm^{-2}. On comparison with the values obtained for the MOVPE wafer QT664 (section 3.1.2),

the lower losses and higher efficiency indicates that the MBE wafer B456 was superior in optical quality. This is substantiated with the ~50% reduction in the threshold current density between the two materials.

400 μm and 600 μm MCPM and T-CPM laser structures were fabricated from B456 material, then mounted, bonded and tested using a CW current supply. Figure 7.3 shows a typical lxi curve and spectrum of a 400 μm MCPM device under full forward bias conditions, showing the threshold current of around 40 mA. When operated under reverse bias conditions, none of the devices tested showed any sign of the spectral doubling or quadrupling associated with the CPM or MCPM action. Fabrication of a second batch of devices was undertaken from a spatially separated sample of the B456 wafer in order to eliminate the possibility of the negative result being due to a local flaw in the crystal structure. This is improbable as the lasers consistently displayed satisfactory slope efficiencies and reasonably low values of threshold current. The second batch behaved in a similar manner to the first, with good CW laser characteristics but showed no evidence of harmonic mode-locking.

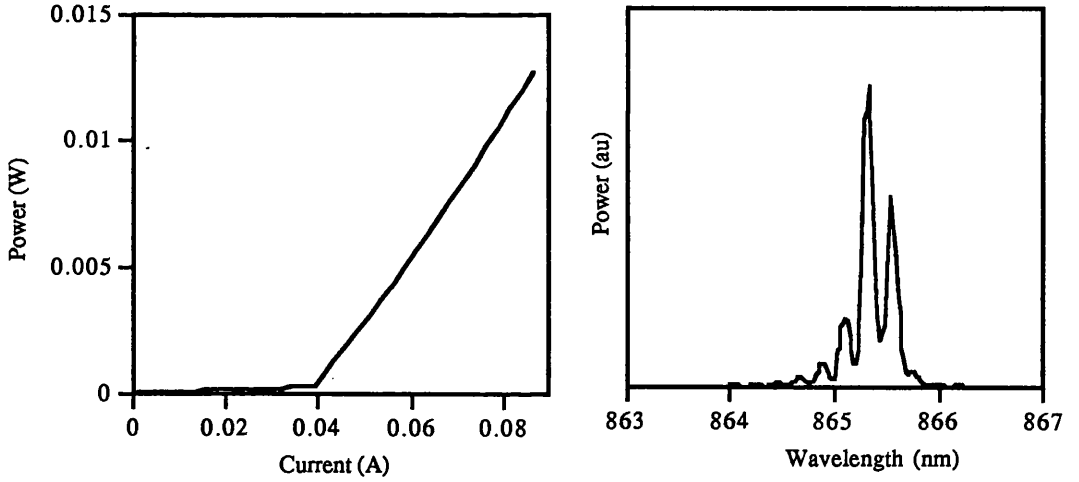

Figure 7.3: B456 400 μm CPM laser: (a) lxi, (b) spectrum, under full forward bias conditions.

Before and after the final GaAs selective etch to remove the p+ capping layer and electrically isolate the absorber and gain sections on the waveguides, the resistance between the sections was measured using the semiconductor parameter analyser. The measured IxV , in figure 7.4, shows that although the contacts are ohmic, the resistance is very low, only 221 Ω after the etch. At this low level of isolation, the effect of the reverse bias on the absorber is reduced by current leaking from the gain section, which is a possible explanation for failure to achieve mode-locking. By using a standard non-selective $SiCl_4$ dry etch to isolate the sections, and etching down to a depth of 0.4 μm (over half the ridge depth), the resistance was increased to 600 Ω, still around half of

the isolation present in the successful MOVPE devices. The decreased level of isolation in the MBE devices compared to the MOVPE devices, both with nominally identical doping concentrations, may be due to back diffusion of beryllium from the p+ GaAs contact layer into the AlGaAs p-buffer waveguide layer during growth, increasing the actual doping concentration to well above the nominal value. Lasers etched to increase the isolation still showed no sign of CPM or MCPM operation.

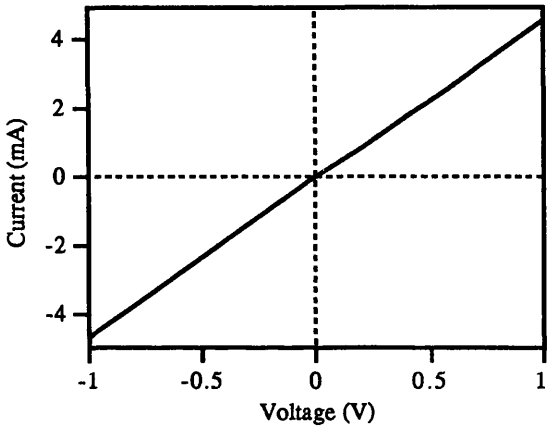

Figure 7.4: VxI between the absorber and gain sections of B456 400 μm CPM laser.

To further investigate the effect of the low isolation, a new MBE wafer (A949) was grown, but with the doping in the p-cladding reduced by a third to $6x10^{16}$ cm^{-3}. Broad area laser characterisation produced values of 600 Acm^{-2} for the threshold current density of a 400 μm laser, internal efficiency of 82% and internal losses of 15.32 cm^{-1}. Again these values revealed A949 to be good laser material. When fabricated into MCPM and T-CPM lasers, the isolation after the final dry etch was increased to the order of 2 kΩ, a considerable improvement on B456. However even with this modification, no mode-locking from 400 μm or 600 μm MCPM or T-CPM lasers was observed.

7.2.2- Fabrication of Backdoped-MBE lasers.

Although the MQW active regions of the MBE grown B456 and A949 laser structures are nominally identical to those of the MOVPE grown QT664, there is one important practical distinction. During MOVPE growth, carbon is incorporated as an impurity throughout the structure and acts as a p-dopant where no other impurities are intentionally incorporated. The origins of this are discussed in Section 6.2.1 in relation to the effect of impurities on the absorption spectra of the MOVPE material. In contrast, MBE grown GaAs/AlGaAs is significantly purer[5] with carbon concentration

in GaAs typically less than $1x10^{14}$ cm^{-3}. This could have important implications for the attainment of high repetition rate mode-locking in GaAs/AlGaAs diode lasers, if the unintentionally introduced dopants present in MOVPE QW layers create a mechanism for the required fast absorption recovery. In order to simulate the effect of the background doping in MOVPE, a MBE wafer was grown with identical structure to wafer A949, but with the active region doped with beryllium to $6x10^{16}cm^{-3}$:

Material: B 741 (background-doped MBE)

P-contact layer	-	0.2μm Be-GaAs ($1x10^{19}$ cm^{-3})
P-buffer	-	1.1μm Be-40% AlGaAs ($6x10^{16}$ cm^{-3})
	-	0.1μm 20% AlGaAs ($6x10^{16}$ cm^{-3})
MQW region		
	-	0.1μm 20% AlGaAs
N-buffer	-	1.8μm Si-40% AlGaAs ($1.1x10^{17}$ cm^{-3})
N-contact layer	-	0.5μm Si-GaAs ($5x10^{18}$ cm^{-3})

SUBSTRATE

MQW: {10nm GaAs ($6x10^{16}$ cm^{-3}) }
{10nm 20% AlGaAs ($6x10^{16}$ cm^{-3})} x3
10nm GaAs ($6x10^{16}$ cm^{-3})

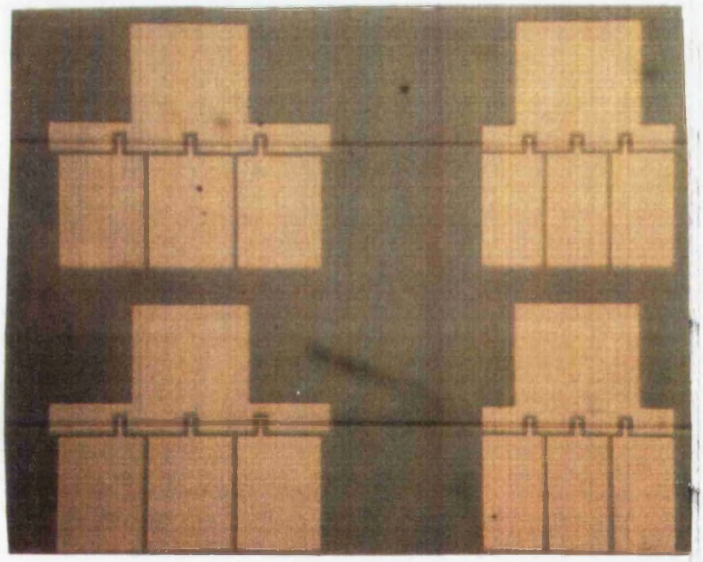

Figure 7.5: Photograph of 600 μm (left) and 400 μm (right) MCPM lasers fabricated from backdoped-MBE material B741.

MCPM and T-CPM lasers were fabricated from wafer B741. Figure 7.5 shows a photograph of 400 μm and 600 μm MCPM devices before the final cleaving stage. When operated under CW current conditions, the devices produced spectra consistent with CPM and MCPM operation. Figure 7.6 shows three spectra corresponding to the

operation of a 400 μm MCPM laser fully forward biased (figure 7.6(a)), with the central absorber only reverse biased (figure 7.6(b)), and with all three absorbers reverse biased (figure 7.6(c)). Two-pulse and four-pulse MCPM action is demonstrated by the doubling and quadrupling of the cavity mode spacing in the latter two spectra. The figures display the repetition rates of the two-pulse and four-pulse mode-locking. Similar evidence of mode-locking was recorded in spectra from T-CPM lasers. To corroborate this result, lasers were tested from a second batch fabricated from B741, and these gave comparably positive results. The essential conclusion drawn here is that the types of CPM and MCPM spectra presented in figure 7.6 could not be obtained from devices made with MBE material unless the active region was deliberately doped.

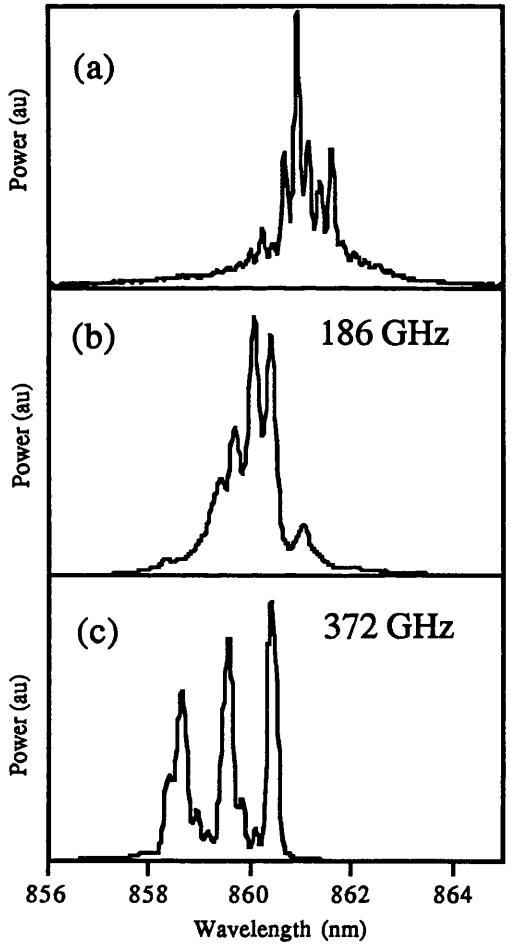

Figure 7.6: Spectra of a 400 μm MCPM laser fabricated in backdoped-MBE material B741, showing (a) forward bias, (b) two-pulse MCPM at 186 GHz and (c) four-pulse MCPM at 372 GHz.

Evidence supporting the above assertion that the presence of active region doping plays a crucial role in high repetition rate mode-locking of GaAs/AlGaAs lasers, can be seen in work carried out by O'Gorman *et al*[6]. Switching experiments were performed using intracavity loss modulation in 500 μm long GaAs/AlGaAs lasers with centrally

located 40 μm absorbers. Despite having the correct geometry for CPM action, the authors do not report mode-locking from these devices. For these devices a novel source was used to provide the aluminium during the MOVPE growth in order to specifically lower the concentration of unintentionally incorporated carbon[7] improving the quality of the QW regions to produce very low threshold current devices[8]. Thus, the above results are consistent with the results presented in this thesis, where low levels of QW doping correspond to a failure to attain high repetition rate mode-locking in GaAs/AlGaAs lasers.

Although devices from B741 were successfully mode-locked, they displayed slightly higher threshold currents, and did not have particularly long lifetimes compared to the devices fabricated from the standard MBE laser structures, B456 and A949. This could arise from the increased beryllium levels present in the active region which can diffuse and cause damage to QW luminescence during operation. The level of background doping used here was arbitrarily chosen at $6x10^{16}$ cm^{-3}. Further work is required to discover the precise level of doping required to achieve mode-locking with improved laser performance.

7.2.3- Effects of doping on absorption spectra.

From the discussion in Section 3.2.4, passive mode-locking via saturable absorption not only requires fast absorber saturation compared to the gain, but the absorption after the passage of a mode-locked pulse must significantly recover, in order to provide loss for the trailing edge of the pulse and allow net pulse shortening over a single transit through the absorber. The CPM and MCPM lasers fabricated and tested in this chapter are all short cavity length devices, with correspondingly high repetition rates. Mode-locked operation of these devices, with pulse round trip periods in the order of a few ps, require a fast subpicosecond component to the absorption saturation recovery. Such a fast component can be supplied by the ultrafast non-linearities associated with the exciton absorption line[9,10]. The absorption spectra of Chapter 6 (figure 6.4) showed that the saturable absorber of the MOVPE grown T-CPM lasers had a large exciton absorption feature, so recovery of the exciton absorption line is a possible mechanism through which mode-locking at high repetition frequencies was achieved.

The presence of impurity atoms in the active region of a diode laser leads to an increased level of non-radiative carrier recombination via the interaction with the created local continuum of states that span the bandgap. However, band to band carrier recombination is still in the order of hundreds of ps - too fast to be an effective mechanism for absorption recovery in high repetition rate mode-locking. Alternately, in external or extended cavity mode-locked diode lasers, the corresponding reduction in

the absorber recovery time can significantly enhance the effectiveness of pulse shortening from the absorber.

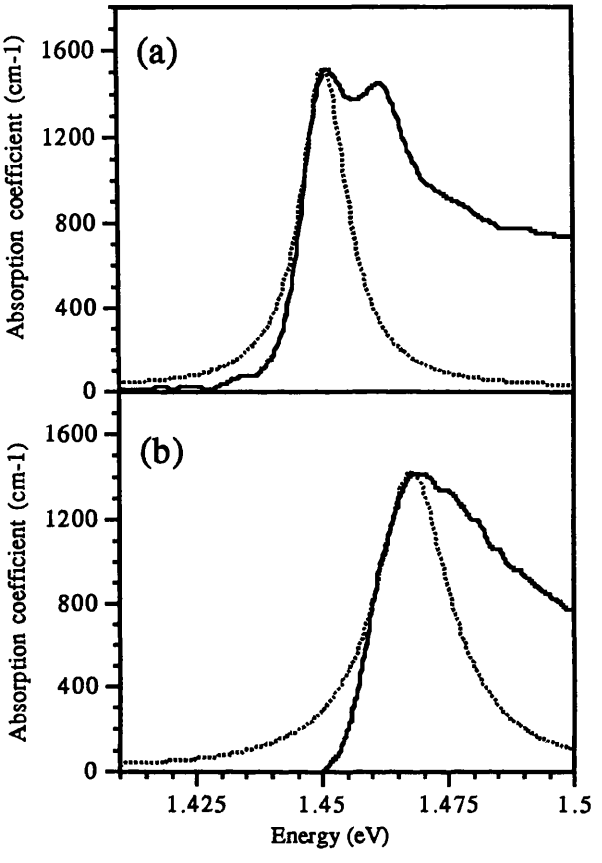

Figure 7.7: TE absorption spectra for (a) standard-MBE material A949, and (b) backdoped-MBE material B741. The solid lines plotted are the measured spectra, with the dotted lines representing best fit Lorentzian profiles for the C1-HH1 transition.

Along with band to band recombination, p-doping of the MQW region of MBE grown GaAs/AlGaAs has an effect on the lifetime of photogenerated excitons. Through lattice phonon, or carrier scattering events, excitons are disassociated into individual carriers. The time over which this takes place can also be affected by the presence of charged impurity atoms in a QW. The field from the impurity atom can interact with that of the exciton which then either ionises or seriously perturbs it. If there is a high probability of finding an impurity atom within the excitonic volume this will significantly reduce the mean exciton lifetime. If the p-doping is at high enough concentrations to force the quasi Fermi-level into the valance band, resulting in a degenerate hole population, the increased carrier scattering will also decrease the exciton lifetime.

An indication of the effect of background doping the active layers of the MBE CPM laser wafers can be observed in measurements of the exciton absorption spectra. The TE absorption spectrum of the saturable absorber of a CPM laser fabricated from standard MBE material A949 is shown in figure 7.7(a). Similarly, the TE absorption spectra for a back-doped MBE B741 CPM laser is shown in figure 7.7(b) These spectra were measured directly using the two-section laser technique detailed in Chapter 6, with 0V bias applied on the absorber sections in each case. Both the heavy-hole and light-hole n=1 exciton peaks are clearly visible in the spectra from A949. However for the backdoped sample, these peaks have broadened and are unresolved. Note also that the absorption edge of material B741 is shifted to a higher energy when compared to the unintentionally doped A949 spectrum. This is an indication of the promotion of the quasi Fermi-level into the valence band due to the presence of carriers from the increased level of p-doping. The spectrum of the backdoped-MBE sample is similar to the absorption spectra of MOVPE material QT664 (figure 6.4) which also shows broadened unresolved heavy/light-hole absorption peaks.

In the absence of any scattering process, the absorption spectrum of a quantum well follows the 2-D density of states, with a series of steps corresponding to the light/heavy-hole transitions from the various conduction and valance sub-bands with sharp exciton peaks at energies just below the onset of each transition (Section 2.3.4). As mentioned above, scattering processes cause a range of possible transition energies to exist, which in turn broaden the bandwidth of the exciton absorption peak. Optical absorption results from the polarisation induced in the semiconductor medium by an incident lightwave (gain coefficient from Chapter 2). Deriving a general expression for the spectral lineshape that ensues from scattering processes, involves the performance of a Fourier transform on the response of the induced polarisation to an impulse light signal[11]. In the case of homogeneous broadening, in which a high scattering probability results in the environment of each state becoming indistinguishable, the general expression can be approximated by a Lorentzian type function[11]. In homogeneous broadening the induced polarisation decays exponentially, with a time constant τ equal to the inverse of the scattering probability per unit time. The Fourier transform in this case results in a Lorentzian shape with the halfwidth of the energy distribution being given by $\hbar/\tau$. Along with the homogeneous broadening from phonons etc., small unavoidable defects and layer width fluctuations in real life semiconductor laser structures leads to the presence of inhomogeneous broadening, which has an associated Gaussian type linewidth. The resulting lineshape in semiconductor lasers can be thought of as lying somewhere between these two extremes.

The relative broadening of the exciton absorption peaks in the spectra of the doped- and undoped MBE MQW material is inversely related to a relative decrease in the exciton lifetime. To obtain a quantitative approximation for this decrease, the exciton

peaks corresponding to the C1-HH1 transition in the TE absorption spectra shown in figures 7.7 (a), and (b), are fitted with a Lorentzian function of the form:

$$\alpha_{ex}(\hbar\omega) = \frac{A_o}{\pi} \frac{\hbar/\tau}{(\hbar/\tau)^2 + (\hbar\omega - E_{ex})^2} \tag{7.2}$$

where E_{ex} is the exciton transition energy in the absence of broadening, A_o is some proportionality constant, and τ is the phenomenologically introduced mean scattering time. It can easily be shown that the value of the halfwidth at half maximum in the Lorentzian expression (7.2) is given by:

$$\delta E = \frac{\hbar}{\tau} \tag{7.3}$$

Using the spectral function (7.2) is obviously an extreme simplification, and by inspection of figures 7.7(a), and (b), the Lorentzian lineshapes, shown by the dashed lines, can be seen to seriously deviate from the measured absorption spectra at the band edge. This arises from the well known *Urbach tail* phenomena[12] in which the fundamental absorption spectrum is observed to decay exponentially at the band edge, while a Lorentzian function decays appreciably slower at $(\hbar\omega)^{-2}$. Several authors have made use of more sophisticated lineshape functions in the modelling of gain spectra in semiconductors[11], but for the purposes of the analysis performed here on the MBE laser spectra, the simple Lorentzian approach provides a useful approximation.

From the spectrum of the standard-MBE A949 material in figure 7.7(a), the halfwidth of the best fit Lorentzian is δE=0.006 eV which from equation (7.3), gives a scattering time of τ=166 fs. From figure 7.7(b), the best fit Lorentzian of the back-doped MBE B741 yields a δE of 0.0095 eV, and a scattering time of τ=105 fs. This corresponds to a decrease in the exciton lifetime of approximately one third due to the introduction of impurities in the QW active region. While this is a large decrease in the exciton lifetime, it is unclear whether it should have a direct contribution to mode-locking, since both times are of the same order.

7.3- Conclusions.

This chapter presents experimental evidence of the crucial role of doping in the attainment of high repetition rate mode-locking of GaAs/AlGaAs MQW laser material. CPM and MCPM lasers were demonstrated using MBE grown epitaxial layers at repetition rates of 186 GHz and 372 GHz, exclusively in devices where p-doping was intentionally incorporated into the MQW.

Evidence of the effect of p-doping is provided from the measurement of the exciton absorption spectra at the QW band edge of both standard-MBE and backdoped-MBE material. With no doping, both the C1-HH1 and C1-LH1 exciton transitions are

resolvable. However with the inclusion of doping, the exciton peaks broaden and become indistinguishable. This broadening can be explained by the reduced exciton lifetime, from 166 fs to 105 fs, caused by the increase in scattering from impurities and holes. The broadened exciton absorption spectrum from the back-doped MBE samples is similar in form to that of the MOVPE MQW material (Chapter 6) used successfully to fabricate CPM lasers.

The linear absorption spectra results clearly show that the form of the exciton absorption is significantly altered due to the presence of impurities. However it is non-linear exciton absorption, which depends both on oscillator strength and exciton lifetime which would provide the ultrafast component required to aid mode-locking. Whether the change in form of the excitonic spectra has an advantageous or detrimental effect on this, can only be discovered by a direct time domain measurement of absorption recovery in doped and undoped MBE structures.

Chapter 7: References.

[1] J.F.Martins-Filho, *Monolithic Colliding Pulse Mode-locked Quantum-well Lasers*, Ph.D. Thesis, University of Glasgow, 1995.

[2] S.Sanders, A.Yariv, J.Paslaski, J.E.Ungar, and H.A.Zarem, "Passive mode locking of a two-section multiple quantum well laser at harmonics of the cavity round-trip frequency," *Appl.phys.lett.* vol.58, pp681-683, 1991.

[3] S.Arahira, Y.Matsui, and Y.Ogawa, "Mode-locking at very high repetition rates more than terahertz in passively mode-locked distributed-bragg-reflector laser diodes," *IEEE.J.Quantum.Electron*, vol.32, pp1211-1224, 1996.

[4] J.F.Martins-Filho, E.A.Avrutin, C.N.Ironside, and J.S.Roberts, "Monolithic multiple colliding pulse mode-locked quantum-well lasers: experiment and theory," *IEEE.J.Sel.Topics.Quantum.Electron*, vol.1, pp539-551, 1995.

[5] T.Achtnick, G.Burri, and M.Iegems, *J.Vac.Sci.Tech*, 7, pp2537, 1989.

[6] J.O'Gorman, A.F.Levi, and W.S.Hobson, "High power switching of multi-electrode broad area lasers," *Electron.lett.* vol.27, pp13-14, 1991

[7] W.S.Hobson, J.P.van der Ziel, A.F.J.Levi, J.O'Gorman, C.R.Abernathy, A.Geva, L.C.Luther, and V.Swaminathan, "Low-threshold GaAs/AlGaAs quantum-well lasers grown by organometallic vapour-phase epitaxy using trimethylamine alane," *J.Appl.Phys.* vol.70, pp432-435, 1991.

[8] W.S.Hobson, A.F.J.Levi, J.O'Gorman, S.J.Pearton, C.R.Abernathy, and V.Swaminathan, "Grinsch GaAs/AlGaAs laser structures grown by OMVPE using a novel aluminium source," *Electron.lett.* vol.26, pp1762-1763, 1990

[9] D.S.Chemla, and D.A.B.Miller, "Room temperature excitonic nonlinear-optical effects in semiconductor quantum well structures," *J.Opt.Soc.Am.B*, vol.2, pp1155-1173, 1985.

[10] H.A.Haus, and Y.Silverberg, "Theory of mode locking a laser diode with a multiple-quantum-well structure," *J.Opt.Soc.Am.B*, vol.2, pp1237-1243, 1985.

[11] M.Asada, chapter 2 in *Quantum well lasers*, P.S.Zory (Ed.), Acedemic Press, 1993

[12] D.D.Dow, and D.Redfield, "Toward a unified theory of Urbach's Rule and exponential absorption edges," *Phys.Rev.B*, vol.5, pp594-610, 1972.

Chapter 8- Long wavelength CPM lasers.

For use in long haul lightwave communications systems, semiconductor lasers are required to operate in the low loss silica fibre window at around 1.55 μm wavelength. A material system which achieves this wavelength is InP/InGaAs/InGaAsP, and the vast majority of previous work on monolithic mode-locking in semiconductor lasers has been based on this phosphide quaternary system[1]. This chapter will describe the realisation of CPM and MCPM ridge waveguide lasers in this long wavelength material.

Two different types of epitaxial structures were used to fabricate the lasers: one with five InGaAs quantum wells which are lattice-matched to InGaAsP barriers, and the other a strained layer structure containing two InGaAs quantum wells. The former structure is based on the standard 1.55 μm MQW design, used previously for long wavelength lasers in the Department of Electronics and Electrical Engineering at the University of Glasgow (McKee *et al*[2,3]). The strained layer structure used in this project was a modification of this, adapted to provide low threshold currents for long cavity length InP/InGaAsP ring lasers[4]. All the wafers used for the long wavelength laser fabrication in this project were MOVPE grown by Chris Button at the central EPSRC III-V semiconductor facility at the University of Sheffield.

Details are given of the two etching methods, wet chemical etching and dry reactive ion etching, which were used in the crucial first stage of fabricating the low damage ridge waveguides for the mode-locked laser structures. The problems encountered in using these two methods, along with their relative advantages and disadvantages are discussed. Finally, spectral results of operating CPM and, for the first time in long wavelength material, MCPM lasers are presented and analysed.

8.1- Long wavelength laser material.

8.1.1- Standard (lattice-matched) wafer structure (MR763).

The design of the standard five QW lattice-matched laser structure used (MR 763) is shown in figure 8.1. The epitaxial layers were grown on an n+ Si doped InP substrate. From the substrate up, the layer specifications are as follows: a 2 μm InP lower n-cladding layer, Si doped a $5x10^{17}$ cm^{-3} ; an unintentionally doped 1 μm waveguide core; a 1.4 μm InP p-upper cladding layer, with the first 200 nm left undoped to reduce the probability of impurities from the cladding diffusing into the active region, and the remaining 1200 nm doped with Zn to a level of 7 $x10^{17}$ cm^{-3} ; a 50 nm InGaAsP layer (bandgap with a wavelength value, λ_g=1.18 μm), Zn-doped at $2x10^{18}$ cm^{-3} ; and finally, a p+ InGaAs contact layer, Zn-doped at a concentration of at least $5x10^{18}$ cm^{-3}. The

50nm InGaAsP layer was included in order to the reduce the effect of the potential step between the InGaAs and InP layers, thus decreasing the series resistance and operational voltage. An important factor in this design is the lowering of the doping level in the p-cladding, from the standard value used (in the order of 10^{18} cm^{-3}) to ~10^{17} cm^{-3}. The purpose of this is to increase the isolation between the absorber and gain sections of the CPM lasers that are ultimately fabricated.

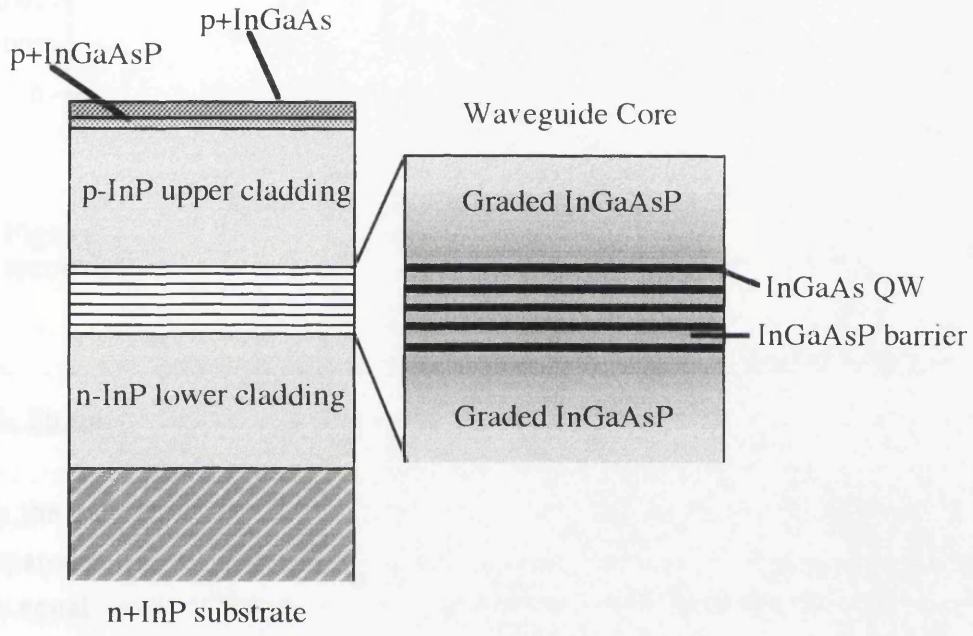

Figure 8.1: MR763 InGaAsP/InP 5 QW wafer schematic diagram.

The active layers contained five 55 Å $In_{0.53}Ga_{0.47}As$ quantum wells with six 120 Å InGaAsP (λ_g=1.26 μm) barriers. Surrounding the wells in both directions is a step graded index region, consisting of a 50 nm InGaAsP (λ_g=1.18 μm) layer and an 80 nm InGaAsP (λ_g=1.08 μm) layer. All the layers used in the structure were lattice matched to InP.

Broad area oxide stripe lasers were fabricated from MR 763 in order to characterise its optical properties (see Section 3.1.2). The values of internal efficiency, internal losses, and threshold current density at infinite length were measured at 70%, 50.8 cm^{-1}, and 485 Acm^{-2} respectively. Figure 8.2(a) shows typical lxi curves for various laser lengths and figure 8.2(b) shows the lasing spectrum of a 600 μm device. Even though the quantum efficiency is reasonable, the high internal loss leads to the high values of current densities shown in figure 8.2(a).

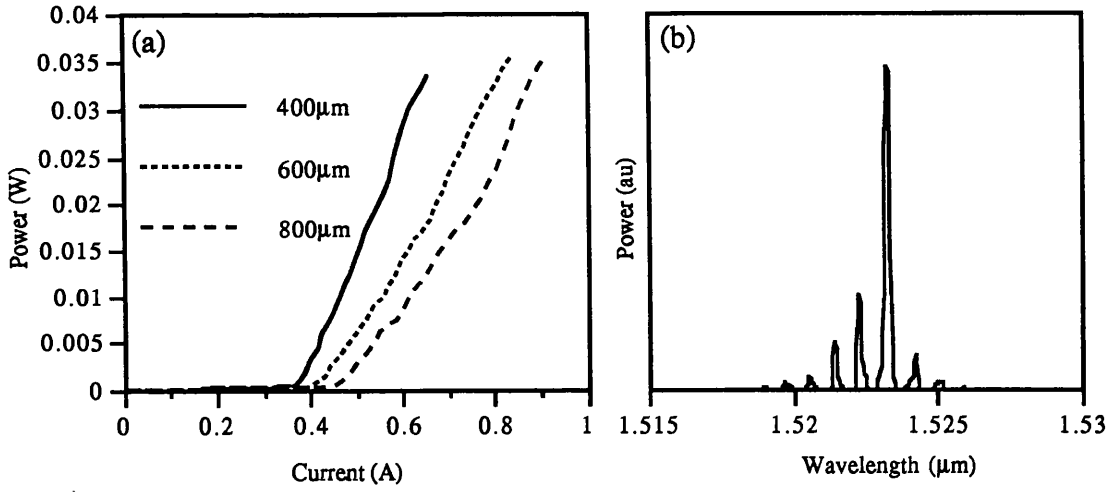

Figure 8.2: (a) 75 μm oxide stripe lasers fabricated from MR763. (b) Laser spectrum of 600 μm long device.

8.1.2- Strained layer wafer structure (MR396).

In the analysis of semiconductor optical gain in Chapter 2, it was found that the transparency condition (equation 2.16) requires the separation of the quasi-Fermi levels to be equal to the bandgap. With the hole effective mass being an order of magnitude higher than the electron effective mass in III-V semiconductors, the valence band density of states is far larger than in the conduction band. Therefore, it requires a higher level of carrier injection to promote the quasi-Fermi level into the valence band, than it does to obtain a degenerate electron population. Lattice mismatches between semiconductor heterointerfaces cause strain effects which can radically alter the band structure[5]. In certain circumstances, the applied strain can act to reduce the density of states in the valence band, and hence lower the carrier density required for threshold transparency. Introduced strain can either be *compressive* or *tensile* in nature, depending on whether the lattice constant of the epitaxial layer is greater or smaller than that of the substrate.

The structure of MR396 was identical to that of MR763 apart from the active layer composition, which contained two 120 Å $In_{.32}Ga_{.68}As$ quantum wells. A level of 32% indium in the wells corresponds to a tensile strain of 1.5% with the InGaAsP barrier (lattice matched to InP). Thijs *et al*[6] produced lasers with threshold current densities as low as 92 Acm^{-2}, in 1.5% tensile strain InGaAs single quantum well material. Using MR396 to fabricate 50 μm wide oxide stripe lasers, Krauss *et al*[4] were able to show a threshold current density at infinite length of 193 Acm^{-2}.

8.2- InP/InGaAsP RWG laser fabrication.

8.2.1-Wet etching method.

Using wet etching exclusively to fabricate ridges in long wavelength material is simple, causes low levels of damage, and avoids the potential difficulties associated with the standard methane/hydrogen dry etching of InP, such as deep damage to the QW layers and passivation due to hydrogen incorporation. However problems can arise in wet etching, due to the fact that etch rates and profiles can depend on the orientation of the masking material to a particular crystallographic plane. Wet etching rates can also be the same in all directions (isotropic), making it difficult to transfer patterns of small dimensions to the semiconductor surface. These features of wet etching render it impractical for use on complex structures that cut through several etch planes, such as ring lasers.

The simple straight RWG design of the CPM lasers used in this project is ideally suited to wet etching. It is important in RWG laser fabrication in InP that the sidewalls of the ridge are passivated, due to high levels of surface recombination. This is in contrast to the fabrication of RWG lasers in GaAs/AlGaAs (Chapters 4 &7) in which the current injection silica window can be significantly wider than the ridge. Passivation of the side walls requires the photolithographic definition and etching of the current injection window on top of the ridge, which in such small dimensions (~3 μm) can be a difficult and time consuming task. The wet etch process developed here also has an advantage of speed and ease of fabrication by using a photoresist ridge etch mask, which is not removed after etching, but remains on until after the SiO_2 deposition stage. It is then used to lift-off the silica from the top of the ridge, providing the laser structure with a self-aligned p-side contact window. This new self-aligned process is an extension of the one used by Cusumano *et al*[7] in dry etched RWG laser fabrication in GaAs/AlGaAs. As well as ease of fabrication, Krauss *et al*[8] showed that with the use of a polyamide mask self-aligned technique, efficiency improvements in GaAs/AlGaAs ring lasers could be observed.

Two particular wet etches were used in the fabrication of ridge waveguides in materials MR396 and MR763, and their constituents are as follows:

Etch.1: 40 Acetic acid: 20 Hydrochloric acid: 15 RO water: 3 Hydrogen peroxide.

The constituents of this etch are chosen to produce a constant etch rate through all three of the relevant compounds (InP, InGaAs, and InGaAsP) at a uniform rate. This was measured at 10 nm per second at 5°C.

Etch.2: 3 Orthophosphoric acid: 1 Hydrochloric acid.

Selective etch for InP. Etches at ~1μm a minute at room temperature and stops on InGaAs/InGaAsP.

Etch.1 is used to remove the InGaAs/InGaAsP contact layers, but as it is isotropic it produces undercutting when used with a waveguide mask. Etch.2 has a crystallographic etch rate dependence, but can provide a near vertical etch profile if ridges are aligned in the β-direction. When aligned in the α-direction, the etch profile is at 55° to the substrate. The long and short flats, provided as standard on the wafer substrates, correspond to the α $(01\bar{1})$ and β (011) directions respectively. Etch.2 is used to etch the waveguide in the upper p-doped InP cladding, and as it is selective, it stops on the InGaAsP layer at the start of the waveguide core.

The complete wet etch self-aligned laser fabrication process (shown schematically in figure 8.3) is given below:

1:-Clean sample using optoclear/acetone/methanol/RO water in ultrasonic bath.
2:-Bake sample for 15 minutes at 90°C to ensure surface is dry.
3:-Spin on primer at 4000 rpm for 30 seconds.
4:-Spin on S1818 photoresist at 4000 rpm for 30seconds. Bake for 30 minutes at 90°C.
5:-Expose lightfield, 4 μm wide, waveguide mask (waveguides aligned along β-flat).
6:-Develop in 50/50 developer/RO water for 1 minute.
7:-Bake for 1 hour 30 minutes at 120°C.
8:-Etch sample in etch.1 for 25seconds at 5°C.
9:-Etch sample in etch.2 for 2 minutes (or until etch stop is reached).
10:-Deposit 200 nm of silica by RF sputtering.
11:-Lift off silica on top of ridge using acetone in an ultrasonic bath.
12:-Prepare for p-contact: deoxidise in 1HCL/4ROwater, then bake for 20 minutes in nitrogen oven.
13:- Evaporate p-contact: 20 nm Ti, 20 nm Pd, 140 nm Au using Plassys metals evaporator.
14:-Evaporate further 20 nm Ti and 140 nm Au, while rocking sample at 45°.
15:-Thin substrate to 150 μm using 9 μm alumina.
16:-Evaporate n-contact: 14 nm Au, 14 nm Ge, 14 nm Au, 10 nm Ni, 200 nm Au.
17:-Anneal contacts in RTA at 360°C for 1 minute.

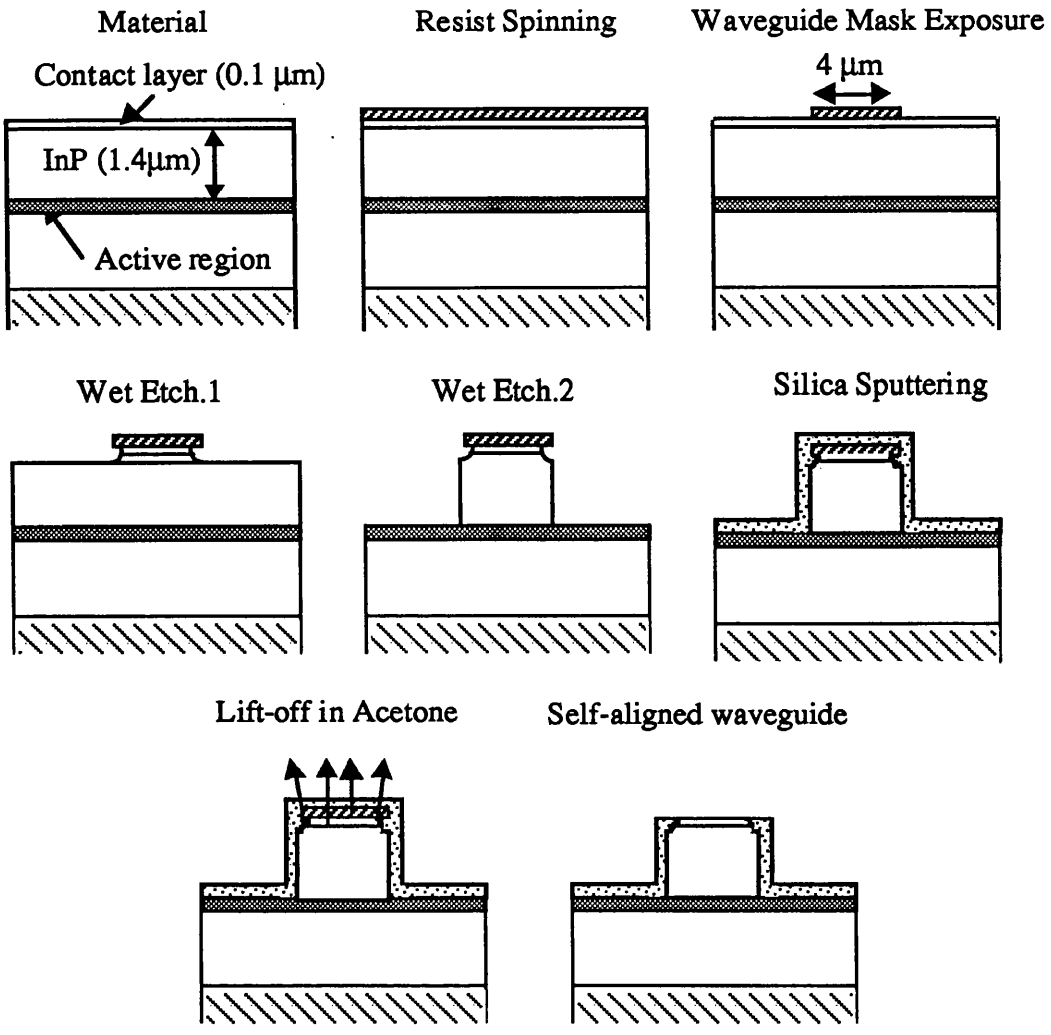

Figure 8.3: Self-aligned wet etch process for long wavelength RWG laser Fabrication.

The resist mask is prepared by S1818 photoresist which, after spinning and baking, gives a thickness of 1.8μm. Without the post development bake (stage 7), the resist does not stand up well to the wet etch. Etch.1 is used for 25 seconds to etch through the contact layers plus 100nm of InP. This overetching into the InP tends to give a smoother surface profile after etch.2. The slight undercut and near vertical walls are displayed in the SEM photograph (figure 8.4(a)) of a wet-etched ridge plus mask. Several different silica deposition techniques were investigated for the passivation process (stage 10). PECVD silica is deposited at too high a temperature (>300°C) to allow subsequent lift-off, and E-beam evaporated silica, while at a much lower temperature, could not provide adequate sidewall coverage. Using RF sputtering with a water-cooled sample mount resulted in both satisfactory passivation of the ridge walls, and a low enough deposition temperature to allow lift-off to take place. Figure 8.4(b) shows an SEM photograph of the ridge after silica deposition and lift-off. Note that the silica has covered the ridge walls even over the undercut region that was overhung with resist during the sputtering.

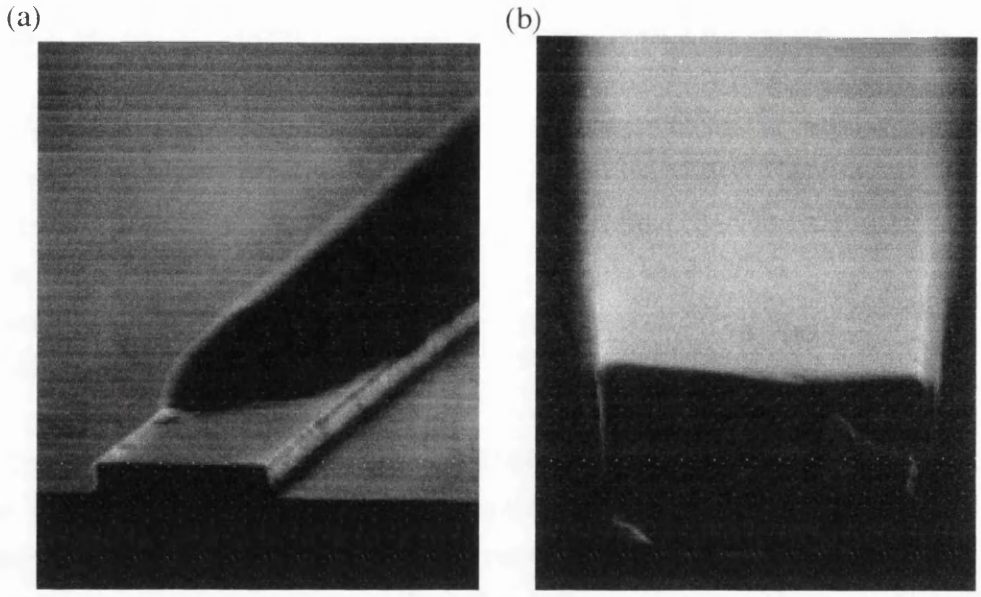

Figure 8.4: SEM photographs of wet etched ridge (a) before silica sputtering, (b) after silica lift-off.

8.2.2-Dry etching method.

To fabricate complex ridge waveguide structures such as rings, T-junctions or multi-mode interference couplers, etc., it is necessary to use anisotropic dry etching, rather than wet etching, in order to produce a uniform etch profile along the entire structure. Reactive ion etching (RIE) of indium containing compounds in halogen based plasmas (e.g. $SiCl_4$) is less successful than in Ga materials, with problems such as low etch rates and poor control of the etch profile. This is due to the indium-halogen compounds formed in these reactions being generally less volatile than the complementary gallium-halogen etch products. Etching of InP using plasmas containing mixtures of methane and hydrogen (CH_4/H_2), has been shown to produce particularly anisotropic features[9,10] by the removal of the In and P as highly volatile organometallic compounds (opposite of MOVPE growth). Although able to produce good etch profiles, CH_4/H_2 etching of InP suffers from the three potential drawbacks: QW damage due to ion induced defects, degradation of electrical properties from hydrogen passivation of dopants, and the formation of a polymer layer arising from the interaction of methyl groups that cannot react with the surface.

The machine used for etching in the University of Glasgow dry etching facility is the Electro-Tech 340. The ET340 allows the control of gas flow rates, power, pressure, and the DC bias which accelerates the ions into the sample substrate. These parameters can

be optimised to produce the highest level of anisotropy with the fastest etch rate. The standard optimised process used in the department to etch InP on the ET340 is:

CH_4/H_2 etch:
Power=100 W
Gas flow: CH_4=3.6 sccm, H_2=26.4 sccm
Table temp: 30°C
Pressure: 14 mtorr
DC bias: -850V

Oxygen clean (to remove polymer):
Power= 50W
Gas flow: O_2=30 sccm
Table temp: 30°C
Pressure: 50 mtorr
DC bias: -850V

The above process was used to etch RWG lasers in MR396 using a SiO_2 etch mask. The etch was performed for twelve minutes, which led to a depth of 0.98 μm. A five minute post etch O_2 clean was used to remove any polymer layer. After the etch the surface morphology was poor. To remove this surface roughness, wet etch.2 from section 8.2.1 was used to etch down to the waveguide core. After silica isolation, contact window etching, and contact deposition and annealing, the devices failed to lase. Many of the devices also had poor contacts , displaying the effects of hydrogen passivation. Figure 8.5 (a) shows the forward bias diode characteristic of a 75 μm wide oxide stripe laser fabricated from MR396, with a low slope resistance 28 Ω and a turn on voltage typical of InP based devices of around 0.6 V. By comparison the forward bias diode characteristic of the dry etched RWG laser has an extremely high resistance (bold line in figure 8.5(b)). Also at a bias of 2.5 V, the current suddenly increases, causing catastrophic damage to the diode. All subsequent measurements of the diode characteristic produce an unrectified VxI plot (thin line in figure 8.5(b)). This can be explained by hydrogen incorporation during the dry etch passivating the contact layer and creating a dielectric. At sufficient fields the dielectric microscopically breaks down, causing large currents to flow through small areas that subsequently destroy the diode.

It is a well known phenomena that during RIE of both InP[11] and InGaAs[12], hydrogen incorporation causes the deactivation of Zn acceptors leading to a high contact resistance and non-ohmic IxV characteristics. These studies also demonstrated that post etch annealing was an effective method of redistributing the hydrogen through the structure, allowing surface hole concentrations to recover to their pre-etch levels. Energetic bombardment of the sample surface during RIE can introduce lattice disorders. Studies have shown that through deep ion channelling, these disorders take the form of non-radiative recombination centres and severely reduce the photoluminescence from quantum wells hundreds of nm below the etch stop[13,14]. It is also noted that RIE damage in general increases with the magnitude of the driving DC bias. Again, through heat treatment of the surface after the etch, the photoluminescence

signal from the quantum wells can be recovered. In this department Dr B.S.Ooi and B.C.Qui demonstrated that by reducing etch bias and by post etch annealing, QW damage due to CH_4/H_2 could be removed[15].

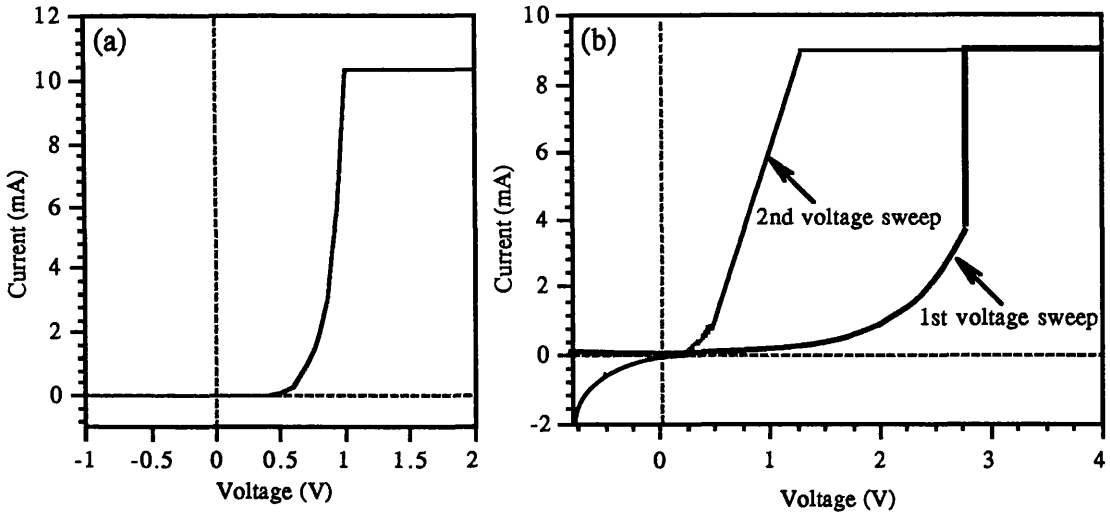

Figure 8.5: Comparison of forward biased diode characteristic in material MR396 fron (a) 75 μm oxide stripe laser, and (b) Methane/hydrogen dry etched laser.

With the assistance of Dr S.Hicks, Dr B.S.Ooi and B.C.Qui, the following low damage dry etch process was developed for the etching of InP/InGaAs/InGaAsP structures:

$CH_4/H_2/O_2$ low damage etch:

Power=50 W

Gas flow: (meter reading %): CH_4=72, H_2=100, O_2=6

Corrected flow (sccm): CH_4=14.4 , H_2=100, O_2=0.3

Table temp: 30°C

Pressure: 50 mtorr

DC bias: -500V

Oxygen was added to the gases at a low flow rate during this etch to remove the polymer as it formed. This has two beneficial effects: hydrogen incorporated into the structure via the polymer is reduced, and the need for potentially damaging post-etch Oxygen clean is removed. To recover etch damage, and to remove any hydrogen passivation, the samples were post etch annealed at 400°C for 1 minute. For this etch PECVD SiO_2 was used as the masking material, as resist or nichrome did not stand up well. The SiO_2 mask is produced by photolithography and C_2F_6 etching in a BP80 dry etch machine.

The complete dry etch process is given below for the fabrication of RWG lasers in MR396 and MR763 (shown schematically in figure 8.6):

1:-Clean sample using optoclear/acetone/methanol/RO water in ultrasonic bath.
2:-Deposit 200 nm PECVD silica.
3:-Spin on primer at 4000 rpm for 30 seconds.
4:-Spin on S1805 photoresist at 4000 rpm for 30 seconds. Bake for 30 minutes at 90°C.
5:-Expose 4 μm lightfield waveguide mask (waveguides aligned along β-flat).
6:-Develop in 50/50 developer/RO water for 1 minute.
7:-Bake for 1 hour at 120°C.
8:-Etch sample in BP80 to remove 200 nm silica.
10:-Remove resist mask with acetone in ultrasonic bath.
11:-Low damage $CH_4/H_2/O_2$ dry etch for 21 minutes (etch depth 1.3 μm).
12:-Anneal in RTA at 400°C for 1minute.
13:-Remove 200nm silica mask in buffered HF for 1 minute.
14:-Deposit 200nm PECVD silica.
15:-Spin on S1805 photoresist at 4000rpm for 30secs Bake for 15 mins s at 90°C.
16:-Align and expose 2μm darkfield contact window mask.
17:-Develop in 50/50 developer/RO water for 1 minute.
18:-Remove 200nm silica from top of ridge in buffered HF for 14 seconds.
19:-Remove resist mask in acetone
20:-Prepare for p-contact: deoxidise in 1HCL/4ROwater, bake in nitrogen oven for 20 minutes.
21:-Evaporate p-contact: 20 nm Ti, 20 nm Pd, 140 nm Au using Plassys metals evaporator.
22:-Evaporate further 20 nm Ti and 140 nm Au while rocking sample at 45°.
23:-Thin substrate to 150 μm using 9 μm alumina.
24:-Evaporate n-contact: 14 nm Au, 14 nm Ge, 14 nm Au, 10 nm Ni, 200 nm Au.
25:- Anneal contacts in RTA at 360°C for 1minute.

Figure 8.7 shows an SEM photograph of a dry etched RWG after stage 18. Note that the etched current injection window is not centred on the top of the waveguide. It is often difficult to produce a precise alignment for such small geometries with UV photolithography.

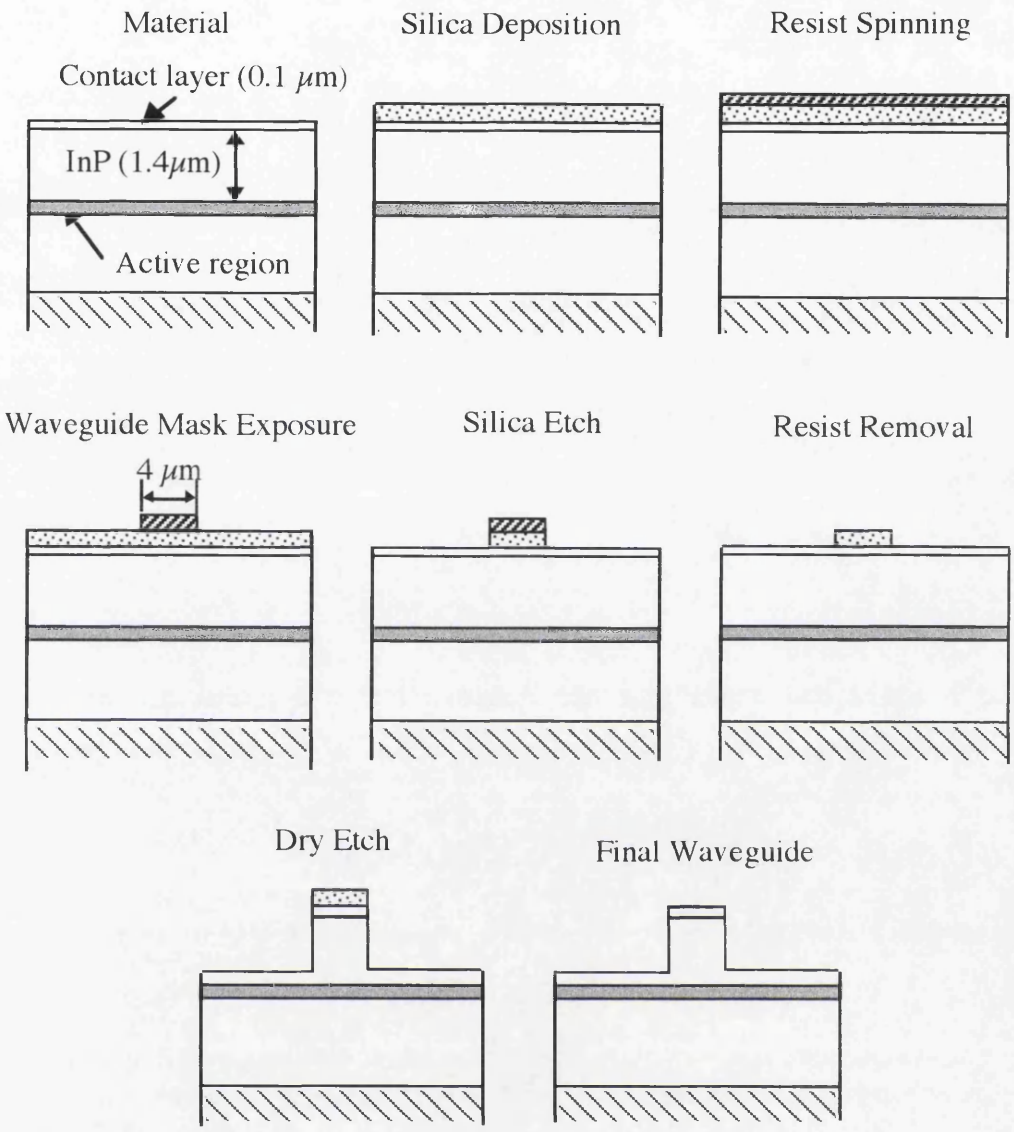

Figure 8.6: Dry etch fabrication process for long wavelength RWG lasers.

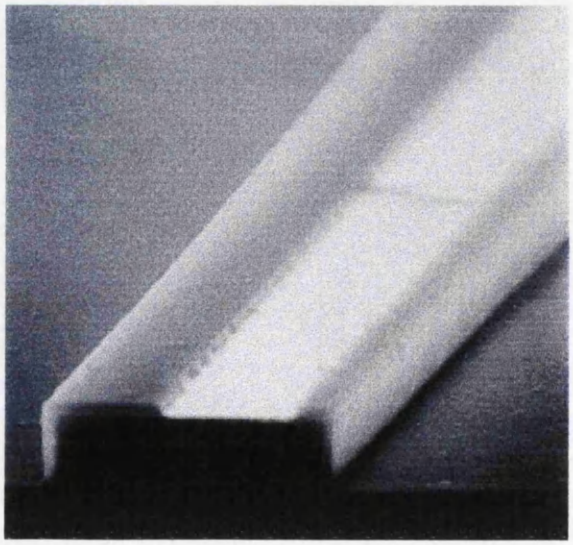

Figure 8.7: SEM photograph of dry etched waveguide after contact window etching.

8.2.3- Dry/Wet etch RWG laser comparison.

To compare the two etch processes, RWG lasers were fabricated using both the strained layer double QW material MR396 and the lattice matched 5 QW MR763 material. The devices were cleaved and tested using the pulsed current laser test rig described in Chapter 4.

Figure 8.8 shows the two best MR763 600 μm long RWG lasers fabricated by each of the processes described above. As can be seen, the wet etched laser has a lower threshold current (36 mA) than the dry etched laser (42 mA). There is also a slight improvement in the slope efficiency in the wet etched case. This result is mirrored in RWG lasers fabricated from MR396 (figure 8.9), where the wet etched laser yields a threshold of 22 mA, and the dry etch 30 mA. The forward bias diode characteristics of the dry etched and wet etched lasers were almost identical, implying that hydrogen passivation effects were either small in the improved dry etch, or were adequately removed by the post etch annealing.

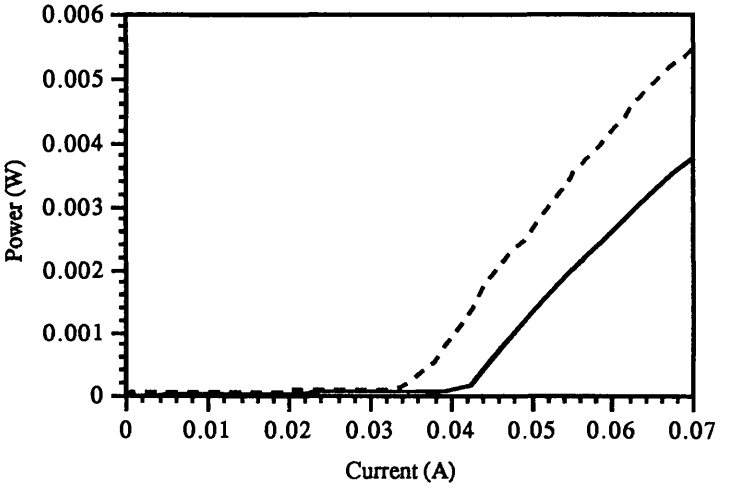

Figure 8.8: Comparison of pulsed current lxi curves from 600 μm RWG lasers fabricated in MR763 via dry etching (solid line), and wet etching (dashed line).

As there is only a slight difference between the performance of the wet etched and dry etched devices, this shows that the dry etch process developed causes low damage and can produce RWG lasers in indium containing semiconductor laser structures comparable to the ultra low damage wet etch. More improvements could be made to the dry etch by further reducing bias levels. Also the consequences of any asymmetry in the current injection window of the dry etched lasers are unknown and could prove to have detrimental effects on their performance.

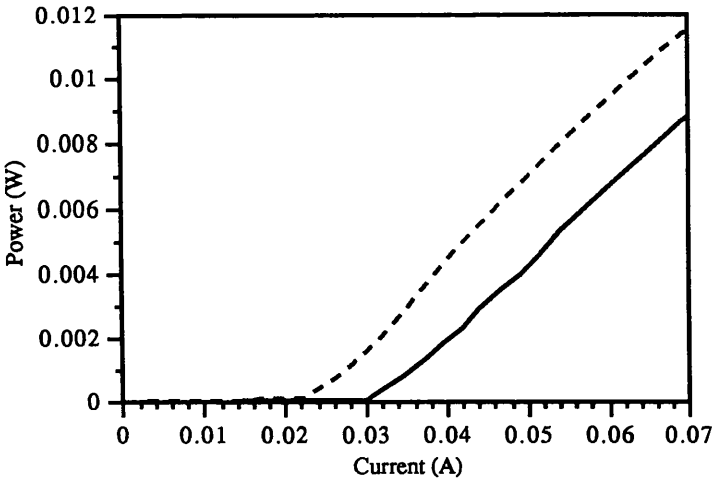

Figure 8.9: Comparison of pulsed current lxi curves from 600 μm RWG lasers fabricated in MR396 via dry etching (solid line), and wet etching (dashed line).

8.3- CPM laser results.

Using the self aligned wet etch technique detailed in section 8.2.1, 600 μm long CPM lasers were fabricated in MR763. The only addition to the stated process was the application of a lift-off mask to define the two-section CPM laser before the p-type evaporation, and the performance of a final etch to isolate the two sections. For this the isotropic wet etch.1 was used for 20 s. After cleaving, the devices were placed in laser clips and tested using the pulsed current test rig, with the reverse bias applied to the saturable absorber via a needle probe. Figure 8.10(a) shows the lxi curves at various absorber bias levels from a 600 μm long device. The cavity mode separation from the lasing spectra, under full forward bias conditions (figure 8.10(b)) for the same device, is 0.56 nm. On application of reverse bias to the absorber, the mode-spacing doubles consistent with CPM operation. The spectrum in figure 8(c) of the device biased at I_g=53 mA and V_a=-1V, gives a $\Delta\lambda_{CPM}$= 1.12 nm corresponding to a repetition frequency of 145 GHz. CPM spectra were observed from this device at reverse bias levels ranging from -1 V to -3.5 V.

The lasing spectra from a second device is shown in figure 8.11. CPM action was observed for this device for a bias range of -1.4V to 4V. In some of the spectra from this device, and in the CPM spectrum displayed in figure 8.10(c), there is an element of asymmetry, with the peak of the gain spectrum appearing on the long wavelength side. From the CPM spectra of figure 8.11 it can clearly be seen that this asymmetry becomes increasingly prominent at higher injection currents. Other groups working on CPM lasers at long wavelengths have reported similar phenomena[16]. Possible explanations include the presence of some self-pulsation envelope to the CPM pulse train, and the

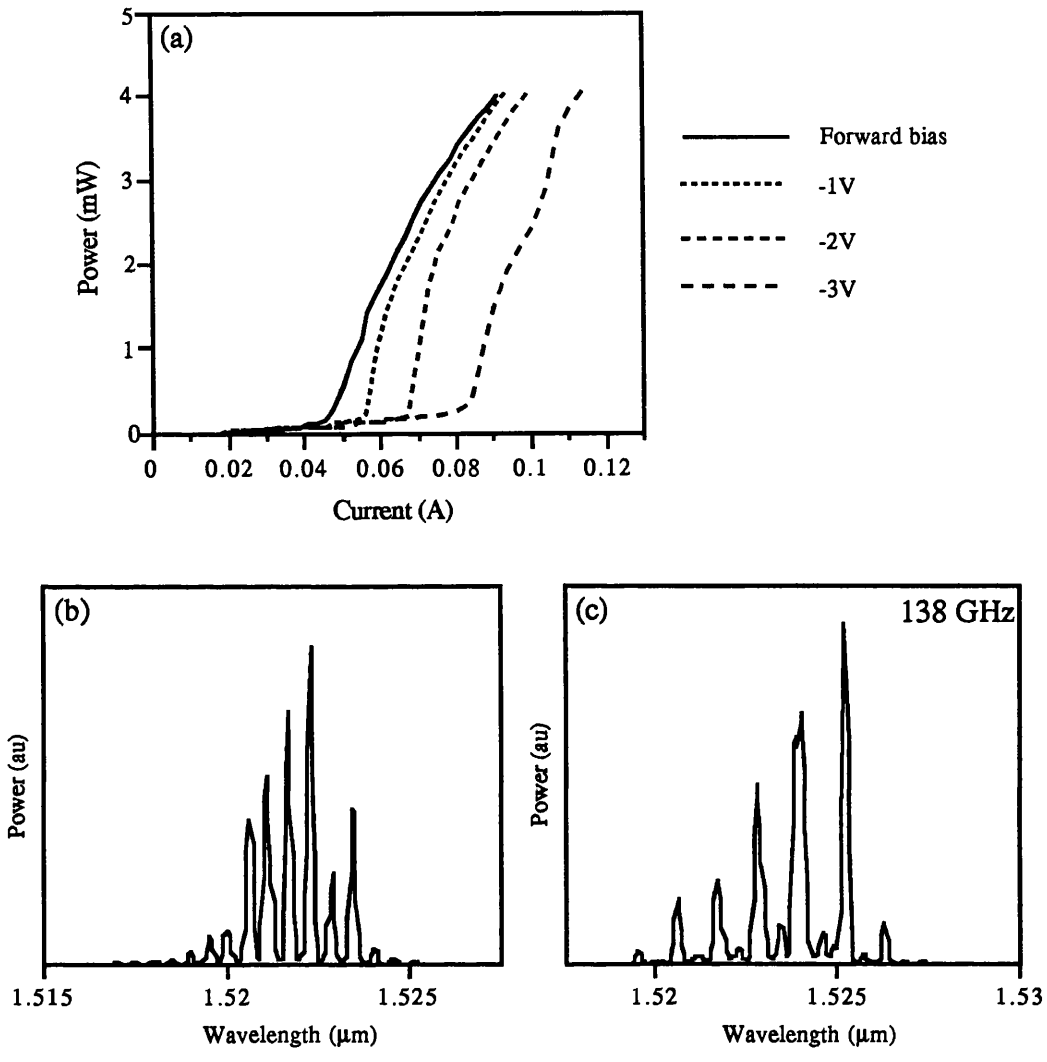

Figure 8.10: Wet etched 600 μm CPM laser from MR763 under pulsed current testing: (a) lxi curves for various reverse bias levels, (b) spectrum of fully forward biased device at 53 mA, (c) CPM spectrum of laser operated at 53 mA with -1 V absorber bias.

effect of self-phase modulation as carrier levels increase. Such effects could only be observed through time domain measurements of the CPM pulse trains. Thus intensity autocorrelation measurements would be required to ascertain the range of forward and reverse bias conditions that would lead to clean transform-limited pulse output, self-pulsation modulated mode-locking, and chirped pulse output. The asymmetry displayed here in some of the spectra from the long wavelength lasers, is in contrast to the highly symmetric spectra that were consistently observed from the CPM lasers fabricated from GaAs/AlGaAs QW material, reported in Chapters 4, 5 and 7 of this thesis.

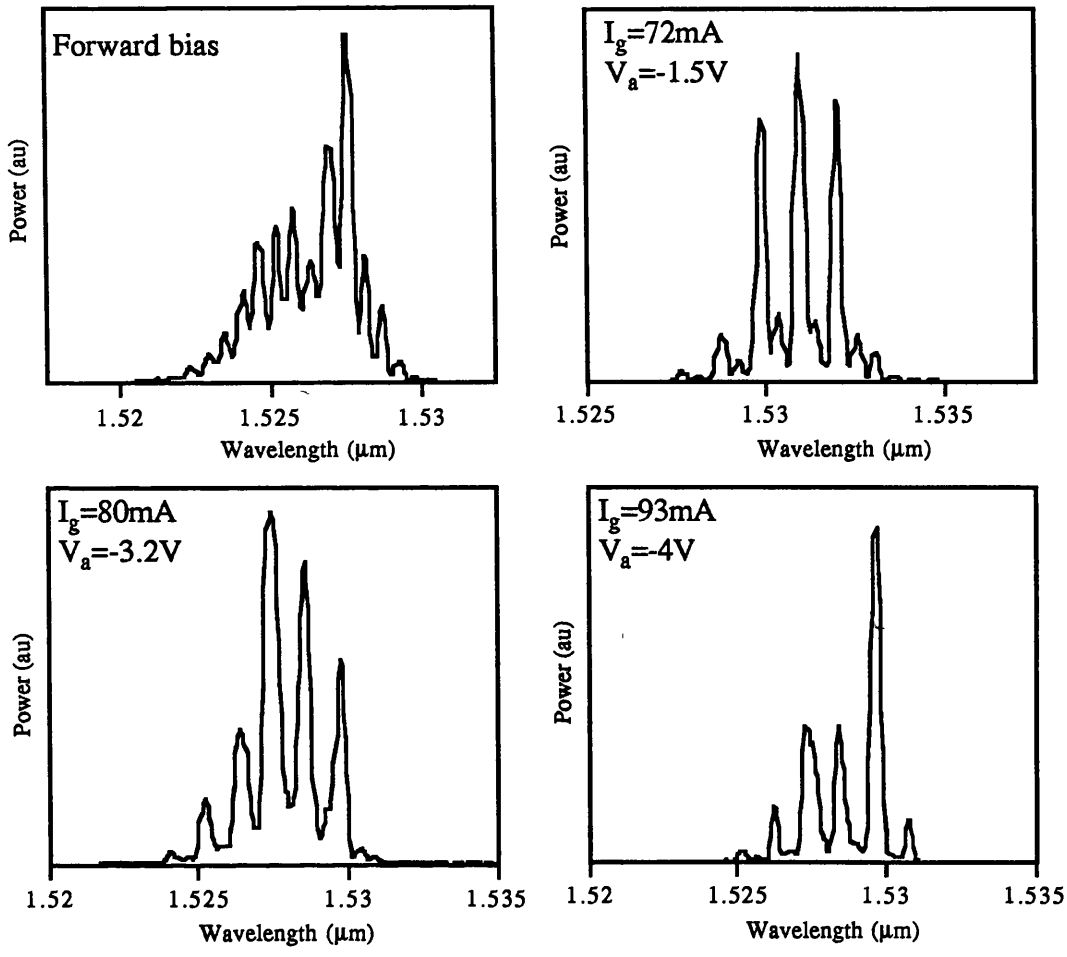

Figure 8.11: Spectra from a 600 μm MR763 laser (wet etched), showing CPM operation over a typical range of bias conditions.

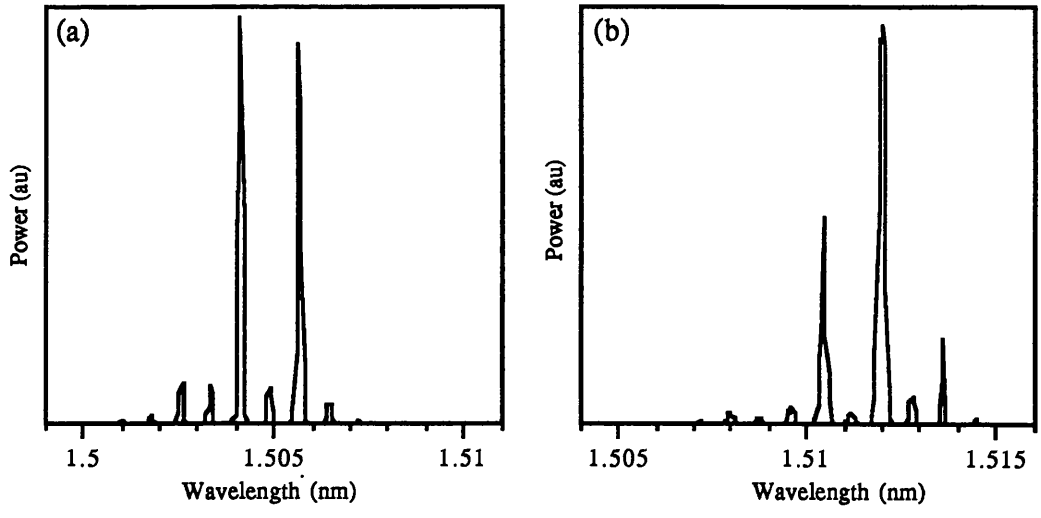

Figure 8.12: Pulsed current CPM spectra of (a) 400 μm MR396 CPM laser (wet etched), and (b) 400 μm MR763 T-CPM laser (dry etched).

CPM spectra were also observed from lasers fabricated in the strained layer MR396 material. The spectra of a 400 μm laser wet etched from MR396 is shown in figure 8.12(a) operating in CPM mode. Dry etching was also successful in producing CPM lasers, as illustrated in figure 8.12(b) with the CPM spectra of a 400 μm dry etched MR763 T-CPM device. The repetition rate of these devices calculated from the mode-separation is approximately 197 GHz.

A 400 μm CPM laser from MR396 was mounted, bonded and operated with a CW current supply. The p-contact used for the long wavelength lasers is Ti/Pd/Au. NiCr is not used here as the nickel diffuses quickly in the InP, and can destroy luminescence from the quantum wells with prolonged use. Ti/Au contacts are highly rectifying, and require annealing to allow adequate current injection. In order to maintain the adhesion to the silica after the annealing, which is necessary for successful wire bonding (see Chapter 4), Pd is added to the recipe to stop the Au from diffusing into the silica. The lxi curve recorded with a reverse bias of -1V on the absorber displayed a large level of hysterisis (figure 8.13(a)), indicating the presence of saturable absorption. The corresponding optical spectrum taken at I_g= 50 mA and V_a=-1V, shows that the device acts as a CPM laser, again with an asymmetric gain spectrum (figure 8.13(b)).

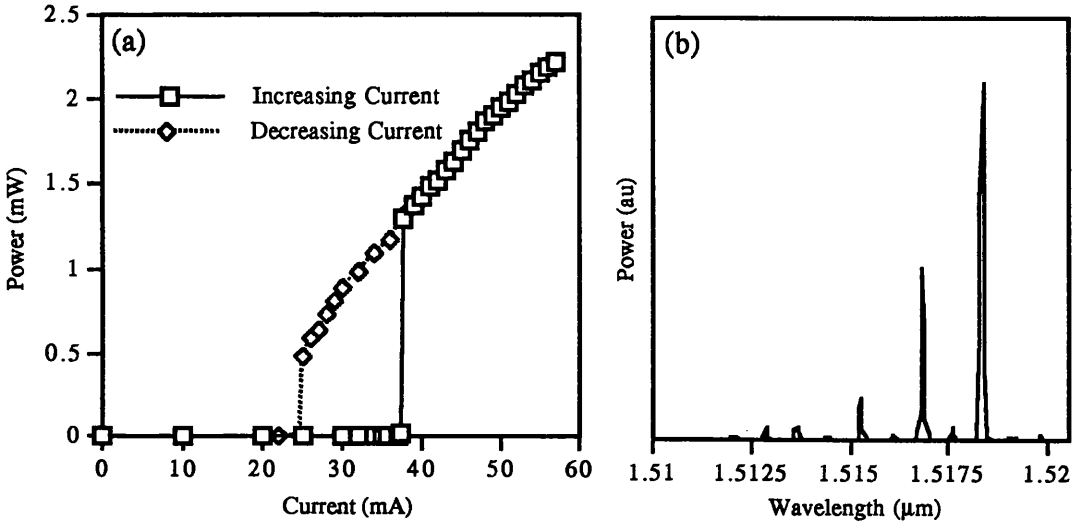

Figure 8.13: (a) Hysteresis in the lxi curve of a 400 μm MR396 laser operating under CW current conditions and -1V reverse bias. (b) Corresponding CPM spectrum from device operating at 50 mA.

8.4- MCPM laser results.

To produce CPM lasers at a wavelength closer to the optimum 1.55 μm, a further strained layer wafer was grown by Dr C Button at Sheffield University. The design was almost identical to that of the 1.5% tensile stained layer MR396, but with the well width increased from 120Å to 130Å. This was an estimate of the required well width to produce output of 1.55μm. The layer specifications are given below:

MR807 double QW stained layer wafer

1000Å	p+ InGaAs	5e18cm^{-3} Zn
500Å	p+ Q1.18	2e18cm^{-3} Zn
12000Å	p - InP	9e17cm^{-3} Zn
2000Å	u - InP	
800Å	u - Q1.05	
500Å	u - Q1.18	
1000Å	u - Q1.26	
130Å	u - $In_{.32}Ga_{.68}As$	
100Å	u - Q1.26	
130Å	u - $In_{.32}Ga_{.68}As$	
1000Å	u - Q1.26	
500Å	u - Q1.18	
800Å	n - Q1.05	6e17cm^{-3} Si
10000Å	n+ InP	1e18cm^{-3} Si

n+ InP Substrate

With this wafer, 600 μm cavity length MCPM lasers (see section 7.1) were fabricated using the self-aligned wet etch process. A photograph of a completed device is given in figure 8.14. This device was mounted, bonded and tested under CW conditions. The lxi curves in figure 8.15 show the effect of the bias on all three absorbers. As expected, the increase in the threshold current due to three absorbers being reverse biased is considerably greater than that due to a single absorber in a CPM laser (see figure 8.10).

The device was operated under two-pulse MCPM and four-pulse MCPM conditions. These modes of operation are shown from the lasing spectra of figure 8.16, with the cavity mode spacing doubling from 0.585 nm to 1.17 nm when the central absorber alone was reverse biased, and quadrupling to 2.34 nm when all three absorbers were reverse biased. This is the first (reported) demonstration of MCPM action in a long wavelength semiconductor laser. From the spectra, the laser produces harmonic mode-locking at repetition rates of 150 GHz and 300 GHz, depending on the bias condition.

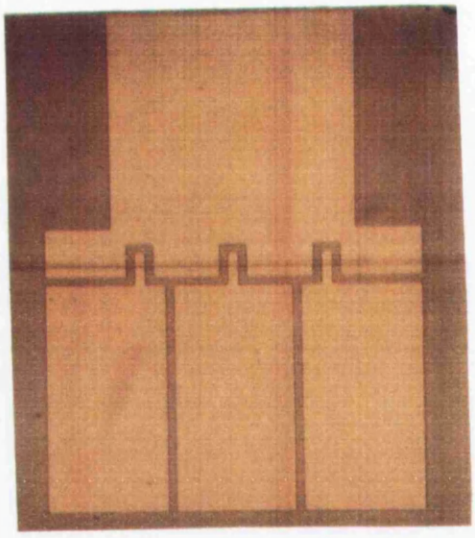

Figure 8.14: Photograph of completed MCPM laser in MR807.

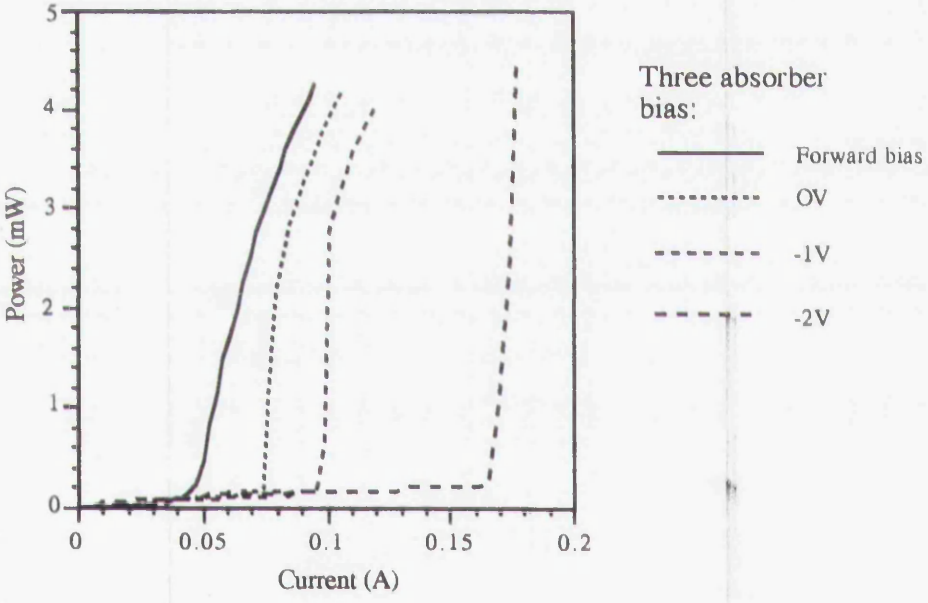

Figure 8.15: lxi curves of a MR897 600μm MCPM laser under various reverse bias conditions.

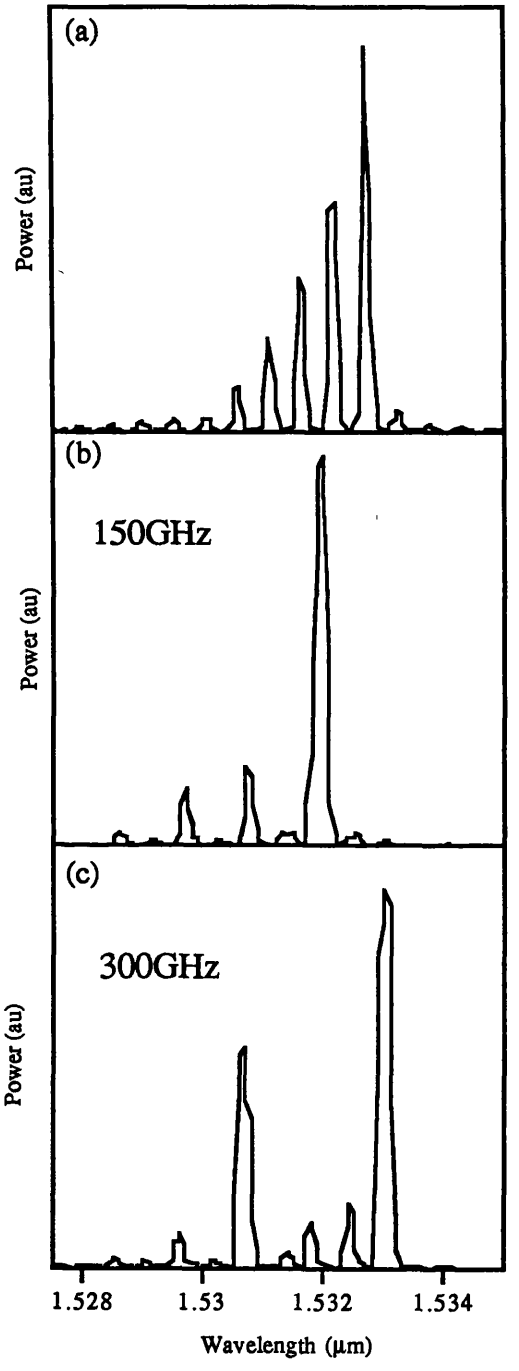

Figure 8.16: 600 μm MCPM laser, fabricated from MR807, operating (a) fully forward biased, (b) two-pulse MCPM at 150 GHz, and (c) four-pulse MCPM at 300 GHz.

8.5- Conclusions.

This chapter has described the successful demonstration of CPM and MCPM ridge waveguide lasers in the InP/InGaAs/InGaAsP material system. The frequency domain measurements presented here are the first reported evidence (to the author's knowledge) of MCPM action in this material system.

The occurrence of deep damage from ions impacting on the semiconductor substrate, along with the associated degradation in the optical properties of the active region, has been illustrated by the failure to fabricate ridge waveguide lasers from methane/hydrogen dry etching. An exclusively wet etch fabrication process, with comparatively little damage is extremely simple, fast, and successful. However, it has been shown that by careful consideration of the harmful properties of methane/hydrogen etching of semiconductors containing indium, and by taking the appropriate countermeasures, dry etching is as viable a process as wet etching to produce low damage ridge waveguide lasers. Using both wet and dry etch techniques, CPM lasers have been fabricated from lattice matched and tensile strained MOVPE grown QW structures.

To corroborate and expand on the results presented here, time domain autocorrelations are required. Due to the constraints of time, this could not be completed as part of the work of this project.

Chapter 8: References.

[1]D.J.Deickson, R.J.Helkey, A.Mar, J.R.Karin, J.G.Wasserbauer, and J.E.Bowers ," Short pulse generation using multisegment mode-locked semiconductor lasers," *IEEE J.Quantum.Electron.*, vol.28, pp.2186-2201, 1992.

[2]A.McKee, C.J.McLean, G.Lullo, A.C.Bryce, R.M.De la Rue, J.H.Marsh, and C.C.Button, "Monolithic integration in InGaAs-InGaAsP multiple-quantum-well structures using laser intermixing," *IEEE J.Quantum.Electron.* vol.33, pp45-55, 1997.

[3]A.McKee, Ph.D Thesis, University of Glasgow, 1996.

[4]T.F.Krauss, H.Pottinger, A.C.Bryce, J.H.Marsh, R.M.De La Rue, C.C.Button and J.S.Roberts, "Large diameter semiconductor ring lasers in tensile strained InP/InGaAsP material", *Integrated Photonics Research (IPR) Conference*, paper IWF3-1, pp520-523, Boston, April/May 1996.

[5]J.J.Coleman, chapter 8 in *Quantum Well Lasers*, P.S.Zory (Ed.), Acedemic Press, 1993.

[6]P.J.A.Thijs, J.J.M.Binsma, L.F.Tiemeijer, and T.van Dongen, "Submilliamp threshold current (0.62mA at 0° C) and high output power (220mW) 1.5μm tensile strained InGaAs single quantum well lasers", *Electron. Lett.*, 28, pp829-830, 1992.

[7]P.Cusumano, J.H.Marsh, M.J.Rose, and J.S.Roberts, "High-quality extended cavity ridge lasers fabricated by impurity-free vacancy diffusion with a novel masking technique," *IEEE Photon.Tech.Lett.*, accepted for publication March 1997.

[8]T.F.Krauss, R.M.DeLaRue, P.J.Laybourn, B.Vögele, and C.R.Stanley, "Efficient semiconductor ring lasers made by a simple self-alighned fabrication process", *IEEE.J.Sel.Topic.Quantum.Electron.*, vol.1, pp757-761, 1995.

[9]I.Adesia, K.Nuuila, E.Andideh, J.Hughes, C.Caneau, R.Bhat, and R.Holmstrom, "Nonostructure fabrication in InP and related compounds," *J.Vac.Sci.Technol.B*, vol.8, pp1357-1360, 1990.

[10]J.W.McNabb, H.G.Craighead, H.Temkin, and R.A.Logan, "Anisotropic reactive ion etching of InP in methane hydrogen based plasmas," *J.Vac.Sci.Technol.B*, vol.9, pp3535-3537, 1991.

[11]T.R.Hayes, W.C.Dautermont-Smith, H.S.Luftman, and J.W.Lee, "Passivation of acceptors on InP resulting from CH4/H2 reactive ion etching," *Appl.Phys.Lett.*, vol.55, pp56-58, 1989.

[12]M.Moehrle, "Hydrogen passivation of Zn acceptors on InGaAs during reactive ion etching," *Appl.Phys.Lett.*, vol.56, pp542-544, 1990.

[13]D.G.Yu, B.P.Keller, A.L.Holmes,Jr, E.L.Hu, and S.P.DenBaars, "Analysis of InP etched surfaces using metalorganic chemical vapour deposition regrown quantum well structures," *J.Vac.Sci.Technol.B*, vol.13, pp2381-2385, 1995.

[14]O.M.Steffensen, D.Birkedal, J.Hanberg, O.Albrektsen, S.W.Pang, "Invesigation of reactive-ion-induced damage of quantum wells by photoluminescence," *J.Appl.Phys.* vol.78, pp1528-1532, 1995.

[15]B.C.Qui, Internal Report.

[16]S.D.Brorson, T.Frank, S.Bischoff, L.Prip, M.Hofmann, J.M.Nielsen, and J.Mork, "Pulsewidth dependence upon gain current and absorber voltage in monolithic CPM lasers," submitted to *IEEE Photon.Technol.Lett* 1997

Chapter 9- Summary and Conclusions.

The most important achievements that have been presented in this thesis are as follows:

1:- The first intensity autocorrelation measurements on the output of monolithic CPM quantum well lasers in the GaAs/AlGaAs material system have been performed, with the results showing the production of ~1 ps transform-limited mode-locked pulses at repetition rates of up to 175 GHz.

2:- A new multi-contact laser technique has been developed for the measurement of gain and loss from forward and reverse biased semiconductor laser material. This technique has been applied to provide the first *in situ* characterisation of the effect of reverse and forward bias on the saturable absorber region of a mode-locked diode laser.

3:- Clear experimental evidence has been presented for the crucial role played by doping in the achievement of high repetition rate monolithic mode-locking in GaAs/AlGaAs quantum well lasers.

4:- Etching techniques for the production of reliable ridge waveguide lasers in the InP/InGaAs/InGaAsP laser material system have been improved, allowing the successful fabrication and operation of CPM lasers at the low loss communications wavelength around 1.55 μm.

5:- The first demonstration of a long wavelength MCPM laser has been achieved, with frequency domain evidence indicating two-pulse and four pulse MCPM behaviour at 150 GHz and 300 GHz.

This work has been concerned with the fabrication and characterisation of monolithic CPM quantum well lasers, in both the short wavelength GaAs/AlGaAs and long wavelength InP/InGaAs/InGaAsP material systems. Some of the numerous potential applications for high repetition rate short pulse laser sources were introduced in Chapter 1, providing ample practical motivation for the study of CPM lasers in both these wavelength ranges. In this final chapter, the work presented in this thesis is summarised, with the most important conclusions and insights discussed.

A broad introduction to semiconductor lasers was provided in Chapter 2. It was shown how optical gain can be generated in externally pumped semiconductor p-n junctions, and how by engineering the bandgap and refractive index through heterostructure epitaxial growth, practical room temperature operation of

semiconductor lasers could be realised. In addition to this was a discussion of the benefits of introducing a refractive index variation parallel to the heterojunction in the form of a ridge waveguide, and the effects of the reducing the active region of a semiconductor heterostructure laser to quantum dimensions. By modelling semiconductor quantum wells using the infinite potential well approximation, it was shown how a set of discrete sub-bands are produced for the energy of the confined electrons and heavy/light holes. The corresponding step-like density of states results in a higher band edge carrier population density, and hence a larger differential gain, during operation than in conventional bulk active region devices. The polarisation of carrier momentum in the plane of a quantum well also leads to polarisation dependent optical gain, with enhancement for TE polarised light due to interaction with both heavy and light hole transitions, compared with TM which can only interact with the light hole. The use of multiple quantum wells to form the active region was shown to have some advantages over single quantum wells, such as an increase in the overlap of the gain to the optical mode, an increase in the differential gain, and an increase in the current at which gain saturation takes place. The increase in the differential gain in quantum well lasers is important for short pulse generation in semiconductor lasers since the corresponding decrease in the linewidth enhancement factor leads to lower levels of self-phase modulation and chirp. Some effects of quantum confinement on the absorption spectrum of a semiconductor quantum wells were also studied, such as the observation of exciton features at each sub-band edge at room temperature. At the conclusion of Chapter 1, a description of the quantum confined Stark effect (QCSE), observed through absorption spectra measurements on the application of electric fields perpendicular to the plane of a quantum well, was included due to the important role that the QCSE plays in controlling saturable absorption in monolithic mode-locked quantum well diode lasers.

In Chapter 3, the methods used to produce short pulses from semiconductor lasers were discussed: namely gain switching, Q-switching, and mode-locking. It was shown that multi-quantum well material was ideal for the production of monolithic cavity mode-locked diode lasers. Because of their highly sub-linear gain-current characteristics, quantum well structures allow the vital condition of fast absorption saturation compared to gain saturation to be fulfilled in the same material, with merely a change in the biasing conditions required. Due to simple electric field control of the energy of the absorption band edge through the QCSE, and the associated ultrafast exciton dynamics, the condition of fast absorption recovery is fulfilled. The evolution of monolithic passive mode-locking in diode lasers was discussed, and the case was presented for the placing of the saturable absorber in the centre of the multi-quantum well diode laser cavity to form a CPM laser, with the added pulse shortening effects allowing the formation of near transform-limited mode-locked pulses.

Chapter 4 described the fabrication technology used in this project to produce CPM lasers in the GaAs/AlGaAs quantum well material system. The method presented here was used for both the MOVPE grown and MBE grown GaAs/AlGaAs lasers. The availability of the low damage $SiCl_4$ dry etching was vital for the successful realisation of these devices. In this chapter, it was shown that devices fabricated from 4 QW MOVPE grown laser material produced the characteristic frequency doubling associated with the attainment of CPM action in diode lasers. These devices also included a side-injection waveguide perpendicular to the normal laser waveguide. The results illustrate that mode-locking behaviour can still be observed with this T-junction type geometry. The mode-locked output of the T-CPM lasers was studied using autocorrelation techniques, and is reported in Chapter 5. Using the non-linear autocorrelation, it was shown that the pulses produced from a 400 μm T-CPM laser were transform-limited with pulsewidths in the order of 1 ps and repeated at a rate of 175 GHz. This result is consistent with the work published by other researchers who have shown that in InP based devices operating around 1.55 μm that short cavity CPM lasers produced essentially transform-limited pulses.

Along with the confirmation that the T-CPM lasers were mode-locked and produced transform-limited pulses, there were other interesting conclusions that could be drawn from the simulations and experimental studies of linear and non-linear correlations presented in Chapter 5. The linear field correlation technique was easier to implement than the non-linear correlation technique, because of the low pulse powers available from the T-CPM lasers. However, the theory and simulations showed that even when a multi-longitudinal mode laser was not operating in a mode-locked regime, peaks were still produced in the linear correlation. The simulations also showed that mode-locking and incoherent multi-mode behaviour could be distinguished by observation of the cross-correlation terms, which in the latter case rapidly die out with increasing path difference. This was corroborated from the experimental results, with the observation of increased inter-pulse coherence from the output of a T-CPM laser when it was operated with a CPM type doubled spectrum. The simulation of an intensity correlation on the output of a multi-mode laser showed that mode-locking action could be determined by inspection of the autocorrelation peak-to-background contrast ratio, and that this ratio converged on a value of 3:1 (in non-background free measurements) as the pulse modulation depth increased towards 100 %.

The saturable absorber absorption spectra of the MOVPE grown T-CPM lasers were studied using the new two-section laser technique presented in Chapter 6. It was shown that there was a large exciton absorption feature in the saturable absorber of these devices. In these measurements the TM absorption spectra contained a single peak, corresponding to the light hole exciton only. However the TE spectra showed a much broader peak, indicating the contributions from both the heavy and light hole

transitions, although these could not be individually resolved with the light hole appearing as a slight shoulder on the high energy side of the main heavy hole exciton peak. The lack of resolution of the light and heavy hole peaks was demonstrated to be due to the presence of unintentionally incorporated carbon impurities in the active regions of MOVPE grown GaAs/AlGaAs laser material. These appear at levels of 10^{16} cm^{-2} and above due to the strong aluminium carbon bond present in the trimethylaluminium, which is used as the source of aluminium during the growth of the AlGaAs layers. The exciton absorption peaks were shown to shift to lower energy and broaden with the application of a reverse bias voltage. This was broadly in line with the predictions of the QCSE, aside from the field dependence of the shift which varied almost linearly with the strength of the applied field, rather than the field squared dependence predicted from theory, although this could be explained by including the effect of the built-in electric field due to the p-i-n laser structure. A broadening of the absorption edge tail following the quantum confined Franz-Keldysh effect was also observed. By using the two-section measurement technique with the absorber forward biased, the sub-linear gain-current density curve was obtained for the MOVPE GaAs/AlGaAs wafer. This showed a good fit with the standard logarithmic relationship for quantum well lasers.

Although the new two-contact laser absorption spectra measurement technique was successful in producing results in broad agreement with theoretical considerations, there is one outstanding problem which limits its full and successful exploitation - accurate measurement of the reference spectrum. This is extremely important because all subsequent measurements are compared with the reference spectrum, to obtain the magnitude of the absorption coefficient. Without an accurate reference level, the absolute value of the absorption coefficient could contain a systematic error of up to the level of a few hundred cm^{-1}, depending on the level of gain present in the absorber region during the measurement of the reference spectrum.

Chapter 7 described the fabrication of CPM and MCPM lasers from GaAs/AlGaAs quantum well structures grown by MBE. It was found that only by p-doping the quantum well active region with beryllium to emulate the background carbon impurities present in the successful MOVPE mode-locked laser wafers, CPM and MCPM spectra could be obtained. On observation of the absorption spectra of intentionally and unintentionally background doped MBE material, it could be seen that the presence of doping had an effect on the form of the exciton absorption peaks at the n=1 transition. In contrast to the MOVPE quantum well laser material, the TE absorption spectrum of an unintentionally doped MBE sample showed two individually resolved peaks at the absorption band edge, corresponding to the heavy and light hole transitions. With the addition of active region background doping to the MBE material, the two peaks became broadened and unresolved, similar to the spectra observed from the MOVPE

material. With the assumption that only homogeneous broadening was present, the decrease in the associated exciton lifetime was estimated to be 166 fs to 105 fs with the inclusion of intentional p-doping. These results indicate that high p-doping levels in the quantum wells, unintentionally incorporated in the MOVPE material, and intentionally incorporated in the MBE material, have a beneficial effect on the non-linear excitonic absorption features, introducing a sufficiently fast component to the absorber recovery to allow high repetition rate mode-locking to occur in these short cavity CPM and MCPM lasers. This conclusion should be confirmed by the performance of time resolved absorption recovery measurements on back-doped and standard MBE material.

The availability of the low damage $SiCl_4$ dry etching allowed the straightforward fabrication of T-CPM and MCPM lasers in the GaAs/AlGaAs material system. In Chapter 8 the standard CH_4/H_2 dry etching of InP based laser material was shown to produce passivation and luminescence damage effects. By using low etch power and bias, and heat treating the surface after etching, it was shown that ridge-waveguide lasers in MOVPE grown InGaAs/InGaAsP quantum well material could be successfully fabricated using dry etching, with threshold currents and efficiencies comparable to lasers which were exclusively wet etched. CPM action was observed from spectral measurements of wet etched lasers produced from both lattice matched, and strained layer long wavelength material. T-CPM lasers, using dry etching to ensure uniform vertical etch profile on both waveguides, were also shown to produce CPM type doubled spectra. Increasing asymmetry in the CPM spectra of operating lasers as current levels increased could indicate the presence of self-phase modulation or coincidental self-pulsation behaviour, and this should be investigated using time-domain measurements such as intensity autocorrelation. The final result presented in this thesis, shows the first experimental evidence (to the authors knowledge) of multiple colliding pulse operation of a long wavelength diode laser, with a 600 μm InGaAs strained layer laser operating at a wavelength 1.53 μm, mode-locking at 150 GHz and 300 GHz.